Final Scientific/Technical Report

Federal Agency and Organization Element

U.S. Department of Energy
National Energy Technology Laboratory [DOE-NETL]

Funding Opportunity Number

DE-FE0028320 [SubTER]: Area of Interest 1

Project Title

Charged Wellbore Casing Controlled Source Electromagnetics (CWC-CSEM) for Reservoir Imaging and Monitoring

Principal Investigator / Submitting Official / PI's Organization

Dr. Yaoguo Li
Colorado School of Mines
Department of Geophysics
1500 Illinois St., Golden, CO 80401

Teaming Members

Colorado School of Mines	University of Utah	New Mexico Tech
Yaoguo Li	Trevor Irons	William Ampomah
Richard Krahenbuhl	Nathan Moodie	Qian Sun
W. Anderson McAliley	Brian McPherson	Robert Balch

United States Geological Survey
Benjamin Bloss

Submission Date

October 30, 2020

Project Period

10/1/2016 – 7/31/2020

Limitations On Public Release

None

Signature of Submitting Official

10/30/2020

ACKNOWLEDGEMENT OF FEDERAL FUNDING

This material is based upon work supported by the U.S. Department of Energy, National Energy Technology Laboratory [DOE-NETL], under Award Number DE-FE0028320.

DISCLAIMER

1. EXECUTIVE SUMMARY

This project addresses the needs of the U.S. Department of Energy (DOE) to develop advanced monitoring technologies and protocols to track the fate of subsurface carbon dioxide (CO2) plumes for carbon storage. Specifically, the project seeks to develop and test a unique and novel system of technologies consisting of electromagnetic data acquisition, coupled multiphysics imaging, and reservoir model enhancement to understand the migration and long-term distribution of CO2 in the subsurface. The overarching objective is to develop an integrated approach for long term monitoring of carbon storage.

The two main components of the project include the methodology development and the test of the method at a field site. The methodology component consists of

1) developing the field procedure and protocol for collecting time-lapse controlled-source electromagnetic (CSEM) data with source electric current injected into the subsurface through wellbore casings;
2) building of background 3D electrical conductivity utilizing multiple sources of data such as supplemental surface transient EM (TEM) surveys, well-logs, and seismic structural information, for enhancing CSEM signal from reservoir depths; and
3) coupled multiphysics simulations and inversion of CSEM data constrained by production data and by structural information from seismic imaging of the reservoir and overlying formations.

The testing component used the field site of Bell Creek Oil Field, which served both as a field laboratory for the method development as well as a test site to evaluate the CSEM signal strengths and the methodology developed in this research project.

We have accomplished all the proposed tasks and developed the methodology as planned. These include the procedure for time-lapse CSEM data acquisition, data processing techniques, integration with 3D conductivity model building, fast reservoir simulation for history matching using machine learning, and interpreting CSEM data with coupling to the reservoir modeling. Collectively, the outcome of these tasks form a coherent workflow that can be applied to monitor dedicated carbon storage in saline reservoirs. The testing component evaluated the applicability and limitations of the method, and concluded that the method would be ideal for monitoring dedicated carbon storage sites utilizing saline reservoirs.

2. PROJECT OVERVIEW

2.1 ORIGINAL PROBLEM STATEMENT

The challenges faced in a carbon capture and storage (CCS) project are due to a unique blend of environmental, economic, logistical, and technical challenges. The result is a challenging mix of tradeoffs in CCS design choices. In an effort to ensure storage permanence, CO2 is typically injected at depths of several kilometers; these depths, however, make monitoring much more difficult and expensive. The depths also decrease resolution of low-cost monitoring techniques such as electromagnetic methods that rely on diffusive fields. In many cases brownfield oil reservoirs are utilized as CCS or EOR-CCS sites for economic reasons of existing infrastructure as well as the economic benefits of producing hydrocarbons simultaneously with CO2 storage. In these instances, geologic seals are known to be of good integrity, and the most likely scenario for leakage is through a wellbore casing (Gasda et al., 2004; Carey et al., 2007), or fault.

State-of-the-art monitoring of CCS projects, in order to ensure long term storage permanence, relies upon a combination of technologies including deep seismic methods, reservoir modeling based on site characterization, and surface-based measurements. Incorporating these signals into a (reasonably-autonomous) dynamic intelligent monitoring system remains a noble goal for long term monitoring. However, many of the (surface-based) monitoring technologies are not responsive to changes in the reservoir, and are more suitable for detecting catastrophic leaks. Embedded sensors are responsive, but often provide information only in the immediate vicinity of the sensor. Furthermore, costs associated with the permanent installation of sensors at the depths of most CCS projects are prohibitive--a single drill hole can cost on the order of a million dollars in many instances. There is a pressing need for cost-effective, deeply responsive monitoring solutions.

For these reasons management of a CCS project is generally attacked in a multi-faceted approach incorporating geologic and reservoir characterization, reservoir simulation, risk analysis, and monitoring. Monitoring technologies include surface based CO2 sensors (i.e., eddy-covariance sensors https://www.licor.com/env/products/eddy_covariance/) as well as borehole monitoring technologies and sensors (i.e., micro-seismic, reservoir pressure and temperature), and geophysical monitoring.

Surface based direct CO2 detection sensors offer an important last line of defense against catastrophic leakage, but are not generally sensitive to movement of CO2 at depth. Monitoring wells equipped with sensors are an important component of a CCS management strategy, but they are generally too expensive to be deployed in even sparse sampling patterns. Reservoir modeling is a powerful CCS tool that is relied upon heavily. The quality of the models is dependent upon good site characterization, data, and modeling skills. While reservoir models do provide information about CO2 movement within the reservoir, validation of the model is difficult with sparse data. Therefore, the uncertainties around models are often large, and managing the risks associated with these uncertainties is a complicated undertaking.

For these reasons geophysical methods represent the most practical way to acquire spatial information about CO2 migration in a CCS project. The development of such information would be readily accommodated by existing CCS workflows. Seismic methods are a natural consideration due to the depths in question. However, time lapse active source seismic is generally prohibitively expensive to use as a routine monitoring technology. Passive seismic can be used to identify faults and pressure changes, but may not provide coverage of the entire reservoir. Furthermore, seismic attributes are not directly related to subsurface fluid typing and may not be sensitive to the migration of CO2 within the reservoir. Gravity methods are promising due to the direct sensitivity to changes in fluid density, but in many CCS reservoirs the signal is too weak to reliably measure and interpret (Krahenbuhl et al., 2011).

We believe that two major technological components are available to develop one such monitoring solution that is low-cost and responsive to CO2 migration at large depths:

1. In the offshore oil industry, controlled-source electromagnetics (CSEM) have earned the reputation of a cost-effective de-risking technology capable of imaging resistors within conductive media. Geologic storage of CO2 presents a similar challenge: the CO2 plume is generally resistive while brines at depth are conductive. Meanwhile, sufficient understanding and field trials have been achieved on a specific variant of the CSEM which utilizes the wellbore casing as energizing electrodes and measures data on the ground surface.
2. There have been significant advances in both coupled modeling of multiphysics data and constrained inversion of geophysical data for reservoir monitoring in oil and gas production. A related advancement is in connecting reservoir simulation results to physical properties that are the basis for geophysical monitoring.

Electrical properties of porous rocks are known to be sensitive to the fluid composition in the interstitial space in a CCS environment (Börner et al., 2013). Geophysical methods for probing electrical conductivity at depth include electrical resistance tomography (ERT), induction EM, CSEM and magnetotellurics (MT). While ERT methods can be done from the surface, in order to obtain a sharp image at depth, it is usually necessary to utilize cross-well measurements. To complicate matters, electrodes must be electrically insulated from casing, or resistive casing must be used (Kiessling et al., 2010). In the case of monitoring deep storage, these requirements pose a significant economic hurdle. Surface based MT and audio-MT methods have the ability to image deep structures--and are therefore valuable exploration tools--but lack the resolution to discern subtle changes of interest in continuous monitoring. Induction EM is generally incapable of imaging the depths necessary for CCS monitoring, and is mostly sensitive to the presence of conductors.

In marine exploration, CSEM methods represent a mature technology that is relied upon to image resistors at depth. On land CSEM is a less common technique, but one which is increasingly being adopted (Streich, 2015). Typically, in CSEM galvanically coupled bipole transmitters inject current into the ground. The transmitters may operate either in the frequency or time domain. In the frequency domain, peak signal is expected in the 0.5-5 Hz range, above which it falls off quickly (Wiranto et al., 2010). The resulting electrical and magnetic fields are then measured on the surface. The electric field (**E**) measurements have been shown to be more sensitive to the presence of resistors at depth than the magnetic field (**H**) measurements, which are more sensitive to conductors. Therefore, land based CSEM utilizing **E** field measurements is a promising and emerging technique for monitoring CCS projects.

Grayver et al. (2014) demonstrate the utility of CSEM for a CCS project using surface based sources and electric-field receivers. Wirianto et al. (2010) demonstrate the benefits of using vertical sources with surface based electric field measurements, although they propose the equivalent/reciprocal case of a single receiver in a borehole and moving sources on the surface. Vilamajó et al. (2015) perform borehole to surface CSEM at a CCS site in Spain and achieve good quality data for a modest target. Their dipole transmitter was strongly influenced by the conductive casing even though it was insulated from it. Tang et al. (2015) present an analysis of the use of a charged wellbore casing (CWC) as a long galvanically coupled electrode. Groundmetrics recently commercially developed similar technology in their TCS-30 CSEM transmitter and capacitively-coupled **E** field receivers (www.groundmetrics.com).

Utilizing CSEM for monitoring CCS projects is therefore an emerging and promising technique, but not without its limitations. The benefit of either vertical electric field receivers or transmitters has been demonstrated numerous times. However, installing this capability is usually prohibitively expensive as it is not (currently) possible to retrofit existing boreholes. The resolution of CSEM is not stellar due to the diffusive nature of electric field propagation. Integration with reservoir and constrained interpretation are promising approaches to maximizing the available information (Liang et al., 2011), but more work is required to establish the relationship between change of electrical conductivity with CO2 distribution and migration. For these reasons, CSEM monitoring of CCS projects has not yet been widely adopted.

2.2 ORIGINAL HYPOTHESIS AND PROJECT APPROACH

We propose the use of legacy wellbore casings as long vertical current injection electrodes in CSEM monitoring at an active CCS-EOR project in order to demonstrate the responsiveness of the method to changes in subsurface fluid distribution. The sensitivity of such surveys has been established, but the technology has not yet been validated in an extended monitoring application.

The use of legacy wellbore casings as electrodes achieves an extraordinary reduction in costs compared to installation of dedicated vertical electrodes or monitoring wells capable of use in a CSEM survey. Any CCS project will contain at the very minimum the injection well, so the technique will be broadly applicable. Additionally, many CCS projects utilize brownfield oil fields due to the fact that such locations are well characterized, have validated and trusted geologic traps, and existing infrastructure. Additionally, injection of CO2 is an effective method for enhanced oil recovery (EOR), and as such external economic factors also can influence site selection.

In order to demonstrate that CWC-CSEM is a responsive technology it will be necessary to find a field site where the reservoir is expected to be dynamic and changing composition rapidly. Since CCS sites are carefully chosen such that leaks are extremely unlikely, this is a difficult condition to find. However, at EOR/CCS sites reservoir fluids are under a constant state of flux due to the utilization of water alternating gas (WAG) injection schedules which utilize alternating patterns of water floods after CO2 injection to chase oil out of the reservoir (**Figure 2.2.1**). Such a field site offers an exciting opportunity for imaging as each of the phases should have distinct electrical conductivity signatures. Imaging WAG cycles will demonstrate the responsiveness of the technique. Additionally, an EOR site allows for validation and calibration through the availability of production data. Having many production holes gives many pieces of validation information.

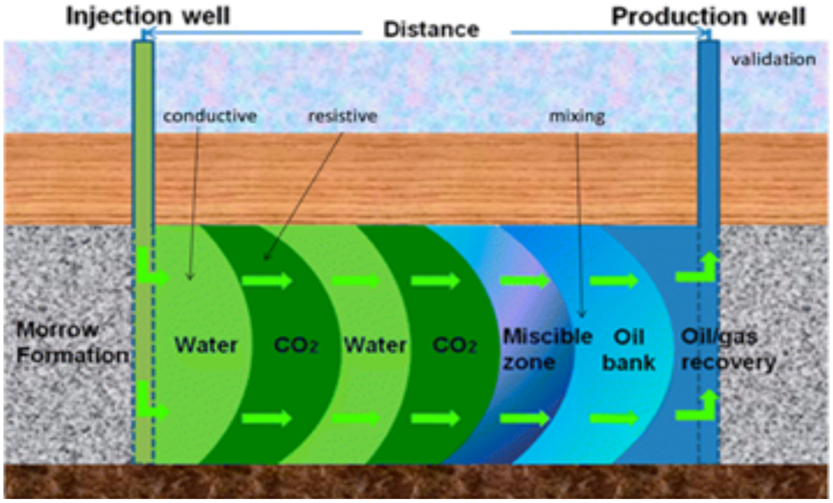

Figure 2.2.1. In a CCS/EOR site alternating injections of water and CO2 are utilized to release trapped gas. As each phase will have unique electrical conductivity signatures an EOR/CCS site is an ideal location for testing and validation of electrical property methods (figure adapted from Dai et al., 2014).

Surveys will utilize state of the art commercially available CSEM instrumentation. High power transmitters and 32 bit digitizers with a broad dynamic range will provide for high fidelity data to be acquired. Tradeoffs between capacitive- and galvanically coupled sensors are numerous. Capacitive sensors can be easier to install, especially in rugged terrain, and have a small footprint. Galvanic sensors have lower noise characteristics and tend to be better calibrated, with less repeatability errors (more stable). Proper calibration is critical for inversion (Minsley et al., 2014). For the proposed field site, installation of galvanic sensors in loose soil will not be problematic, and considering the need for stable time-lapse data, we elect to use galvanically coupled E field receiver sensors.

All receivers will be surface located in order to ensure no disruption in field operations at the active site. As a result, the proposed work will not require access to any borehole internals. Electrically coupling casings will be minimally disruptive to field operations, and due to the high power transmitter, we will have flexibility in which casings are needed for use as transmitters. Additionally, we prefer surface based receivers as measurements in multiple locations can be made simultaneously and do not require access to the wellbore interior. The downside of this approach is near surface sensitivity and noise. The use of 32 bit A:D converters along with noise mitigation algorithms, reference station noise cancellation (Oettinger et al., 2001), filtering, despiking, and digital processing can be employed. Rapidly acquired central loop sounding transient electromagnetic data will be collected in order to apply static corrections (Sternberg et al., 1988).

Previous demonstrations of CSEM to monitor CCS projects have focused on method validation and have not incorporated the well characterized reservoir geometry or production data into analysis and inversion. Constraining results with this information will maximize the available information. Since dissolved phase CO2 will have negligible impact on the electrical conductivity of brines, it is important to stress that the CSEM is not a standalone monitoring product. However, by integrating with reservoir models, the reliability of the models can be improved and better understanding of the geospatial distribution of CO2 can be achieved. Furthermore, as we are imaging the whole overburden, leaks will also be detected, where the effects of CO2 in the dissolved phase of fresh water will be discernible.

Integration of CWC-CSEM into an effective monitoring program requires establishing mechanisms to get information both to the reservoir model and from it. This need will impact nearly all activities of the project. The first stages of the project will involve forward modeling the CWC-CSEM response at the field site based on an initial relationship between saturations and electrical conductivity. This relationship will be revisited throughout the project and refined as more information is made available. Coupled modeling capabilities will allow for the simulation of CWC-CSEM data directly from reservoir models. This capability will enable novel statistical analysis of the uncertainty of reservoir parameters with respect to electrical ones.

A conceptual flowchart of the proposed project is illustrated in **Figure 2.2.2**. The overarching objective is to improve the reservoir model through integration of geophysical monitoring data. The starting point of the proposed methodology consists of the existing reservoir model (green oval), seismic imaging and production data (gray ovals) that were used to build the reservoir model. We carry out time-lapse monitoring using charged well-casing CSEM at the site. A near-surface EM survey will also be conducted to deal with statics caused by near-surface inhomogeneity. The EM data will be interpreted through constrained and coupled inversion with constraints from seismic image of the reservoir and from production data. The electrical conductivity will be linked to fluid saturations and reservoir porosity via Archie's law. The reservoir properties imaged from EM inversions will be integrated back into the reservoir model for refinement. The components inside the dashed green rectangle are those within the proposed project, and the gray ovals outside are available at the site for use in the project.

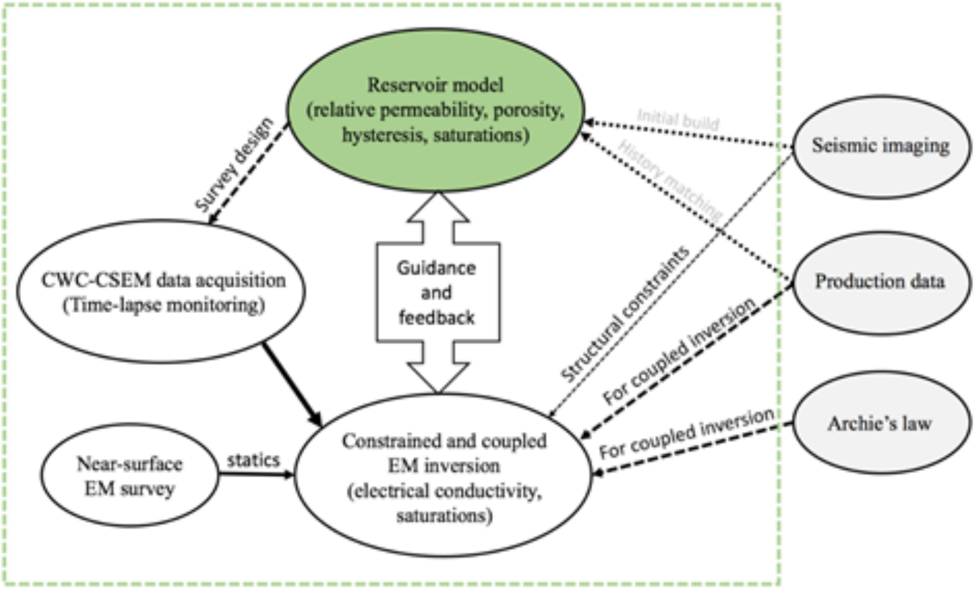

Figure 2.2.2. The proposed project with essential components and their relationship.

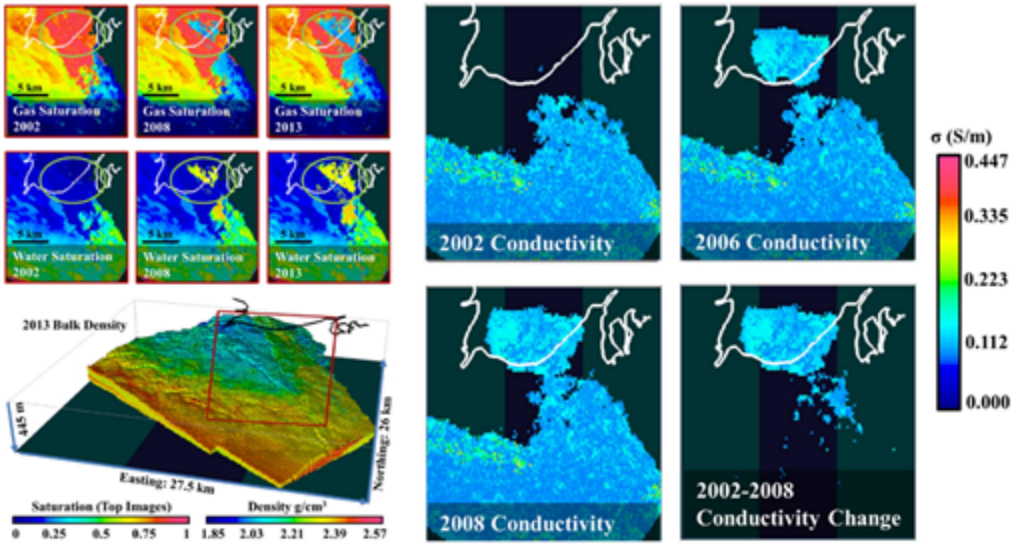

Figure 2.2.3. Example reservoir models for Prudhoe Bay converted to electrical conductivity. The upper left panel illustrates gas and water saturations within the reservoir at different epochs, and the lower left image is the reservoir density distribution. The remaining panels are the developed 3D distributions of electrical conductivity and conductivity change for the same epochs by combining the saturations and porosity (not shown) from the reservoir models (Krahenbuhl et al., 2016).

An important and unique component of the proposed project is the integration of the reservoir models and production data with geophysical monitoring. The reservoir simulations both guide the geophysical monitoring design and receive feedback from the geophysical monitoring. A crucial technology to support this endeavor is the linkage between the reservoir model with geophysical properties. **Figure 2.2.3** highlights the advances in this arena with application to Prudhoe Bay gas-cap water injection (Krahenbuhl et al, 2016). Additional work is required for adaptation to CCS with site specific information, and the essential capability and expertise are available.

A detailed reservoir model exists at FWU with the full suite of reservoir properties. Based on it, reservoir simulations can be carried out to meet the needs of the proposed project. **Figure 2.2.4** displays a depth slice of the porosity distribution extracted from the FWU reservoir model.

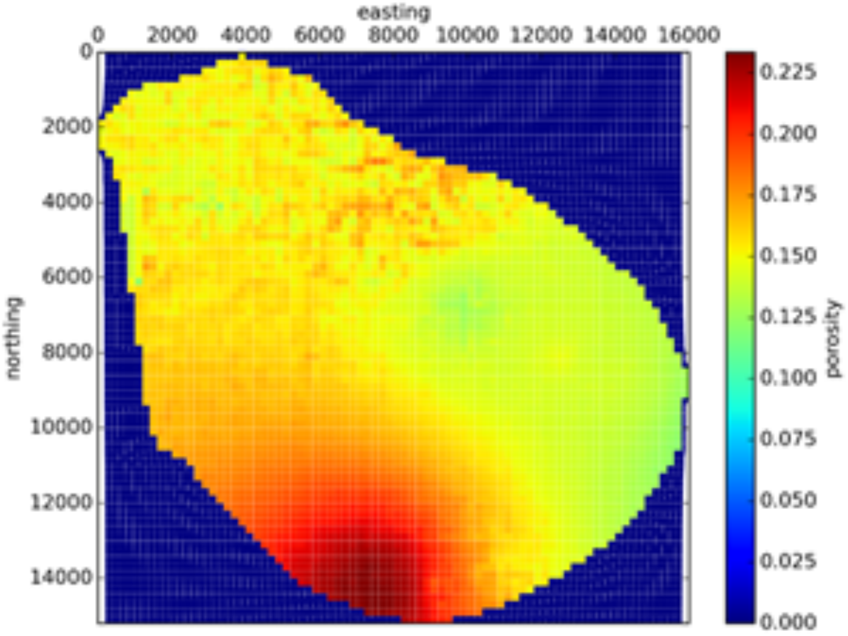

Figure 2.2.4. Porosity distribution at a depth slice within the FWU field site from the reservoir model.

2.3 ORIGINAL PROJECT OBJECTIVES

The objectives of the project are to:

- Demonstrate the use of CWC-CSEM as an effective tool for time lapse monitoring and large scale imaging of CO2 in the subsurface within the context of a CCS project.
- Leverage other monitoring techniques and data in order to establish relationships between electrical conductivity.
- Develop coupled modeling capabilities such that reservoir models can be directly input

into electrical modeling algorithms.

- Utilize prior knowledge of the field site and near surface electromagnetics into a constrained inversion of the CWC-CSEM data.
- Develop an integrated framework for inversion and analysis of CWC-CSEM data
- Revisit history matching of production data in conjunction with CWC-CSEM derived reservoir parameters. This step will allow for the reintegration of the monitoring technology into the reservoir model.

2.4 ORIGINAL PROJECT FIELD SITE

We propose collecting data at the Farnsworth field unit (FWU), which is the active CCS-EOR site, utilized by the Southwest Regional Partnership (SWP) on Carbon Sequestration, a DOE-NETL funded project. As such the FWU is well characterized, monitored, and studied. The FWU is located in the Anadarko Basin in northern Texas.

2.5 FIELD SITE CHANGE: FARNSWORTH UNIT TO BELL CREEK

Securing and retaining access to the originally proposed field site location represented one of the biggest project risks. During the second quarter of the project, the team was informed that major changes in management would be occurring at Chaparral Energy, LLC (operator of Farnsworth Unit) the proposed field site for data collection and simulation. These structural changes at Chaparral were in response to low oil prices which resulted in a Ch. 11 bankruptcy restructuring for the company. For these reasons, Chaparral necessarily adopted a policy of declining any research opportunities that could possibly incur cost. As such, Chaparral energy informed the team of their decision to decline our request for performing extensive CWC-CSEM surveys using Chaparral owned boreholes. This notification presented a significant set-back for the project as reservoir modeling, EM simulations, and field planning for Farnsworth had already begun. We immediately began the process of investigating alternative field sites for the project. The most promising development toward this occurred through multiple conversations, over phone and in person, with representatives from Denbury Resources Inc. Denbury is an industry leader in CO2-EOR operations and was excited to apply and utilize state-of-the-art imaging and monitoring technologies at their CO2-EOR sites. Denbury have expressed a keen interest in collaboration. Denbury would not only allow our project access to one of their CO2 EOR sites, but they have expressed a strong interest in our project outcomes and they have offered several reservoir site options as a result. This includes site access, as well as the reservoir simulation models, seismic, injection and production data, all of which are critical for the SubTER project. The most promising site from their list for our purposes is the Bell Creek reservoir in Montana. The reasons we identified this site as a promising alternative project location were as follows:

- There was an existing agreement between Denbury and CSM for Bell Creek that could be easily extended to the SubTER project
- The Phase 5 area of interest at Bell Creek had not seen any CO2 yet, which is ideal for instigating a monitoring project.
- Extensive production data are available allowing for the history matching objectives of the

project to be retained
- CO2 injection would begin within a few months, aligning closely (although slightly delayed) with the timing of the project
- There is a large collection of boreholes available for use as electrodes to energize the subsurface, which is essential for the CWC-CSEM surveys.
- Surface land ownership and use at Bell Creek are simpler than at FWU where extensive agricultural use limited survey access depending on the season and crop rotation schedule.

In the third project quarter we requested approval from NETL for the site change and this was approved. The contract with Denbury and EERC began immediately and a formal agreement was signed between CSM and Denbury Resources Inc by the fourth quarter.

2.6 ORIGINAL IMPACT STATEMENT

There is a need for the development of responsive monitoring techniques for CCS projects capable of long term monitoring and verification of storage permanence. This is due to a lack of cost-effective tools that are able to probe to the required depths and be sensitive to changes in the makeup of storage reservoir fluids. Responsive monitoring technologies need to be sensitive not only to the distribution of CO2 within the reservoir, but also in any part of the overburden where leakage may occur.

The proposed project is designed to validate and address the requirements stated above. The proposed technology relies upon legacy infrastructure and will require a minimal amount of hardware installation. It will be possible to install sensors permanently with minimal additional effort. The choice of an EOR-CCS site was made in order to validate the responsive nature of the method and to leverage existing efforts by DOE-NETL in this arena. At the field site the operator's use of water alternating gas injection patterns will provide a distinct imaging target.

3. METHODOLOGY

Here we describe the methodology for all aspects of the project, and the workflow from data collection through reservoir modeling to comparing possible conductivity models and inversion for reservoir conductivity. The first step is geophysical data acquisition. Next, an initial reservoir model is developed, and a machine learning-assisted history matching workflow produces a suite of plausible reservoir saturation cases. These saturation models are converted to electrical conductivity models. Then, the processed geophysical data can be compared with modeled data for each of the saturation cases to distinguish between them. Additionally, we propose a method to directly and efficiently invert the geophysical data for reservoir conductivity. Reservoir saturations can be interpreted from this inversion result.

3.1 SURVEY DESIGN & DATA ACQUISITION

Data acquisition consists of the collection of two types of geophysical data: time-lapse controlled source electromagnetic (CSEM) data, and transient electromagnetic (TEM) data. Here we describe the methods used to collect these data. Four data collection campaigns were carried out at the Bell Creek field, spanning nearly two years. The dates of the campaigns were October 10-18, 2017, May 25-June 6 2018, September 30-October 12, 2018, and July 14-26, 2019.

Controlled source electromagnetic survey

The CSEM field campaigns were carried out as follows. We connected a 30 kW Zonge GGT-30 transmitter to two well casings at a time. During the first two campaigns, we used two 12 AWG transmitter wires per casing running in parallel to minimize resistance. However, we found that we could achieve the same amount of current with a cleaner transmission signal (one that more closely resembled a square wave) using a single 10 AWG wire, and did so in the last two campaigns. Generally, well casings were used as both of the transmitter electrodes. Transmitter wells were spaced about 2 km apart (**Figure 3.1.1**). We used three wells in any given campaign, transmitting between two wells at a time. One well pair was oriented in the northeast-southwest direction, and the other in the east-west direction. One well was shared between both pairs.

We transmitted a 100% duty cycle square waveform at a range of frequencies between 0.125 Hz and 16 Hz, logarithmically spaced by a factor of two. In addition, we transmitted at 0.125 Hz with a 50% duty cycle. The duty cycle refers to the percentage of the current transmission waveform that is non-zero; a 100% duty cycle indicates a square wave that toggles between positive and negative current, and a 50% duty cycle corresponds to a waveform that cycles between four stages: positive current, zero current, negative current, and zero current. One transmission "sweep" consisted of transmitting at least 64 periods at each frequency, from lowest to highest, followed by sixteen periods at 0.125 Hz with a 50% duty cycle (**Table 3.1.1**). We ensured that every receiver recorded data during at least three sweeps per well pair. The transmitter signal was recorded at a sampling rate of 4096 Hz. The nominal transmitted current was 30 A, which required output voltage between 200 V and 600 V, depending on the well pair.

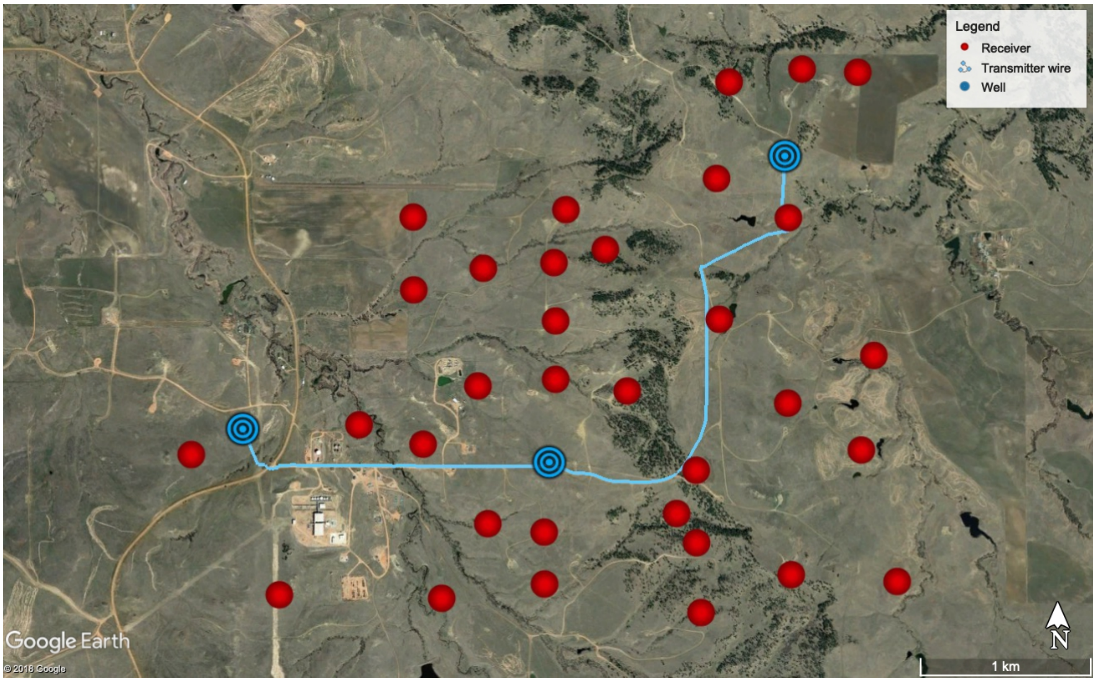

Figure 3.1.1: CSEM survey layout for the May 2018 campaign. Red dots indicate receiver locations. Blue dots represent the wells used as transmitter electrodes, and the blue lines represent transmitter wires.

Table 3.1.1: CSEM transmission sweep schedule, in the order transmissions were carried out.

Frequency, Hz	Duty cycle	Number of periods	Duration, min:sec
0.125	100%	64	8:32
0.25	100%	96	6:24
0.5	100%	128	4:16
1	100%	192	3:12
2	100%	256	2:08
4	100%	256	1:04
8	100%	512	1:04
16	100%	1024	1:04
0.125	50%	16	2:08

Receiver stations were spaced roughly 400m apart. Zonge Zen receivers logged data at a sampling rate of 4096 Hz during active transmission. Receivers measured two horizontal components of the electric field at every station. Non-polarizing Ag-AgCl electrodes were used. 100m receiver electric dipoles were placed in an 'L' configuration, allowing orthogonal dipoles to share one electrode. The high impedance of the Zens' input channels ensured that the measurements of the two components of the electric field would remain independent, despite sharing a common electrode. Two or three spatial components of the magnetic field were also measured at most stations. Zonge Ant-4 magnetic coils were used to measure the orthogonal magnetic fields. Overnight, the receivers assumed a passive magnetotelluric recording schedule, logging data at 256 Hz with short intervals at 4096 Hz. See the CSEM survey results section for information about the final survey geometry.

Transient electromagnetic survey

Transient electromagnetic (TEM) soundings provide information about near-surface conductivity. While these data are not sensitive to the conductivity of the reservoir, they do provide useful information about near-surface conductivity which aids in the interpretation of the CSEM data. Twenty TEM stations were collected using an ABEM WalkTEM. **Figure 3.1.2** shows the locations of the stations. All transmitter loops were 40x40 m. At each location, a series of measurements were taken using two centrally located in-loop receivers with effective areas of 5 m^2 (RC005) and 200 m^2 (RC200), respectively. Additionally, two transmitter moments were used: 1) low moment (LM) - 1 turn; ~1 Ampere current, 2) high moment (HM) - 1 turn; ~seven Ampere current. Typically, a sounding consisted of six measurements repeated 25 times. These six measurements consist of four transmitter moment-receiver pairs (LM-RC005, LM-RC200, HM-RC005, and HM-RC200) and two noise measurements (No-RC005 and No-RC200) are recorded during a period with no transmissions. Each measurement spans 39 logarithmically-spaced time windows, ranging from 0.01 ms to 5 ms.

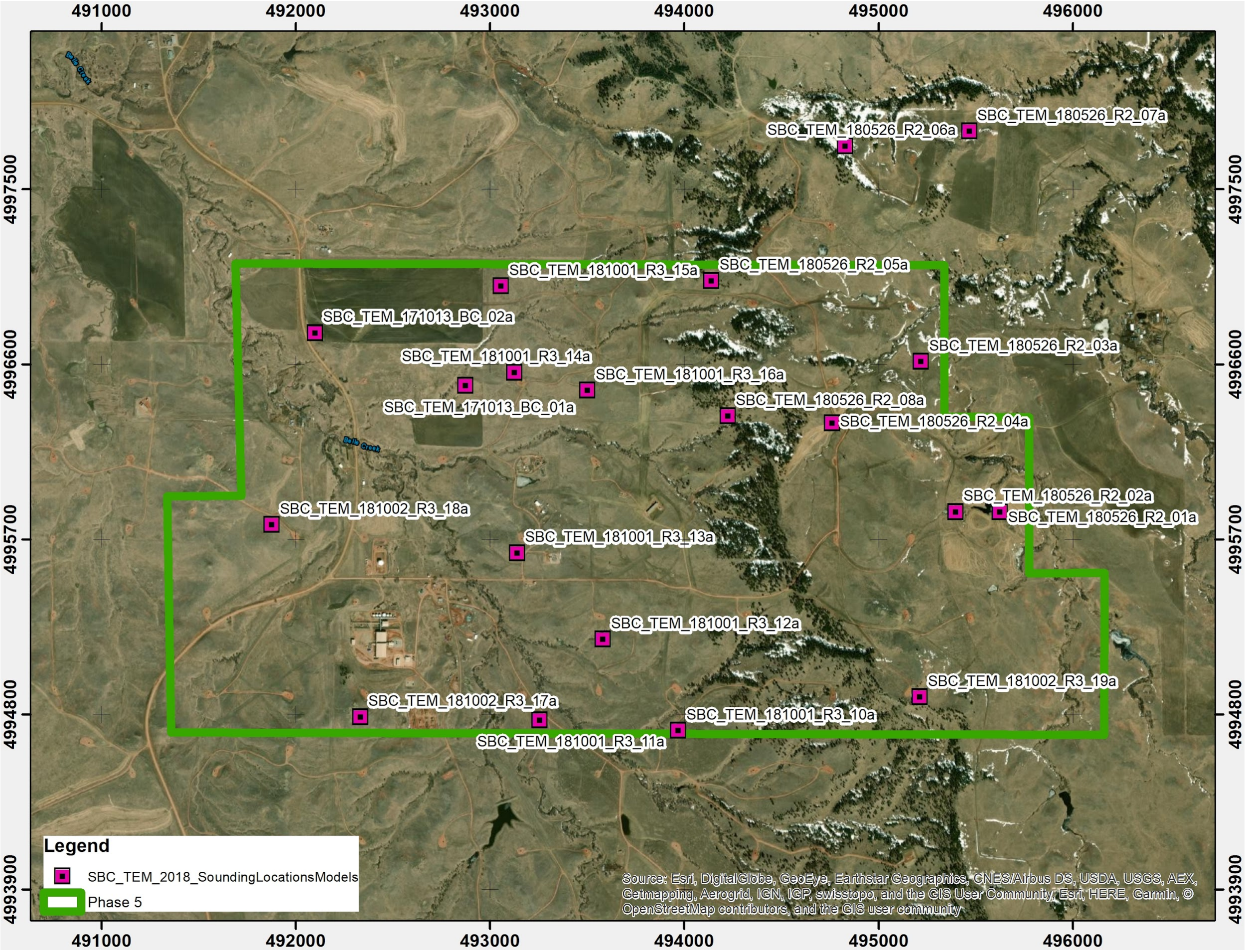

Source: Esri, DigitalGlobe, GeoEye, Earthstar Geographics, CNES/Airbus DS, USDA, USGS, AEX, Getmapping, Aerogrid, IGN, IGP, swisstopo, and the GIS User Community, Esri, HERE, Garmin, © OpenStreetMap contributors, and the GIS user community

Figure 3.1.2: TEM survey layout. Pruple squares indicate TEM station locations. These stations were not all occupied in a single campaign, but rather the data were accumulated over the course of multiple campaigns.

3.2 RESERVOIR SIMULATION

Bell Creek Model Development

EERC Model and Data

The initial geologic model was provided to the SubTER team by the Energy & Environmental Research Center (EERC) in a Petrel© project and a suite of ancillary data within the 'Curator Data Set.' It contained well information, historical production and injection data, formation surfaces for all the formations from the Pierre to the Skull Creek, LAS well logs, limited pressure and temperature data, a static output (rescue file) from the Eclipse simulator, and surface infrastructure maps. The Petrel project contained detailed 3D data for the Shell Creek, Springen Ranch, Bell Creek Sands (Muddy), and Rozet formations, including facies, total porosity, effective porosity, permeability, water saturation, and formation pressure. All of the wells within the EERC model boundary were included along with any associated well logs. **Appendix A3.1** contains the complete list of data supplied by EERC.

A couple of deficiencies with this model required that we rebuild the model from scratch and history match it to get the water saturation and conductivity distribution for the reservoir for the dates we were in the field. First, the EERC model did not include a fluid model with oil properties and water salinity, relative permeability and capillary pressure data, and injection and production bottom-hole pressure limits. There was also no time associated with any initial properties, such as water saturation and pressure distributions. Without a known date for this data, we could not use it. Following up with EERC about this missing data, we received no response and excluded it from our study. Secondly, and more importantly, our survey area extended beyond the EERC model's northern boundary, requiring the extension to the north.

Fluid model

A fluid model, including oil properties and water salinity, was not included in the Curator dataset from EERC. Through discussions with the field engineers and site operators and tools available in Petrel, we were able to estimate a compositional oil model consistent with an oil lacking the light volatiles like methane and ethane. We obtained water chemistry data from the operator during the field survey campaign in May 2018.

Fluid properties estimations

Analysis of production data and conversations with the site operator indicates that there has been minimal historical production of methane (C1) or other volatiles (C2 – C4), and the reservoir is mostly heavy oil components. For this reason, the lightest oil components have been removed or set to a low fraction while the heaviest components are assigned to the highest fraction. It is also assumed no CO_2 is naturally present. After testing, we developed a nine component compositional oil model that is believed to broadly represent the oil at Bell Creek (**Table 3.2.1**). The phase envelope and fingerprint plots for the oil model are shown in **Figure 3.2.1**.

Table 3.2.1. Compositional Oil Model representing the volatile depleted state seen at Bell Creek. The study site's oil is considered a 'dead oil,' with the low mass volatiles (C1 thru C4) removed or set to a low fraction. The heavy oil components dominate the fluid model.

Compositional Oil Model - Depleted State

	CO2	N2	C1	C2	C3	C4	C5	C6	C7+
Liquid Phase	0	0	2.67	2.29	1.75	2.36	8.56	26.3	56.07
Vapor Phase	0	0	46.71	22.95	11.65	8.44	6.43	3.82	0

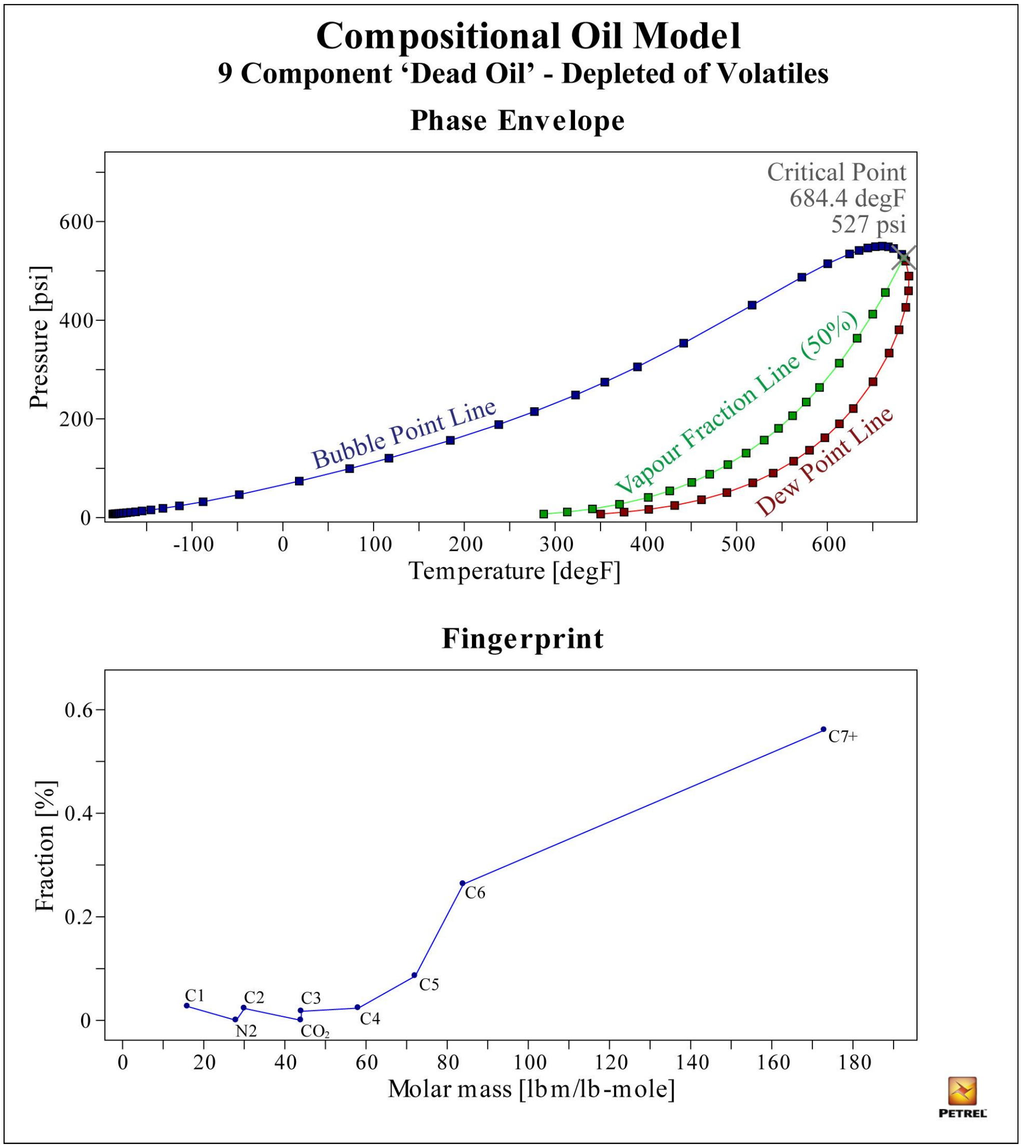

Figure 3.2.1. Phase envelope (top) and oil fingerprint (bottom) for this study's fluid model. Note the CO_2 and N_2 are set to 0, and C1 thru C4 are set to a low fraction.

Water Chemistry

We obtained water Chemistry data from the operator during the May 2018 field survey (**Table 3.2.2**). The produced water's resistivity was of particular interest to our study, as was needed to calculate the reservoir conductivity. From the limited samples the operator had available, the reservoir brine conductivity is calculated to be about 0.73 S/m using Archie's Law (Equation 3.2.1), with an average of 6177 TDS (**Table 3.2.2**).

$$Cond(S/m) = (\frac{1}{0.6}) * 0.73 * \phi^{1.9} * {S_{wat}}^{2} \qquad \text{(Eq. 3.2.1)}$$

With φ being porosity and S_{wat} the water saturation.

Table 3.2.2. Water chemistry data for the Muddy Formation.

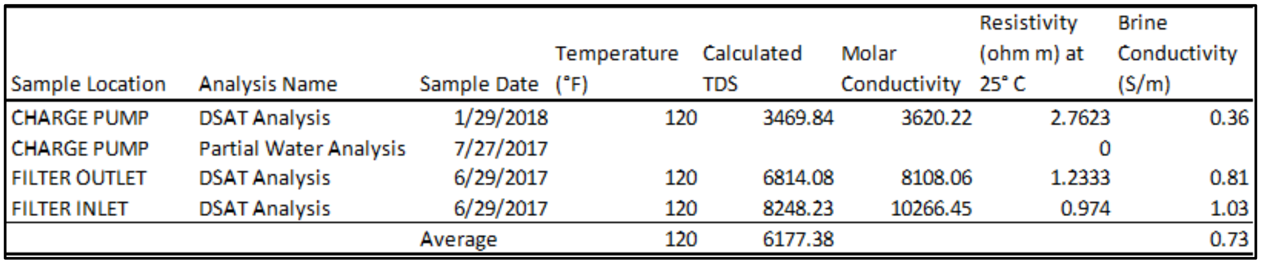

Sample Location	Analysis Name	Sample Date	Temperature (°F)	Calculated TDS	Molar Conductivity	Resistivity (ohm m) at 25° C	Brine Conductivity (S/m)
CHARGE PUMP	DSAT Analysis	1/29/2018	120	3469.84	3620.22	2.7623	0.36
CHARGE PUMP	Partial Water Analysis	7/27/2017				0	
FILTER OUTLET	DSAT Analysis	6/29/2017	120	6814.08	8108.06	1.2333	0.81
FILTER INLET	DSAT Analysis	6/29/2017	120	8248.23	10266.45	0.974	1.03
		Average	120	6177.38			0.73

Relative Permeability and J-Function data

The Curator data set did not contain relative permeability and capillary pressure relationships. Relative permeability and capillary pressure relationships were developed from data contained in an Exxon document "*Engineering & Geologic Study: Bell Creek Consolidated (Muddy) Unit Area*" provided by the operator (Exxon Company, 1990). This document contains J-function data that allows for relative permeability and capillary pressure curves to be estimated. A 'J' Function (J_{Sw}) combines capillary pressure (Pc), permeability (k), porosity (φ), interfacial tension between oil and water (σ), and the contact angle of water (θ) to create a plot of 'J' values versus water saturation. By rearranging the formula to solve for capillary pressure, we get Equation 3.2.2. The initial report does not contain wettability data. We use an interfacial tension of 24 dynes/cm^2 with a contact angle of 5° for the gas/oil fluid pair and interfacial tension of 28 dynes/cm^2 with a contact angle of 55° for the oil/water fluid pair. A capillary pressure curve is calculated from the 'J' Function curve h=145' (**Figure 3.2.2**).

$$Pc_{res} = \frac{\sigma_{res} \cos \theta_{res}}{\left(\sqrt{k/\phi}\right)_{res}} * J_{(S_w)}$$

(Eq. 3.2.2)

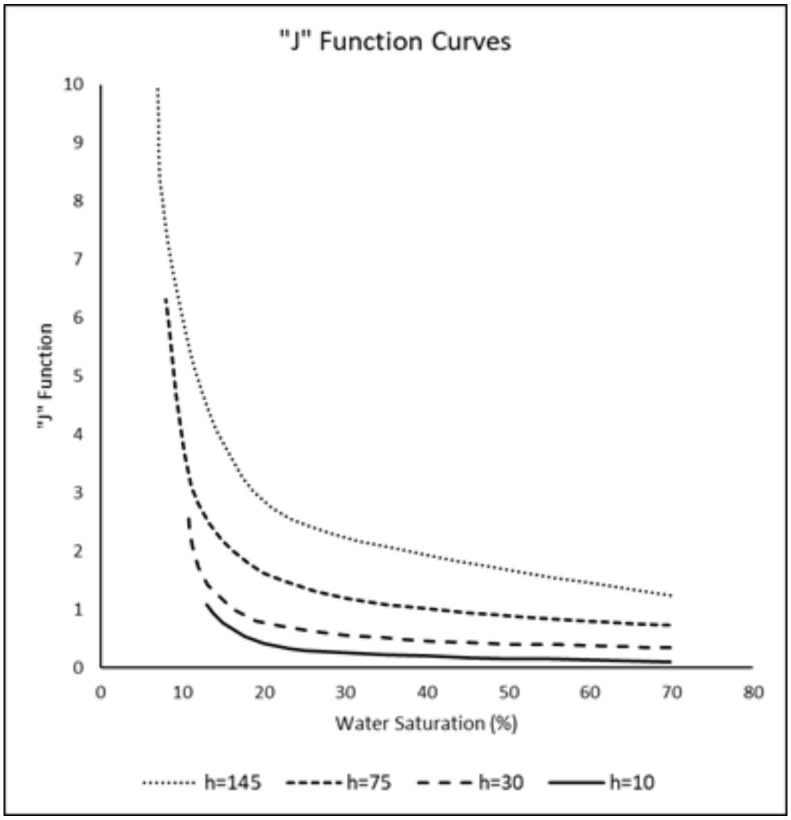

Figure 3.2.2. J-function data for the Bell Creek Field. The data from curve h=145' is used to create the relative permeability and capillary pressure curves.

The relative permeability can now be estimated from the capillary pressure data using an empirical formula (Fatt and Dykstra, 1951; Honarpour, 2018) modified to describe a three-phase fluid system. Equation 3.2.3 calculates the wetting phase relative permeability (k_{rw}) while Equation 3.2.4 calculates the non-wetting phase relative permeability (k_{rnw}) for each of the fluid pairs; oil/water and gas/oil. The critical and end-points are selected from these relative permeability and capillary pressure curves and assigned to Petrel's relative permeability and capillary pressure creation dialog. We are taking an additional 'fitting' step because the machine learning work will use the critical and end-points and curve numbers as their algorithm variables. The relative permeability and capillary pressure curves are shown in **Figure 3.2.3**.

$$k_{rw} = \frac{\int_{S_{rw}}^{S_w} dS_w \Big/ P_c^{2+2b}}{\int_{S_{rw}}^{S_{max}} dS_w \Big/ P_c^{2+2b}}$$

(Eq. 3.2.3)

$$k_{rnw} = \frac{\int_{S_w}^{S_{max}} dS_w \Big/ P_c^{2+2b}}{\int_{S_{rw}}^{S_{max}} dS_w \Big/ P_c^{2+2b}}$$

(Eq. 3.2.4)

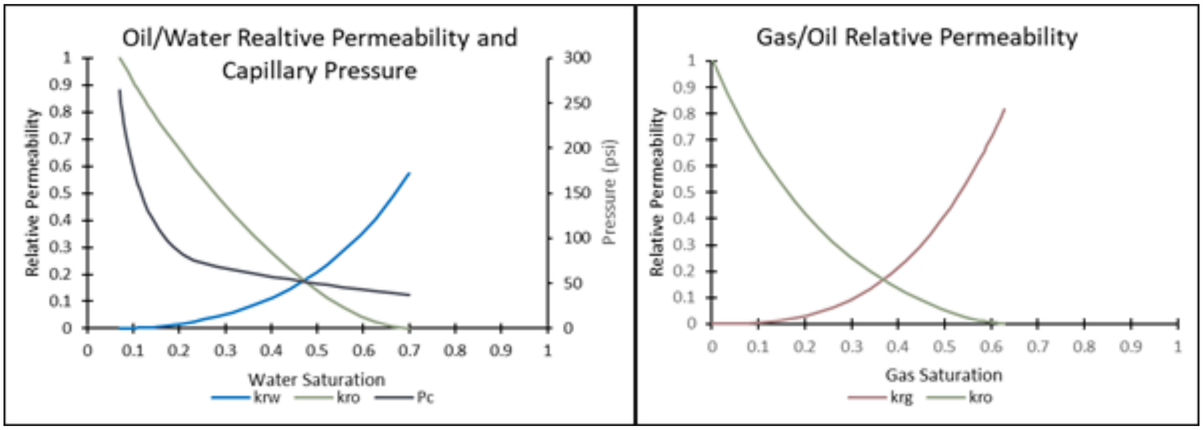

Figure 3.2.3. Relative permeability and capillary pressure relationship derived from J-function data.

Historical Production and Injection data

We received historical production and injection data covering the period from June 1967 thru August 2019 from the operator and the Montana Board of Oil & Gas Conservation (**Figure 3.2.4**). The data is imported into Petrel to create a historical production and injection schedule for each of the well in the model. The wells are set to rate control with the historical production data are used as the target rate. A maximum bottom-hole pressure constraint of 80% lithostatic is assigned to the injection wells. It is interesting to note that there are two distinct phases in the 'gas' production data. This is due to the low volume of volatile components in the original oil in place. Early in the field's lifetime, circa 1967 to 1975, this limited volume is produced, and no further CH_4 production happened in this field. Since 2013, there has been significant CO_2 injection into Bell Creek for EOR operations. The CO_2 is being produced shortly after injection leading to the second spike in gas production shown in **Figure 3.2.4**.

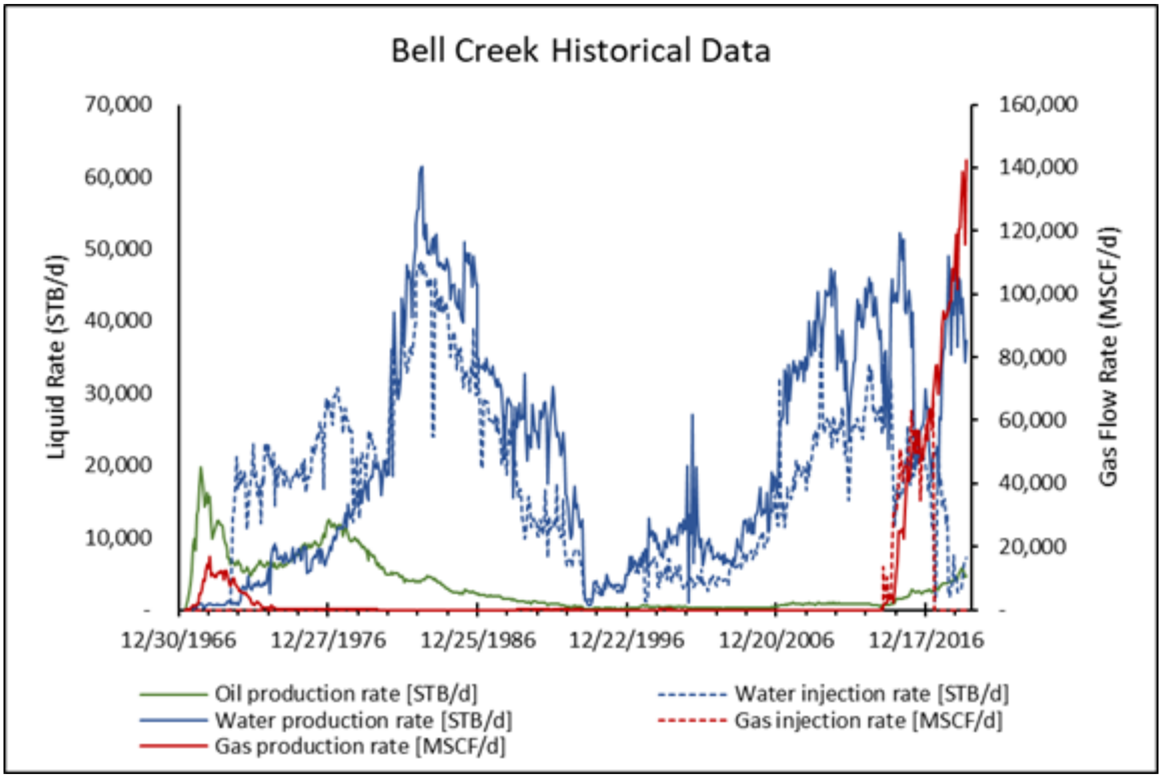

Figure 3.2.4. Historical production and injection data for the Bell Creek Field provided by the operator.

Geologic and Simulation Models

The geological model is the foundation for the EM modeling work, requiring a full 3D electrical conductivity model encompassing everything from 'heaven to hell,' or from the atmosphere to the basement granite. The EM simulations will be our tie to the CWC-CSEM and TEM data collected in the field. This requirement necessitates the need to expand the geological model provided by EERC to include all the formations from the surface to below the Skull Creek, ideally down to the basement granite. We created a geologic model from the model and data provided by EERC, supplemented with well logs, formation tops from the Montana Board of Oil & Gas Conservation, and petrophysical data from the literature. The geologic model, shown in **Figure 3.2.5**, is created by adding the formation surfaces below the Skull Creek, including the Dakota, Fall River, Lakota, Charles, Mission Canyon, and Lodge Pole Formations (the deepest formation with depth data). This added approximately 1700-ft (500-m) below the target reservoir to the geological models. The target reservoir is within the Bell Creek Sands / Muddy Formation (red arrow in **Figure 3.2.5** and **Figure 3.2.6**). Petrophysical properties were not assigned to any of the formations above the Shell Creek Formation and below the Rozet Formation because they are not part of the simulation models and only used to generate the EM model's structural framework. This geological model framework is then used to create the simulation model for machine learning (ML) assisted history matching work.

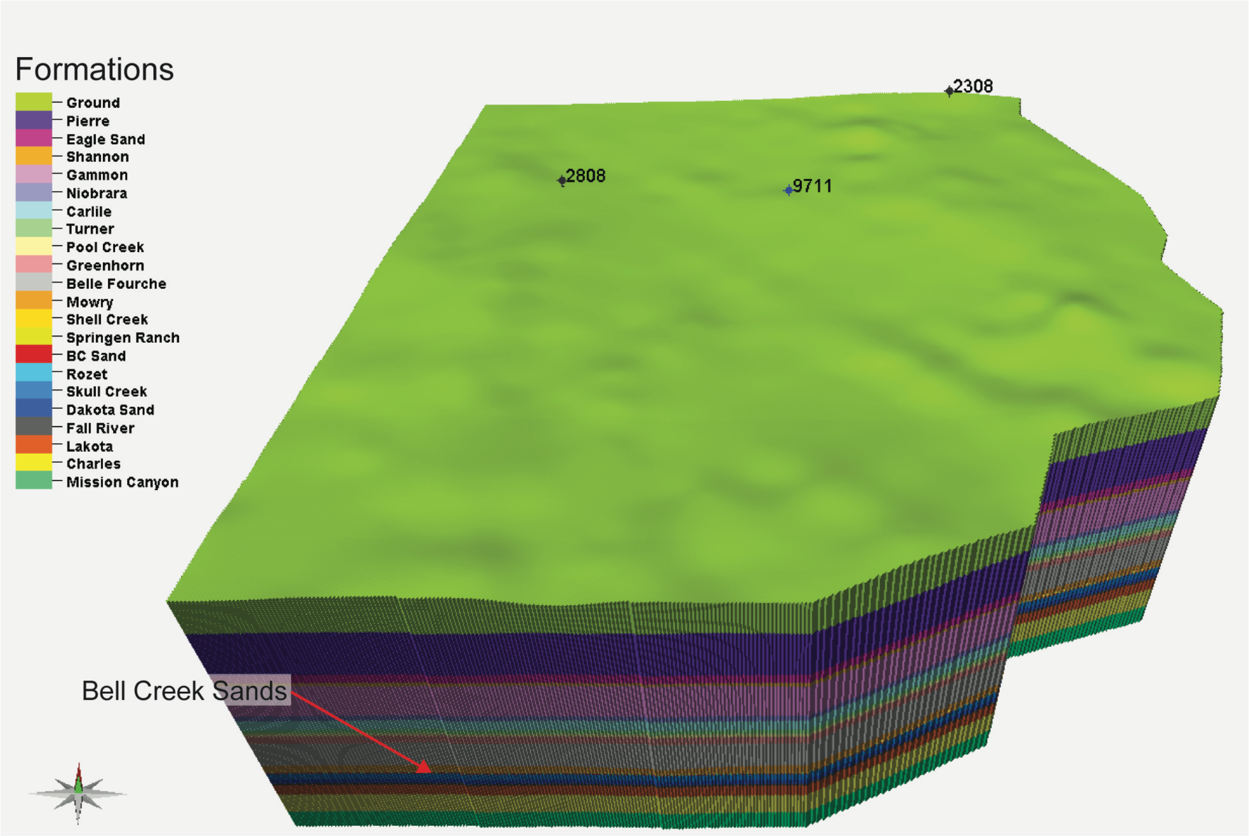

Figure 3.2.5. The geological model is built from the EERC data, showing the formations from the ground surface to the Mission Canyon Formation at the base. The Bell Creek Sands are the thin red formation indicated with the arrow. The figure has no vertical exaggeration. The three project wells are noted on the figure, 2808, 9711, and 2308.

With the geological model now constructed, a coarse grid simulation model is extracted. The grid is up-scaled from 50ft x 50ft cells at 434 x 536 x 45 cells (10,468,080 total cells) for the geological model to a coarser grid with 100ft x 100ft cells at 174 x 188 x 14 cells (457,968 total cells). Only the Shell Creek Formation, Springen Ranch Formation, Bell Creek Sands/Muddy Formation, and the Rozet Formation are included in the simulation model. Pressure and water saturation properties are up-scaled from the EERC data. Gas saturation (Sg) is assumed zero based on production records. There is no oil saturation (S_o) in the EERC data, so we assumed S_o to be 1 - water saturation (S_W).

Due to physical constraints on transferring large volumes of data over the internet, a copy of the entire Petrel project, encompassing the EERC model, the geologic model, and the up-scaled simulation grid, is physically sent to the New Mexico Tech (NMT) team for their machine learning assisted history matching work. NMT then further up-scaled the simulation model to aid in rapidly running a large volume of simulations. The cell size for NMT's very coarse simulation model is 1148 ft x 1148 ft (350 meters x 350 meters), 11.5x coarser than the base model.

Reservoir Model Expansion

The northern extent of the reservoir model provided to the project by EERC ends more than a mile south of our northernmost field survey site. We identified that the reservoir model should extend beyond the survey area. To address this problem, we created a second geologic model that expanded the domain to the North. **Figure 3.2.6** shows the expanded geologic model with the three project wells highlighted, 2808, 9711, and 2308.

Well location, elevation, total depth, and formation top data for 60 wells covering the new model's expanded area are obtained from the Montana Board of Oil & Gas Conservation database. We also received updated production and injection data through August 2019 for all operational wells in the field, including the new wells to the North and West. This data is imported into the Petrel project.

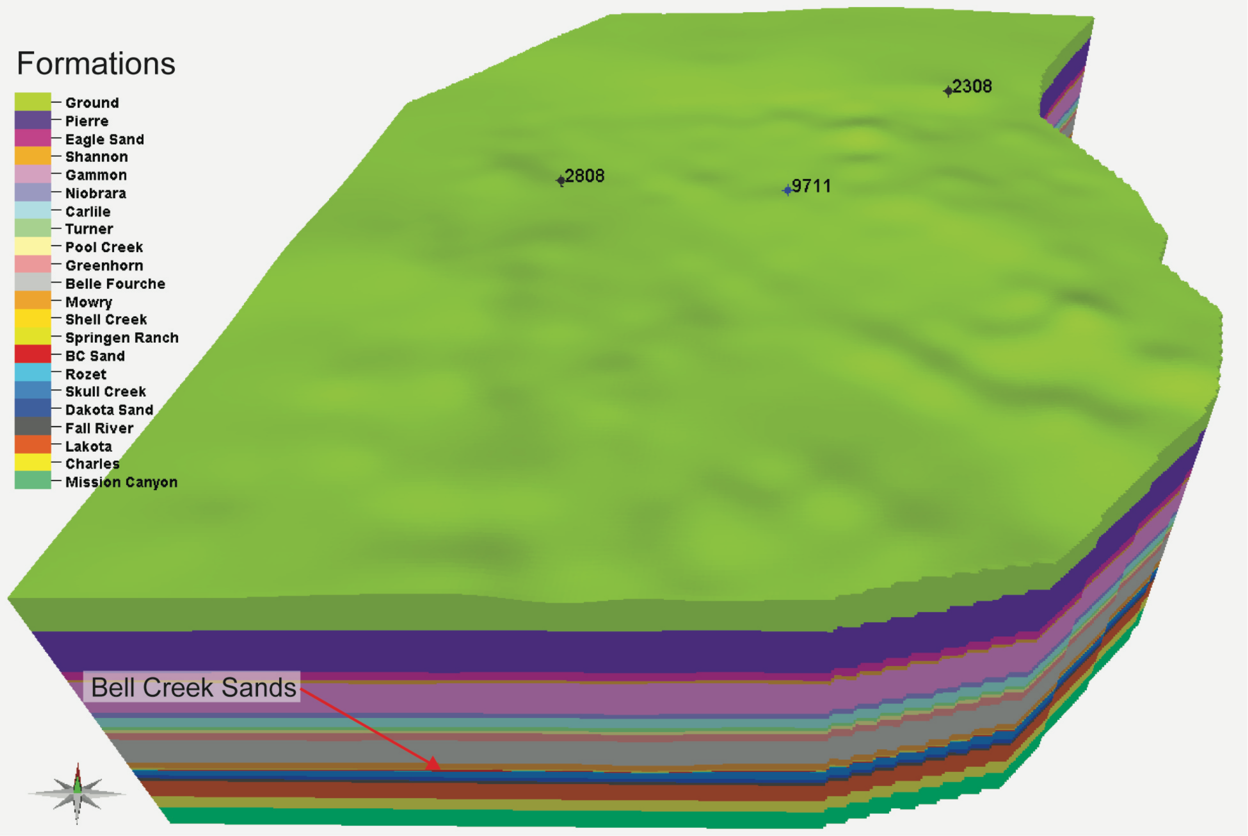

Figure 3.2.6. The expanded geological model showing the formations from the ground surface to the Mission Canyon Formation at the base. The Bell Creek Sands are the thin red formation indicated with the arrow. The figure has no vertical exaggeration. The three project wells are noted on the figure, 2808, 9711, and 2308.

The well tops are used to contour surfaces for all 22 geologic formations from the ground surface to the Mission Canyon Formation. While the target formation is the BC Sands, or often called the 'Muddy' Formation, we developed surfaces for the geological model that encompassed the entire stratigraphy from the ground level to the Mission Canyon Formation, the deepest formation with data. This was done to establish the framework for the expanded EM model and the flow simulations. **Figure 3.2.7** compares the old model domain (blue polygon) to the new model domain (red polygon) and shows all of the wells used to contour formation surfaces. In **Figure 3.2.7**, production wells have a filled circle symbol, injection wells have an open circle with an arrow, the project wells have a closed circle with a cross, and the rest of the wells are exploration or plugged and abandoned wells symbolized with an open circle and a cross.

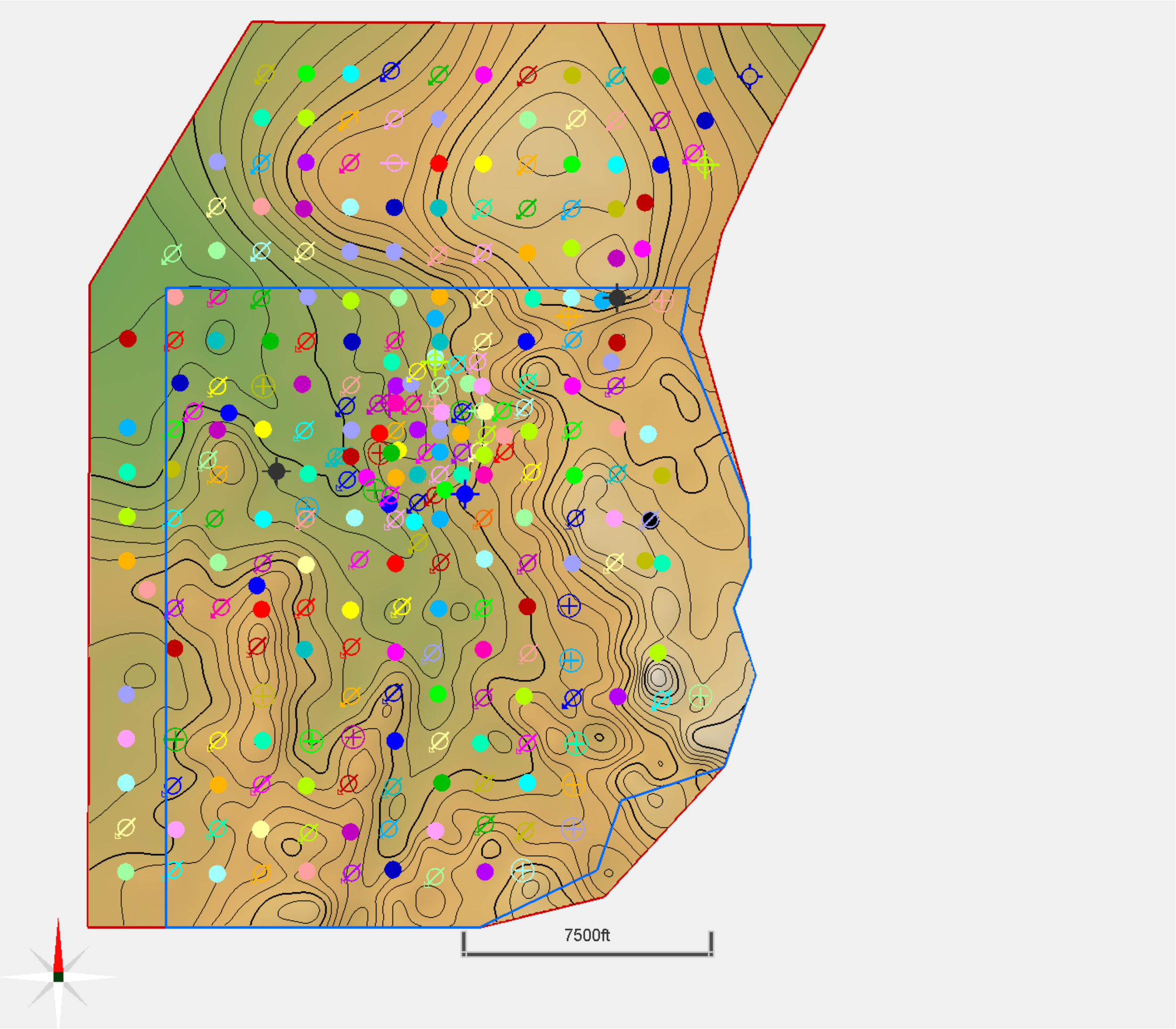

Figure 3.2.7. Contoured ground surface with all the wells used to create the formation surfaces and the large model domain boundary (red polygon) and the original model domain (blue polygon).

From the expanded geologic model, a volumetric zone consisting of the Springen Ranch Formation, Shell Creek Formation, Bell Creek Sands/Muddy Formation, and the Rozet Formation is gridded to 50ft by 50ft cells in the I,k, for a total of 10,468,080 total cells. Of those cells, only 8,705,976 are active, with the rest outside the model domain and set to inactive.

A facies model is constructed next using well-log data and information from a formation analysis study performed by Exxon in July 1990 titled *Engineering & Geologic Study of the Bell Creek Consolidated (Muddy) Unit Area* (Exxon Company, 1990). The report identified three distinct zones within the Bell Creek formation with eight different facies and a ninth carbonate facies from the EERC dataset. The porosity and permeability distribution are derived from well log data and empirical relationships. The facies, porosity, and permeability are upscaled to the geologic grid resolution. These up-scaled well logs are then co-kriged to the facies model and populated across the domain using the sequential gaussian simulation method in conjunction with the variogram data from the facies analysis. See **Appendix A3.2** for a detailed description of the methods used.

The simulation model domain is now extracted for the fine-scale geologic model by up-scaling to 150ft x 150ft cells. The up-scaling gives a grid size of 145(i) x 179(j) x 14(k) for a total of 363,370 cells. Of those cells, 297,341 have defined properties. Similar to the smaller domain model, only the Shell Creek Formation, Springen Ranch Formation, Bell Creek Sands/Muddy Formation, and the Rozet Formation are included in the simulation model. The initial pressure was assumed to be hydrostatic for simplicity, but testing indicated that hydrostatic plus 2000 psi gave a better match to historical production data. The initial water saturation was estimated using the reservoir quality index (RQI) approach. The oil saturation is then calculated at $1-S_w$, with the gas saturation assumed to be 0.

Once the NMT team had achieved their goals (see section *Use of a Machine-learning assisted workflow to structure a history-matched simulation model*), they provided their simulation model and the input parameters for 500 history matched simulations to the UU team. Data transfer limitation discussed above required that the simulation suite run at New Mexico Tech be re-run at the University of Utah. The NMT team varied the following 15 parameters: Maximum Capillary pressure (Pcmax), the residual water saturation on the oil/water relative permeability curve, the residual gas saturation on the gas/oil relative permeability curve, the minimum water saturation, the critical gas saturation, the Corey water, gas, oil/water, and oil/gas exponents, the maximum water relative permeability at residual oil saturation, the maximum oil relative permeability at maximum oil saturation, the maximum gas relative permeability at minimum water saturation, and permeability modifiers applied on the I, J, K permeability. Out of the 500 cases, we identified 31 cases from 5 clusters for high-resolution simulations with the Bell Creek expanded model using cluster analysis. **Table A3.3.1** in **Appendix A3.3** shows the parameters used in all 31 cases. From the 31 cases, a sub-set of the most interesting eight cases was exported for the EM modeling step. These eight simulations were also run on the very coarse grid model to compare to the fine grid expanded model. See **Appendix A3.4** for a detailed description of how each of the simulation cases is created.

Data Output for EM Modeling

The appropriate data is output to text files for the EM modeling using our workflow outlined in **Appendix A3.5**. Out of the 31 high-resolution simulation cases, two cases from clusters 0, 1, and 3 and one case each from clusters 2 and 4 are identified for EM modeling. Five time-steps, corresponding roughly to our field dates, are output for each case; September 30, 2017, May 31, 2018, September 30, 2018, May 31, 2019, and July 31, 2019. A water saturation delta is calculated between September 30, 2017, and July 31, 2019, to aid in selecting eight models for output to the EM modeling step. In each cluster, we are looking for water saturation deltas that exhibit the most variation between cases.

In cluster 0, we chose cases 25 and 339. The water saturation delta for all cases in this cluster is indistinguishable from each other except for case 339. In cluster 1, case 37 and case 241 exhibited the most significant difference between cases. The cases within cluster 1 also look very similar to each other and the cases in cluster 0. Cluster 2 only outputs a single case for EM modeling because there are only two cases in the cluster, and both cases look very similar. Case 412 is chosen because it exhibits a greater degree of variance in water saturation over case 225 compared to the rest of the data across all clusters. Two cases are chosen from cluster 3, case 14, and case 234. Simulation case 14 is very similar to the majority of the data, while case 234 shows the most variation compared to 14. The final case exported for EM simulations is case 227 from cluster 4. There is only a single case in this cluster, so only one is exported. The difference in water saturation looks very similar to the majority of the data. See **Appendix A3.6** for water saturation delta maps of each of the cases selected for output to the EM modeling step.

Machine-Learning Assisted History-Matching

The overall objective of the history matching study is to structure a reservoir model with a set of reservoir characterization parameters that could make predictions of the fluid production to agree with the field historical data. Based on the preliminary simulation runs, a basic comprehending of the uncertain parameter sensitivities and the computational overheads required by the history matching process can be obtained. The internal boundary condition of the current reservoir model is constrained by the oil production rates of the producers, and the fluid injection rates of the injectors. The primary output tracked to calculate the history matching error is the water and gas production rate. We apply secondary constraints to the bottomhole pressure of the wells to be 800 psi and 3228 psi at the producers and injectors, respectively. The history matching runs tune the permeability multipliers ranging from 0.1 to 10 of the base permeability distributions to investigate the general response of the model. The preliminary results show a promising result of oil production matching. Moreover, further efforts need to be expended to improve the gas and water production matching. At this stage, a larger volume of simulation runs needs to be prepared to decide the reservoir properties to be tuned other than the permeability multiplier. However, the reservoir model we are using is computational expensive, which potentially limits the sensitivity and history matching studies since we must investigate a significant amount of running time. To address the issue, we utilized a robust history matching workflow that assisted the history matching procedure in this work.

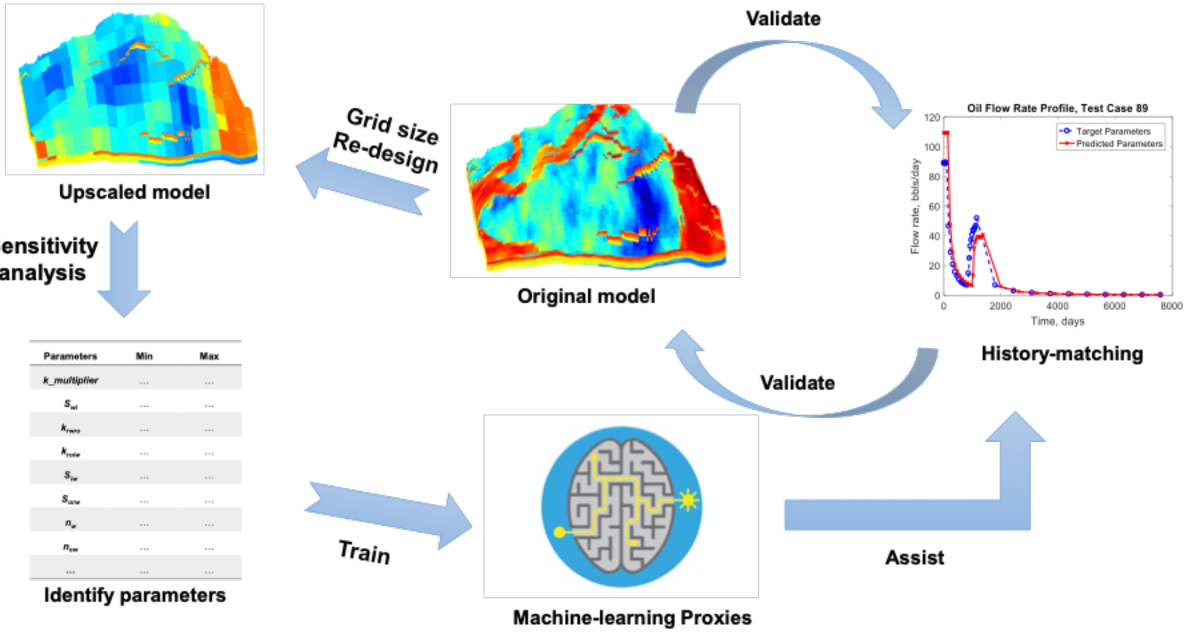

Figure 3.2.8. Proposed history-matching workflow

As shown in **Figure 3.2.8**, the general history matching workflow is illustrated, which employs a synergetic process of numerical reservoir simulation and machine-learning technologies to achieve a much faster and more accurate history-matched model. The critical modules of the workflow are discussed in the following steps:

1. Model upscaling: Establish a upscaled reservoir model by re-design the grid size of the current reservoir model, our target is to reduce the grid dimension from 174×188×14 (total of 457,968) to 87×94×5 (total of 40,890) which is about 11 times smaller. To eliminate the concerns related to numerical dispersion, we will gradually reduce the grid resolution and check the impact of using a coarser grid system. We will stop the grid coarsening when the disparities observed from the production response becomes significant (5% of margin).
2. Sensitivity analysis: Once the upscaled model is developed, we will deploy it to prepare a certain volume of runs and conduct sensitivity analysis to find out the impactive reservoir parameters to the production response. Besides the permeability multiplier, we will include the permeability aspect ratio, relative permeability curves and capillary pressure data in the sensitivity analysis.
3. Proxy model training: The data set created in the sensitivity analysis study could be utilized to train a proxy model that mimics the high-fidelity model. We will develop an artificial neural network model to assist the history matching study. The fast computational speed of the proxy model would accelerate the history matching processes by orders of magnitudes. In this work, we attempt to train two different versions of proxies: the forward-looking proxy which predicts the reservoir response using a set of reservoir properties as input, and an inverse history matching proxy which inversely generated the suitable reservoir properties to match the field historical data.

4. Machine-learning (ML) assisted history matching: The procedures summarized in **Figure 3.2.9** illustrates the machine-learning module of the workflow. Using the developed proxy models, we will go through a workflow to find satisfactory history matching results. The field history will feed to the inverse history matching model and predict the reservoir properties. Such prediction will be examined by re-running the high-fidelity numerical model. If the production response generated from such check yield good matching quality against the historical data, the solution can be identified as a valid characterization of the reservoir system. Otherwise, the prediction from the inverse proxy will be used as an educated initial guess. The forward-looking proxy will collaborate with a global optimizer to minimize the history matching error. At this stage, large volume of simulation runs will be carried to search for the reservoir parameters yielding satisfactory matchings with the field data.
5. Validation with the original reservoir model: The solution obtained by the artificial-intelligence assisted history matching workflow will be tested by the original reservoir model with finer grid system. The worst scenario is that the matching results generated from the finer reservoir model using the reservoir properties determined by the AI-workflow is not satisfactory, we will modify the parameters with much less volume reservoir simulation runs using the solution as an initial guess.

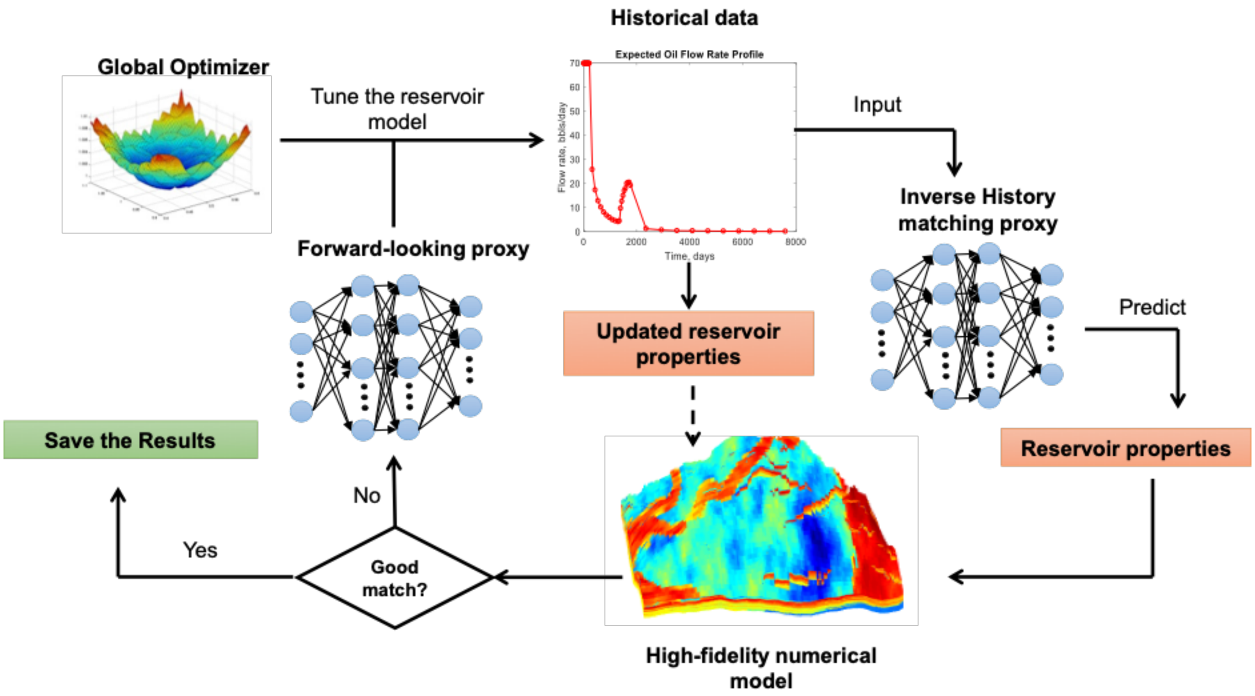

Figure 3.2.9. Illustration of the machine-learning assisted module

Efforts will be put in to realize the proposed history matching workflow. When the electromagnetic inversion data becomes available, we will include that data in the history matching process. However, there are uncertainties in the fluid model of the current model. We recommend conducting a detailed fluid analysis to understand the fluid composition, and eliminate the uncertainties arising from this aspect. When a history-matched model is established, we will structure a forecasting model which is competent to track the fate of the CO2 gas in a long-term period.

Application of machine-learning assisted history matching protocol in Bell Creek Formation

The objective of this section is to discuss the procedures and results by implementing the proposed machine learning assisted protocol to improve the accuracy and computational efficacy of the history matching study of the Bell Creek formation. As shown in **Figure 3.2.10 (a)** and **(b)**, an upscaled reservoir model is established using a reduced grid block dimension with 15,582 active grid cells, which is approximately 25 times coarser than the original model. **Figure 3.2.11** shows the oil production rate comparison by running the original and upscaled model. The oil rate profiles show negligible disparities, which indicate that the upscaling of the grid system does not introduce significant numerical dispersion. And more importantly, the CPU time required to run the original reservoir model is approximately 70 hours using a HP Z8G4 workstation (192 GB physical memory and 16 cores used in parallel processing), while the upscaled model requires 30 to 40 minutes of computational time to run the model. Thus, the upscaling of the model successfully reduces the computational overhead by 100 times without introducing remarkable numerical errors. Furthermore, such an upscaled model can be used in the history matching study by preparing batch simulation runs.

The reservoir properties tuned in this work include the oil/water capillary pressure date, relative permeability curves, and the permeability multipliers along the lateral (x- and y-) and vertical (z-) directions (**Table 3.2.3**). Notably, the capillary pressure and relative permeability data are calculated using Brook and Corey and Corey's correlation, respectively.

Table 3.2.3. The tuning reservoir properties and the ranges

	Capillary pressure coefficient	Corey's formulation coefficients											Permeability multiplier		
	Pc_{max}, psi	S_{orw}	S_{org}	S_{irrw}	S_{gc}	n_w	n_{ow}	n_{og}	n_g	k_{rwmax}	k_{romax}	k_{rgmax}	mod x	mod y	modz
Minimum	20.00	0.05	0.05	0.10	0.00	1.00	1.00	1.00	1.00	0.20	0.50	0.80	0.10	0.10	0.01
Maximum	150.00	0.35	0.35	0.30	0.10	7.00	7.00	7.00	7.00	0.90	1.00	1.00	8.00	8.00	0.10

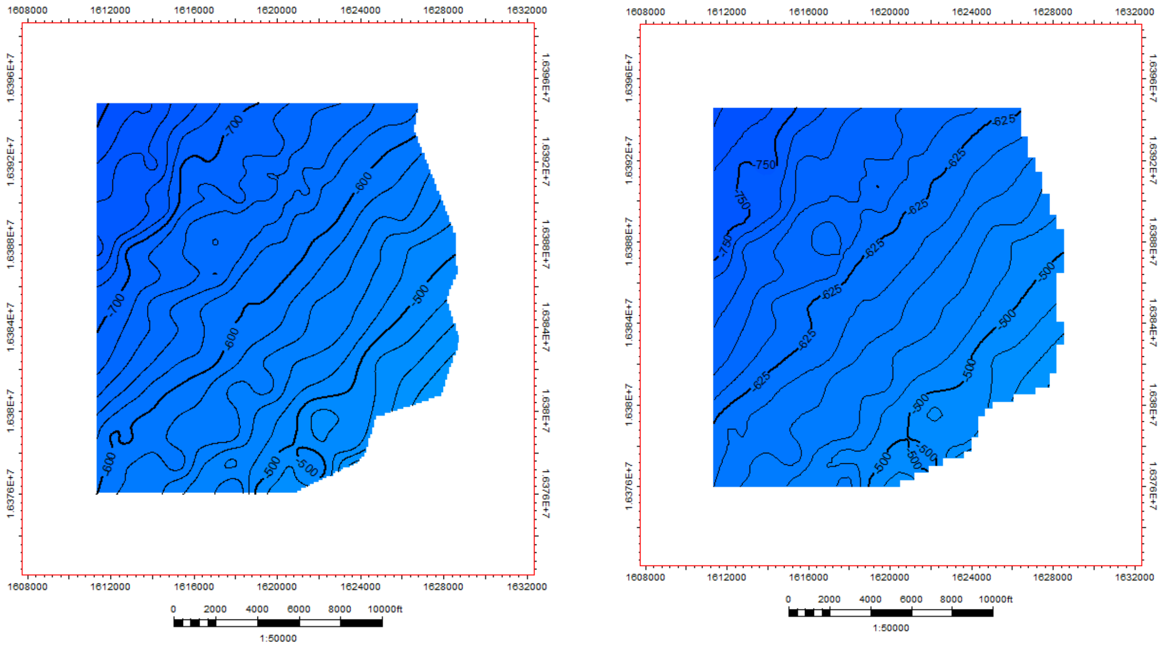

(a) Original Reservoir Model: Grid dimension: 175×189×15; Total Number of active cells: 457,968

(b) Upscaled Reservoir Model: Grid dimension: 50×54×7; Total Number of active cells: 15,582

Figure 3.2.10. Original (**a**) and upscaled reservoir model (**b**)

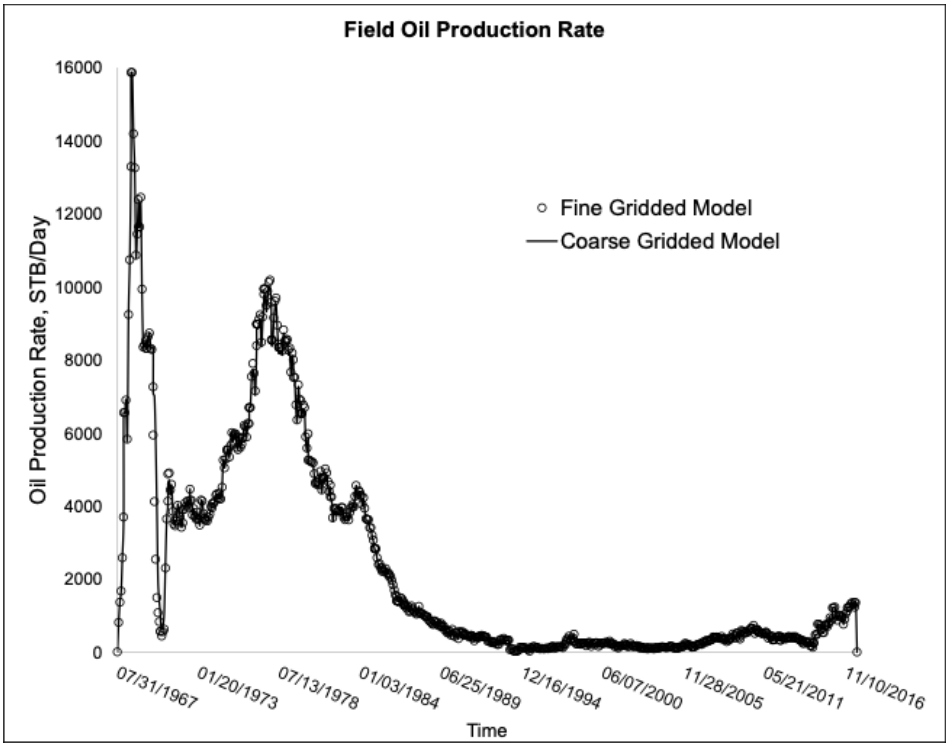

Figure 3.2.11. Comparison of the oil production of the fine and coarse gridded models

A total of 200 numerical simulation runs are prepared by randomly assigning the reservoir properties within the prescribed ranges, which structures a one-to-one relationship between the tuning reservoir properties against the forecasting results. In **Figure 3.2.12**, the results from the 200 batch simulation runs are presented. There are cases amongst the numerical experiments showing promising matching quality. As displayed in **Figure 3.2.13**, one of the best representative cases indicates good oil production matching, but the water and gas production still need improvements. However, to improve the history matching quality would demand more simulation runs. To further tune the simulation model, a machine-learning based proxy model will be trained using the results from the 200 batch simulation runs as knowledge-base. Once the proxy model is trained, it will be coupled with a global optimization algorithm to minimize the history matching error.

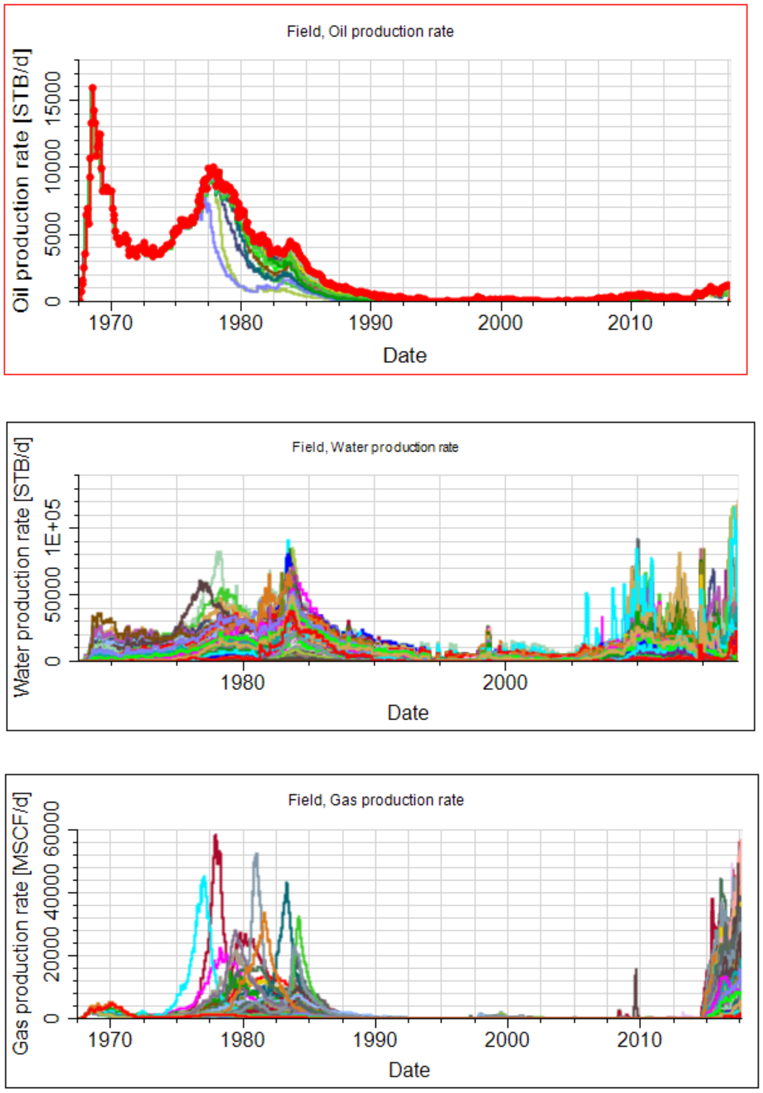

Figure 3.2.12. Results from batch simulation runs

In this work, three multi-layer neural network (MLNN) models are trained to predict the oil, water and gas production rates as a function of time. The input of the MLNN models would be the tuning reservoir properties. During the development stage of the proxy models, we use 180 of the data for training and validation, and 20 runs for blind testing applications. It is worth emphasizing that the cases used in the blind testing applications are different with the training data to ensure the generalization capability of the model.

In **Table 3.2.4**, the architecture and blind testing errors of the MLNN models are summarized. Promising error margins are observed from the average values of the blind testing applications. To further investigate the reliability of the proxy models, we present one best, average quality and one worst blind testing case in **Figure 3.2.14**. It can be observed that, even for the worst scenario case, the MLNN models effectively mimic the high-fidelity numerical model. Thus, these proxies can be employed as an expert system to further minimize history matching error.

Table 3.2.4. The architecture and blind testing application performance of the MLNN models

	Topology*	Transfer function	Average testing error
Oil rate model	[81,66,95]	Logistic function	1.9%
Water rate model	[22]	Tangent function	20%
Gas rate model	[31,100,100,94]	Logistic function	8.2%

*Note: the topology vector indicates the number of hidden layer and number of hidden neurons of the MLNN model. For instance, the gas rate NN model has four layers with 31, 100, 100 and 94 hidden neurons in each layer.

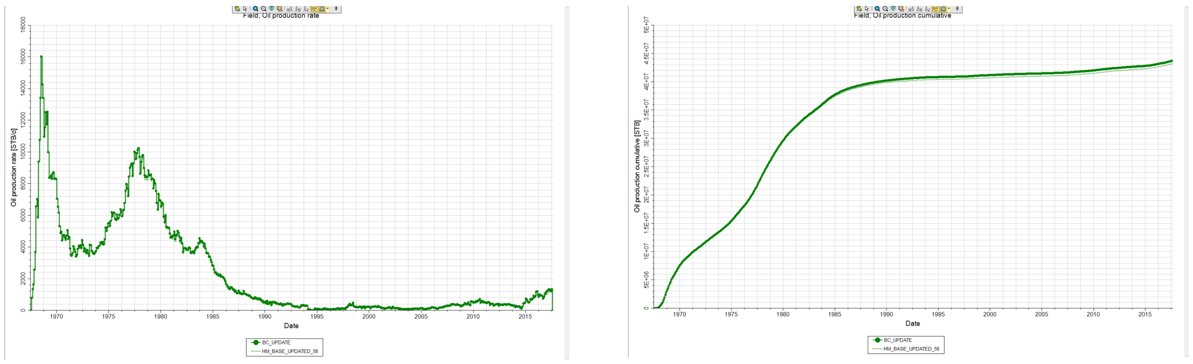

(a) **Oil rate**

(b) **Cumulative oil production**

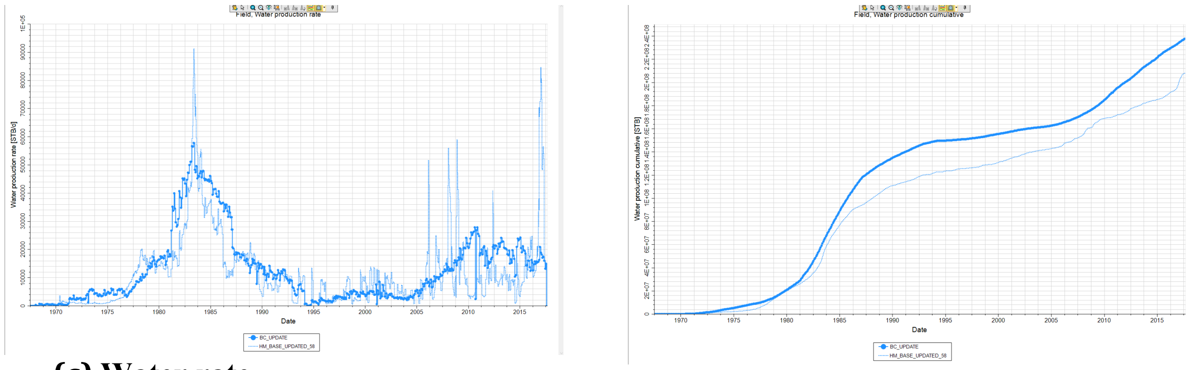

(c) **Water rate**

(d) **Cumulative water production**

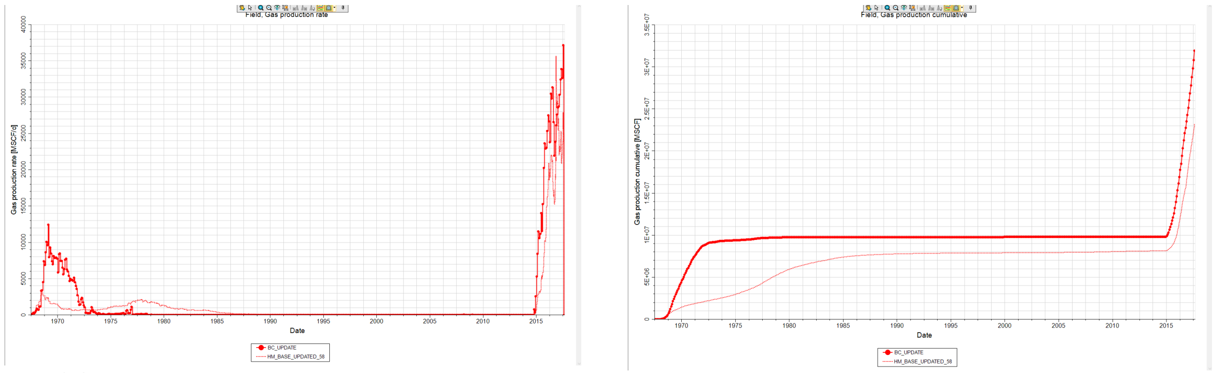

(e) **Gas rate**

(f) **Cumulative gas production**

Figure 3.2.13. A representative case amongst the history matching runs.

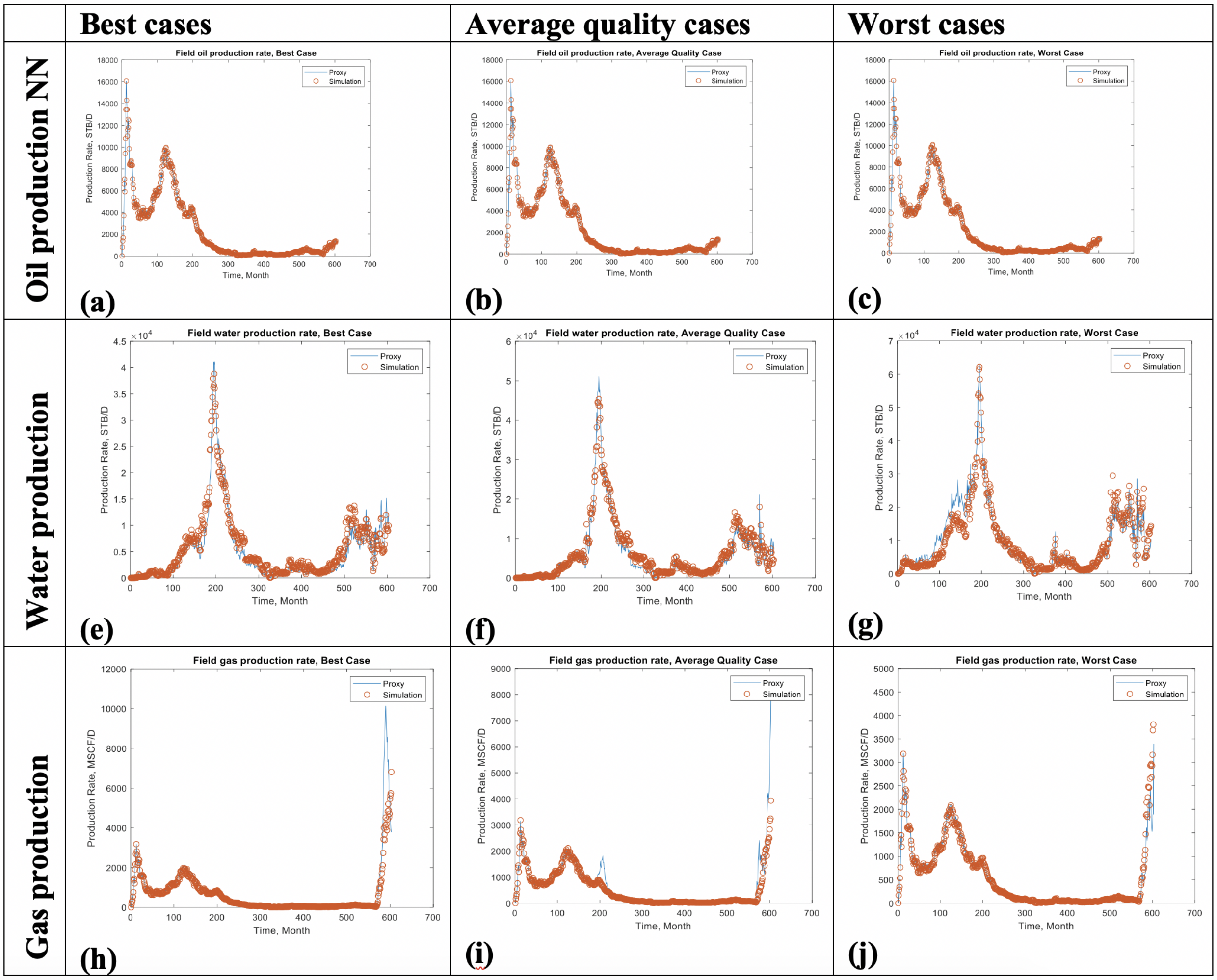

Figure 3.2.14. Blind testing applications of the MLNN models

Afterwards, the MLNN model is coupled with particle swarm optimization to minimize the history matching error function, which is defined as the sum of the mean square errors of the oil/water/gas rate matchings. In **Figure 3.2.15**, the evolutionary process of the PSO algorithm is presented. The PSO optimization converges at 326 iteration to achieve the minimum history matching error. It is worthy to point out that each PSO iteration employs 100 particles to find the leading solution, which means that 32,600 simulation runs are needed to complete the optimization process. The use of the proxy enables the history matching study to be accomplished within a reasonable period of time, because the computational overhead is prohibitively intensive even using the upscaled reservoir model.

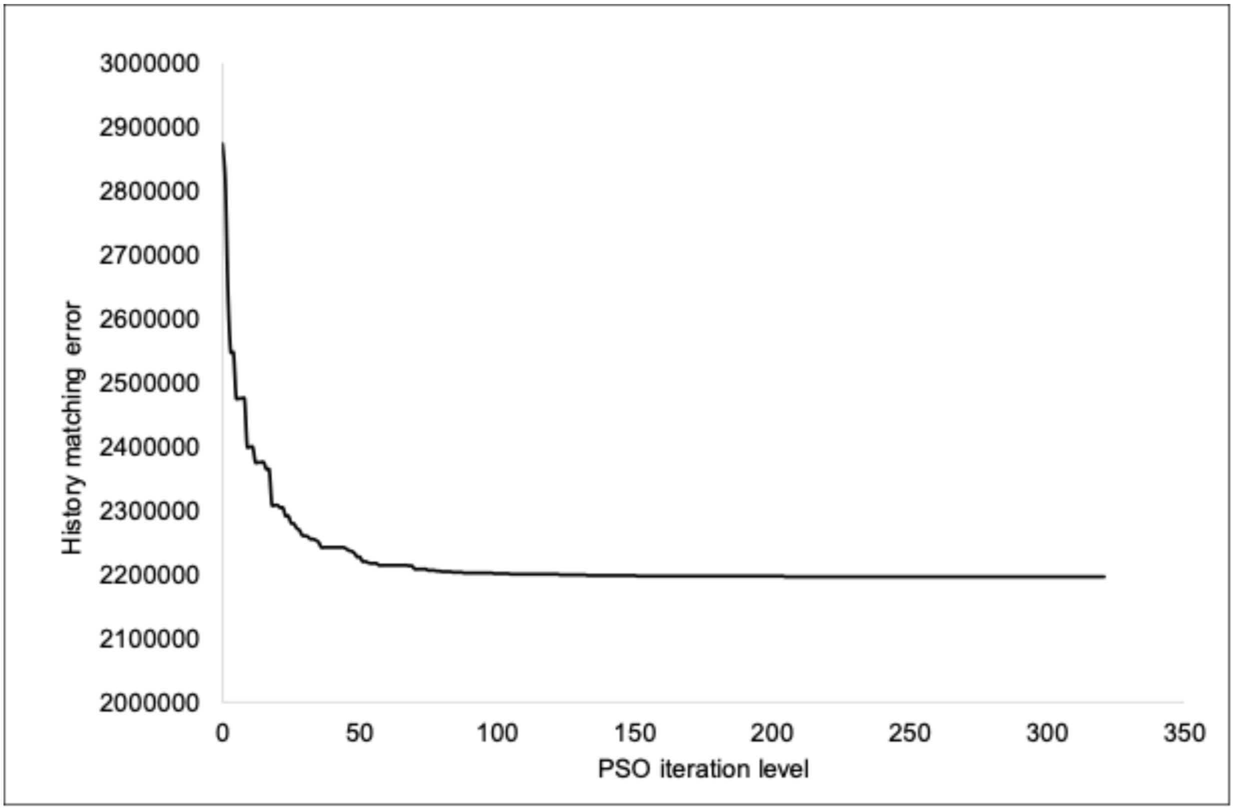

Figure 3.2.15. Evolutionary process of PSO algorithm

Pc_{max}, psi	S_{orw}	S_{org}	S_{irrw}	S_{gc}	n_w	n_{ow}	n_{og}	n_g	k_{rwmax}	k_{romax}	k_{rgmax}	modx	mody	modz
30.515	0.185	0.165	0.298	0.028	4.476	6.985	6.997	3.129	0.685	0.595	0.804	7.129	3.237	0.099

Table 3.2.5. Optimum history matching solution

3.3 INTEGRATED MODEL CONSTRUCTION TO LINK RESERVOIR SIMULATIONS AND FIELD EM DATA

A crucial aspect of the project is to understand and reproduce the link between reservoir simulation models and geology to the physical property distributions at the site. Such a link has the ability to guide the CWC-CSEM field surveys at the front end, and act as a feedback mechanism into the reservoir simulations at the back end. Within this project, we have developed a practical method for establishing such a link between the reservoir simulation models of the CO2-EOR field site, the large-scale 3D conductivity variations above and below the reservoir, and the 3D and time-varying distributions of electrical conductivity from production activities. Full details into the underlying workflow developed to create such a 3D and time-varying conductivity site model with demonstration of its application to the simulation of predicted CWC-CSEM data has been published within the Expanded Abstracts and presented in a Special Section on CO2 Monitoring at the 2019 Annual Society of Exploration Geophysicists Meeting and Exhibition. For brevity, we provide here a summary of the essential components of this work. Additional details into the development for this section of the project are available at Krahenbuhl et al., 2019.

Building A 3D Conductivity Site Model

The construction of a representative 3D and time-varying conductivity model of the Bell Creek field site must start at the ground surface, drop through the significant geologic sequences, incorporate the detailed reservoir simulation data within the injection/production interval, and continue to extend below the reservoir to depth. To accomplish this, the complete site models are developed in two primary stages. The first is the creation of detailed time-varying conductivity models of the dynamic production interval as reservoir simulations are updated over time. The second is building the larger background model for the Bell Creek field site through the multiphysics integration of seismic, borehole resistivity, and field TEM data. To accomplish these two overarching objectives for building the full site model, the complete process can be divided into a sequence of five interrelated tasks as presented here.

Step 1: Reservoir Simulation Modeling

A dynamic reservoir model consistent with current field conditions is critical to design field surveys and interpret the resulting CSEM data. To accomplish this, a geological model previously developed by North Dakota Energy & Environmental Research Center (EERC) was leveraged to create an up-to-date 3D dynamic model of the reservoir interval. The porosity field, **Figure 3.3.2**, was constructed from the collection of well logs at the site, calibrated to core data, and distributed stochastically across the reservoir interval by a facies model.

Simulations are then run using historical production and injection data, and model parameters such as the fluid model and relative permeability model are varied to provide a suite of plausible solutions. Given that history matching provides a non-unique solution, having multiple realization that match field data is a desired outcome (**Figure 3.3.1**). These results are then used as initial conditions for predictive simulation covering the dates of the project's field work. The final result of the reservoir modeling step is the generation of fluid saturation distributions over time, water in particular, that can then be converted to conductivity in step 2.

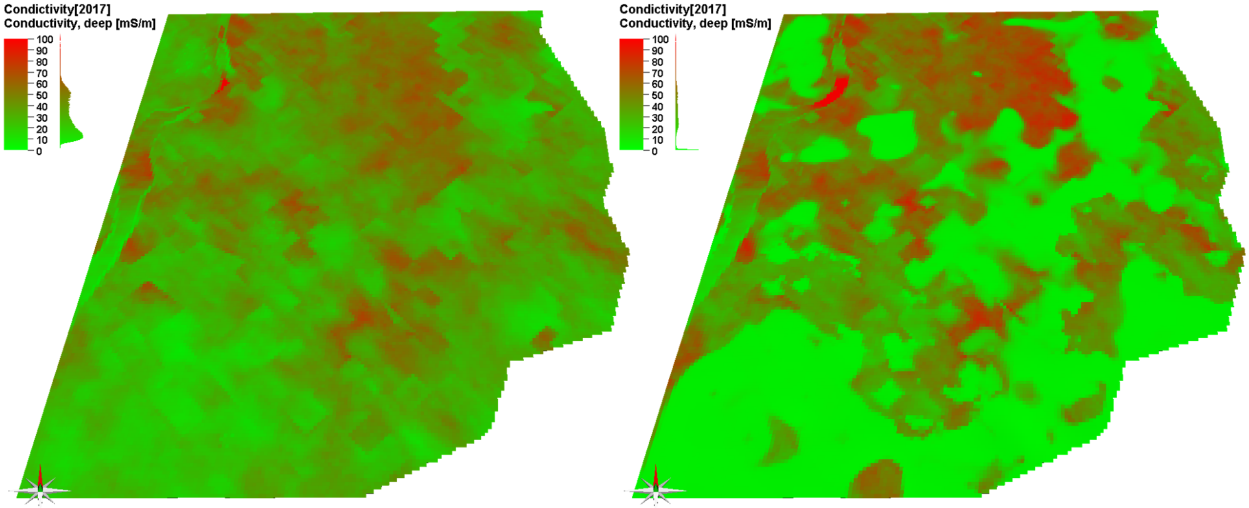

Figure 3.3.1: Reservoir simulation modeling. The two images illustrate different CO2 concentrations while satisfying the same production history.

Step 2: Conversion to Electrical Conductivity

To construct a sequence of conductivity models for Bell Creek, we apply Archie's equation (Archie, 1942) with the 3D reservoir porosity model and dynamic saturation models (e.g., **Figure 3.3.2**). We implement Archie's equation as:

$$\sigma_B = \frac{1}{a}\sigma_w \varphi^m S_w^n \,, \qquad \text{(Eq. 3.3.1)}$$

where a is a tortuosity factor [= 0.6], σw is the conductivity of injected water measured on site [= 0.733 S/m], φ is the 3D porosity model (**Figure 3.3.3**), m is cementation factor [= 1.9], Sw are the 3D time-varying saturation models (**Figure 3.3.3**), and n is Archie's saturation exponent [= 2.0]. One of the resulting conductivity models for Bell Creek is illustrated in **Figure 3.3.2**, **Figure 3.3.3**, and **Figure 3.3.5** for a single time-state of the field.

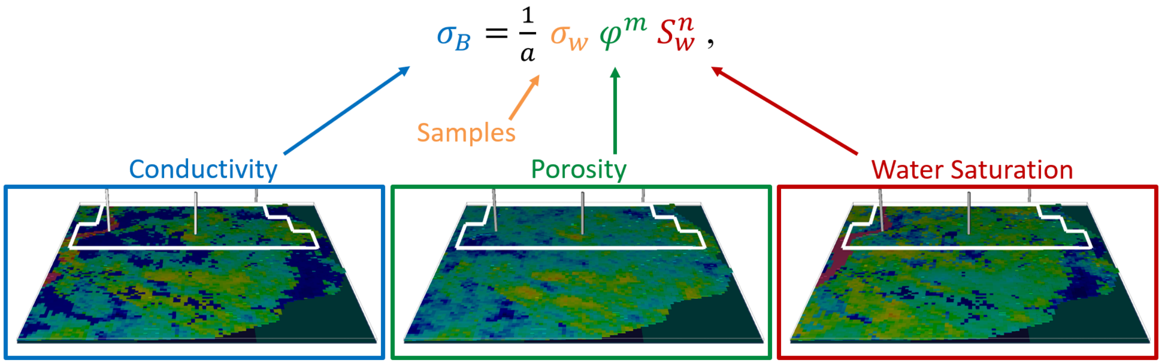

Figure 3.3.2: Application of Archie's Law to convert 3D static and time-varying reservoir simulation data, specifically porosity and water saturation, into conductivity.

Step 3: Incorporating Seismic Horizons

The first two steps focus on the task of updating the dynamic reservoir model within the production interval and converting those simulations to conductivity. The remaining steps focus on building the larger background conductivity model and integrating the two into complete and representative site models that would be consistent with the timing of each CWC-CSEM field survey. To accomplish this, the first step is to build the complete over- and under-burden for the site. For this we use seismic horizons from previous site investigations as structural data to delineate the significant stratigraphic layers and formation boundaries within the larger geologic model. A subset of the horizons are presented in **Figure 3.3.3** along with the surface topography and reservoir interval.

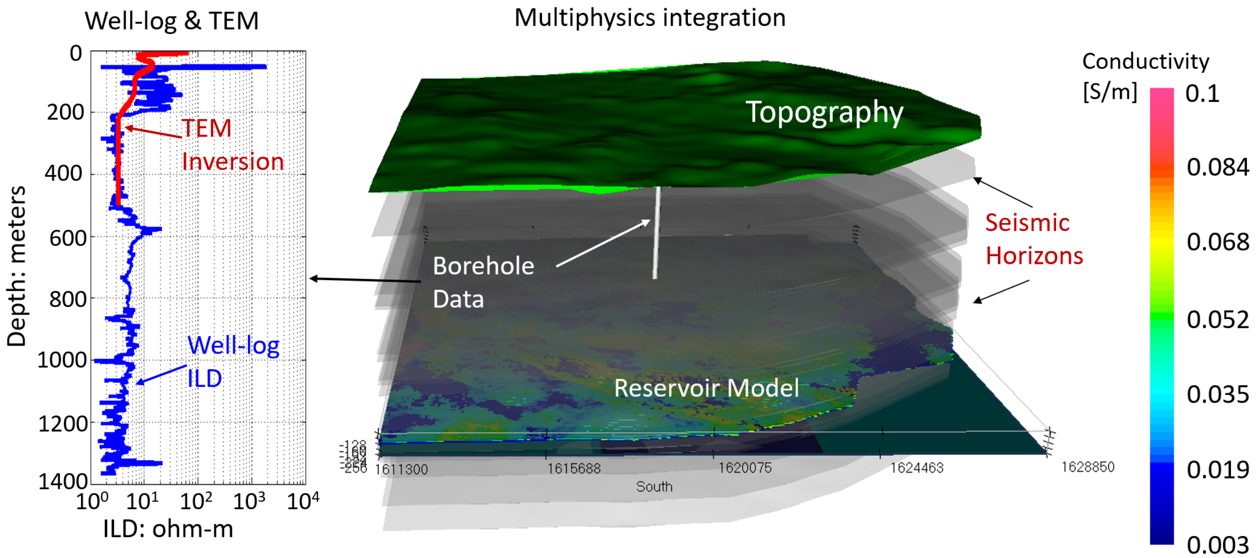

Figure 3.3.3: Multiphysics integration of geology, seismic, reservoir simulation, and borehole data into a complete 3D site conductivity model.

Step 4: Adding Deep Induction Log and Inversion of TEM Data

Once the significant formation boundaries have been defined within the over- and under-burden, the next step is to incorporate representative conductivities for each of the stratigraphic layers. To accomplish this, we integrate the resistivity data from a collection of boreholes throughout the site with the inversion results of TEM field data collected during each CWC-CSEM field campaign. An example of the overlapping borehole ILD and TEM data used to define the background conductivity model are presented in **Figure 3.3.3** (left panel), and **Figure 3.3.4**. The resulting 3D conductivity site model, prior to incorporating the detailed reservoir interval from step 2, is presented in **Figure 3.3.4** along with one of the ILD borehole logs from the field site.

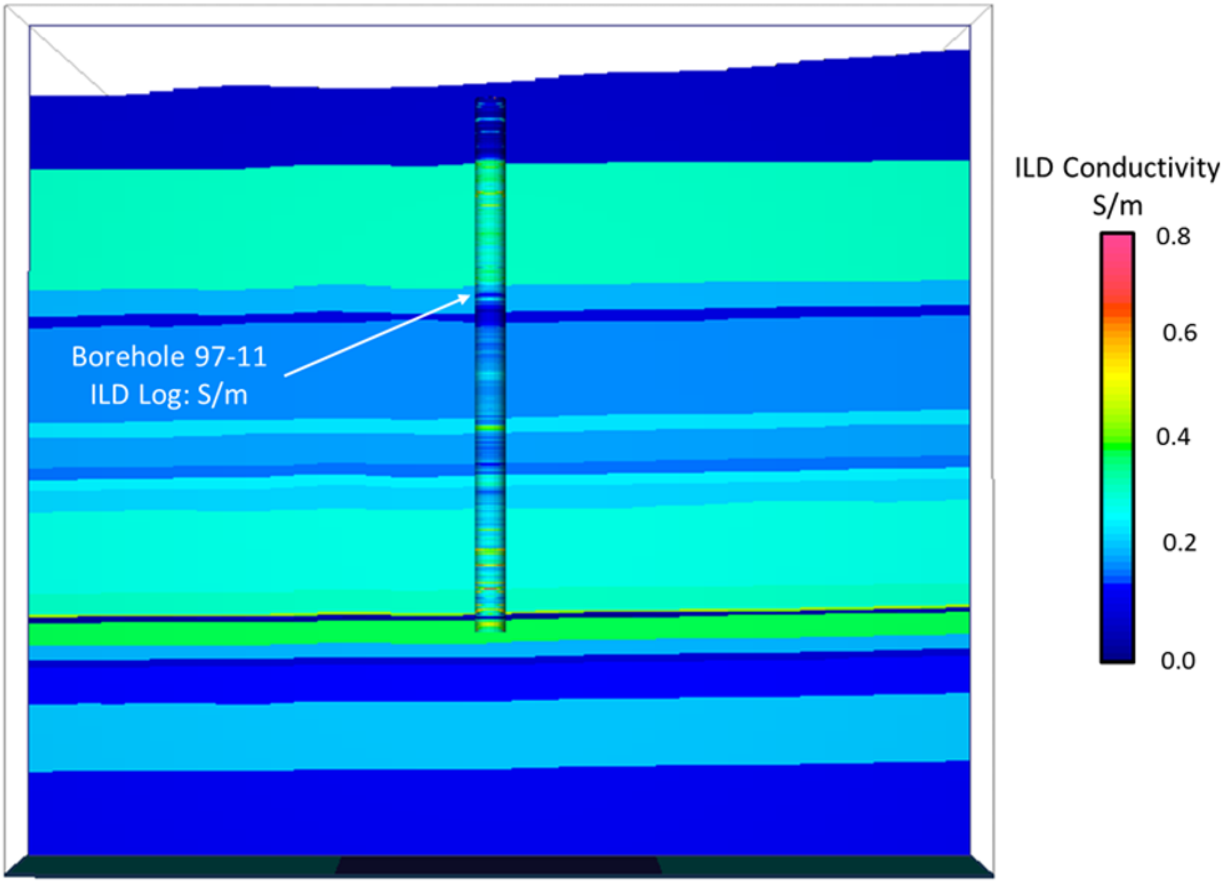

Figure 3.3.4: The large-scale 3D conductivity site model after filling in the horizons with borehole resistivity and TEM inversion data.

Step 5: Merge the Background and Reservoir Models

The final step to build the complete site model is to bring the two previously constructed models together. To accomplish this, the detailed reservoir model, at any time, is inserted into the larger background model at the appropriate depth interval. An important component to this step is allowing the reservoir model to be updated independently over time, converted to conductivity, and incorporated into the full site model without the need to rebuild the complete background. Results of the final 3D conductivity site model for one time-state, including the over-burden, under-burden, and detailed reservoir data, are illustrated in **Figure 3.3.5**.

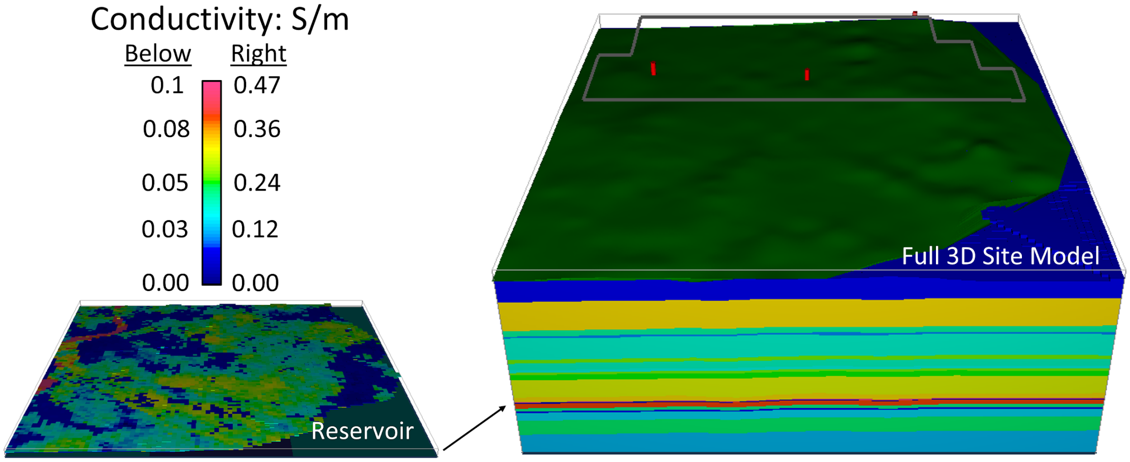

Figure 3.3.5: Final 3D conductivity site model including the relevant geological sequences and the reservoir interval at one time-state inserted at the appropriate depth. The gray lines on the topography define the Phase 5 production area and the three red points on the topography are the locations of three legacy wells utilized for the CWC-CSEM field surveys.

Demonstration: CWC-CSEM Simulations

We briefly demonstrate the application of the developed site model (**Figure 3.3.5**) to simulating the predicted CWC-CSEM responses as one step in the larger problem of reservoir imaging and monitoring of injected CO2 during enhanced oil recovery.

Simulations of the CWC-CSEM surveys are carried out in a two-step process: 1) determining the current distribution in the casings, and 2) combining this response into a 3D numerical solution of Maxwell's equations. The current in the borehole casing is calculated using a method of moments approach (Schenkel and Morrison, 1990). Within this formulation, the response of the casing is calculated using a superposition of Dyadic Green's Functions in the presence of an active transmitter source (Tang et al., 2015). Once the response of the borehole has been determined, the 3D Maxwell's equations are solved using a decoupled vector and scalar potential formulation called EMSchur3D (Irons et al., 2012).

Performance of the 3D EM solver is greatly influenced by the choice of sparse matrix solver which is called repeatedly. The underlying system is complex-symmetric but not Hermitian. As a result, many solvers are not optimized for this system. Benchmarks suggest that the complex symmetric variant PARDISO (Kourounis et al., 2018) is the best performing solver when sufficient memory is available (**Table 3.3.1**). Iterative and hybrid solvers are less memory intensive, but run significantly slower (Guennebaud et al., 2010).

Field electromagnetic data collected at the surface may then be compared to electromagnetic simulations based on reservoir model realizations and Archie relations (**Figure 3.3.6**). This workflow allows for validation and/or reduced uncertainty in reservoir modeling parameters.

Table 3.3.1: Timing examples using EMSchur3D on a test problem of dimensionality 50x50x25 cells. All times were on twin socket featuring Xeon(R) CPU E5-2670 CPU's and utilizing up to 28 physical cores. The PARDISO direct solver (D) had the best performance, but also the greatest memory requirements. The BiCGSTAB iterative solver (IS) was less performant, but also had a much lower memory footprint.

Solver	Solution error	Setup Time (min)	Solve time (min)	Total time (min)
SuperLU (D)	4.9e-30	4.6	0.43	5.02
PARDISO (D)	5.2e-30	0.18	0.34	0.52
BiCGSTAB (IS)	2.6e-29	0.0	2.17	2.17
BiCGSTAB w/ILU (IS+D)	8.3e-30	0.57	1.92	2.48

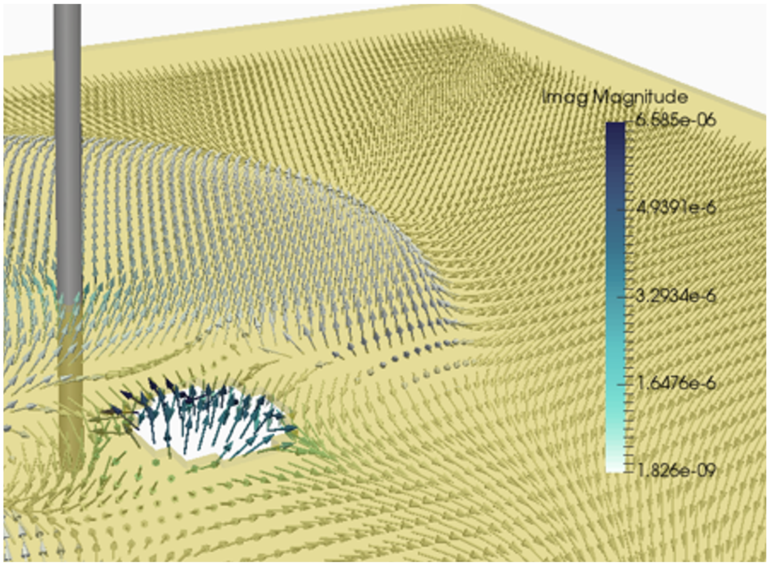

Figure 3.3.6: EM simulation data using the presented workflow. Electric field lines flowing around a resistive CO2-plume is shown.

Summary

Within this project component, we have successfully developed a method for the integrated development of 3D electrical conductivity models of an oil field for CO2-EOR monitoring with charged wellbore casing controlled source electromagnetics (CWC-CSEM) and presented its application at the Bell Creek Oil Field. Such developments are critical for understanding and reproducing the link between reservoir simulation models and geology to the physical property distributions at the site. They additionally provide an ability to guide the CWC-CSEM field surveys at the front end, and act as a feedback mechanism into the reservoir simulations at the back end.

3.4. CSEM DATA PROCESSING

Controlled-source electromagnetic data consist of time series of components of the electric and magnetic fields, paired with a time series of the current output from the transmitter. It is more efficient to perform electromagnetic modeling in the frequency domain than the time domain, though. Therefore, in order to compare observed data with modeled predictions, the data must be transformed into the frequency domain. Furthermore, the receiver signals are linearly dependent on the transmitter signal, so they may be normalized by the transmitter signal without loss of information. When this is done in the frequency domain, the result is a complex function of frequency known as a response function. The purpose of data processing is to convert time series data into response functions, and, in the process, to mitigate the effects of noise on the recovered response functions.

Processing workflow

The first step is to pair a transmitter time series with a receiver component time series and window each to their overlapping time range (**Figure 3.4.1**). The transmitter and receiver signals undergo the same processing steps for consistency's sake.

Once the time series have been windowed, 60 Hz noise is filtered out. This can be done by means of a lockin filter (Strack, 1992) or a notch filter. A lockin filter (**Figures 3.4.2a**, **3.4.2b**) removes a 60 Hz sinusoid, and is applied as follows. First, a running mean computed over a window of 1/60 s is subtracted from the signal. Then, a 60 Hz sinusoid is fitted to each portion of the demeaned signal that is not soon after a transmitter polarity change. For the portion of the signal that occurs soon after a polarity change, the sinusoids that were fitted to the adjacent portions of the signal are linearly interpolated based on time. This 60 Hz sinusoid is subtracted from the original signal to obtain a denoised signal.

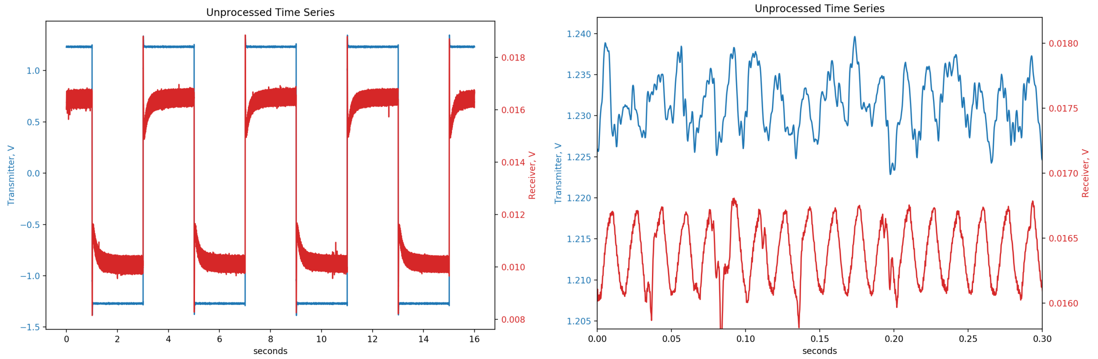

(a) (b)

Figure 3.4.1: Part of a pair of receiver (Ex component) and 0.25 Hz transmitter time series, shown at (a) a scale of seconds and (b) a scale of milliseconds. The transmitter time series is shown in blue, and the receiver time series is in orange.

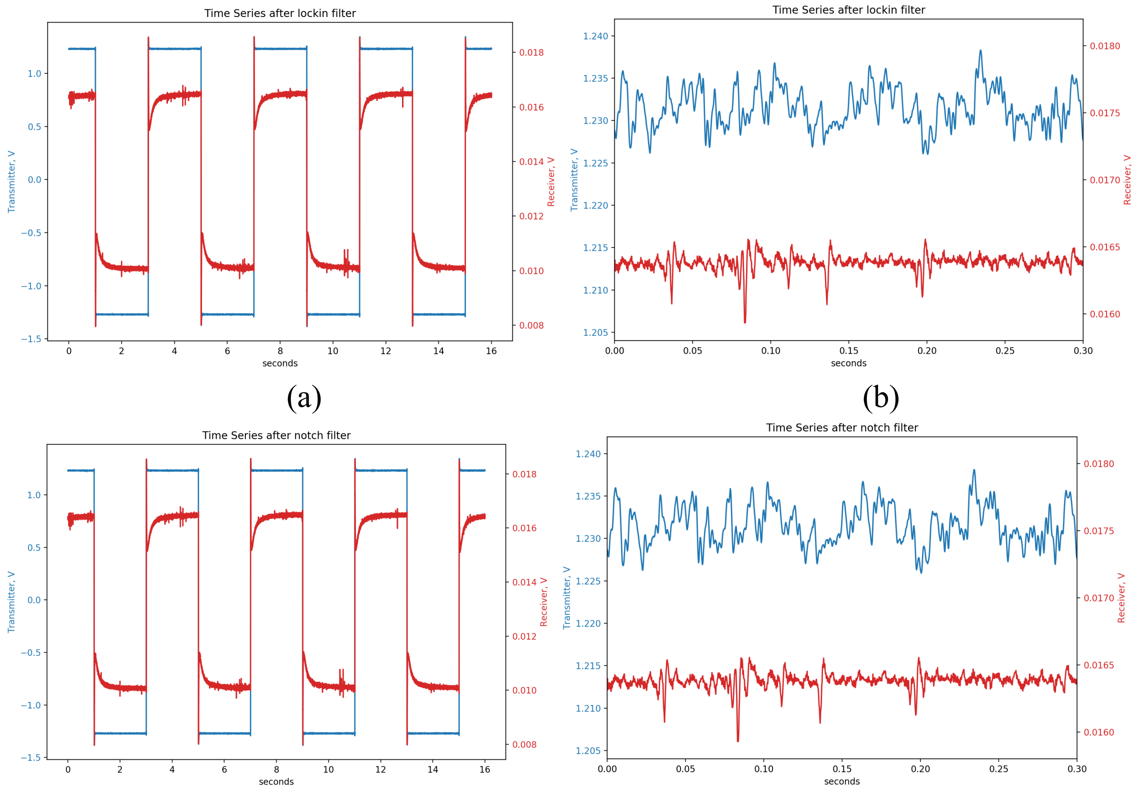

(a) (b)

(c) (d)

Figure 3.4.2: The same signals as shown in **Figure 3.4.1a** after filtering 60 Hz noise. (a) The results of applying a lockin filter plotted on the scale of seconds. (b) The results of applying a lockin filter plotted on the scale of milliseconds. (c) The results of applying a notch filter centered at 60 Hz plotted on the scale of seconds. (d) The results of applying a notch filter centered at 60 Hz plotted on the scale of milliseconds. The two different approaches yield similar results at both scales.

A 60 Hz notch filter is another common method for removing 60 Hz noise (**Figures 3.4.2c**, **3.4.2d**). **Figure 3.4.2** shows that the difference in the filtered signal between these two approaches is small. We applied a lock-in filter to the portions of a signal that are 100 samples after a transmitter on-time and 40 samples before the next.

After filtering 60 Hz noise, the next step is to apply a drift correction (**Figure 3.4.3**). For this step, a robust running mean is computed by averaging over a time window equal to one transmitter period. If the signal were centered around 0 V (i.e. no DC component) and if it were purely periodic with a period equal to the period of the transmitted signal, then the running mean would be zero everywhere. The running mean is subtracted from the signal to yield a drift corrected signal.

Fourier coefficients are computed for the drift corrected signals at the frequency of transmission, and at the 3rd, 5th, 7th, and 9th harmonics of that frequency. The Fourier coefficient of the receiver is divided by the Fourier coefficient of the transmitter signal to yield the value of the response function at a single frequency. These Fourier coefficients are computed using a short-time Fourier transform, so a windowing function and a window stride must be chosen. After testing various options, we chose a simple rectangular windowing function with a length and a stride of one transmitter period. Our testing indicated that the choice did not strongly affect the transfer functions, but it did significantly affect estimates of the variance. The rectangular window offers high sensitivity in the presence of random noise, high spectral resolution, and a maximal number of time windows and therefore a maximal number of estimates of the transfer function. Disadvantageously, the rectangular window exhibits high spectral leakage. However, since the frequencies of transmission, power line noise, and cathodic protection are all known, spectral leakage can be minimized by choosing window lengths strategically. Additionally, Fourier coefficients for window sizes of any integer number of transmitter periods can be derived from Fourier coefficients for a window size of one transmitter period, simply by averaging Fourier coefficients from adjacent time windows.

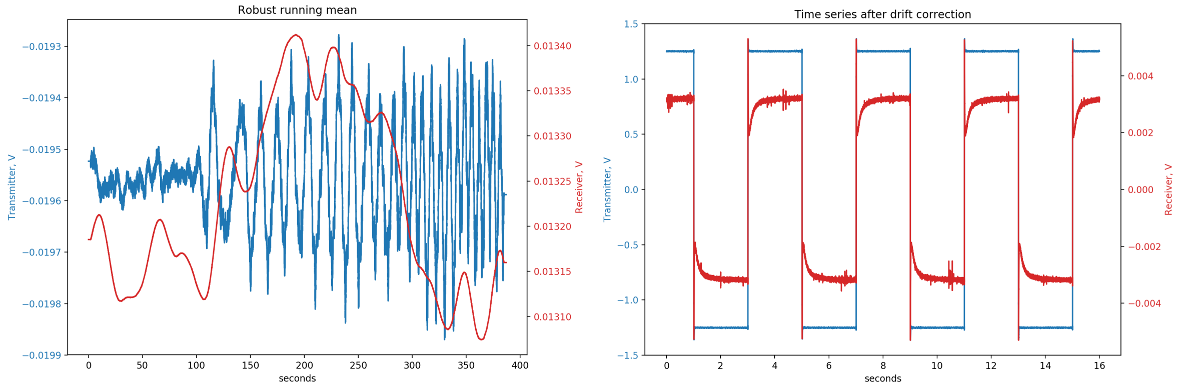

(a) (b)

Figure 3.4.3: (a) The robust running mean for the transmitter and receiver signals shown in **Figure 3.4.2a**. (b) The drift corrected transmitter and receiver signals. Transmitter signals are shown in blue, and receiver signals are in orange.

Averaging Fourier coefficients from adjacent time windows, or equivalently, using a large time window, is a way to minimize the effect of cathodic protection noise. In the Bell Creek field, pipelines are protected from oxidation via pulses of galvanic current that occur on either a 5 s or a 10 s cycle. This cathodic protection noise can cause wide variations in our processed data. To mitigate that effect and avoid unrealistically high variance, we average Fourier coefficients such that the length of the equivalent time window equals an integer number of cathodic protection cycles. For example, for a 0.25 Hz transmission, each Fourier coefficient corresponds to a 4 s time window. Taking the mean of five coefficients from adjacent windows is equivalent to using one 20 s rectangular window. Such a window contains exactly two 10 s cathodic protection cycles. Thus, Fourier coefficients at transmission frequencies will not vary greatly from one 20 s window to the next, and the variance among different windows is lessened. Furthermore, spectral leakage of the cathodic protection signal into the frequency of transmission and its harmonics is minimized, so long as the transmission frequency and harmonics are not themselves harmonics of the cathodic protection frequency. Unfortunately, this happens for transmission frequencies of 0.5 Hz, 1 Hz, 2 Hz, 4 Hz, 8 Hz, and 16 Hz. No choice of windowing function can remove this effect.

Robust averaging and variance estimation

The short time Fourier transform returns many estimates of the Fourier coefficient at each frequency, one for each window. In order to average the coefficients robustly, we use a regression-M estimate. Regression-M estimation is commonly used for robust MT data processing (Egbert and Booker, 1986), and has been applied to CSEM data (Streich et al., 2013).

Regression-M estimation provides estimates of both the response function and its variance at each frequency. In our implementation, we begin with least-squares estimates of the response function and its variance, derived by minimizing the sum of squares of differences between the measured receiver Fourier coefficients and the predicted receiver Fourier coefficients, which are the products of the transmitter Fourier coefficients with the response function. An iterative process is begun. The observed receiver values are modified by down-weighting residuals that are more than 1.5 times the error scale away from zero, where the initial error scale estimate is the standard deviation of the residuals. Then, the conditionally weighted residuals are added back to the predicted receiver coefficients. New response function estimates are obtained by least squares using the modified receiver observations. Using the new response function estimates, new predicted receiver coefficients and residuals are computed. Then, the error scale estimate is updated, computed as the square root of the sum of the squared residuals divided by 0.7784 (2N-2), where N is the number of measured Fourier coefficients. The value 0.7784 accounts for the bias in the scale estimate resulting from decreasing larger residuals. This value was derived by assuming a normal distribution Egbert and Booker (1986). This process is repeated until an objective function fails to decrease by more than $2\text{x}10^{-7}$%. The objective function we use is the Huber norm of the residuals with a threshold of 1.5 times the standard deviation estimate.

Difference data

Processed CSEM data consist of response functions. A response function describes the complex response of a receiver component to the transmitted current as a function of frequency. After processing time-series data to obtain these response functions (McAliley et al., 2019), we wish to obtain the differences in the response functions that result from changes in the conductivity between survey campaigns. We refer to these differences as difference data. The difference of two response functions, though, will include the effects of changes in survey geometry between campaigns (receiver locations and transmitter wire paths). We expect the primary field from the transmitter wire to be stronger than the secondary field from conductivity changes within the reservoir. Therefore, changes in survey geometry will cause errors in interpretation if they are ignored. If the receiver locations and transmitter wire paths are measured in each campaign, then those effects can be mitigated by including the survey changes during modeling.

3.5 CSEM MODELING AND INVERSION

Controlled source electromagnetic modeling

History-matched reservoir modeling provides multiple candidates for the time-varying distribution of fluids in the reservoir. We compute a corresponding conductivity model for each time step of each candidate, as described in the section on conductivity model construction. Next, we must evaluate the conductivity models against our CSEM data and determine which models fit the observed electromagnetic data. Therefore, we must compute response functions for each conductivity model at every frequency for which we have data.

To compute CSEM data in the frequency domain, we solve the following boundary value problem for the electric field:

$$\nabla \times \mu_r^{-1} \nabla \times E + i\omega\mu_0\sigma E = i\omega\mu_0 J_s, \qquad \text{(Eqs. 3.5.1)}$$
$$\hat{n} \times E = 0, \hat{n} \cdot H = 0,$$

where E and H are the electric and magnetic field vectors as functions of position and frequency ω, μ_r is relative magnetic permeability, μ_0 is vacuum permeability, i is the imaginary number, σ is electrical conductivity, and J_s is the source current density. The normal to the boundary of the domain is denoted by $\hat{n}$, and the boundary conditions listed constitute the perfect electrically conducting boundary. The use of these equations implies a quasi-static approximation; i.e., they imply the assumption that $\sigma \gg \omega\varepsilon$ where ε is permittivity, and thus that the behavior of the fields is dominantly diffusive rather than wave-like. In this study, we assume uniform vacuum permeability, i.e., $\mu_r = 1$. Once the electric field has been computed, the magnetic field can be computed quickly by Faraday’s Law.

Three dimensional modeling is performed using the open-source code emg3d, by Werthmüller et al. (2019). The code uses a finite volume discretization on a tensor mesh and the multigrid method to solve the above BVP numerically. In principle, the three dimensional solver should be sufficient to compute electromagnetic fields. Two issues confound such a naive application of the solver, though. Both issues relate to the sizes of discretized cells on the mesh. First, computed fields are inaccurate within a few cells of a source current (transmitter wire). The smallest cell size on our mesh is 60 m to a side, and some of our receivers fall within 60 m of a transmitter wire, so this issue must be addressed. Second, the modeling must account for conductive steel well casings which were electrically connected to our transmitter. The cross-sectional diameter of such a casing is approximately 0.1 m, far less than the minimum cell size. In principle, both issues can be addressed by using a very finely discretized mesh. However, computing fields on a sufficiently fine mesh, especially on a tensor mesh, would be prohibitively computationally costly.

To address the first issue of small transmitter-receiver offsets, we use a primary-secondary formulation. In such a formulation, primary fields arising from the wire source are computed for a simple conductivity model such as a uniform half space. Such primary fields can be computed analytically or semi-analytically, so they are accurate even at small offsets. Then, secondary fields that arise from conductivity differences between the fully 3D conductivity model and the simple primary conductivity model are computed using a 3D numerical solver. Streich (2009) provides a complete derivation of the primary-secondary formulation. To compute primary fields, we use empymod, a semi-analytic 1D electromagnetic modeling code written by Werthmüller (2017),

The second issue of incorporating well casing effects into the model can be addressed by applying the method of moments to compute electrical currents in well casings. Tang et al. (2015) describe this approach in detail for a casing in a half space. Here we provide a brief overview of the method. First, each casing is discretized into multiple small segments. For our model, we use a segment length of 5 m. Next, an interaction matrix Γ is formed. Each column of the interaction matrix describes how a current in one segment contributes to the electric field in every other segment. Tang et al. (2015) derive an analytical expression for terms of this matrix for equally-sized segments within one vertical casing. We use that expression for segments in the same well. For segments in different wells, we use numerical integration in conjunction with empymod to compute interaction terms. Incident electric fields E^{in} from the transmitter wires are then computed at each segment. Assuming constant electric field and current within each segment, the current in each casing segment J can then be computed by solving a linear system of equations, given the well casing resistivity ρ_c,

$$(I\rho_c - \Gamma)J = E^{in}. \qquad \text{(Eq. 3.5.2)}$$

Tang et al. (2015) also describe how to combine the method of moments with the primary-secondary formulation. The primary field is defined to be the field due to both the wire sources and the casing current sources in a homogeneous half space, and the secondary field is then the field that arises due to deviations in conductivity from that of the primary half space model.

Table 3.5.1: Conductivity of each unit used in the final 3D model.

Unit	Conductivity (S/m)
Ground Surface	0.18
Pierre	0.18
Eagle	0.18
Shannon	0.18
Gammon	0.18
Niobrara	0.18
Carlile	0.18
Turner	0.18
Pool Creek	0.18
Greenhorn	0.18
Bell Fourche	0.18
Mowry	0.18
Shell Creek	0.465
Springen Ranch	0.425
Bell Creek	Saturation dependent
Rozet	Saturation dependent
Skull Creek	0.395
Dakota	0.212
Fall River	0.083
Lakota	0.18
Charles	0.18
Mission Canyon	0.18

We constructed a three dimensional conductivity model. We assigned one conductivity value to each stratigraphic unit, chosen by taking the harmonic average of conductivities of that unit from well logs. We used seismic horizons to locate units in our model. We found, however, that fields calculated for this model did not match our observed fields as well as a homogeneous half space model of 0.18 S/m. Therefore, we modified the model, setting the conductivities of all layers except those near the reservoir depth to 0.18. **Table 3.5.1** shows the conductivities used in our final 3D model.

During modeling, we found that our mesh was insufficiently fine to handle topographic effects, creating artifacts in the modeled fields. We therefore constructed a three dimensional conductivity model without topography. A constant value of 1135 m was chosen for the land surface elevation. The tops of well casings were truncated or extended as needed such that they all reach the land surface in the model.

Casing currents

Conductive steel-cased wells are notoriously difficult to incorporate into 3D numerical PDE solvers because the casing segments must be finely discretized, and the high conductivity contrast introduces large numerical errors. We side-step this difficulty by using the method of moments to compute electric currents in casings, then treating those casing currents as sources in a numerical PDE solver. To do so, we follow the method-of-moments approach outlined by Tang et al. (2015). In this approach, a linear system of equations must be constructed and solved for current along the length of the casing. We have ported code into Python to solve this modeling step. Doing so allows us to generalize the approach to incorporate multiple well casings and more spatially complex models of the electrical conductivity of the subsurface. **Figure 3.5.1** shows computed currents along a 1365 m vertical casing in a conducting halfspace of 0.18 S/m, excited by a 2000 m wire carrying current at 0.125 Hz. These parameters reflect our experimental parameters at Bell Creek.

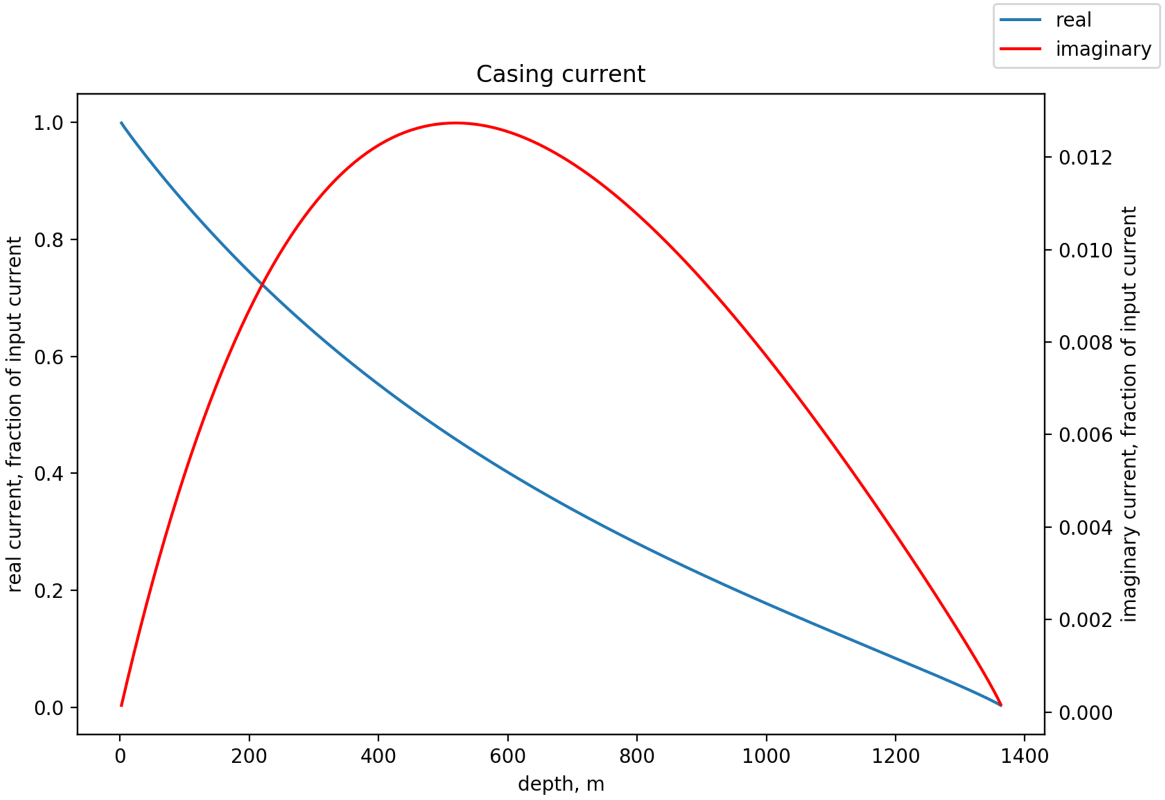

Figure 3.5.1: Current distribution along a vertical casing excited by a horizontal wire at the surface of a halfspace, computed in Python.

Tang et al. (2015) computed each one casing's current, ignoring the effects of one casing on another. We expanded our casing current modeling capability to include inter-casing effects. We compute those interactions by numerical integration. Since we energized two casings at once in our survey, one at each end of our transmitter wire, this algorithmic advancement increases our modeling accuracy. The code to model casing currents is publicly available, and can be found at https://github.com/AndyMcAliley/em_casing.

Sensitivity computation

Computing the sensitivity of CSEM data to reservoir conductivity changes serves two purposes. First, it provides a sense of where within the reservoir our data can detect saturation changes. Second, it is necessary to invert data for conductivity changes. Here, we show a method for efficiently computing the sensitivity of difference data to conductivity changes.

Let us define F_i as a directional component of either the electric or magnetic field as measured at one receiver location at one particular time. Following McGillivray et al. (1994), the sensitivity of F_i to a conductivity perturbation in a volume V_j of homogeneous conductivity σ_j is

$$\frac{\partial F_i}{\partial \sigma_j} = \int_{V_j} \left(\vec{E}_i^{\dagger} \cdot \vec{E} \right) dv, \qquad \text{(Eq. 3.5.3)}$$

where $\vec{E}$ is the electric field arising from the transmitter source, and $\overrightarrow{E_i}^{\dagger}$ is the adjoint electric field. The adjoint field is the field due to an electric or magnetic (depending on F_i) dipole source located at the receiver and oriented in the direction of the field component F_i.

We are interested in the sensitivity of the data difference ΔF_i to a conductivity change $\Delta\sigma_j$ within a volume. Since changes in fluid saturation can result in conductivity changes that vary over many orders of magnitude, it is preferable to invert for changes in the logarithm of conductivity. Therefore, we define a sensitivity matrix J such that its elements are

$$J_{ij} = \frac{\partial F_i}{\partial m_j} = \sigma_j \int_{V_j} \vec{E}_i^{\dagger} \cdot \vec{E} dv, \tag{Eq. 3.5.4}$$

where $m_j = \ln\sigma_j$. A first order approximation to the data difference of one field component is

$$\Delta F_i \approx \sum_{j=1}^{M} \frac{\partial F_i}{\partial m_j} \Delta m_j, \tag{Eq. 3.5.5}$$

where M is the number of discretized model cells. We discretize the model domain within the reservoir layer into rectilinear prisms and numerically compute the integral in Equation 3.5.2 over each model cell for all data to form **J**. Thus in matrix-vector form,

$$\vec{\Delta F} \approx \mathbf{J}\vec{\Delta m}. \tag{Eq. 3.5.6}$$

Inversion of CSEM data

We present a workflow to recover relative change in reservoir conductivity from time-lapse CSEM data that incorporates the effects of steel casings on the data. The recovered conductivity change can then be combined with the reservoir model to estimate fluid saturation changes. We utilize time-lapse difference data because it is more robust to the influences of infrastructure and variations in shallow conductivity. Our imaging algorithm is computationally efficient and simple to implement.

To recover relative conductivity change in the reservoir, we invert the data by Tikhonov regularization. We minimize an objective function ϕ, which is a linear combination of the data misfit ϕ_d and the model regularization term ϕ_m, scaled by a regularization parameter β , as

$$\phi = \phi_d + \beta\phi_m. \tag{Eq. 3.5.7}$$

The model regularization term is a combination of measures of the smallest and flattest model. The data misfit requires a way to predict data, given a model. In this case, the data cannot be predicted accurately after perturbing the conductivity without a 3D forward modeling algorithm. However, it can be approximated by using the linearized sensitivity matrix, as

$$\Delta\vec{F} \approx \mathbf{J}\Delta\vec{m}. \tag{Eq. 3.5.8}$$

Here, ΔF_i is a difference in a directional component of either the electric or magnetic field as measured at one receiver location over one particular epoch. The linearized sensitivity matrix **J** can be formed as described above. Then, the data misfit can be computed as

$$\phi_d \approx \left\| \mathbf{W_d} \left(\vec{d}^{obs} - \mathbf{J}\vec{m} \right) \right\|_2^2, \tag{Eq. 3.5.9}$$

where $\underline{d}^{obs}$ is a vector of differences in measured fields between two campaigns, $\mathbf{W_d}$ is a diagonal matrix of the reciprocals of the estimated standard deviations of the data errors, **J** is the sensitivity matrix, and $\vec{m}$ is a vector of changes in the logarithms of conductivities of model cells between campaigns (the Δ symbol has been dropped for convenience).

For land CSEM, the minimum error in the data can be estimated based on repeated measurements (McAliley et al., 2019). Additional data errors arise from uncertainty in recorded receiver and transmitter locations, and changes in near-surface conductivity due to variations in water saturation and temperature. These errors can be estimated and used to obtain a target data misfit. In this case, however, there is also error introduced by ignoring the nonlinearity in the forward modeling. Therefore, the target data misfit should account for modeling errors in addition to errors in the observed data.

The regularization parameter β controls how well the recovered model fits the observed data. A value of β can be chosen such that the data misfit of the recovered model matches the target data misfit. Alternatively, heuristic methods to estimate the optimal target misfit can be used such as the L-curve criterion or generalized cross-validation. Regardless, multiple inversions should be performed with different values for β, and the results of these inversions taken together should inform the interpretation of the data.

In conclusion, we have developed and implemented a workflow to image changes in reservoir conductivity from time-lapse CSEM data. It employs simple, fast forward modeling to compute sensitivities that allow for 3D linearized inversion for conductivity changes. The workflow accounts for both variations in survey layout and the electromagnetic effects of steel casings.

4. RESULTS / ACCOMPLISHMENTS

We now describe the results of each step of our workflow, from field data acquisition through reservoir simulations and history matching to electromagnetic modeling and inversion. We also highlight accomplishments and technology products that our team developed, including a machine learning history matching workflow, a CSEM data processing workflow, and a publicly available data processing Python library that facilitates interactive visualization and quality control of CSEM data.

4.1 SURVEY DESIGN & DATA ACQUISITION

Controlled source electromagnetic survey

Figure 4.1.1 shows the final time-lapse survey layout. Due to delays and equipment issues during the October 2017 campaign, we only recorded data at 10 receiver stations (**Figure 4.1.1a**). In May 2018, we expanded to 33 receiver stations (**Figure 4.1.1b**). We used sub-aerial dig-free installations of the magnetometers, developed by Oregon State University (Schultz et al., 2017). In October 2018, we again used sub-aerial magnetometer installations. The western well that we used in October 2017 and May 2018 was inaccessible due to renewed production, so we chose a nearby well to use for transmitting (**Figure 4.1.1c**). In July 2019 we used the same western well as October 2018 (**Figure 4.1.1d**).

The change in transmission well between the second and third campaigns limits our time-lapse data. In each campaign there are two transmitter configurations: one that runs northeast-southwest, and one that runs east-west. The wells used for the northeast-southwest configuration were unchanged throughout all four campaigns, so time-lapse data for that well pair is available for all epochs. The east-west configuration was the same among the first two campaigns, and among the last two campaigns, so time-lapse data for that well pair is only available for the October 2017 to May 2018 epoch, and for the October 2018 to July 2019 epoch. Furthermore, there are few receiver stations in the longest epoch, October 2017 to July 2019, due to the limited number of stations in the first campaign. Therefore, when we show time-lapse data plots in this report, we show data for the epoch from May 2018 to July 2019 for the northeast-southwest transmitter well pair. These time-lapse data have the most time elapsed between campaigns while still having over thirty receiver stations active.

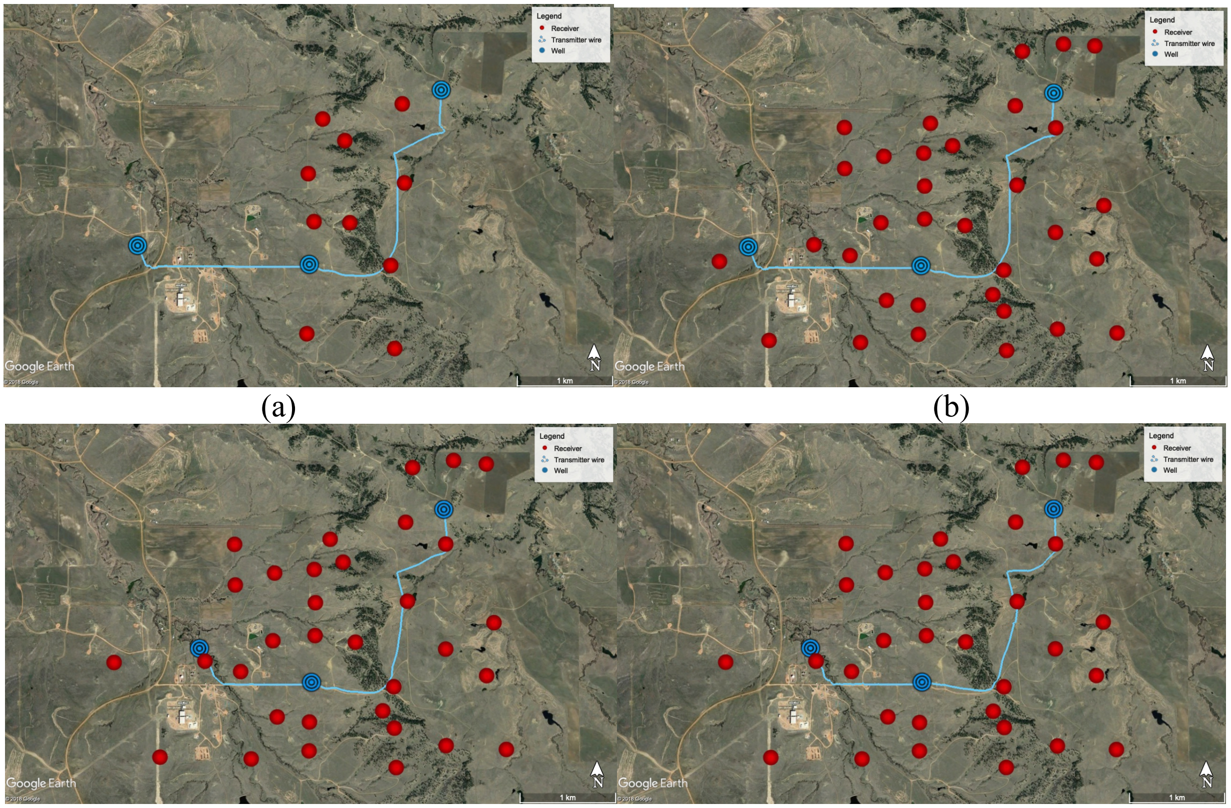

(a) (b)

(c) (d)

Figure 4.1.1: CSEM survey layout for (a) October 2017, (b) May 2018, (c) October 2018, and (d) July 2019 campaigns. Red dots indicate receiver locations. Blue dots represent the wells used as transmitter electrodes, and the blue lines represent transmitter wires. In October 2018, 10 receiver stations recorded data, while 33 stations recorded data in May and October 2018. In October 2018 the western transmitter well was inaccessible, so we were forced to transmit on a nearby well instead.

Transient electromagnetic survey

Data processing took place within the SPIA TEM processing environment (version 3.3.1.0, Aarhus GeoSoftware, Aarhus Denmark). Data processing entails importing raw transients, assuming 5 percent error on all time gates, rejection of raw transients that show signs of noise and/or contamination, rejection of time gates that fall below the noise floor and show signs of noise and/or contamination, and averaging the remaining data with error analysis to produce a single sounding curve for every transmitter moment-receiver pair.

Processed data for every station were inverted in the SPIA TEM processing environment (version 3.3.1.0, Aarhus GeoSoftware, Aarhus Denmark). Careful analysis of model domain was performed to ensure that the model space was sufficient to fit the inverted data. Final depth range for all models begin at the surface and extend to 300 m depth - one station (SBC_TEM_180526_R2_07a) has a model that extends to 350 m depth due to late-time data showing minimal contamination from the nearby infrastructure. Final models used a 50 ohm-meter starting resistivity and a 20 layer, "blocky" style inversion (the inversion kernel applies an L1 norm on the vertical resistivity derivative. This pushes the layers to the fewest number of gradients within the model space, regardless of the gradient across any given layer interface). Layer thicknesses were fixed and logarithmically increase with depth. The inversion calculates an estimate of sensitivity to the data with depth. This sensitivity is represented by the two depth-of-investigation (DOI) channels. DOI_Conservative values represent the bottom of the model with a high sensitivity to the data. DOI_Standard values represent the bottom of the model where sensitivity to the data is assumed to be adequate (Christiansen and Auken, 2012, https://doi.org/10.1190/geo2011-0393.1).

Due to heavy infrastructure in this area many of these individual transients and time gates were culled yielding models that had shallower sensitivity to the geology than we had hoped. Given these cultural effects, typical DOI estimates are between 150 and 300 m (see **Figure 4.1.2a**).

Inversion results are provided in the digital data release both in tabular format as well as plotted with both the data and model spaces presented. An example of the data plots are presented in **Figure 4.1.2b**. See **Appendix A5** for plots of all processed data and inverted models.

One time-domain EM sounding was in relatively close proximity to an existing well with a deep induction log (ILD). **Figure 4.1.2c** shows a comparison between the inverted model and the ILD. The inversion result matches the induction log, while also predicting a resistive overburden. The TEM inversion can be used to better define the electrical resistivity of the near-surface, which can in turn inform the interpretation of time-lapse CSEM data for saturation changes at the depth of the reservoir.

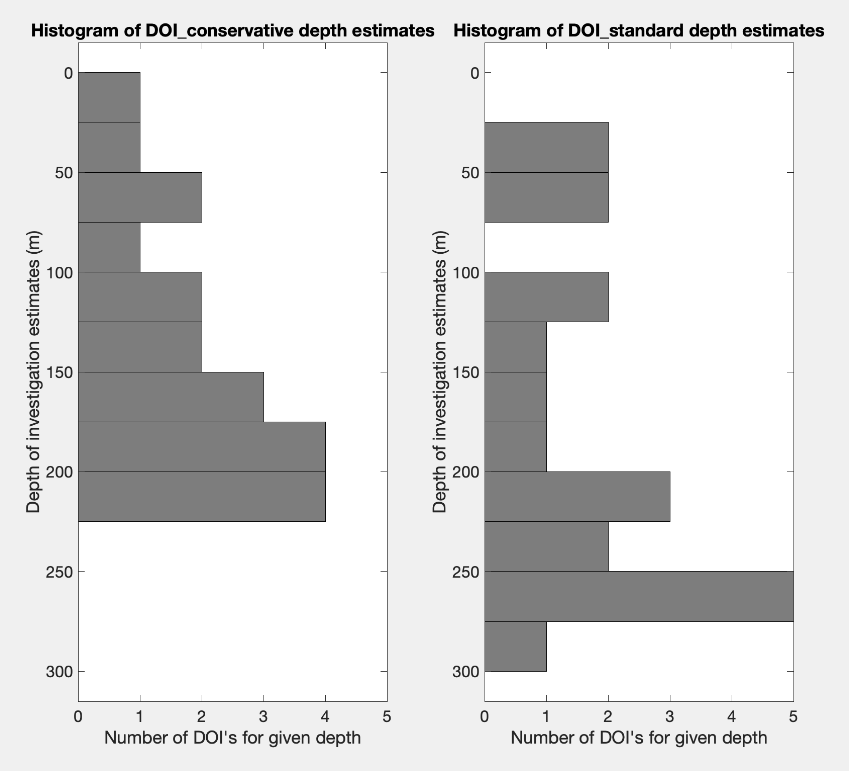

a)

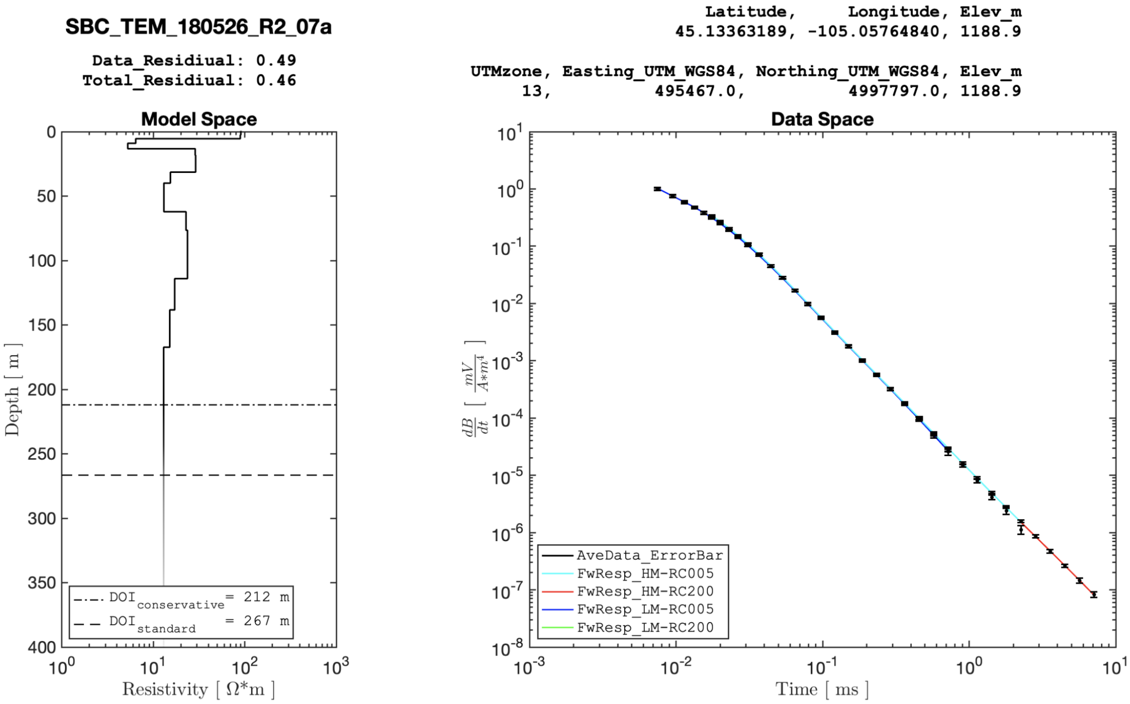

b)

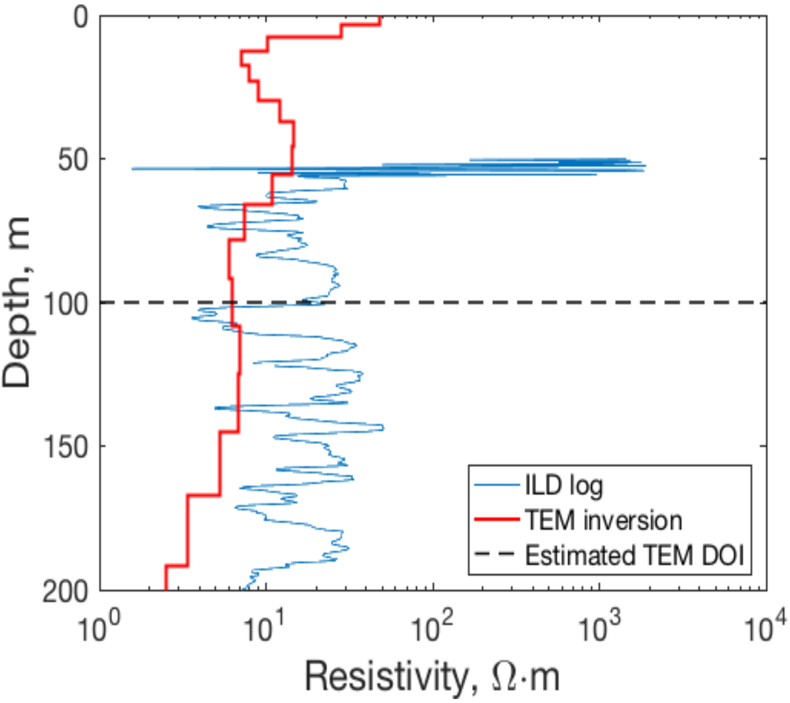

c)

Figure 4.1.2: **a**) Comparison of both “DOI_conservative”, and “DOI_standard” depth-of-investigation (DOI) estimates for all 20 stations. **b**) Example of data and model plots for SBC_TEM_180526_R2_07a. **c**) Smooth inversion of TEM data from sounding location SBC_TEM_171013_BC_01a, plotting alongside a deep induction log (ILD) from nearby well. The dashed black line indicates the minimum estimated depth of investigation.

4.2. RESERVOIR SIMULATION

Initial Model Building

A statistical analysis of the oil production volume and rate is carried out to understand how well the ML-assisted history matching performed in the coarse low-resolution model compared to the higher resolution original model. The ML-assisted history matching work is done on the low-resolution model, and then those parameters applied to the high resolution expanded model. The ML-assisted history matching work is done at our partner institute, New Mexico Tech, and due to data transfer limitations, we are provided the parameters from their work. We ran the full dynamic simulation on both the coarse, low-resolution model and the high resolution, expanded model. A suite of single-factor analysis of variance (ANOVA) statistical tests is performed on the oil production rate datasets for both the coarse and fine resolution models. We then analyzed the oil production rate between observation and the eight cases exported for EM modeling in more detail using a t-test and a regression analysis.

Coarse Model

The oil production rate is an excellent match to the historical data except for the period between 1976 and the early 1990s. During this time, all the model cases exhibit a reduction in the oil production rate compared to the observed data (**Figure 4.2.1**). An ANOVA analysis is applied to the coarse resolution model cases to determine if the ML-assisted cases are from the same underlying population or if there is significant variation between datasets. This analysis indicates a significant variation between the datasets, with a P-value of 0 and F (7.62) is much larger than F_{crit} (1.88), indicating that the whole dataset does not come from the same underlying population distribution as the observed data. If we analyze only the 8 ML-assisted cases and exclude the base case (HM_BASE_UPDATED_240 from **Figure 4.2.1**), the results are almost the same if not a little worse. See **Table A3.7.1** in **Appendix A3.7**.

We apply a two-sample t-test assuming equal variances to each of the 8 ML-assisted cases and the Base Case, comparing against the observed dataset. For all the ML-assisted cases, F is much larger than F_{crit}, and the P-value is 0, indicating that the sample means significantly differ from the overserved mean. The base case has a P-value of 0.255 and a t-stat less than t_{crit}, indicating that there was about a 25% probability that the base case is from the same underlying population as the observed dataset. The results reinforce what is observed in the ANOVA analysis. The ML-assisted history matching cases and the base case are not from the same underlying distribution. See **Table A3.7.2** in **Appendix A3.7** for the complete t-stats for all eight ML-assisted history matched cases and the base case.

Regression analysis is used to analyze the correlation between the simulated data and the observed data. The coarse-resolution model cases show a range of correlations (R^2 values) to the observed dataset from very high at 0.983 for the HMBase240 case to 0.698 for AIHM-CASE37. All the cases showed a fairly high standard error of between 387 STB/d for HMBase240 to 1646 STB/d for AIHM-CASE37, indicating that the data is not from the same underlying population (see **Table**

A3.7.3 in **Appendix A3.7**).

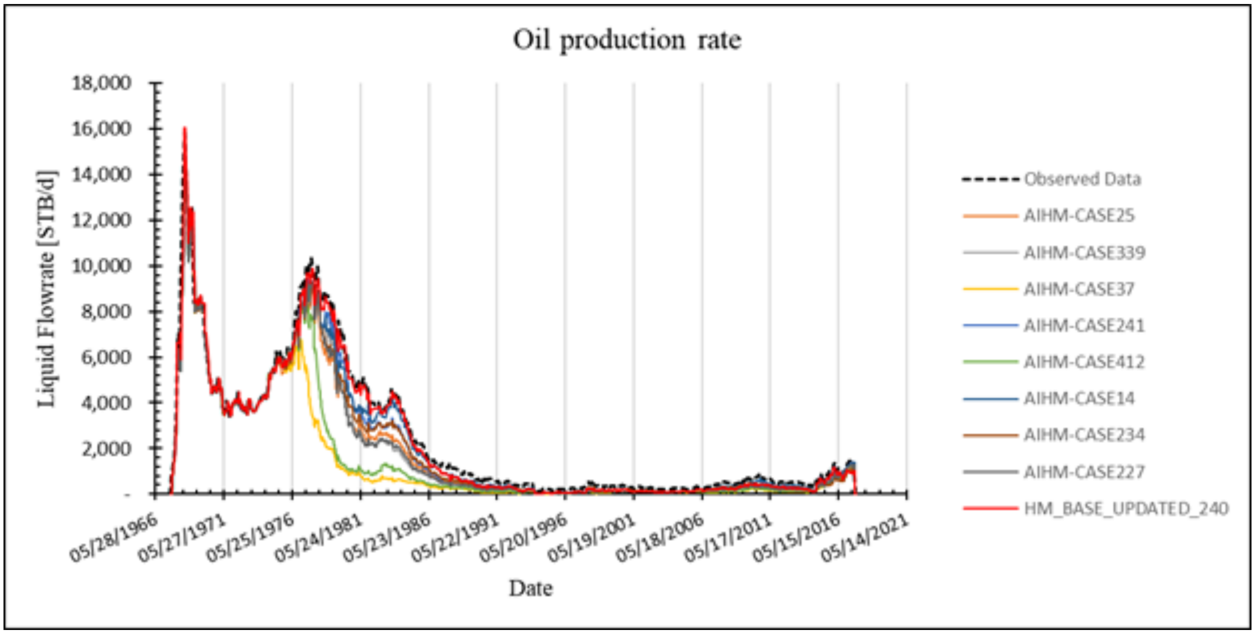

Figure 4.2.1. Oil production for the coarse-resolution model cases.

Overall the statistical analysis indicates that while there is a high correlation between the ML-assisted history matched cases and the observed dataset, they are not from the same underlying population. When the average field pressure through time is analyzed, the oil production rates' behavior is explained. The coarse simulation grid model reduces the pressure below most of the oil components' miscibility point, volatilizing them and driving excess gas production. **Figure 4.2.2** shows that for all cases except the base case (HM_BASE_UPDATE_240), the pressure drops to atmospheric between 1973 and 1976. This is creating a non-physical condition within the reservoir and leads to erroneous results. Given more time and resources, a complete redesign of the coarse grid model used for the ML-assisted history matching would need to be done. Even the base case model's pressure is reduced to levels well below what is known to have taken place in the field.

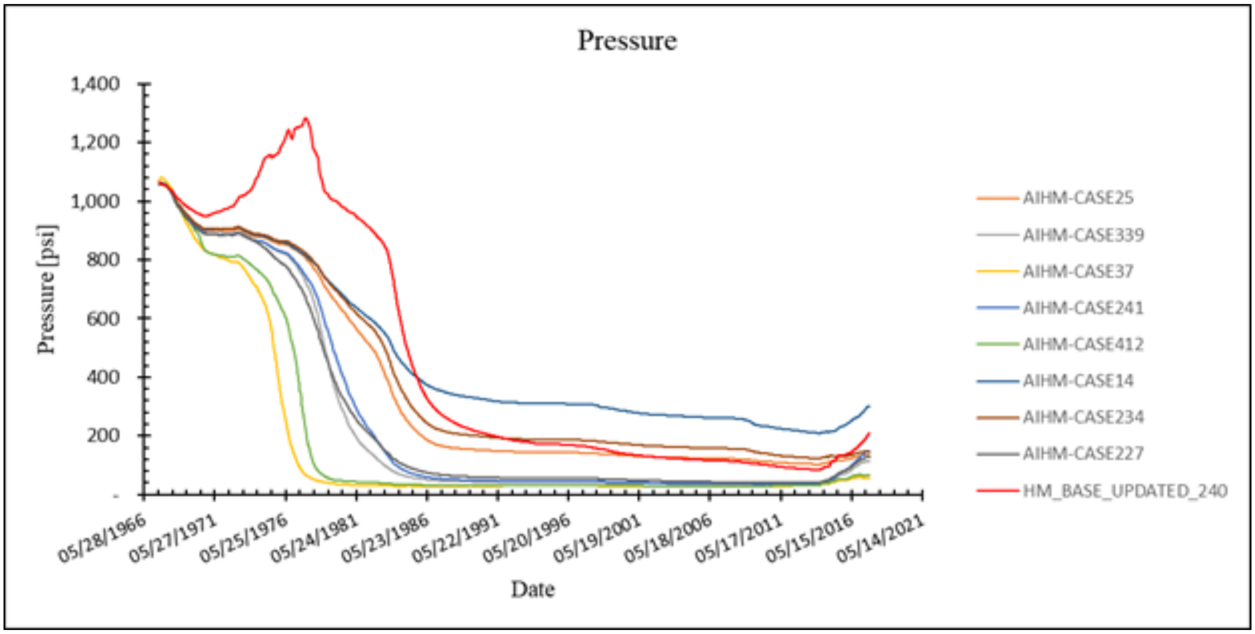

Figure 4.2.2. The average field pressure for the coarse-resolution model cases.

This coarse of a model grid could be why we observe non-physical pressure conditions within the reservoir. For future work, a finer grid resolution is desired. A lot of the reservoir information is lost when up-scaling from a cell size of 100ft by 100ft to a cell size of 1148ft by 1148ft. Interestingly, when the same parameters are applied to the fine-scale simulation model, there is an excellent match to production data, and the pressure field responds in the expected way.

Fine Model

The results for the fine grid model are very different than what we observed for the coarse model. There is a good match between all the cases and the observed data for the oil production rate (**Figure 4.2.3**). The worst performing case is the base case (HMCGLD-Base3_2). During the base case development, the pressure would drop below the miscibility point during the early phase of the simulation. Permeability is increased by 10x over the initial values developed from the log data, allowing the pressure to remain above the miscible point throughout the entire simulation. The ML-assisted history matching cases increase the overall permeability in the I, J, K, giving an even better match to the observed oil production rate.

Analyzing these model cases using the ANOVA indicates that there is very little statistical difference between the datasets. F is less than F_{crit}, and the P-value is 0.999, indicating that these can all be considered from the same underlying population. If we remove the base case, as we did for the coarse grid analysis, the results are the same. See **Table A3.7.4** in **Appendix A3.7**.

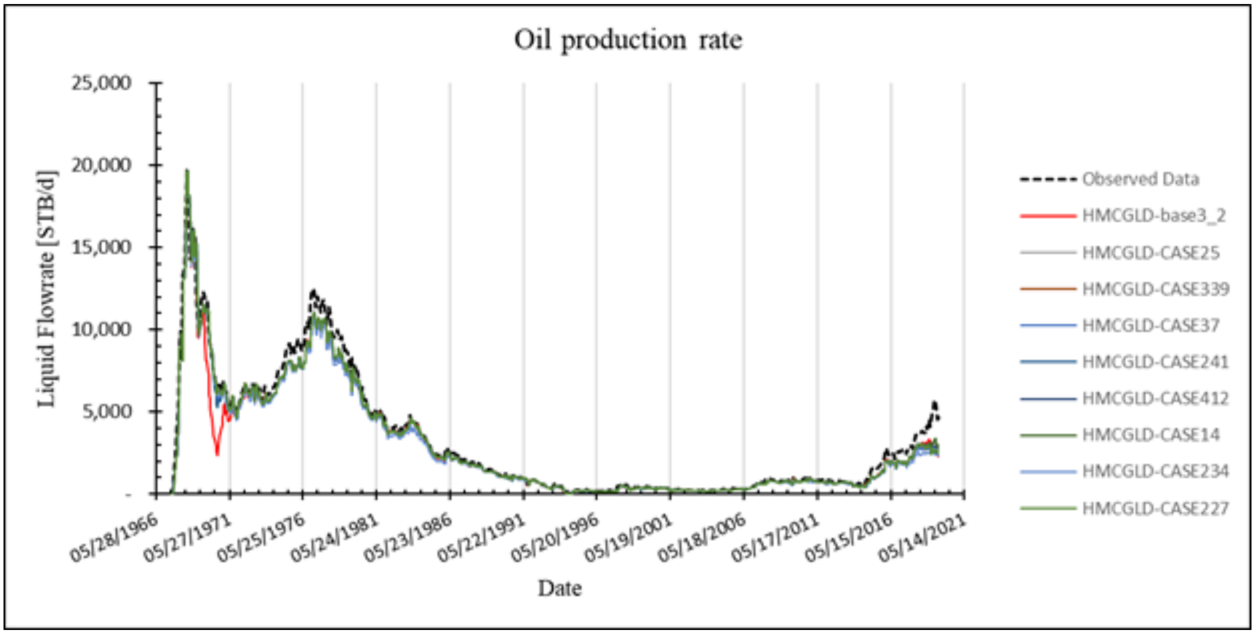

Figure 4.2.3. fine resolution oil production.

To get a better understanding of how well the simulated data correlated to the observed data, two sample t-tests assuming equal variances were performed. The results for the fine resolution model cases indicate that for all cases t is less than tcrit, indicating that there is a possibility they are all from the same underlying population. The P-value is low, between 0.165 and 0.052, indicating that there is a low chance the cases are all from the same population as the observed dataset. The t-test also indicates that the observed data is consistently higher than any individual case; see **Table A3.7.5** in **Appendix A3.7**. The data's correlation to the observed data was explored using regression analysis. The fine resolution model cases show a very high correlation to the observed dataset, with R^2 values of 0.963 to 0.976, but also fairly high standard error of between 568 STB/d to 712 STB/d (**Table A3.7.6** in **Appendix A3.7**).

The oil production rate analysis indicates that the ML-assisted history matched cases are highly correlated with the observed data. But when a t-test and regression analysis is done on select cases, the fit disappears. Statistically, each case is highly correlated but from a different underlying population from the observation dataset. This is a desirable result because it gives statistically distinct water saturation maps for each case, part of the project's goals.

The fine grid model's average field pressure is in stark contrast to what is seen in the coarse grid model. The pressure plotted in **Figure 4.2.4** shows less variation in pressure than the coarse grid, and more importantly, the pressure mimics more closely what we expected. There is an initial pressure drop during the early oil production phase of operations. Then the pressure increased as the water injection phase re-pressurizes the field and stabilized the pressure.

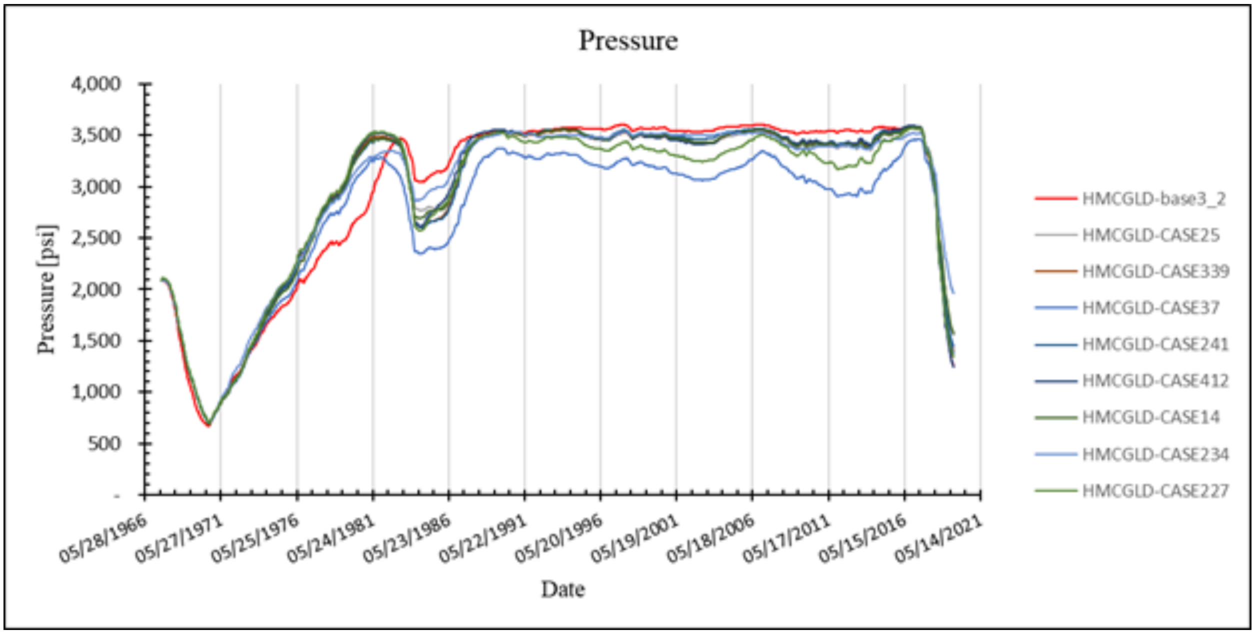

Figure 4.2.4. Pressure for the fine resolution model.

Machine Learning Assisted History Matching

The finalized history matching results are displayed in **Figure 4.2.5**. Promising matching quality can be observed for the oil and water production rates. And the optimum solution of the reservoir characteristic data is listed in **Table 3.2.5**. This particular solution is also confirmed by high-fidelity numerical modelling as shown in **Figure 4.2.6**. The gas rate matching at the early stage of the project exhibits relatively high error, which is due to the uncertainties introduced by the initial fluid composition. However, when the reservoir is depleted and the CO_2 injection starts, the matching quality becomes much better. Such observation indicates a good characterization of the relative permeability, capillary pressure and absolute permeability multiplier determined by the proposed workflow.

In conclusion, the proposed workflow is capable of obtaining a history matching solution quite effectively. For the future actions, the following suggestions can be considered:

1. The gas production prediction does not fit production at early times, due to the uncertainties of the fluid composition. Since there is little information about the composition information of the reservoir fluid, it is difficult to impose physical constraints on this aspect. However, during the CO_2 flood period, the gas production rate matches very well with the field data, which indicates that the permeability field and relative permeability data characterize the multiphase flow mechanisms quite effectively.
2. The lack of field pressure data also introduces uncertainty to the history matching results. When more field pressure data becomes available, it can be used to screen the history matching results with more physical constraints. Besides, the current promising matching

with the fluid production data indicates that the saturation variation within the system is well-captured. Therefore, these results can be employed for the further investigation of the water saturation distributions.

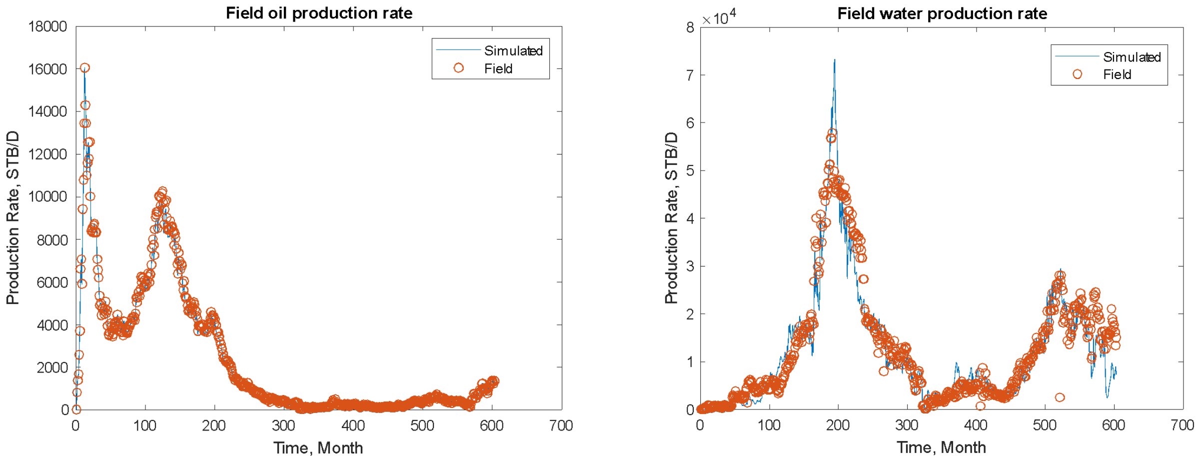

(a) Oil rate matching **(b)** Water rate matching

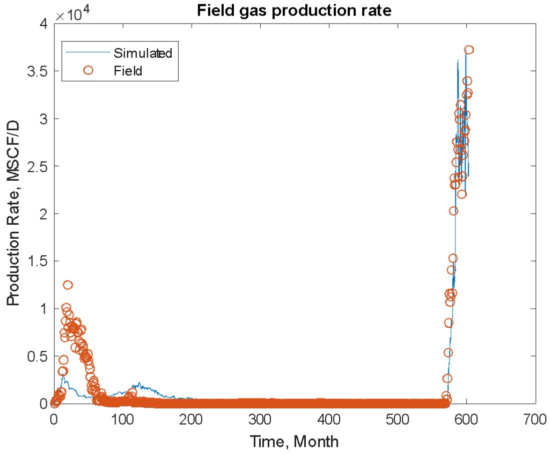

(c) Gas rate matching

Figure 4.2.5. Finalized history matching results found by the machine-learning model.

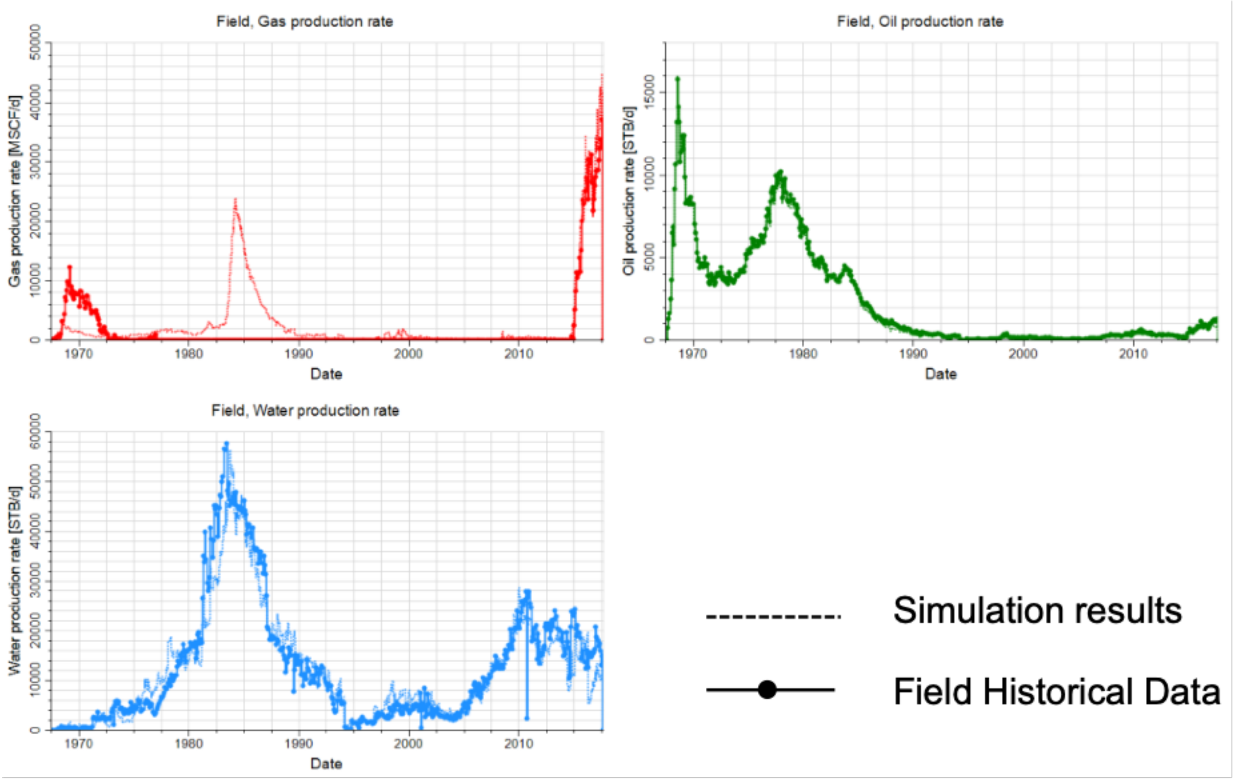

Figure 4.2.6. Finalized history matching results confirmed by the high-fidelity numerical model.

4.3. CSEM DATA PROCESSING

DoZen: data processing software

A custom CSEM data processing software library named DoZen was developed to process data from this project. It contains functions to read the data formats used by Zonge instruments, apply our custom processing workflow, visualize data and metadata, and implement quality control measures. The code is written in Python and is openly available for download, use, or modification at https://github.com/AndyMcAliley/DoZen. See the **Appendix A4** for a description of DoZen's capabilities.

Processed data

Processed response function data for each campaign have many dimensions: response function frequency, electromagnetic field component, receiver station location, transmitter configuration, frequency, and campaign. The high dimensionality makes visualizing the data difficult. **Figures 4.3.1** and **4.3.2** show different views of the data. **Figure 4.3.1** shows the data at all receiver stations at once, for one frequency, one field (two horizontal components), one transmitter configuration, and one campaign at a time. **Figure 4.3.2** shows data at all frequencies and campaigns at once, but for one field component, one receiver location, and one transmitter configuration at a time. The difficulty of visualizing the data was one motivating factor for developing DoZen. It allows data to be plotted interactively, which is crucial for high dimensional data exploration.

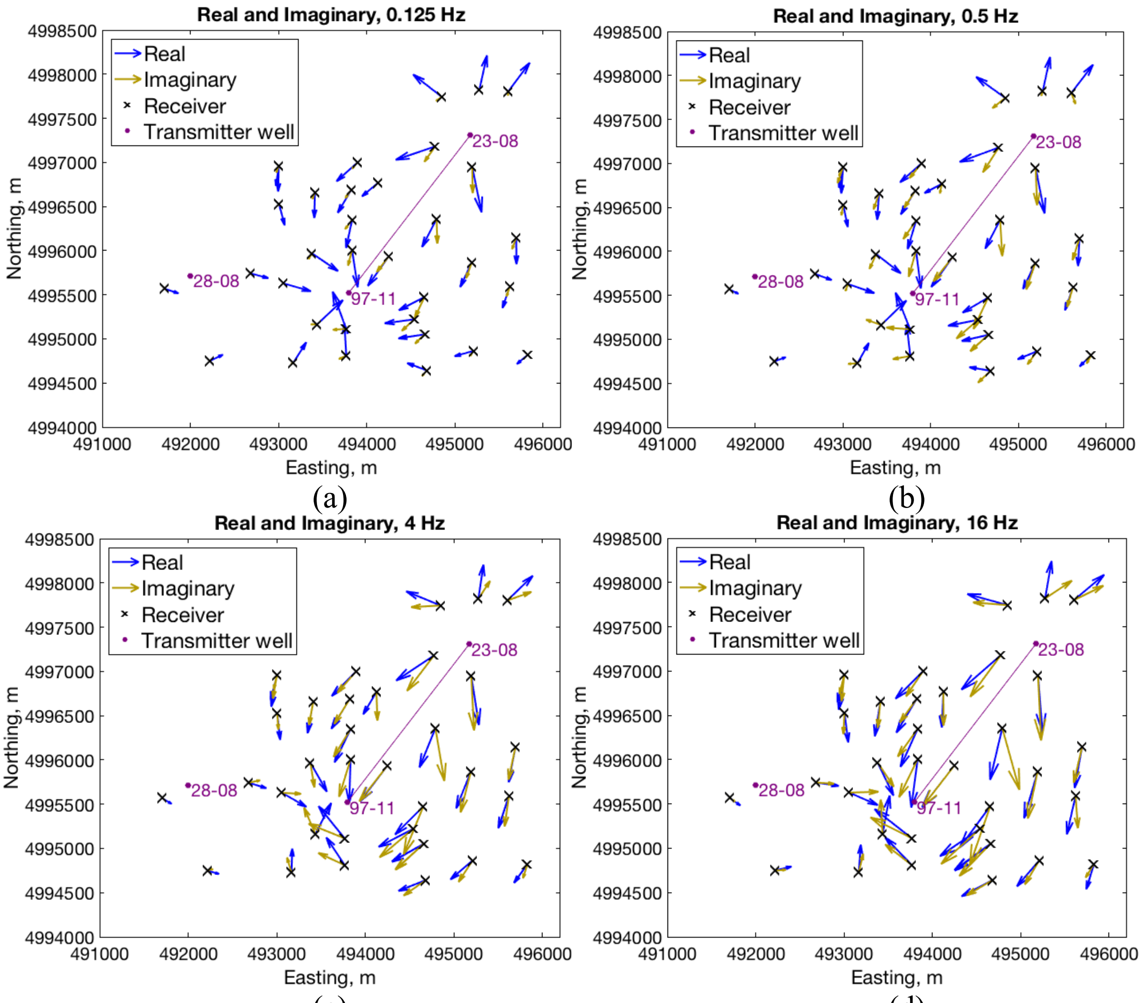

(a) (b) (c) (d)

Figure 4.3.1: Real and imaginary components of the electric field response functions for the May 2018 campaign, transmitting between wells that are separated along the northeast-southwest direction, at (a) 0.125 Hz, (b) 0.5 Hz, (c) 4 Hz, and (d) 16 Hz. Blue arrows show the x and y components of the real parts of the electric field response functions, and yellow arrows show the imaginary parts. The magenta dots represent transmitter wells, and the magenta line connects the two transmitter wells used for these data. The arrows are scaled logarithmically so that the spatial pattern of the response functions is easy to discern.

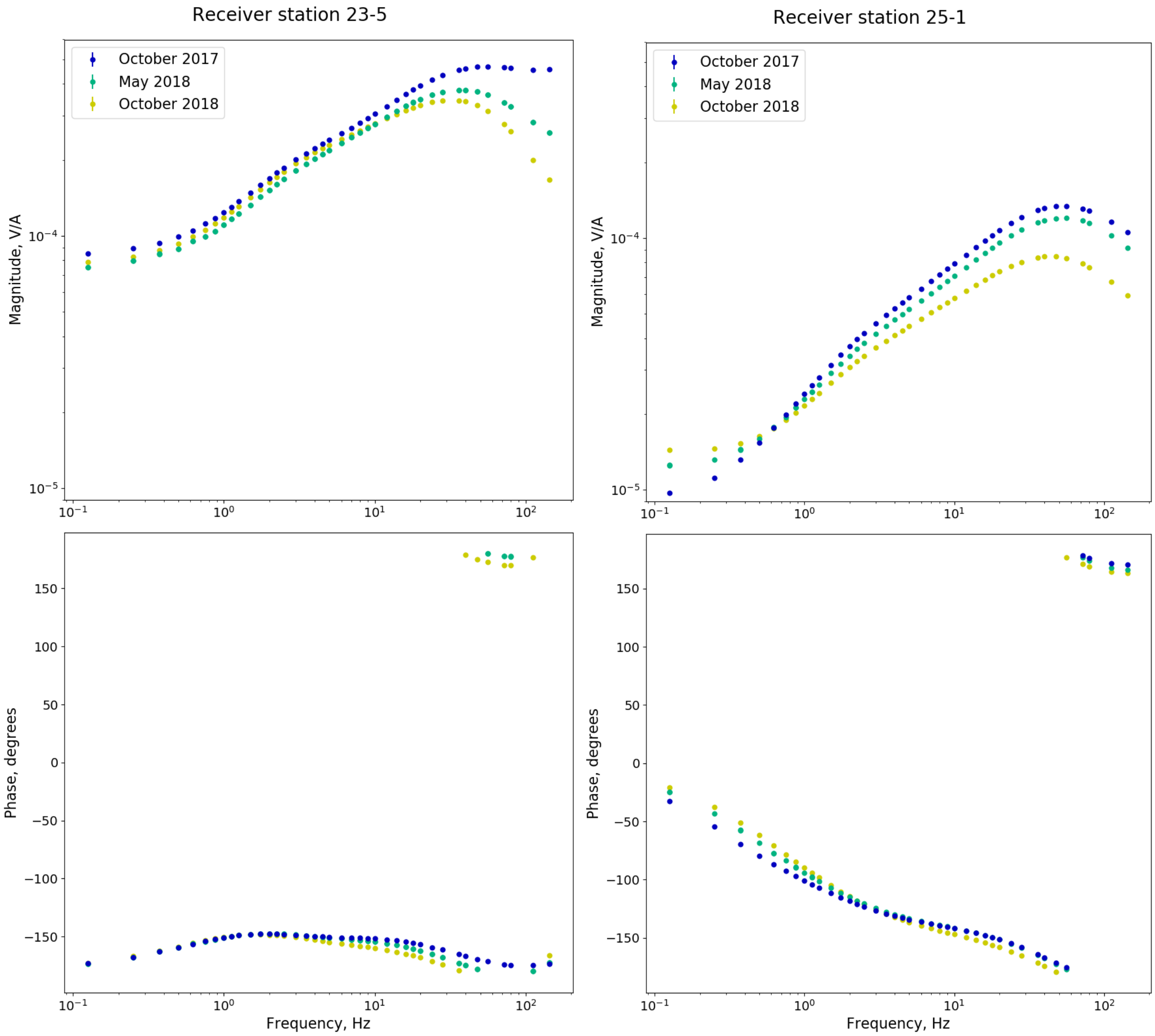

(a) (b)

Figure 4.3.2: Response functions for receiver stations (a) 23-5 and (b) 25-1 for three field campaigns. Shown are response functions for the component of the electric field in the north direction, for the transmission well pair that is separated along the northeast-southwest direction.

While the data plots allow for quality checks, the relationship between these data and reservoir saturations is too complicated to directly interpret the data. Thus, forward modeling and inversion are required to draw meaningful conclusions from CSEM data.

Data variance

We have investigated the variance in the processed data. **Figure 4.3.3** shows the variability of the signal between periods. This can be investigated by breaking the transmitter and receiver signals apart into individual periods based on the transmitter frequency, and comparing each period to the others. **Figure 4.3.3a** shows, in effect, a histogram for each sample within a period. Both the transmitter signal and the receiver signal demonstrate little correlation between how they vary and proximity to polarity changes, except that the samples on which polarity changes fall have high variance, especially for the transmitter. This can be seen clearly in **Figure 4.3.3b**.

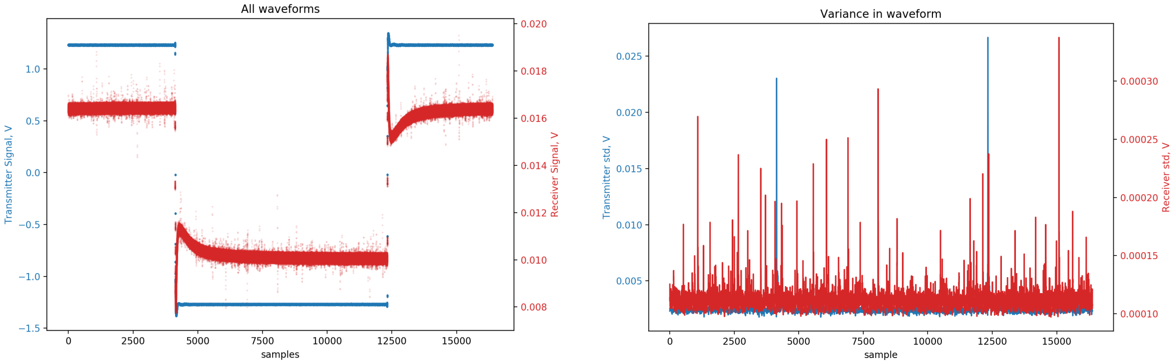

Figure 4.3.3: (a) Every period of the transmitter and receiver signals from Figure 3.4.2b, plotted atop one another to visualize the variance between periods at each sample. (b) The standard deviation for each sample in Figure 4.3.3a. The two blue spikes correspond to polarity changes in the transmitter signal.

Fourier coefficients are computed for every period of the signals. **Figure 4.3.4** shows the quotients of the receiver coefficients divided by the transmitter coefficients for each period. Here, the window within which each Fourier coefficient is moved by only one quarter of a period from one point to the next in the plot, in order to demonstrate how the start and end points of the window with respect to transmitter polarity changes determine how the quotients vary. In essence, the location of the window with respect to polarity changes determines the angle of the line along which samples vary. In **Figure 4.3.4**, the points are roughly arranged as a plus sign. Samples that are distributed vertically from the mean tend to correspond to windows that start at polarity changes, while samples that are scattered horizontally away from the mean correspond to windows that begin and end halfway between polarity changes. Thus, the choice of when processing windows begin and end determine whether variance is contained largely within the real part of the quotients or the imaginary part. The mean, however, is unaffected by this choice.

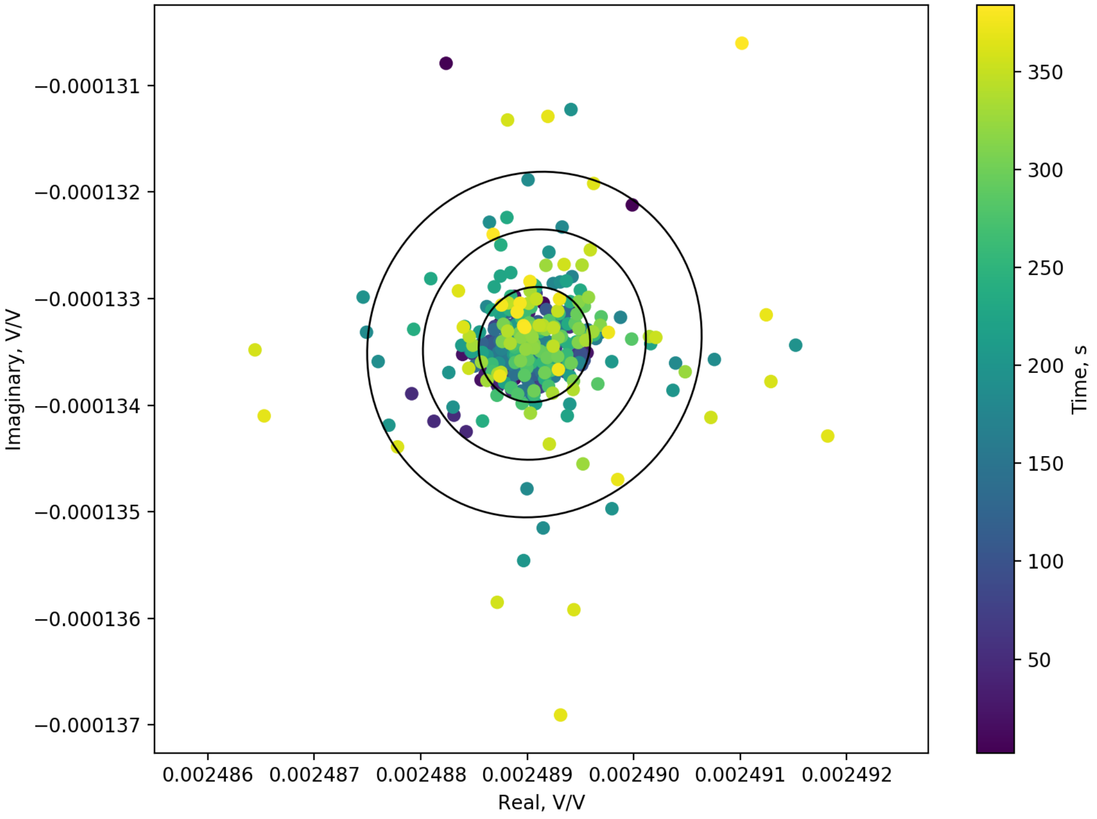

Figure 4.3.4: Quotients of receiver and transmitter Fourier coefficients computed at each period of the signal, plotted in the complex plane. The black ellipses indicate regions within one, two, and three standard deviations of the mean. The points are colored by the time at which the corresponding period occurs within the signal. Dark points correspond to periods that occur early while light colors indicate periods that occur near the end of the signal.

Analysis of signal magnitude and variance

Tietze et al. (2015) analyzed the use of time-lapse borehole-to-surface CSEM for monitoring injected CO_2 at the Bockstedt oil field. They modeled the change in field strength at the surface resulting from a resistivity change from 16 Ωm to 0.6 Ωm in a three-dimensional reservoir at 1200 m depth, which is similar to the Bell Creek field. The modeling results indicate differences on the order of 10^{-9} V/(Am^2) for the inline electric field component at low frequencies, and 10^{-12} V/(Am^2) at high frequencies. The cross-line component of the magnetic field exhibited an absolute difference upwards of 10^{-10} A/(Am^2).

At Bell Creek, our measured electric field response differences are on the order of 10^{-6} V/A at low frequencies (**Figures 4.3.5a** and **4.3.5b**). After accounting for receiver and transmitter dipole lengths, this corresponds to differences on the order of 10^{-10} V/(Am^2). At high frequencies, differences are on the same order of magnitude or larger. The large differences at high frequencies are likely due in part to changes in receiver location or transmitter wire path. Since the locations of receivers and transmitter wire path are recorded during each campaign, the effects on the time-lapse signal can be mitigated.

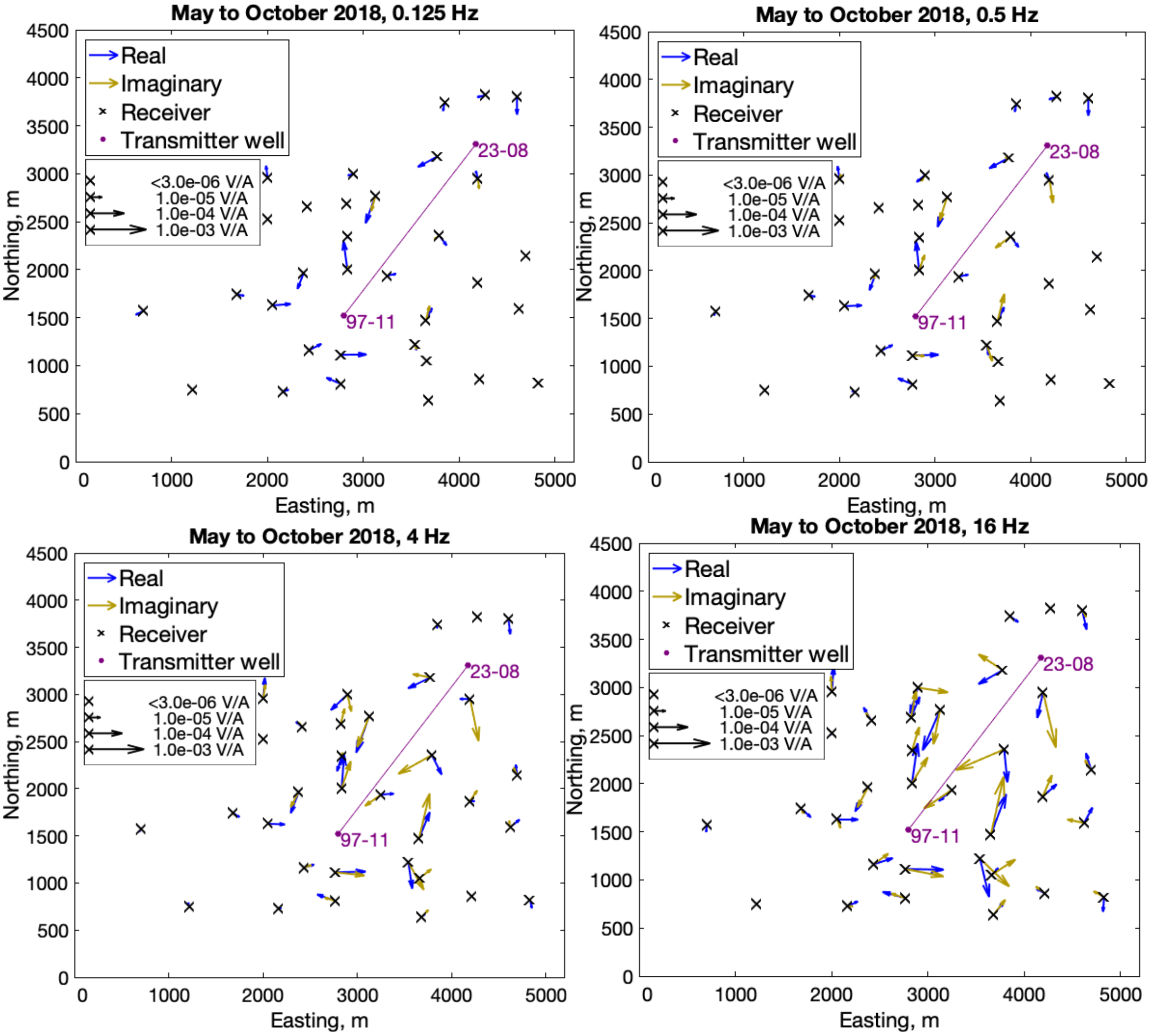

Figure 4.3.5: Time-lapse response difference between May 2018 and October 2018. Real and imaginary components of the electric field response functions, transmitting between wells that are separated along the northeast-southwest direction at (a) 0.125 Hz, (b) 0.5 Hz, (c) 4 Hz, and (d) 16 Hz.

The magnetic field response difference at the lowest frequency is on the order of 10^{-5} μT/A. These values correspond to differences on the order of 10^{-9} A/(Am^2) after accounting for the transmitter dipole length. Like the electric field data, high frequency magnetic response differences are equally large or larger.

Standard deviations are estimated based on response functions computed from different time windows of the signal (**Figure 4.3.6**). Estimated standard deviations of the magnitude of the response functions are less than one percent of the magnitude, which are significantly below the magnitude of the time-lapse differences. **Table 4.3.1** summarizes the magnitudes of time-lapse responses and the estimated standard deviations at low and high frequencies.

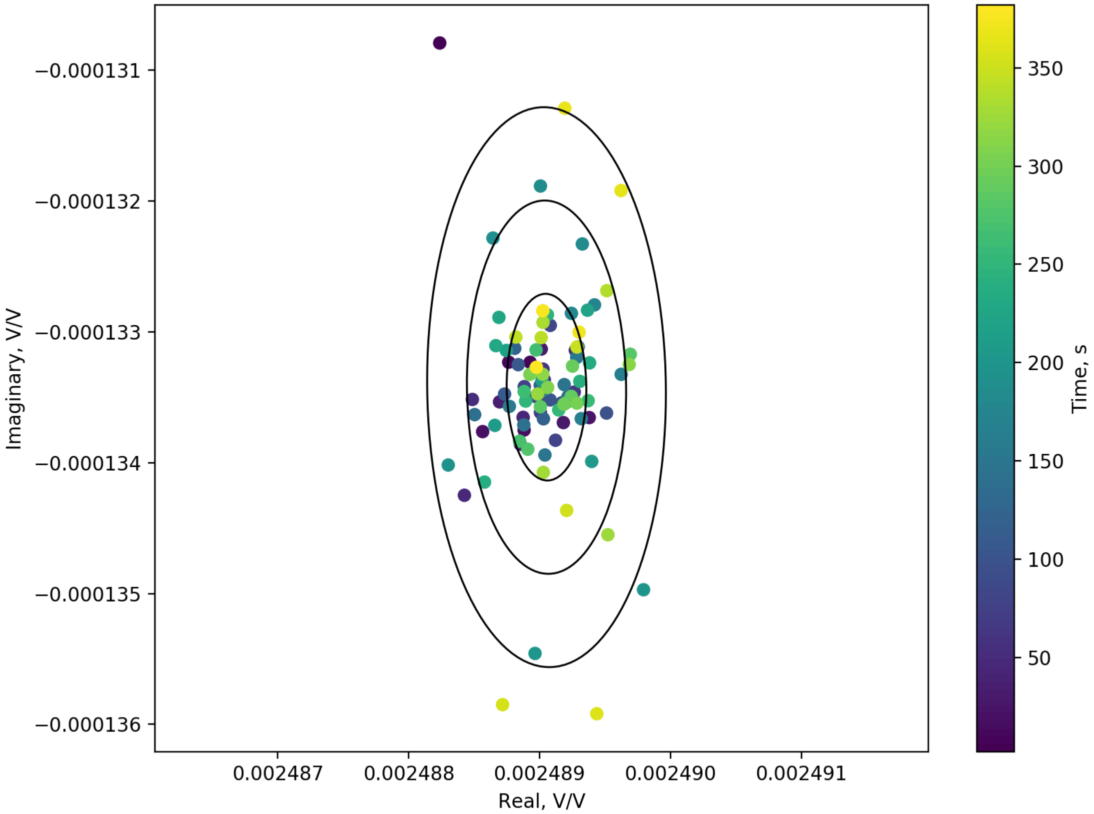

Figure 4.3.6: Response function estimates plotted in the complex plane, for the northeast-southwest aligned transmitter well pair, northing component of the electric field at receiver 279, at 0.25 Hz, measured in October 2018. Each dot represents the response function estimate computed using a moving boxcar window. Dark dots correspond to windows that are applied to early parts of the time-series data, and light dots to later windows. The three concentric ellipses indicate distances of one, two, and three standard deviations from the mean. Here, the majority of the variance is in the imaginary part. We find that the beginning and end positions of the windows

determine whether the majority of the variance is contained in the imaginary component, the real component, or a combination. These values are averaged via an M-regression estimate to yield an estimate of the value of the response function and its variance.

Table 4.3.1: Average order of magnitude of differences between May and October 2018 in measured CSEM response functions, and order of magnitude of standard deviations of response functions estimated via M-regression. The difference data are two to three orders of magnitude larger than the standard deviations, demonstrating a strong time-lapse signal.

	Measured data difference	Estimated standard deviation
E-field, low frequency	10^{-6} V/A	10^{-8} V/A
E-field, high frequency	10^{-5} V/A	10^{-7} V/A
B-field, low frequency	10^{-6} μT/A	10^{-7} μT/A

We compared the variance for individual transmissions (**Figure 4.3.7a**) to that for repeated transmissions (**Figure 4.3.7b**). From this analysis, we find that the average variance among repeated transmissions is two orders of magnitude larger than that of individual transmissions, and thus the standard deviation is one order of magnitude greater. At low frequencies, though, the increase in standard deviation between individual measurements and repeated measurements is not as great. The observed time-lapse signal at low frequencies remains one order of magnitude greater than the estimated standard deviation among repeat transmissions.

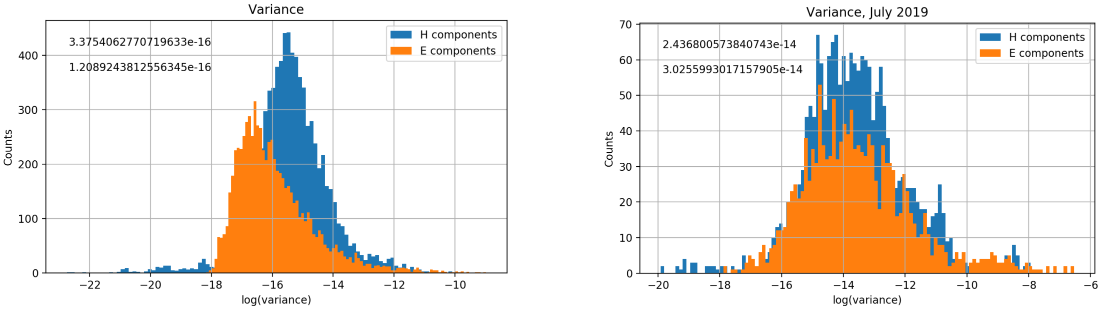

(a) (b)

Figure 4.3.7: Histograms showing the base 10 logarithm of the response function variance **(a)** within individual transmissions, and **(b)** among repeat transmissions for electric and magnetic components. The numbers in the upper left are the geometric means of the variance for the magnetic and electric field components, respectively.

We find that the measured time-lapse CSEM signal well exceeds the estimated standard deviation of the measurements. Additionally, the magnitude of the time-lapse response difference agrees with the expected magnitude as published by Tietze et al. (2015), for both the electric and magnetic fields. These differences are significantly larger than the variance in the data, and the differences are coherent across multiple frequencies. Some part of the differences are due to small changes in survey geometry, which can be taken into consideration during modeling and inversion. The sign of the differences is consistent among multiple receiver stations, which also suggests that a time-lapse signal arising from CO_2 movement is detected by the survey.

4.4. CSEM MODELING AND INVERSION

Sensitivity analysis

As a first step towards inversion of CSEM data for reservoir conductivity change, we computed the sensitivities of the difference data to changes in electrical conductivity within the reservoir. **Figure 4.4.1** shows the sensitivity of the east-west component of the electric field of one receiver to conductivity change throughout the reservoir. In general, the sensitivities depend on the conductivity model, including lateral variations. Here, though, we compute only the sensitivities for a homogeneous background conductivity model with well casings. The sensitivity is highest near the ends of the electrodes, and it depends on the receiver component.

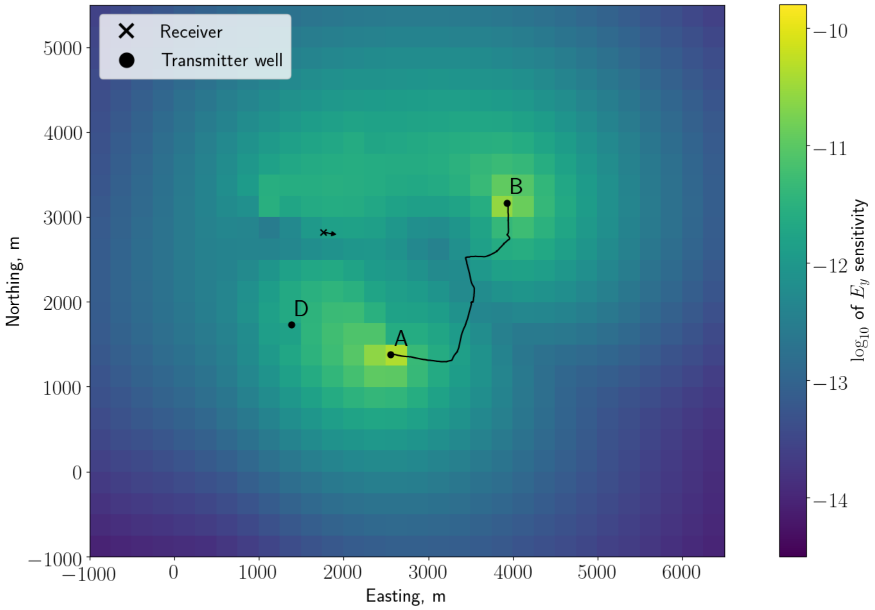

(a)

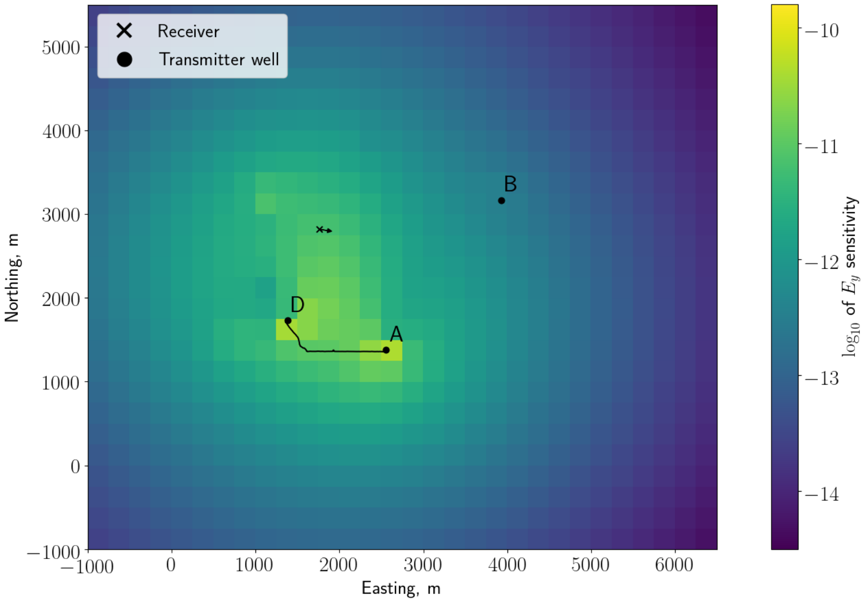

(b)

Figure 4.4.1. Sensitivity of the east-west component of one electric field difference datum (black x) to conductivity change in the reservoir at 0.125 Hz for (a) a northeast-southwest oriented transmitter, and (b) an east-west oriented transmitter wire. The black arrow points in the positive direction of the receiver dipole, and its length is the length of the receiver dipole, to scale.

CSEM linearized inversion results

Next, we present the results of linearized inversion of the measured CSEM difference data. In order to invert the data, the effects of changes in survey geometry must be removed. Therefore, we compute the electromagnetic fields of a background conductivity model with well casings. We compute responses using each campaign's survey geometry separately. We difference the modeled responses for separate campaign geometries. These differences are applied to the corresponding difference data to correct for changes in geometry between campaigns. **Figure 4.4.2** shows observed difference data before and after corrections. The correction is negligible except for receiver stations that are within about 300 m of the transmitter wire, or about 1000 m of an energized casing.

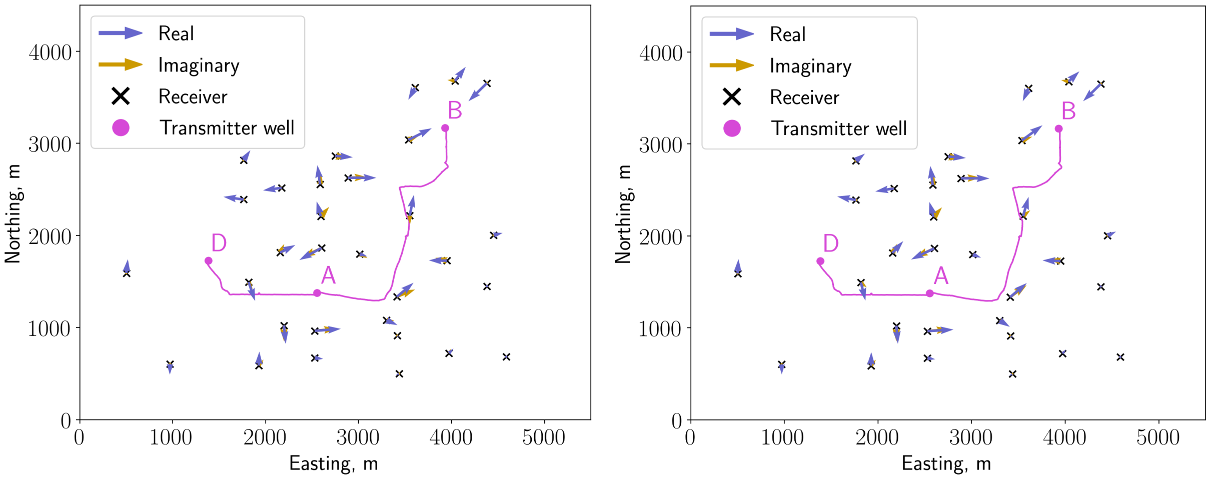

(a) (b)

Figure 4.4.2. (a) Electric field difference data before corrections for survey geometry changes are applied, and (b) after corrections.

Applying our linearized inversion workflow to the field data, we recover distributions of time-lapse conductivity change within the reservoir (**Figure 4.4.3**). As expected for smooth regularization, the recovered conductivity has smooth spatial variation. The recovered models show patterns of conductivity change which can be interpreted as regions where fluid saturations have changed. A change in fluid saturation from conductive brine to resistive gas should cause the conductivity of the reservoir to change by roughly a factor of ten. **Figure 4.4.3** shows that the recovered conductivity changes are far larger. The marginal effect of large conductivity contrasts on electromagnetic fields at the surface diminishes as the contrast increases. Since we are using linearized sensitivities computed for a model with no lateral conductivity contrast, our estimated residuals do not account for this effect. Therefore, we interpret relative highs and lows in conductivity change from the recovered conductivity change models.

The largest conductivity changes occur near charged well casings. This is likely an artifact of the inversion since the sensitivities are highest near casings, as shown in the 2020 Q1 report. Few areas of no change exist in the recovered models, which is not consistent with expectations. Much of the change may be due to near surface conductivity changes, or near surface infrastructure which alters the sensitivities. Furthermore, the data misfit indicates errors that are several orders of magnitude higher than the expected data errors. This indicates that the modeling is not sufficiently capturing the governing physics, possibly due to the simplified background conductivity, the assumption of linearity, or the assumption that all conductivity change occurs within the reservoir. Thus, we conclude that, while we recover models of conductivity change, it is difficult to infer saturation changes in the reservoir from the recovered models.

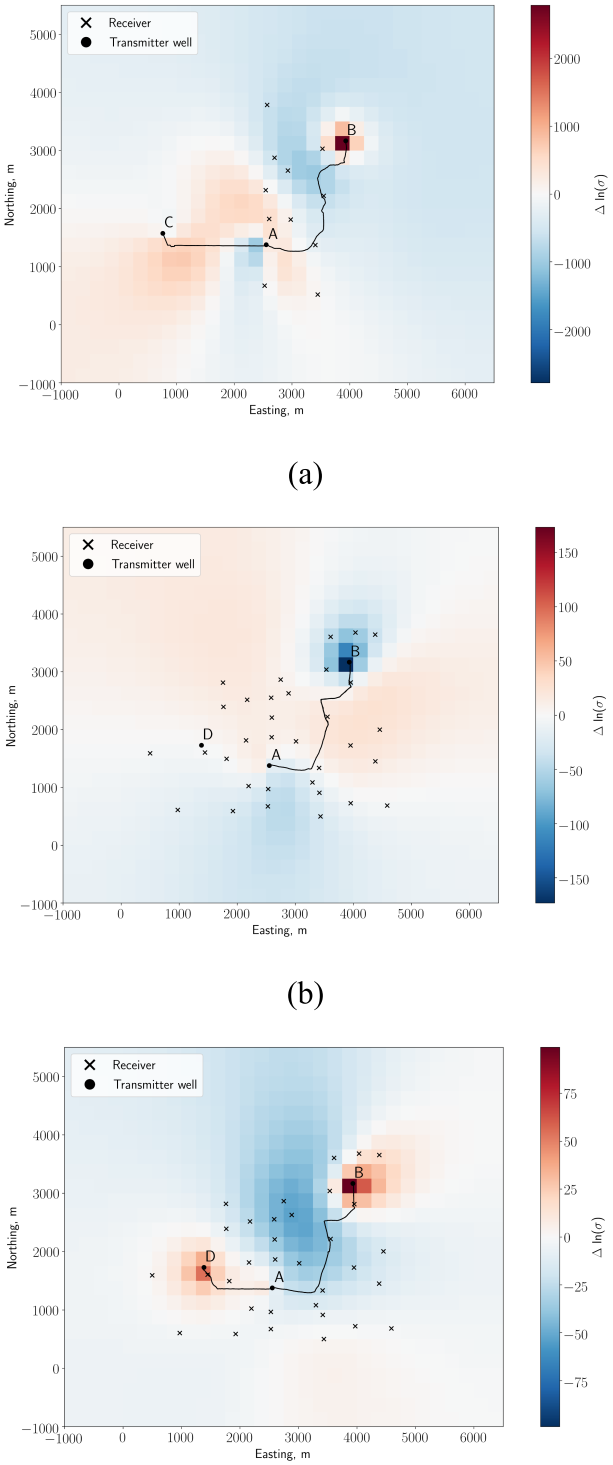

(a)

(b)

(c)

Figure 4.4.3. Inverted relative conductivity change over epochs (a) October 2017 to June 2018, (b) June 2018 to October 2018, and (c) October 2018 to July 2019.

CSEM Modeling Results

Following the 3D EM modeling methodology above, we computed CSEM data for the conductivity models derived from reservoir simulation. We found that the CSEM data are unable to detect the predicted saturation changes. To reach this conclusion, we analyze the data in three ways: comparing field magnitudes, comparing plots of fields, and comparing the data misfit for the different saturation cases generated by the reservoir history matching workflow.

First, we compare field magnitudes. Recall that this process involves computing primary fields, which arise from the transmitter wire over a homogeneous half space with well casings, and secondary fields, which arise from deviations in conductivity from the half space. Note that changes in the field that are due to saturation changes in the reservoir are entirely captured in the secondary field. The predicted secondary difference is the difference between secondary fields from two different campaigns. The difference is due to two factors: changes in reservoir saturation and hence reservoir conductivity, and changes in survey geometry between the campaigns. Therefore, while it is not equal to the time-lapse signal of interest, the predicted secondary difference provides an upper limit on that signal.

Table 4.4.1 allows a comparison of the orders of magnitude of different predicted and observed quantities. The predicted secondary difference is significantly smaller than all of the columns, indicating that these data are not sensitive enough to capture information about changes in reservoir saturation. The observed standard deviation is derived from repeated measurements, as described in the data processing methodology. It fails to capture many sources of error, including positioning errors, modeling errors, and any systematic errors. Therefore, it is likely much smaller than the error in our data. Using it as a lower bound on data error, we find that the upper bound on the time-lapse signal falls below this lower bound on error. Thus, no matter how well we capture the electromagnetic physics, the reservoir properties, and account for infrastructure and systematic noise sources, we cannot expect to detect reservoir saturation changes from the CSEM data.

Table 4.4.1 provides useful information for future experiments. The predicted difference data are much greater than the predicted secondary difference. Therefore, the predicted difference data are dominated by the predicted primary difference data, which arise only from survey geometry changes. Thus, the predicted difference data provide estimates for the magnitude of the effect of small variations in survey geometry on difference data. The observed difference data are greater than the predicted difference data by a factor of 2 or more. This indicates that other sources of error exist which, taken together, have a greater magnitude than survey geometry errors. These sources of error could be due to changes in infrastructure between campaigns, such as new pipelines. They could also arise from changes in the near-surface conductivity, features like additional well casings and pipelines that are not included in the model, and cathodic protection noise. Since the observed standard deviation is much lower, they are not due to random instrument noise. This magnitude of systematic error could be expected in CSEM data collected at other active oil fields like the Bell Creek field. Caution is advised if the expected time-lapse signal magnitudes are not significantly larger than the magnitude of our observed data.

Table 4.4.1. Magnitudes of predicted difference in secondary fields, predicted CSEM difference data, observed difference data, and robust estimates of standard deviations among repeated

observations, for the epoch from May 2018 to July 2019 and for transmitter well pair 97-11 to 23-08. The ranges are the 10% quantile and the 90% quantile. The predicted secondary differences arise mainly from saturation changes in the reservoir. The predicted difference data - modeled predictions of the actual observations - are dominated by the effects of changes in survey layout between campaigns.

	Predicted secondary difference	Predicted difference data	Observed difference data	Observed standard deviation
E-field at 0.125 Hz, (V/m)/A	8×10^{-12} to 5×10^{-11}	1×10^{-9} to 8×10^{-8}	4×10^{-9} to 2×10^{-7}	7×10^{-11} to 3×10^{-9}
E-field, 1 Hz, (V/m)/A	9×10^{-12} to 9×10^{-11}	3×10^{-9} to 2×10^{-7}	8×10^{-9} to 4×10^{-7}	2×10^{-11} to 1×10^{-9}
E-field, 16 Hz, (V/m)/A	5×10^{-13} to 5×10^{-12}	6×10^{-9} to 1×10^{-6}	3×10^{-8} to 3×10^{-6}	5×10^{-11} to 1×10^{-9}
B-field, 0.125 Hz, μT/A	8×10^{-10} to 5×10^{-9}	1×10^{-7} to 1×10^{-5}	3×10^{-7} to 4×10^{-5}	3×10^{-8} to 8×10^{-6}
B-field, 1 Hz, μT/A	1×10^{-9} to 4×10^{-9}	3×10^{-7} to 1×10^{-5}	1×10^{-6} to 6×10^{-5}	2×10^{-8} to 4×10^{-6}
B-field, 16 Hz, μT/A	1×10^{-11} to 7×10^{-11}	3×10^{-7} to 3×10^{-5}	2×10^{-6} to 7×10^{-5}	2×10^{-8} to 5×10^{-6}

Examining plots of the observed and predicted fields reinforces these conclusions. **Figure 4.4.4** shows the total field response for a single campaign at the lowest transmission frequency. The modeled total fields and observed total fields have a reasonable match in magnitude and spatial pattern, with some noticeable differences. In time-lapse data, some of those differences subtract out. Some remain, though, due to the non-linear relationship between EM fields and conductivity. Therefore future studies may warrant modification of the subsurface conductivity model such that the single-campaign data can be predicted to a high degree of accuracy.

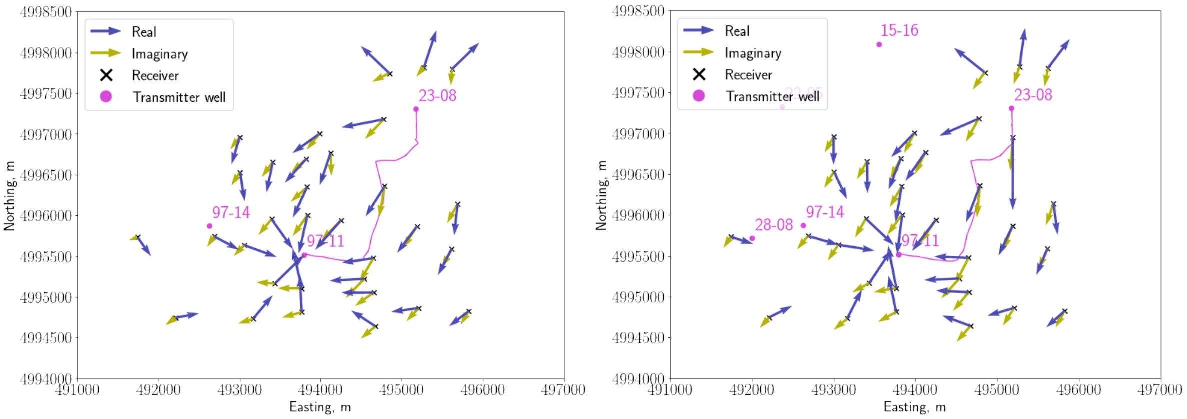

(a) (b)

Figure 4.4.4: Horizontal electric field response at 0.125 Hz from July, 2019, (a) observed and (b) predicted. The transmitter wire path for these data is shown in magenta. Field arrows are scaled logarithmically.

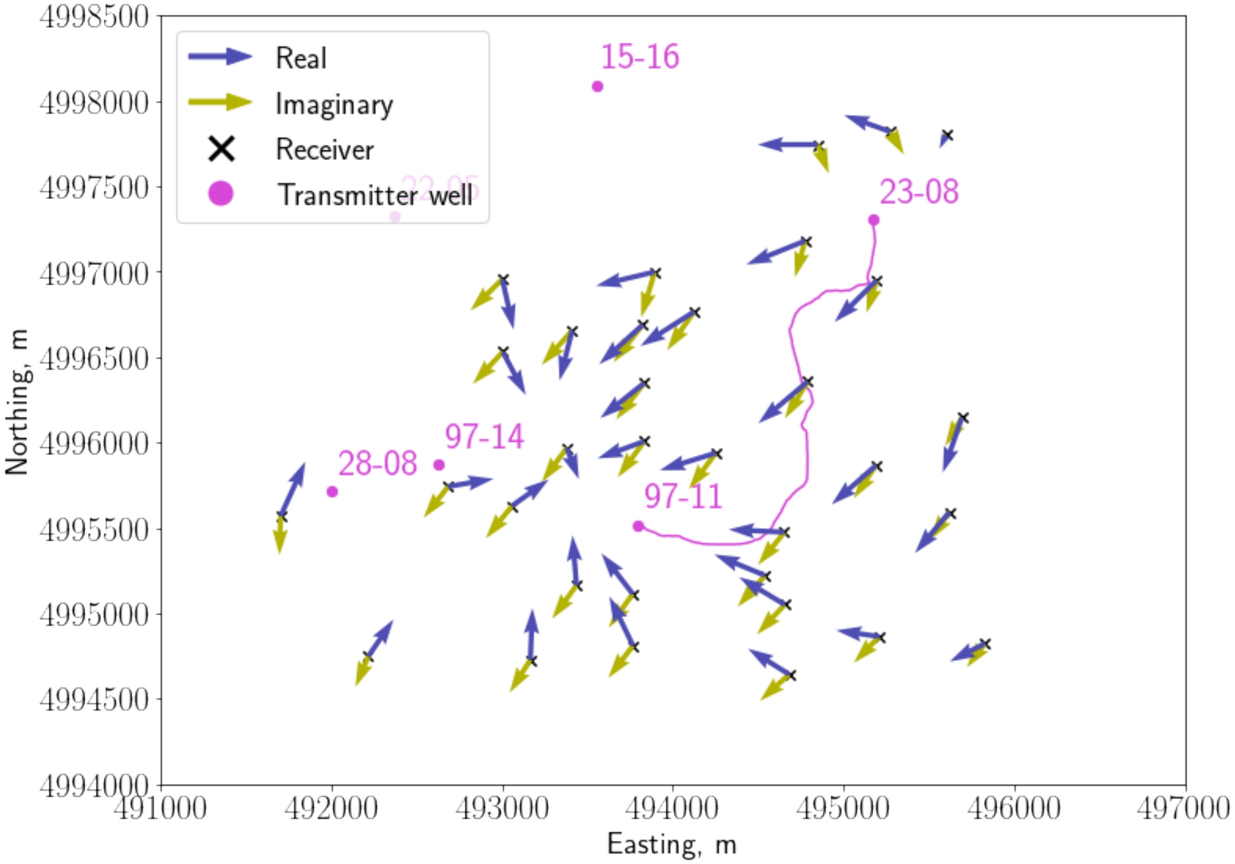

Figure 4.4.5: Secondary electric field difference data at 0.125 Hz from May, 2018 to July, 2019. These data are not corrected for changes in survey geometry. The transmitter wire path for these data is shown in magenta. Field arrows are scaled logarithmically. Note that the scaling used for this quiver plot is different from all other quiver plots because the data have much smaller magnitudes.

The predicted secondary electric field difference data are shown in **Figure 4.4.5**. They exhibit an ordered spatial pattern across the survey area. Contrast this with **Figure 4.4.6a**, which shows observed difference data. The observed data show no such pattern. Note also that the observed difference data do not agree with predicted difference data. **Figures 4.4.6** and **4.4.7** compare the two for electric and magnetic fields, respectively. While predicted and observed data are of similar orders of magnitude, the data are not alike. The predicted data are due to changes in transmitter and receiver locations. The seemingly random pattern in the observed data suggests three conclusions. First, the difference data do not arise from changes in reservoir saturation. Second, they do not arise from survey geometry changes alone, since they do not resemble the predicted data. Third, they are influenced by local effects, as opposed to effects that influence all parts of the survey area equally.

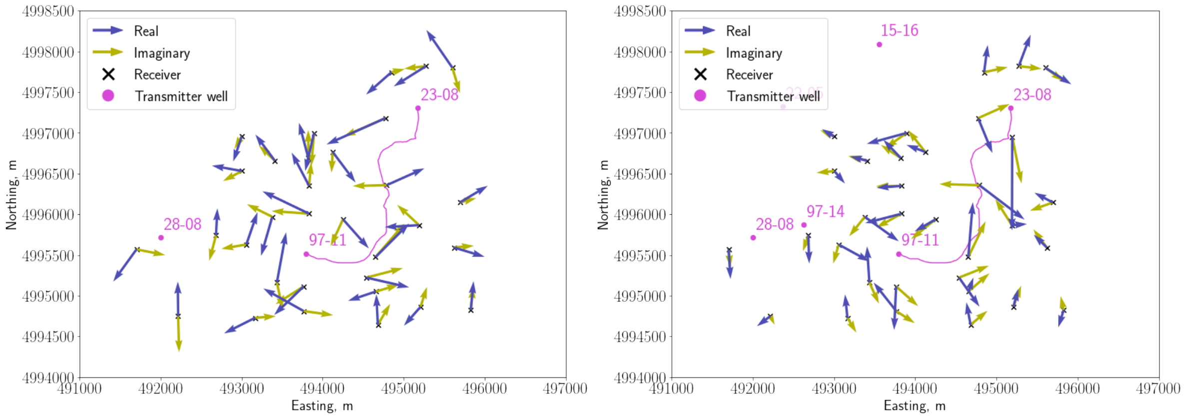

(a) (b)

Figure 4.4.6: Horizontal electric field difference data at 0.125 Hz from May, 2018 to July, 2019, (a) observed and (b) predicted. These data are not corrected for changes in survey geometry. The transmitter wire path for these data is shown in magenta. Field arrows are scaled logarithmically.

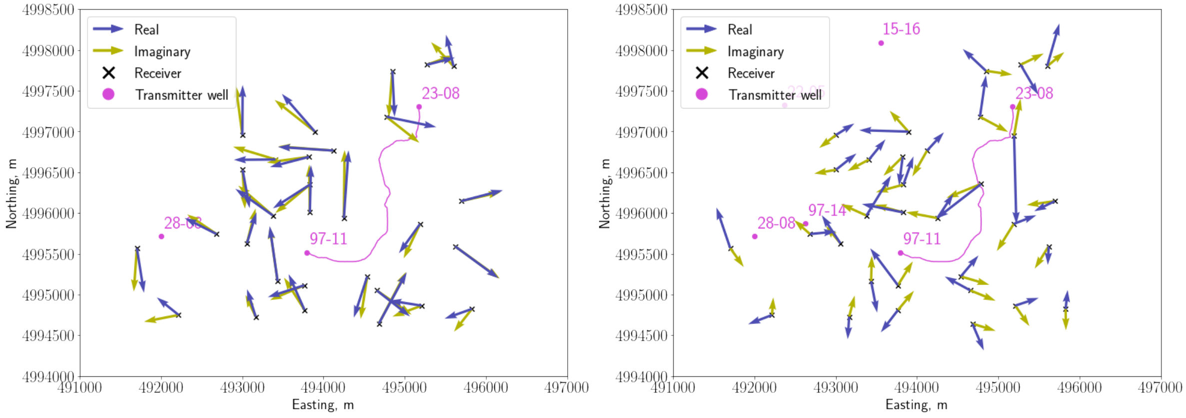

(a) (b)

Figure 4.4.7: Horizontal magnetic field difference data at 0.125 Hz from May, 2018 to July, 2019, (a) observed and (b) predicted. These data are not corrected for changes in survey geometry. The magenta line is the transmitter wire path. Field arrows are scaled logarithmically.

Finally, we compare data misfits for the ten reservoir saturation cases provided by history matching analysis. Data misfit is the norm of the scaled difference data residual vector. We computed difference data residuals as follows. We predicted the fields at the receiver locations for each campaign separately. Then, for a given epoch, we subtracted the later campaign's fields from the earlier campaign's fields to obtain predicted difference data. Note that receiver locations vary between campaigns. We compute each campaign's data at the receiver locations for that campaign, and we apply no correction to the difference data for the change in location. In this way, these predicted data are not the same as the corrected difference data used in the linearized inversion. Difference data residuals are simply the observed time-lapse difference, uncorrected for location, minus the predicted difference data, as

$$r = (d_2 - d_1) - (p_2 - p_1), \qquad \text{(Eq. 4.4.1)}$$

where r is a vector of difference data residuals, d_1 and d_2 are vectors of measured response functions from two different campaigns, and p_1 and p_2 are vectors of predicted response functions for two different campaigns, using the transmitter and receiver locations that are specific to each campaign.

Data misfit is the norm of the difference data residuals, scaled by their standard deviations. We compute both the l_1 and l_2 norms. The general expression for the l_p norm of the residuals is

$$\left(\sum_{i=1}^{n} \left|\frac{r_i}{\sigma_i}\right|^p\right)^{1/p}, \qquad \text{(Eq. 4.4.2)}$$

where n is the number of data and σ_i is the standard deviation of the i^{th} residual.

To quantify the agreement with the CSEM data, we computed data misfits for the ten different saturation cases. With six epochs (campaigns 1 to 2, 1 to 3, 1 to 4, 2 to 3, 2 to 4, and 3 to 4), 40 frequencies, one to three transmitter configurations, 10 to 33 receiver stations, and four or five EM field components, the total number of difference data for one modeled case is 28535. **Table 4.4.2** lists the data misfit values. The values are identical to many significant digits, again demonstrating that the CSEM data are not sufficiently sensitive to distinguish different saturation cases. The large data misfit values reflect the poor fit between predicted and observed difference data with respect to the standard deviations of the observed data. This indicates that there are effects on the data that are not accounted for.

Table 4.4.2: CSEM data misfit, by sum of absolute errors and by sum of squared errors, for the 10 cluster analysis cases. The misfit is nearly the same among all cases.

Case number	l_1 norm of difference data residual	l_2 norm of difference data residual
339	1661154319	376542768.9673
25	1661154337	376542768.9617
37	1661154409	376542768.9544
241	1661154384	376542768.9694
412	1661154249	376542768.9615
14	1661154299	376542768.9486
234	1661154416	376542768.9612
227	1661154297	376542768.9670

5. DISCUSSIONS

We collected time-lapse CSEM data over two years at the Bell Creek oil field during injection operations. The data acquisition process facilitated the development of the workflow, and the acquired data themselves also serve as a specific test case.

Despite the high levels of electromagnetic noise at the field, we were able to process the data and estimate their noise level. There is a measurable and significant signal in the time-lapse difference data which is much greater than the effects of changes in survey locations between campaigns, and greater than random instrument noise expected in such surveys. The project has developed a sound survey procedure and data processing methodology to acquire time-lapse CWC-CSEM data that are coherent in time.

We found that the CSEM data are unable to detect the predicted saturation changes in the Bell Creek reservoir, based on the forward EM simulations using fluid saturation changes from reservoir modeling. Furthermore, the ten different saturation realizations examined are not distinguishable by the CSEM data. The depth of the reservoir and the conductive shale overburden weaken the time-lapse EM signal. More unexpectedly, a complex injection schedule of water and CO2 reduced the saturation contrast in the reservoir, and the brine was less conductive than the average reservoir brine for typical carbon storage sites.

Although it is coherent in time, the measured time-lapse EM signal does not exhibit a coherent spatial pattern. It is concluded that this signal is due largely to changes in conductive infrastructure over the course of the time-lapse survey, such as newly installed pipelines and power lines.

Our observed data provide an estimate of the noise level to be expected at an active oil field. This estimate establishes the basic ambient noise parameter for future surveys. This field-data derived estimate is essential for future feasibility studies and survey planning to determine if CSEM monitoring will be effective at other injection sites.

Machine learning assisted history matching was able to produce a very good match to observed production across many model permutations. The parameters produced a better history match with the fine-scale simulation model than with the very coarse-scale model. Statistically, there were significant differences between each of the cases, resulting in slightly different saturation maps. However, the differences in these saturation maps are too small, and it will be difficult to distinguish any differences in EM modeling results because of the low brine conductivity, the large depth of the reservoir, and the conductive overburden above the reservoir at this site.

6. CONCLUSIONS

The project is aimed at developing the methodology and workflow of charged wellbore casing controlled-source electromagnetic (CWC-CSEM) method for carbon storage monitoring. The objectives are:

1. developing the field procedure and protocol for collecting time-lapse controlled-source electromagnetic (CSEM) data with source electric current injected into the subsurface through wellbore casings and associated data processing techniques,
2. developing the procedure for building background 3D electrical conductivity model utilizing multiple sources of data such as supplemental surface transient EM (TEM) surveys, well-logs, and seismic structural information, for use in time-lapse CSEM data interpretation,
3. developing a coupled multiphysics simulation and inversion method for CSEM data constrained by production data and structural information from seismic imaging, and
4. testing the methodology at a field site.

We have accomplished all the proposed tasks and developed the methodology as planned. These include the procedure for time-lapse CSEM data acquisition, data processing techniques, integration with 3D conductivity model building, fast reservoir simulation for history matching using machine learning, and interpreting CSEM data with coupling to the reservoir modeling.

The testing component of the project measured significant time-lapse CSEM responses. However, we have determined that it is not related to the injections since our modeling has indicated that the combination of the lower brine conductivity in the reservoir, and the hybrid CO2/WAG injection cycles could not have produced significant CSEM responses. We note that this site was made available to the project after the original site selected in the proposal changed ownership and we had only limited access.

Despite the null outcome of the measured data in relationship to the actual injection cycles at the test site, the primary component of the project is a success and has accomplished the planned research and development for the field procedure and methodology of using charged wellbore casing CSEM to monitor carbon storage.

The developed method and associated workflow are general and have broad applicability. The ideal sites for employing this technique would be the fit-for-purpose carbon-storage sites using saline reservoirs, where the brine fluid is highly conductive and its displacement by injected CO2 would lead to significant change in electrical conductivity.

7. RECOMMENDATIONS

We recommend that future surveys include a detailed site-specific feasibility study before this technology is applied. The feasibility study must include basin conductivity, reservoir geometry, brine conductivity, and fluid injection and production predictions.

Strong communication with local landowners and site operators is necessary to obtain approval for survey plans. Friendly relationships with local residents and authorities support data collection in myriad ways. They can also improve local perceptions of the CO2 injection project as a whole.

Permanent emplacement of transmitter and receiver stations will minimize the effects of changes in survey geometry, which we found to be two orders of magnitude greater than the data standard deviations.

The machine learning assisted history matching method produced an ensemble of plausible reservoir models which acceptably fit the production data. However, the resulting saturation models were similar to one another. Further development of this novel method, especially by incorporating uncertainties in the facies model, may improve its capability to capture the full distribution of plausible saturation models, which CSEM data can further refine to produce CO2 distributions that fit all available data.

This technology is best applied in areas that are far from cultural sources of electromagnetic noise such as power lines and cathodically protected pipelines. Our study provides an estimate of the expected noise level in time-lapse CSEM data at an active oil field; feasibility studies for future CO2 monitoring efforts in such environments should examine both the expected signal strength arising from CO2 movement and the expected cultural noise. If the noise level equals or exceeds signal strength, steps must be taken to model the effects of changing infrastructure. While active oil fields are noisy electromagnetically, CO2 storage sites would be more amenable to CSEM time-lapse monitoring.

8. REFERENCES

Archie, G.E., 1942. The electrical resistivity log as an aid in determining some reservoir characteristics. Petroleum Transactions of AIME, 146, 54-62.

Börner, J. H., Herdegen, V., Repke, J.-U. and Spitzer, K. (2013),The impact of CO2 on the electrical properties of water bearing porous media – laboratory experiments with respect to carbon capture and storage. Geophysical Prospecting, 61: 446–460. doi: 10.1111/j.1365-2478.2012.01129.x

Carey, William J., Marcus Wigand, Steve J. Chipera, Giday WoldeGabriel, Rajesh Pawar, Peter C. Lichtner, Scott C. Wehner, Michael A. Raines, George D. Guthrie Jr. (2007), Analysis and performance of oil well cement with 30 years of CO2 exposure from the SACROC Unit, West Texas, USA, International Journal of Greenhouse Gas Control, Volume 1, Issue 1, April 2007, Pages 75-85, ISSN 1750-5836, http://dx.doi.org/10.1016/S1750-5836(06)00004-1.

Dai, Zhenxue, Richard Middleton, Hari Viswanathan, Julianna Fessenden-Rahn, Jacob Bauman, Rajesh Pawar, Si-Yong Lee, and Brian McPherson (2014), An Integrated Framework for Optimizing CO2 Sequestration and Enhanced Oil Recovery. Environmental Science & Technology Letters, 1 (1), 49-54, doi: 10.1021/ez4001033

Egbert, G. D., and J. R. Booker, 1986, Robust estimation of geomagnetic transfer functions: Geophysical Journal International, 87, 173-194.

Exxon Company, U., 1990. Engineering & Geologic Study: Bell Creek Consolidated (Muddy) Unit Area, Carter & Powder River Counties, Montana, Midland.

Fatt, I., & Dykstra, H. (1951). Relative permeability studies. Journal of Petroleum Technology, 3(09), 249-256.

Gasda, S. E, S. Bachu, M.A. Celia (2004), The potential for CO2 leakage from storage sites in geological media: analysis of well distribution in mature sedimentary basins. Environmental Geology, 46 (6-7), 707-720

Grayver, A. V., Rita Streich, and Oliver Ritter (2014). 3D inversion and resolution analysis of land-based CSEM data from the Ketzin CO2 storage formation. GEOPHYSICS, 79(2), E101-E114. doi: 10.1190/geo2013-0184.1

Guennebaud, Gaël, B. Jacob, and others, 2010. Eigen v. 3, http://eigen.tuxfamily.org. Accessed March 28, 2019.

Honarpour, M. M. (2018). Relative permeability of petroleum reservoirs. CRC press.

Irons, T., Y. Li, and J. R. McKenna, 2012. 3D frequency-domain electromagnetics modeling using decoupled scalar and vector potentials: SEG Technical Program Expanded Abstracts 2012, 1–6.

Kiessling, D. C. Schmidt-Hattenbergera, H. Schuett, F. Schilling, K. Kruegera, B. Schoebel, et al.(2010). Geoelectrical methods for monitoring geological CO2 storage: first results from cross-hole and surface–downhole measurements from the CO2SINK test site at Ketzin (Germany) Int. J Greenh. Gas Control, 4, pp. 816–826

Kourounis, D., A. Fuchs, and O. Schenk, 2018. Towards the next generation of multiperiod optimal power flow solvers, IEEE Transactions on Power Systems, vol. PP, no. 99, pp. 1–10, 2018.

Krahenbuhl, R.A., Y. Li, W. A. McAliley, N. Moodie, T. Irons, and B.R. Bloss, 2019: Integrated Model Construction for CO2-EOR Monitoring via Charged-Wellbore Casing Controlled-Source Electromagnetics. 89th Ann.Internat. Mtg, Soc. Expl. Geophys., Expanded Abstracts

Krahenbuhl, R.A., A. Reitz, Y. Li, S. Wagner, and J. Konkler, 2016, Prudhoe Bay reservoir model: making the link between seismic and borehole data to gravity, electrical and EM methods. 86th Ann.Internat. Mtg, Soc. Expl. Geophys., Expanded Abstracts

Krahenbuhl, R., Y. Li, and T. Davis, 2011 The Leading Edge, Special Issue (Time-Lapse measurements). Understanding the applications and limitations of time-lapse gravity for reservoir monitoring. The Leading Edge, 30, Issue 9, 1060 - 1068.

Liang, L., Abubakar, A., & Habashy, T. M. (2011). Production Monitoring Using Joint Inversion of Marine Controlled-source Electromagnetic Data And Production Data. Society of Exploration Geophysicists.

McAliley, W. A., B. R. Bloss, T. Irons, N. Moodie, R. Krahenbuhl, and Y. Li, 2019, Analysis of land-based CSEM data for CO2 monitoring at Bell Creek, MT: SEG Technical Program Expanded Abstracts 2019, 1039–1044.

McGillivray, P. R., D. W. Oldenburg, R. G. Ellis, and T. M. Habashy, 1994, Calculation of sensitivities for the frequency-domain electromagnetic problem: Geophysical Journal International, 116, 1–4.

Minsley, Burke, M. Andy Kass, Greg Hodges, and Bruce D. Smith (2014). Multielevation calibration of frequency-domain electromagnetic data. GEOPHYSICS, 79(5), E201-E216. doi: 10.1190/geo2013-0320.1

Oettinger, G., V. Haak, J.C. Larsen (2001). Noise reduction in magnetotelluric time-series with a new signal–noise separation method and its application to a field experiment in the Saxonian Granulite Massif. Geophysical Journal International, 146(3), 659-669. doi:10.1046/j.1365-246X.2001.00473.x

Schenkel, C. J. and H.F. Morrison, 1990, Effects of well casing on potential field measurements using downhole current sources. Geophysical Prospecting, 38, 663-686. doi:10.1111/j.1365-2478.1990.tb01868.x

Strack, K.-M., 1992, Exploration with deep transient electromagnetics: Elsevier Amsterdam.

Streich R., 2009. 3D finite-difference frequency-domain modeling of controlled-source electromagnetic data. Direct solution and optimization for high accuracy. Geophysics 74, F95–F105.

Streich, R., 2015, Controlled-Source Electromagnetic Approaches for Hydrocarbon Exploration and Monitoring on Land. Surveys in Geophysics, 37(1), 47-80. doi: 10.1007/s10712-015-9336-0"

Streich, R., M. Becken, and O. Ritter, 2013, Robust processing of noisy land-based controlled-source electromagnetic data: Geophysics, 78, E237-E247.

Sternberg, B. K., Washburne, J. C., & Pellerin, L. (1988). Correction for the static shift in magnetotellurics using transient electromagnetic soundings. Geophysics, 53(11), 1459-1468. Streich, Rita (2015), Controlled-Source Electromagnetic Approaches for Hydrocarbon Exploration and Monitoring on Land. Surveys in Geophysics, 37(1), 47-80. doi: 10.1007/s10712-015-9336-0"

Tang, W., Li, Y., Swidinsky, A. and Liu, J., 2015. Three-dimensional controlled-source electromagnetic modelling with a well casing as a grounded source: a hybrid method of moments and finite element scheme. Geophysical Prospecting, 63(6), pp.1491-1507.

Vilamajó, E., Rondeleux, B., Queralt, P., Marcuello, A. and Ledo, J. (2015), A land controlled-source electromagnetic experiment using a deep vertical electric dipole: experimental settings, processing, and first data interpretation. Geophysical Prospecting, 63: 1527–1540. doi: 10.1111/1365-2478.12331

Werthmüller, D., 2017, An open-source full 3D electromagnetic modeler for 1D VTI media in Python: empymod: Geophysics, 82(6), WB9-WB19; DOI: 10.1190/geo2016-0626.1.

Werthmüller, D., W. A. Mulder, and E. C. Slob, 2019, emg3d: A multigrid solver for 3D electromagnetic diffusion: Journal of Open Source Software, 4(39), 1463; DOI: 10.21105/joss.01463.

Wirianto, M., Mulder, W. A. and Slob, E. C. (2010), A feasibility study of land CSEM reservoir monitoring in a complex 3-D model. Geophysical Journal International, 181: 741–755. doi: 10.1111/j.1365-246X.2010.04544.x

9. APPENDICES

A1: PRESENTATIONS AND PUBLICATIONS

I. One abstract for presentation at the 2017 AIChE Annual Meeting (Topical Conference: Advances in Fossil Energy R&D).
   a. Monitoring Carbon Sequestration Using Charged Wellbore Controlled Source Electromagnetics and Integrated Reservoir Models

II. One oral paper and extended abstract at AEGC conference which features a heavy emphasis on non-seismic methods.
   a.

III. Two presentations and a poster presented at the 2018 AGU annual meeting:
   a. Validation and development of multiphase reservoir simulations with controlled source electromagnetics
   b. Devising a framework to couple geophysical measurements (CSEM) with reservoir simulations to monitor CO2 plume movement.
   c. Time-lapse Charged Wellbore Casing Controlled Source Electromagnetic Surveys for Monitoring Injected Carbon Dioxide

IV. Two conference presentations given at the 2019 SEG annual meeting:
   a. Integrated Model Construction for CO2-EOR Monitoring via Charged-Wellbore Casing Controlled-Source Electromagnetics
   b. Analysis of land-based CSEM data for CO2 monitoring at Bell Creek, MT

V. One abstract has been accepted for presentation at the AICHE annual meeting.
   a.

A2: INFORMATION DISSEMINATION

A custom CSEM data processing software library named DoZen was developed to process data from this project. It contains functions to read the data formats used by Zonge instruments, apply our processing workflow, visualize data and metadata, and implement quality control measures. The code is written in Python and is hosted at https://github.com/AndyMcAliley/DoZen. The code to model casing currents is publicly available as well, and can be found at https://github.com/AndyMcAliley/em_casing.

A3: RESERVOIR MODELING

A3.1: Curator Data Set Contents

All Data is referenced to North American Datum 1927 UTM Zone 13 North (feet).

The following data is contained within the Curator Data Set folder and has also been imported into a Petrel project for ease of viewing.

- **Well heads**
  - File Format – ASCII (Well Heads)
  - A text file (tab delimited) file has been included for import into most software programs
  - An Excel spreadsheet has been included for easier viewing and manipulation
  - The following columns are contained with the files:
    - UWI
    - Well name
    - Surface X
    - Surface Y
    - Kelly bushing elevation – Corrected to LiDAR surface elevation
    - Total Depth
- **Data for legacy wells not contained within data boundary (22-02 and 15-14)**
  - Well heads
  - Well logs (raster and LAS)
  - Horizon tops
  - Only 2 wells
- **Perforations**
  - File Format- Well Event data (ASCII) (.ev)
    - Format for import into Petrel
  - An Excel spreadsheet has been included for easier viewing

- **Boundaries**
  - File Format - ASCII (CPS-3 lines)
  - Development Phase boundaries 1-9
  - Entire area of development phase boundaries 4 and 5 are included along with

a portion of development phases 2, 3, and 6

- Data boundary
  - Data is clipped on the eastern margin to the Bell Creek Field Boundary

- **Horizon tops**
  - File Format – ASCII (Petrel well tops)
  - Picked from well logs at each well location
  - A text (tab delimited) file has been included for import into most software programs
  - An Excel spreadsheet has been included fore easier viewing and manipulation
  - All horizon tops have been picked and checked for accuracy by geologists/geomodelers at the EERC
  - The following horizons tops have been picked for wells within the data boundary and are contained with the Horizon_Tops_Above_Muddy file
    - Pierre
    - Eagle
    - Shannon
    - Gammon
    - Niobrara
    - Carlile
    - Turner Sand
    - Pool Creek
    - Greenhorn
    - Bell Fourche
    - Mowry
  - The following horizons tops have been picked for wells within the data boundary and are contained with the Horizon_Tops_Muddy file
    - Springen Ranch
    - Shell Creek
    - Bell Creek Sand
    - Rozet
    - Skull Creek

- **LAS well logs**
  - File Format - LAS
  - One file per well
    - Each curve in the log suite for the corresponding well are contained within one file named as UWI number
- **Pressure and temperature gradients from drill stem tests**
  - File Format – ASCII (Petrel points with attributes)
  - Gradients were extrapolated from the depth of the drill stem test to surface
  - Simulation model is isothermal (temperature held constant during simulation)
- **Surfaces**
  - File Format - ASCII (IRAP Classic Grid)
  - Interpolated from horizon tops
  - Convergent interpolation gridding algorithm
  - Grid size – Shell Creek through Skull Creek
    - 41.25 ft x 41.25ft
    - Half the size of seismic resolution
    - Rotated -44.50 degrees to match seismic rotation allowing for more accurate seismic inversion into grid.
  - Grid size – ground surface through Mowry
    - 50 ft x 50 ft
    - No rotation
  - The following surfaces are included in the data set:
    - Ground surface- generated from LiDAR points
    - Pierre
    - Eagle
    - Shannon
    - Gammon
    - Niobrara
    - Carline
    - Turner Sand

    - Pool Creek
    - Greenhorn
    - Bell Fourche
    - Mowry
    - Shell Creek
    - Springen Ranch
    - Bell Creek Sand – Target reservoir
    - Rozet
    - Skull Creek

- **Static model properties**
  - File Format – Rescue
  - Properties clipped from a static model that covers the entire Bell Creek Field area
  - Grid Size – 41.25 ft by 41.25 ft by 23 layers
    - Shell Creek to Springen Ranch – 1 layer
    - Springen Ranch to BC Sand – 1 layer
    - BC Sand to Rozet – 20 layers
    - Rozet to Skull Creek – 1 layer
  - Each cell contains the following properties
    - Facies
      - Facies logs were assigned to each well based on seismic and well log interpretation
      - Facies logs were upscaled into the grid
      - Facies were distributed using multiple point statistics conditioned by training images
        - Separate training images were created for each geobody (area of similar geologic properties)
      - Facies model was used to further constrain petrophysical properties of porosity and permeability.
    - Total porosity
      - Total porosity logs were calculated using well logs and were

calibrated to core data.

    - Total porosity logs were upscaled into the grid.
    - Distributed by variogram based sequential Gaussian simulation within each facies.
- Effective porosity
    - Effective porosity logs were calculated using well logs and total porosity logs and were calibrated to core data.
    - Effective porosity logs were upscaled into the grid.
    - Distributed by variogram based sequential Gaussian simulation within each facies.
- Permeability
    - Permeability logs were calculated via a neural network that compared core porosity and permeability and bulk density logs.
    - Permeability logs were upscaled into the grid.
    - Distributed bivariately with effective porosity using a porosity/permeability cross plot.
- Water saturation
    - Distributed using a J-function methodology.
        - Calculate Reservoir Quality Index (RQI).
            -
            - K= permeability
            - Φ = effective porosity
        - Calculate normalized porosity (PHIZ).
            -
            - Φ = effective porosity
        - Calculate Flow Zone Indicator (FZI).
            -
        - Define Flow Units (FU) based on FZI values.
        - J-function was applied to each flow unit.
            - Excellent-quality reservoir
            - Good-quality reservoir

            - Medium-quality reservoir
            - Low-quality reservoir
            - Very low-quality reservoir
        - Formation pressure
            - Distributed using pressure gradient from DST multiplied by measured depth plus atmospheric pressure.
        - Zones/Segments
            - A property that separates all cells based on the layer within which they are contained.
        - Measured depth
            - Depth from the kelly bushing to the center of the cell.

- **Interferometric Synthetic Aperture Radar (InSAR) data**
    - File Format – Petrel points with attributes (ASCII)
        - X, Y, Z values are to spatially locate points
        - Columns are elevation above sea level of the ground surface at the date in the column heading. Each date is an attribute within the point set in Petrel.
    - ALOS data
        - Ground elevation data from the ALOS satellite from January 13 2007 to January 24 2011.
    - CSK
        - Ground elevation data from the CSK satellite from September 11 2015 to May 8 2016

- **LiDAR**
    - File Format – Petrel points with attributes (ASCII)
    - Z is in feet above sea level of the ground surface
    - Used to generate the ground surface

The following data is contained only within the Curator Data Set folder.

- **Raster well logs**
    - File Format - TIFF
    - Multiple files per well

        - § Separate file for each TIFF image raster
    - o Named as UWI_ "Logname"

- **Production and Injection Database**
    - o File Format – Excel Spreadsheet
    - o Database of historic production and injection from 1967 to July 2017 for each well within the data boundary.

- **Well Status**
    - o File Format – Excel Spreadsheet
    - o File containing:
        - § Well Name
        - § UWI
        - § Well Status as of May 2017

- **Pipelines and Infrastructure map**
    - o File Format – PNG image
    - o Map showing current location of pipelines and infrastructure within the data boundary.

A3.2: Facies modeling

A facies model is constructed next using well log data and information from a formation analysis study performed by Exxon in July 1990 titled *Engineering & Geologic Study of the Bell Creek Consolidated (Muddy) Unit Area* (Exxon Company, 1990). The report identified three distinct zones within the Bell Creek formation, with eight different facies. The first zone is the silty shale zone characterized by a spontaneous potential (SP) of less than a 50% deflection from the Clean Sand facies value as measured from the shale baseline (Exxon Company, 1990). The second zone is Zone1 and is characterized by three different facies with distinct SP and Gamma-Ray curve cut-offs. The Clayfilled Sand has a greater than 90% SP deflection but less than 18 ohms in the deep induction resistivity log (ILD). The Moderately Clayfilled Sand has an SP deflection between 50% and 90% and resistivities of between 18 and 30 ohms. The Moderately Clean Sand has an SP deflection greater than 90% and greater than 30 ohms of ILD resistivity. The third zone, Zone2 also consists of three distinct facies, a clay filled sand characterized by less than 15 ohms induction log resistance, Dirty Sand characterized by an SP deflection of between 50% and 90% from the shale baseline, and Clean Sand characterized by an SP deflection greater than 90%. The cut-offs for the facies model described above were derived from data presented in the Exxon report's appendix and are summarized in **Table A3.2.1** (Exxon Company, 1990).

Table A3.2.1 Facies cut-off data from Exxon's engineering and geologic study of the Bell Creek Sands/Muddy Formation.

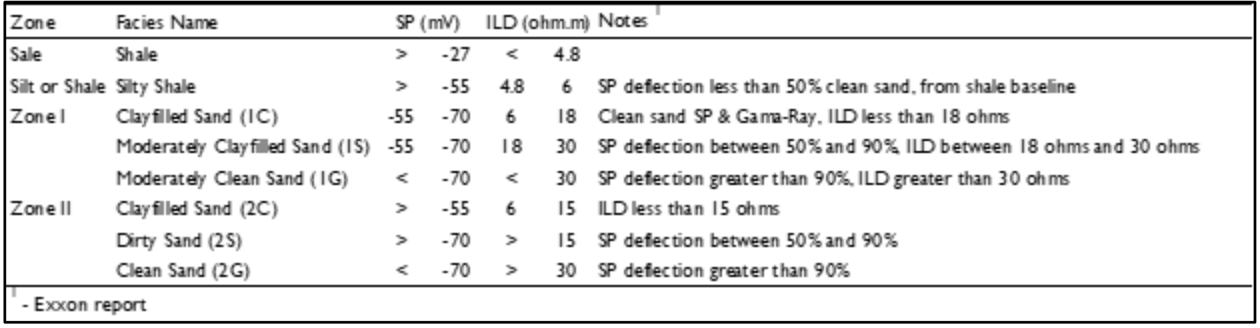

Zone	Facies Name	SP (mV)		ILD (ohm.m)		Notes [1]
Sale	Shale	>	-27	<	4.8	
Silt or Shale	Silty Shale	>	-55	4.8	6	SP deflection less than 50% clean sand, from shale baseline
Zone I	Clayfilled Sand (1C)	-55	-70	6	18	Clean sand SP & Gama-Ray, ILD less than 18 ohms
	Moderately Clayfilled Sand (1S)	-55	-70	18	30	SP deflection between 50% and 90%, ILD between 18 ohms and 30 ohms
	Moderately Clean Sand (1G)	<	-70	<	30	SP deflection greater than 90%, ILD greater than 30 ohms
Zone II	Clayfilled Sand (2C)	>	-55	6	15	ILD less than 15 ohms
	Dirty Sand (2S)	>	-70	>	15	SP deflection between 50% and 90%
	Clean Sand (2G)	<	-70	>	30	SP deflection greater than 90%

[1] - Exxon report

The facies cut-offs identified above were applied to the Spontaneous Potential (SP) and Resistance (ILD) well logs to identify the different facies within the Bell Creek Sands/Muddy Formation as well as the overlying Springen Ranch and Shell Creek formations, and the underlying Rozet Formation. A ninth carbonate facies, not listed in the Exxon report but shown in EERC's facies model along the western border of the field, was also identified. Variograms of each of the facies are created to aid in populating data across the model domain. The facies were then populated across the model domain using the sequential indicator simulation algorithm. **Figure A3.2.1** shows a realization of the facies model for layer 25 in the Bell Creek Formation.

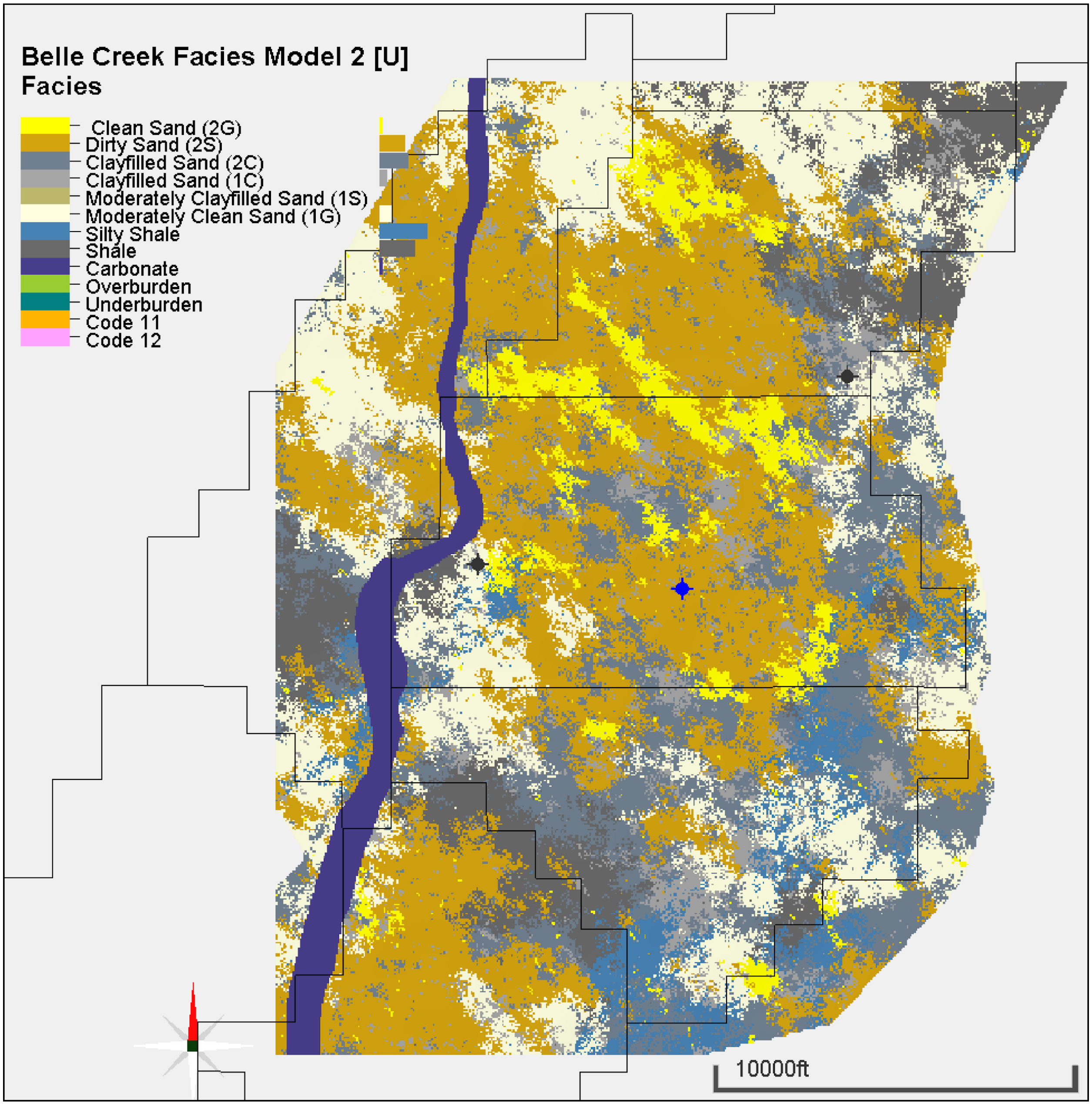

Figure A3.2.1 Facies model of the Bell Creek Formation. Shown here is layer 25, the middle of the Bell Creek Formation. Facies codes Overburden, Underburden, Code 11, and Code 12 are not used in this facies model but were present in the Petrel template used to display the data.

The porosity and permeability distribution were derived from well log data and empirical relationships. The first step in determining porosity from well logs is to create a calculate the volume of shale (Vsh) well log for each well using the gamma-ray (GR) well log and assuming a linear relationship (Equation A3.2.1)

$$Vsh = \frac{GR_{log} - GR_{min}}{GR_{max} - GR_{min}}$$

(Eq. A3.2.1)

Next, a density porosity (PHID) well log is calculated from the density (RHOB) well log and Vsh well log using Equation A3.2.2, where ρ_{ma} is the matrix density of 2.65 g/cm3, ρ_f is the fluid density of 0.85 g/cm3, ρ_{sh} is the shale density of 2.6 g/cm3, and ρ_b is the density (RHOB) well log value. The Exxon field report indicates that the shale density (2.6 g/cm3) is very similar to the sandstone density (2.65 g/cm3) in this field, so the Vsh correction is small.

$$\Phi_{den} = \frac{\rho_{ma} - \rho_b}{\rho_{ma} - \rho_f} - Vsh\left(\frac{\rho_{ma} - \rho_{sh}}{\rho_{ma} - \rho_f}\right)$$

(Eq. A3.2.2)

The Exxon report indicated that the porosity from density is an accurate measure of this field's true porosity so it was used to create the porosity distribution used in the rest of the modeling (Exxon Company, 1990). Most of the wells are lacking neutron porosity, so this makes using density porosity a favorable approach for calculating porosity from the most available well logs.

The last step is to calculate a permeability well log for each well from the density porosity well log using the Morris & Briggs formula (Equation A3.2.3) with assumed residual water saturation (S_{wir}) value of 20% (Exxon Company, 1990).

$$k = 250 * \frac{\Phi^3}{{S_{wir}}^2}$$

(Eq. A3.2.3)

The porosity and permeability well logs were then scaled-up to the geological model grid resolution in preparation for populating the data across the model. Figure A3.2.2 shows the measured and derived well logs. The gamma-ray (GR), neutron porosity (NPHI), spontaneous potential (SP), deep induction log resistivity (ILD), and density log (RHOB) are measured well logs and part of the EERC data. The porosity (POR), log permeability (Logk_MG), up-scaled porosity (POR[U]), and up-scales log permeability (Logk_MG[U]) are derived from the measured well logs.

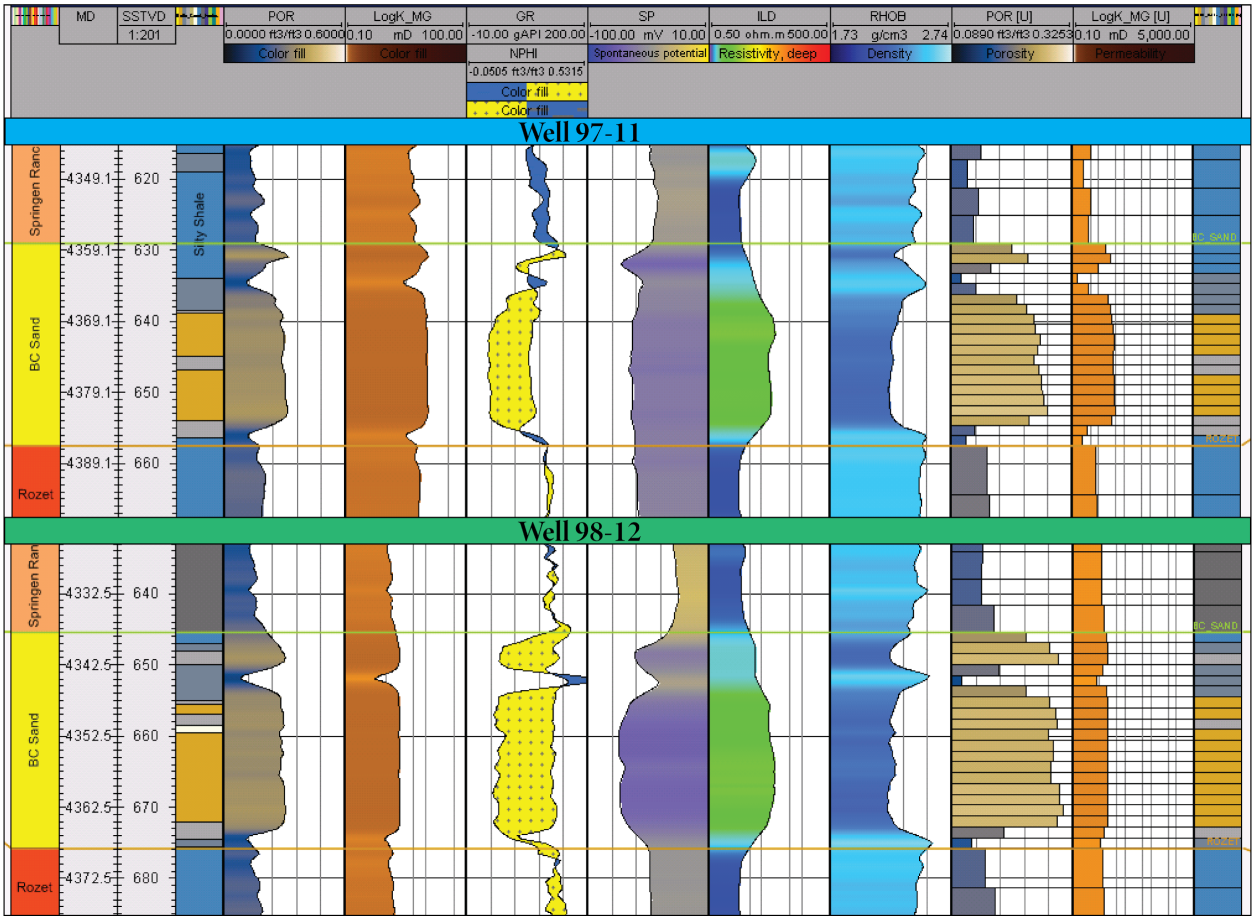

Figure A3.2.2 Sample of the well logs used to create the facies model and porosity distributions in the updated geological model.

These up-scaled well logs were then co-kriged to the facies model and populated across the domain using the sequential gaussian simulation method in conjunction with the variogram data from the facies analysis. The final porosity distribution is shown in **Figure A3.2.3**.

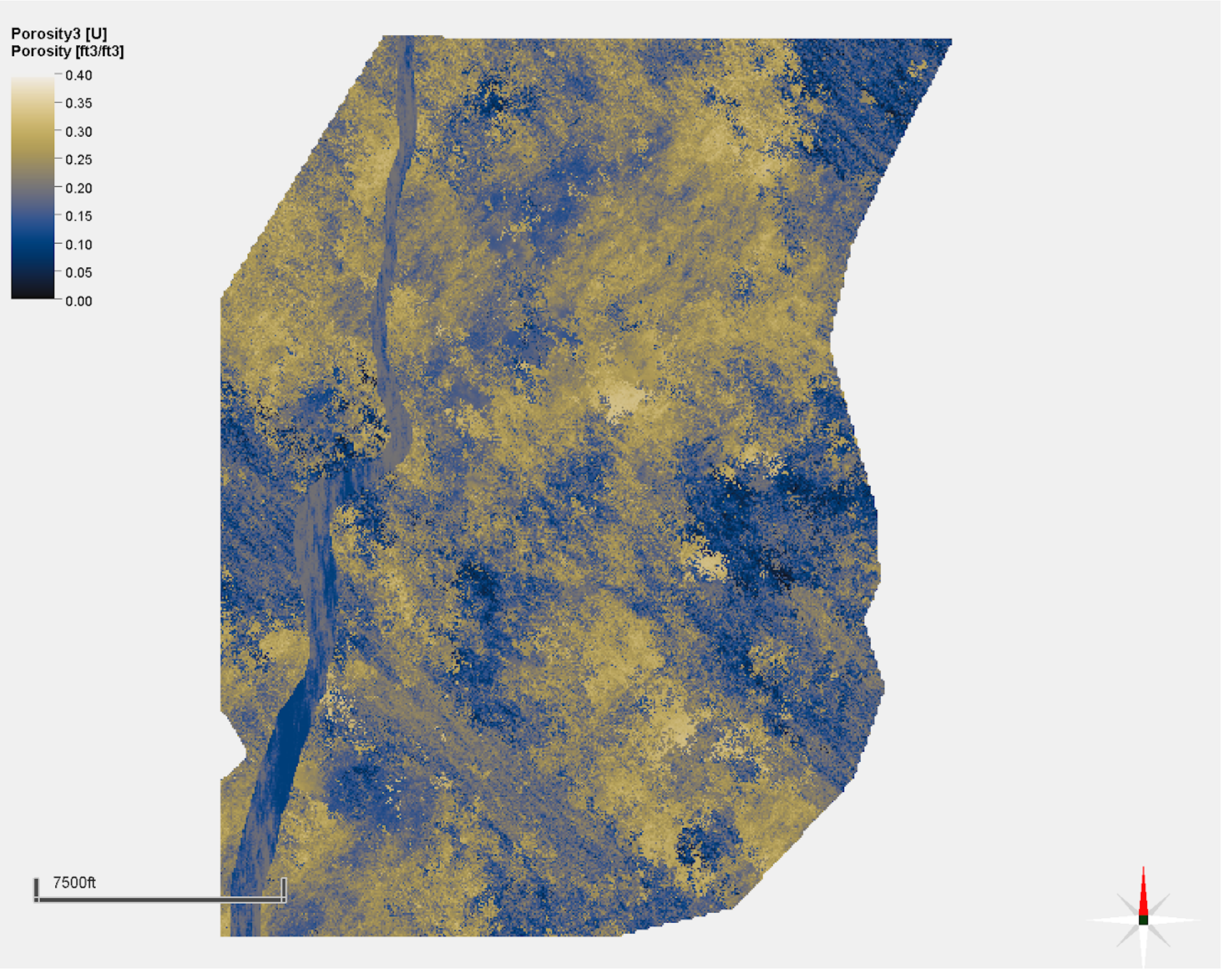

Figure A3.2.3 Porosity distribution for the expanded model.

To populate the permeability across the reservoir, the log of the permeability needs to be taken so that it can be related to the porosity. A log permeability well log calculated on the up-scaled permeability well log. This data is then co-kriged with the porosity distribution and populated across the domain using the sequential gaussian simulation method. Finally, the log permeability is converted back into permeability. The permeability distribution is shown in **Figure A3.2.4**.

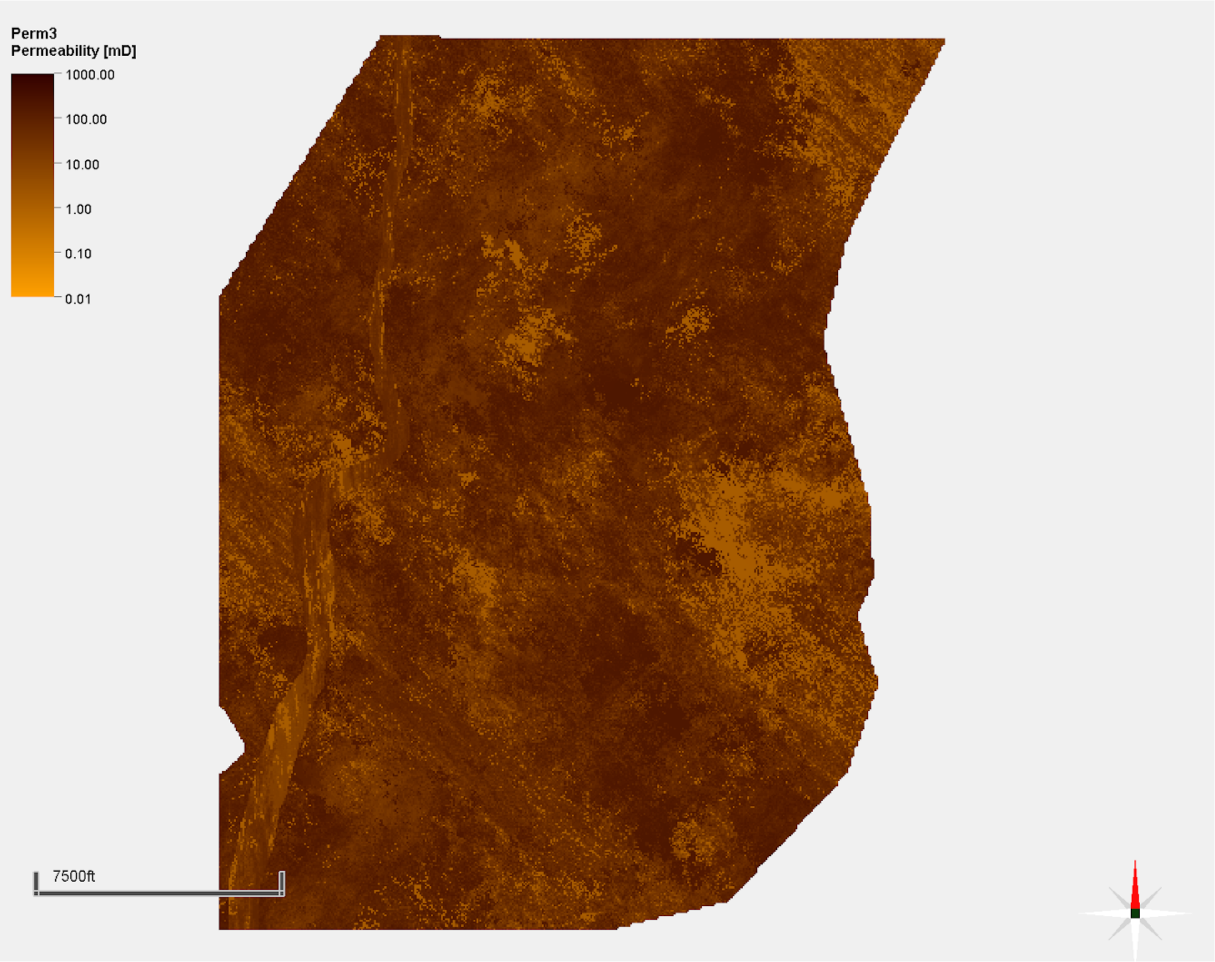

Figure A3.2.4 Permeability distribution in the expanded model.

A3.3: MML History Matching Parameters

Table A3.3.1. MML history matching parameters for fluid model and the permeability.

											krw	Kro	krg			
Cluster	FID	Pcmax	Sorw	Sorg	Swmin	Sgcr	nw	now	nog	ng	@Sorw	@Somax	@Swmin	modz	mody	modx
0	25	31.393	0.213	0.286	0.265	0.022	5.407	6.986	6.997	6.918	0.551	1.000	0.973	0.099	7.954	3.184
0	76	26.296	0.210	0.265	0.267	0.015	5.389	6.986	6.997	6.918	0.596	1.000	0.978	0.099	7.505	2.899
0	125	30.371	0.185	0.167	0.298	0.029	4.464	6.985	6.997	3.095	0.685	0.598	0.804	0.099	7.122	3.211
0	130	34.742	0.190	0.349	0.215	0.076	5.564	6.986	6.590	1.092	0.598	1.000	0.802	0.099	7.592	4.558
0	178	30.976	0.214	0.287	0.264	0.022	5.421	6.985	6.997	6.918	0.552	1.000	0.972	0.099	7.954	3.139
0	331	32.554	0.186	0.345	0.217	0.074	5.517	6.985	6.681	1.091	0.611	1.000	0.802	0.099	7.399	4.521
0	339	37.356	0.189	0.184	0.298	0.033	4.543	6.985	6.997	2.918	0.623	0.555	0.802	0.099	7.954	3.779
0	435	31.167	0.213	0.286	0.265	0.022	5.419	6.986	6.997	6.918	0.555	1.000	0.971	0.099	7.954	3.162
1	31	26.581	0.183	0.158	0.298	0.027	4.525	6.891	6.997	3.074	0.739	0.607	0.805	0.099	6.755	2.976
1	37	21.523	0.262	0.349	0.295	0.004	4.336	6.928	3.248	1.210	0.327	0.721	0.930	0.099	7.695	2.987
1	91	21.473	0.234	0.349	0.298	0.022	4.366	6.985	4.594	2.281	0.379	0.629	0.875	0.099	7.843	4.475
1	141	24.388	0.217	0.207	0.264	0.043	5.066	6.986	6.997	4.913	0.463	1.000	0.877	0.099	7.954	4.426
1	196	21.431	0.178	0.157	0.298	0.025	4.475	6.930	6.997	3.282	0.779	0.645	0.807	0.099	6.466	2.765
1	236	24.268	0.180	0.156	0.298	0.026	4.497	6.889	6.997	3.124	0.768	0.616	0.805	0.099	6.581	2.841
1	241	26.092	0.208	0.127	0.298	0.033	4.576	6.374	6.997	2.559	0.832	0.666	0.816	0.082	5.900	2.033
1	353	21.431	0.179	0.158	0.298	0.026	4.484	6.912	6.997	3.231	0.779	0.641	0.808	0.099	6.473	2.744
2	255	48.248	0.222	0.154	0.255	0.000	5.116	6.986	6.997	6.918	0.399	1.000	0.855	0.099	7.954	5.324
2	412	43.935	0.190	0.349	0.298	0.048	4.323	6.986	5.587	1.095	0.508	0.778	0.802	0.099	7.926	5.486
3	14	21.432	0.229	0.178	0.298	0.002	4.794	6.986	6.997	6.918	0.720	1.000	0.998	0.069	6.511	2.190
3	19	21.438	0.227	0.174	0.298	0.000	4.809	6.985	6.997	6.918	0.730	1.000	0.998	0.069	6.470	2.306
3	32	21.432	0.227	0.177	0.298	0.001	4.870	6.986	6.997	6.918	0.726	1.000	0.998	0.072	6.467	2.348
3	128	21.431	0.227	0.184	0.298	0.004	4.882	6.986	6.997	6.918	0.719	1.000	0.998	0.072	6.511	2.199
3	137	21.433	0.191	0.123	0.298	0.024	4.614	6.986	6.997	5.095	0.637	1.000	0.808	0.099	7.015	4.379
3	234	23.162	0.213	0.247	0.279	0.012	5.226	6.986	6.997	6.918	0.624	1.000	0.993	0.094	7.336	2.578
3	292	21.431	0.252	0.233	0.250	0.032	6.054	6.162	6.997	6.918	0.731	1.000	0.969	0.089	6.061	2.047
3	306	25.988	0.210	0.267	0.270	0.016	5.348	6.986	6.997	6.918	0.591	1.000	0.981	0.099	7.578	2.877
3	398	23.437	0.208	0.258	0.269	0.014	5.366	6.986	6.997	6.918	0.616	1.000	0.981	0.099	7.380	2.839
3	421	21.433	0.229	0.176	0.298	0.001	4.769	6.986	6.997	6.918	0.718	1.000	0.998	0.068	6.518	2.227
3	443	21.790	0.255	0.202	0.250	0.017	6.087	5.939	6.997	6.918	0.760	1.000	0.976	0.088	5.558	1.896
3	490	21.431	0.223	0.199	0.291	0.006	4.937	6.986	6.997	6.918	0.705	1.000	0.998	0.077	6.672	2.139
4	227	81.841	0.177	0.217	0.269	0.004	5.356	6.985	6.994	4.746	0.599	0.999	0.802	0.099	7.954	7.378

A3.4: Building the simulation cases

The ML history matching varied the relative permeability and capillary pressure relationship, and the permeability distribution in the I,J,K. The relative permeability and capillary pressure relationship is defined in Petrel's *Make rock Physics* dialog, under the *Reservoir Engineering* tab, and requires the input of 18 variables to define the oil/water, gas/oil, and oil/water capillary pressure. Create a new saturation function (*Saturation* tab) called Bell Creek Case ## and check '*Use correlation for oil-water*' under the *Capillary pressure* section (**Figure A3.4.1**). The ML assisted history matching work varied nine of these parameters; maximum capillary pressure (Pcmax), residual oil in the oil-water relative permeability pair (S_{orw}), residual oil for the gas-oil relative permeability pair (S_{org}), residual water saturation ($S_w$min), residual gas saturation (S_{gcr}), Corey oil (Corey O/W) and water (Corey Water) exponents for the oil-water relative permeability, Corey oil (Corey O/G) and gas (Corey Gas) exponents for the gas-oil relative permeability, the maximum water relative permeability at residual oil saturation (k_{rw}@S_{orw}), the maximum oil relative permeability at max oil saturation (k_{ro}@$S_o$max), the maximum gas relative permeability at residual water saturation (k_{rg}@$S_w$min), and the water saturation at 0 capillary pressure (S_w@Pc=0). The S_w@Pc=0 is calculated as 1-Sorw-0.01 per Petrel/Eclipse rules. These are entered into the appropriate boxes (Figure A3.4.1) and the rest of the values are left as default.

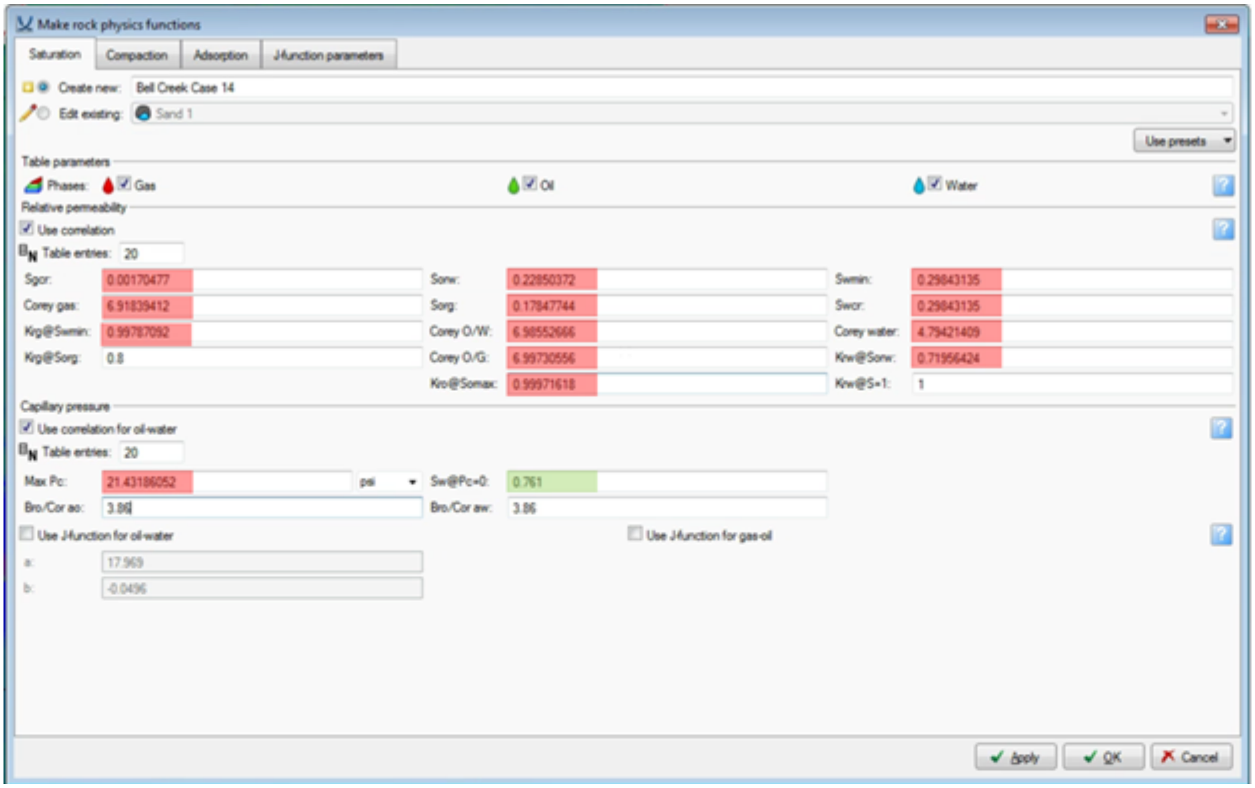

● Create new: Bell Creek Case 14
○ Edit existing: Sand 1

Phases: ☑ Gas ☑ Oil ☑ Water

☑ Use correlation

Table entries: 20

Sgcr: 0.00170477
Corey gas: 6.91839412
Krg@Swmin: 0.99787092
Krg@Sorg: 0.8
Sorw: 0.22850372
Sorg: 0.17847744
Corey O/W: 6.98552666
Corey O/G: 6.99730556
Kro@Somax: 0.99971618
Swmin: 0.29843135
Swcr: 0.29843135
Corey water: 4.79421409
Krw@Sorw: 0.71956424
Krw@S=1: 1

☑ Use correlation for oil-water

Table entries: 20

Max Pc: 21.43186052 psi
Sw@Pc=0: 0.761
Bro/Cor ao: 3.86
Bro/Cor aw: 3.86

☐ Use J-function for oil-water
☐ Use J-function for gas-oil

a: 17.969
b: -0.0496

Figure A3.4.1 Rock physics dialog for creating the relative permeability and capillary pressure relationships.

Each of the ML history matching cases varied the I, J, K permeability by applying modifiers to the base permeability. In Petrel, the calculator tool is used to create the I, J, K permeability maps for each of the 31 simulation cases. This was done by simply multiplying the base permeability by the modifier to create the permx, permy, permz property maps for each model case.

Now the *Simulation* tab is selected and the *Define case* dialog is then chosen from the *Simulation* section. This dialog will have the data from the last simulation case created already populated, select *Create new* and name the case HMCGLD-CASE#. If not select edit existing and the base case from the drop down menu and then select *Create new*. This will ensure that all the data used in the base case is transferred over to the new ML-assisted case. Change the Title and comments to match the case and cluster the data is from (**Figure A3.4.2**) and then select the *Grid* tab. Specify the Permeability I, J, and K created from the ML-assisted case data (**Figure A3.4.3**) and select the *Functions* tab. Under the Function tab, the appropriate saturation function is dropped into the *Drainage relative permeability* model using the default three-phase combination model (**Figure A3.4.4**). The model is then checked for consistency using the *Check* button. Once that has been completed, and there are no errors, the simulation model is exported using the *Export* button. Once done, the dialog is closed by clicking the *OK* button.

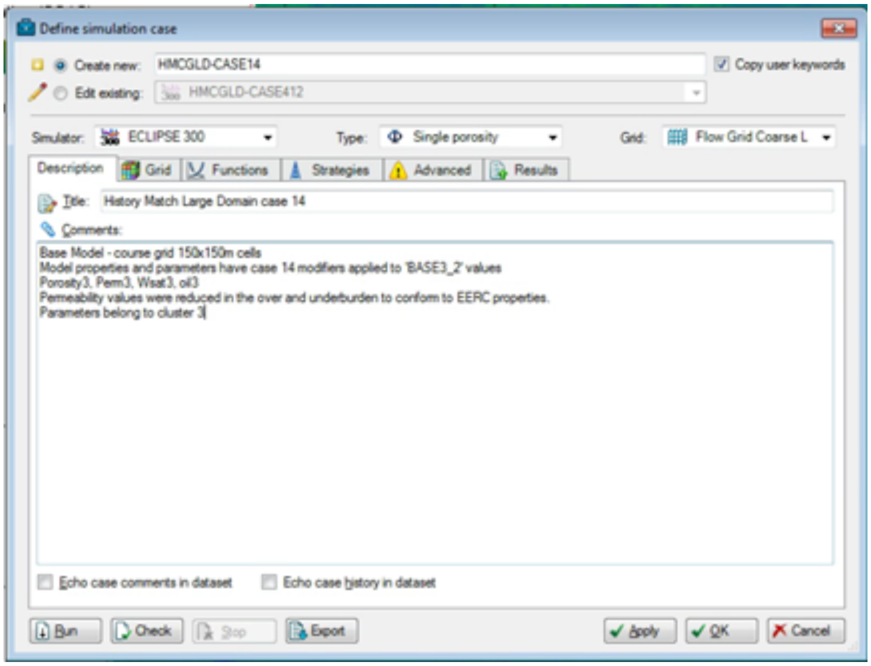

● Create new: HMCGLD-CASE14
☑ Copy user keywords
○ Edit existing: HMCGLD-CASE412
Simulator: ECLIPSE 300
Type: Single porosity
Grid: Flow Grid Coarse L
Title: History Match Large Domain case 14
Comments:
Base Model - course grid 150x150m cells
Model properties and parameters have case 14 modifiers applied to 'BASE3_2' values
Porosity3, Perm3, Wsat3, oil3
Permeability values were reduced in the over and underburden to conform to EERC properties.
Parameters belong to cluster 3
☐ Echo case comments in dataset
☐ Echo case history in dataset

Figure A3.4.2 Define simulation dialog showing the Description tab.

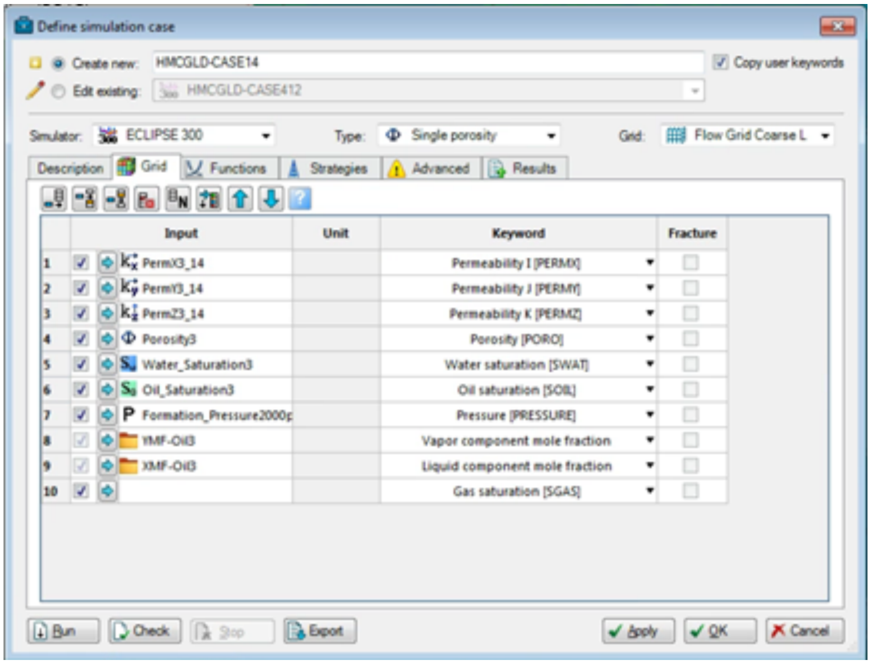

● Create new: HMCGLD-CASE14 ☑ Copy user keywords
○ Edit existing: HMCGLD-CASE412

Simulator: ECLIPSE 300 Type: Single porosity Grid: Flow Grid Coarse L

		Input	Unit	Keyword	Fracture
1	☑	PermX3_14		Permeability I [PERMX]	☐
2	☑	PermY3_14		Permeability J [PERMY]	☐
3	☑	PermZ3_14		Permeability K [PERMZ]	☐
4	☑	Porosity3		Porosity [PORO]	☐
5	☑	Water_Saturation3		Water saturation [SWAT]	☐
6	☑	Oil_Saturation3		Oil saturation [SOIL]	☐
7	☑	Formation_Pressure2000p		Pressure [PRESSURE]	☐
8	☑	YMF-Oil3		Vapor component mole fraction	☐
9	☑	XMF-Oil3		Liquid component mole fraction	☐
10	☑			Gas saturation [SGAS]	☐

Figure A3.4.3 The Grid tab.

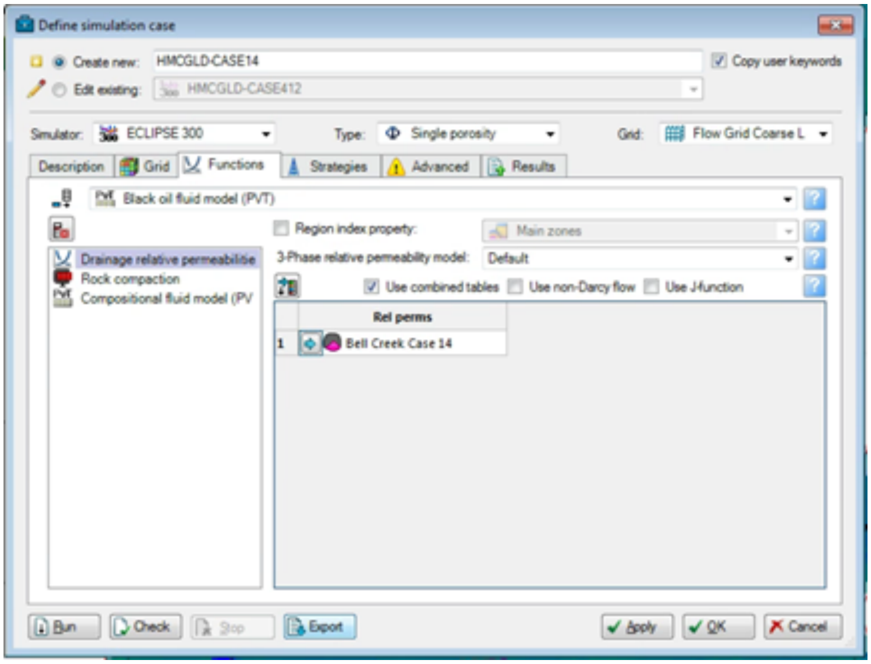

● Create new: HMCGLD-CASE14 ☑ Copy user keywords
○ Edit existing: HMCGLD-CASE412

Simulator: ECLIPSE 300 Type: Single porosity Grid: Flow Grid Coarse L

Black oil fluid model (PVT)

☐ Region index property: Main zones

3-Phase relative permeability model: Default

☑ Use combined tables ☐ Use non-Darcy flow ☐ Use J-function

	Rel perms
1	Bell Creek Case 14

Figure A3.4.4 The Function tab.

The simulation model is now almost ready to be run. A few things need to be checked in the simulation files before transferring to the CHPC and running on the cluster. Navigate to the project's simulation folder within the Petrel project (projectname.sim) from the file explorer. Open the newly created simulation folder and open the simname.DATA file in a text editor (notepad++) and remove the MULTISAVE and MULTIOUT keywords and data. We want all the data in a single output file. Open the simname_SCH.INC file and remove the comments after ENDSKIP keyword and before the WELSPEC keyword. This is just house cleaning. These comments can accumulate in this file if you use the previous simulation model case as the template for the next model case. Open the simname_SOL.INC file next and check the INCLUDE files it is calling out. If there are any that refer to a file outside the simulation case folder, they need to be deleted. Example: '..\HMCGLD-CASE412\HMCGLD-CASE412_YMF.INC' / when it should look like: 'HMCGLD-CASE14_YMF.INC' /. All data the Eclipse simulator needs should be contained within the simulation case folder (project standard). The last file to edit is the simname_SUM.INC file. Petrel will write output keywords that are not needed for this file, and it is cumbersome to change it in the Petrel Define case dialog, so a quick file edit ensures all cases output the same data. Open the HMCGLD-CASE120_2 folder and the HMCGLD-CASE120_2_SUM.INC file and copy the contents. Now erase the contents of the new case simname_SUM.INC file and paste the copied values. Save all and close.

A3.5: Export data from Petrel for EM modeling

1. Right click on a property that will be output (Oil Saturation)
    a. Select "Export Object"
2. 'Export As' dialog box
    a. Name file 'results.txt'
    b. Select Gslib properties (ASCII) as 'save type'

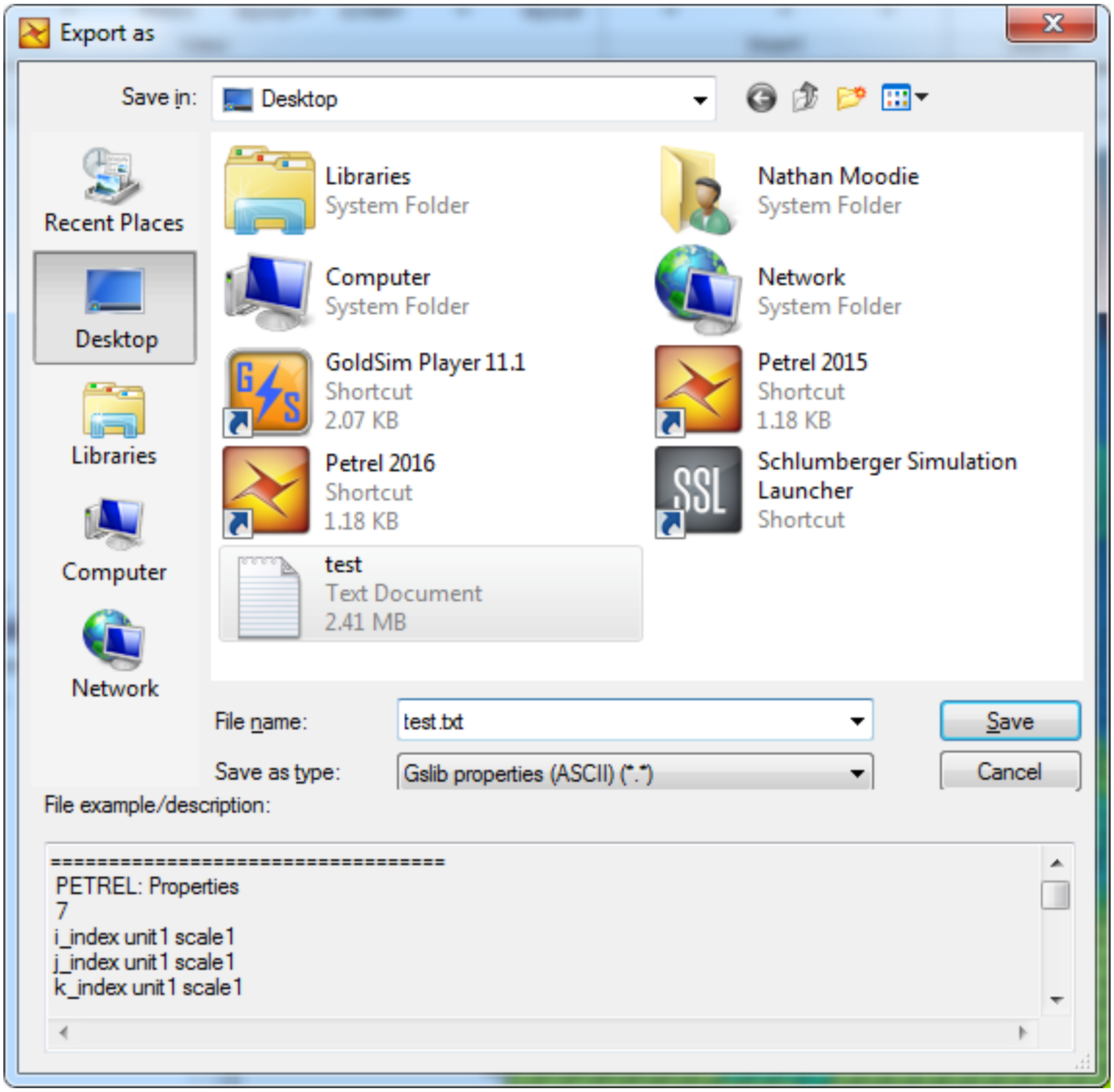

Save in: Desktop

File name: test.txt

Save as type: Gslib properties (ASCII) (*.*)

File example/description:

```
==================================
PETREL: Properties
7
i_index unit1 scale1
j_index unit1 scale1
k_index unit1 scale1
```

3. Properties selection box
   a. Check all properties that will be exported
      i. Porosity, Permeability, oil saturation, water saturation, gas saturation, pressure

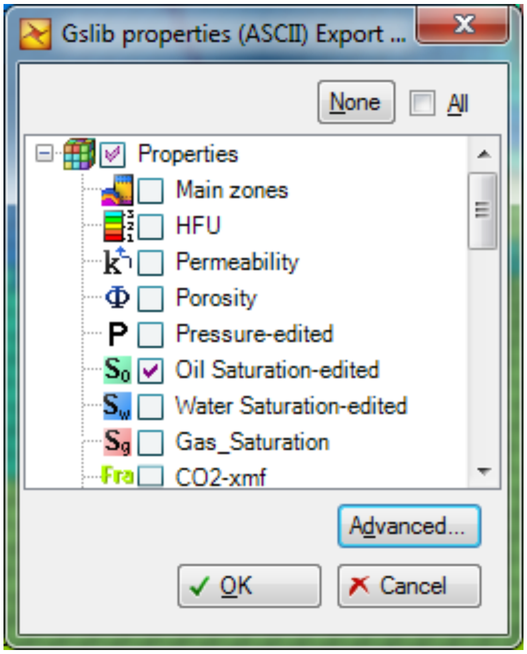
Gslib properties (ASCII) Export ...

☐ All

☑ Properties
- ☐ Main zones
- ☐ HFU
- ☐ Permeability
- ☐ Porosity
- ☐ Pressure-edited
- ☑ Oil Saturation-edited
- ☐ Water Saturation-edited
- ☐ Gas_Saturation
- ☐ CO2-xmf

b. Click 'Advanced' button
   i. Check 'Include cell index'
   ii. Check 'Include cell center coordinates'
   iii. Click 'OK'

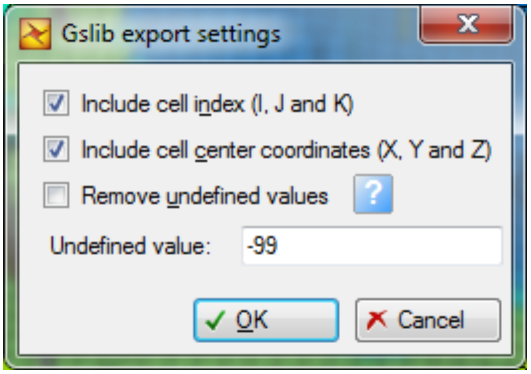
Gslib export settings

☑ Include cell index (I, J and K)

☑ Include cell center coordinates (X, Y and Z)

☐ Remove undefined values

Undefined value: -99

4. Remove ‘over-burden’ [layers 1-5] and ‘under-burden’ [layers 12-14] from text file
   a. Open file in a text editor and delete all rows with z=1 to 5 and z=12 to 14.

A3.6: Delta water saturation, permeability in X, Y, Z, relative permeability and capillary pressure plots

Cluster 0

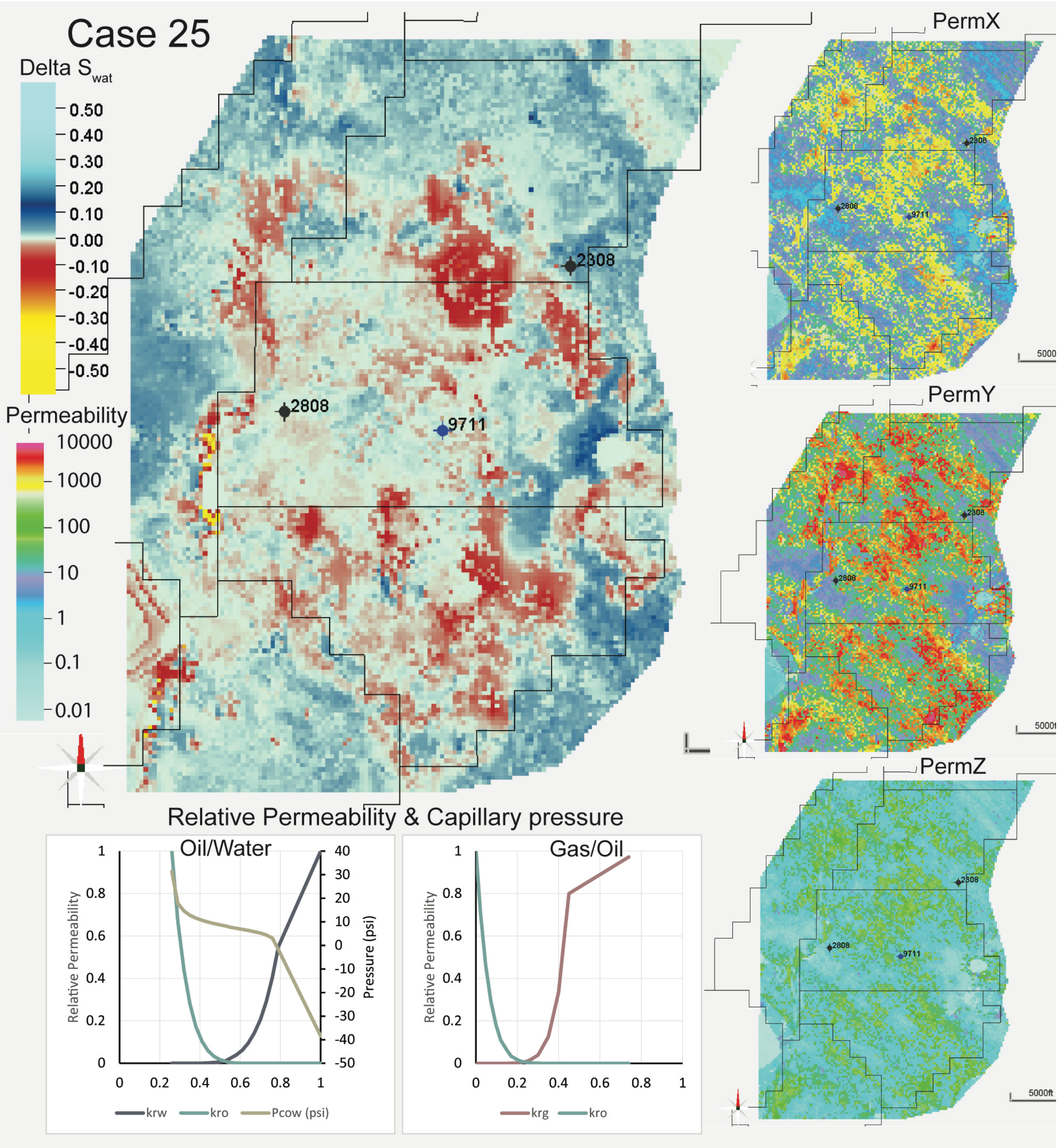

Figure A3.6.1 This figure shows the difference in water saturation between September 30, 2017, and July 31, 2019 for Case 25 in the large central plot. The permeability assigned to the X, Y, and Z is shown on the right and the oil/water and gas/oil relative permeability, with oil/water capillary pressure.

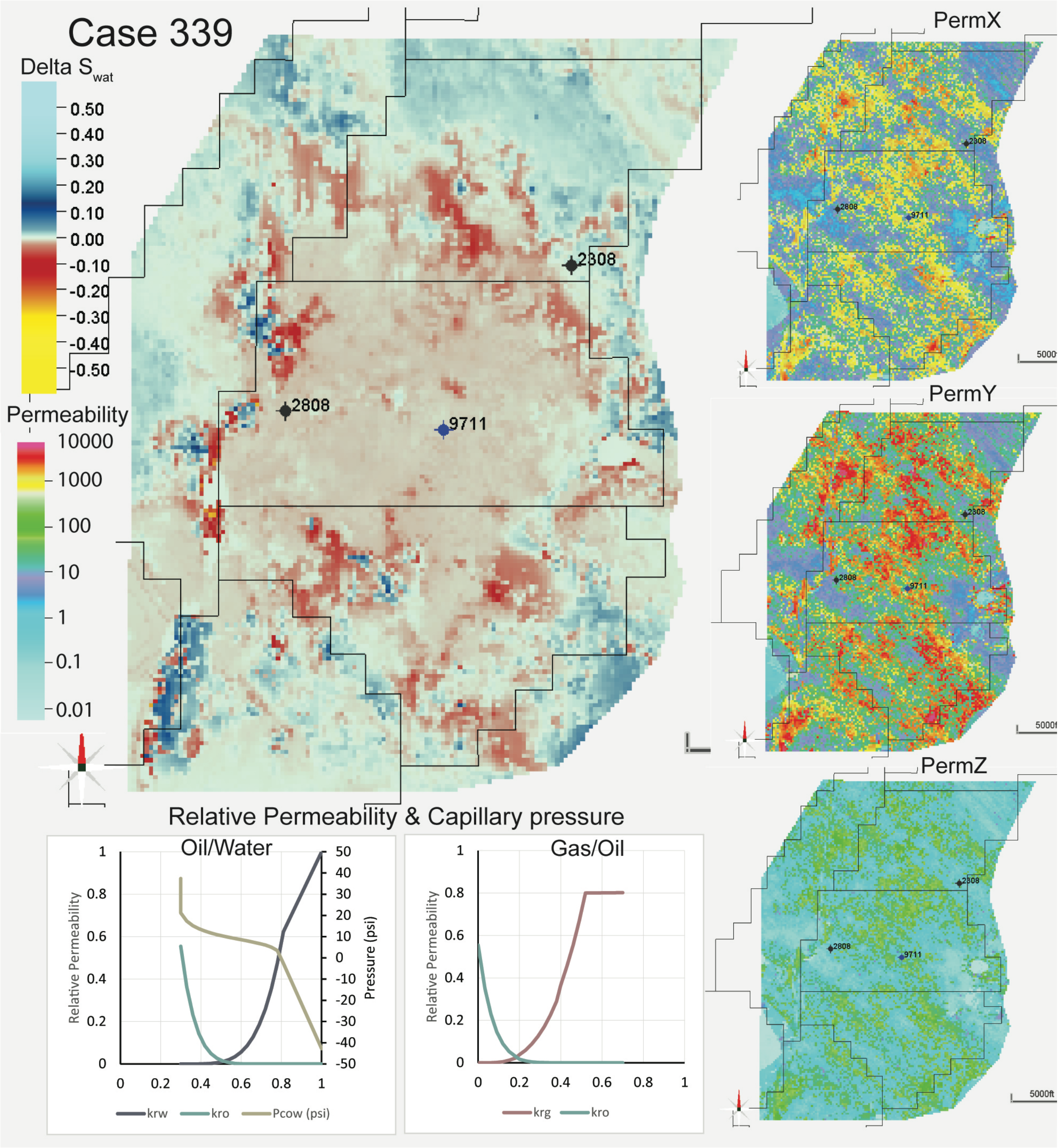

Figure A3.6.2 This figure shows the difference in water saturation between September 30, 2017, and July 31, 2019 for Case 339 in the large central plot. The permeability assigned to the X, Y, and Z is shown on the right and the oil/water and gas/oil relative permeability, with oil/water capillary pressure.

Cluster 1

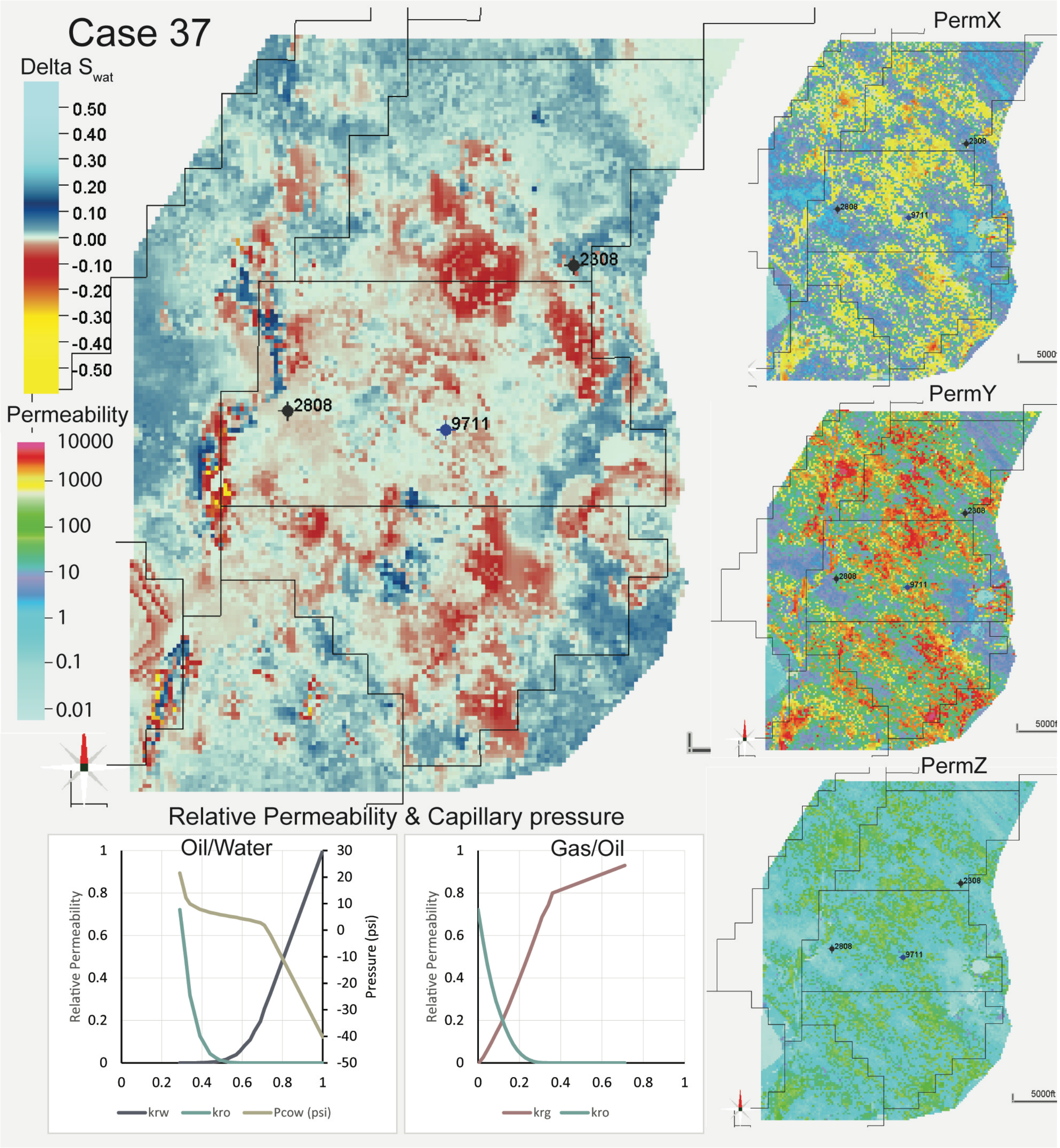

Figure A3.6.3 This figure shows the difference in water saturation between September 30, 2017, and July 31, 2019 for Case 37 in the large central plot. The permeability assigned to the X, Y, and Z is shown on the right and the oil/water and gas/oil relative permeability, with oil/water capillary pressure.

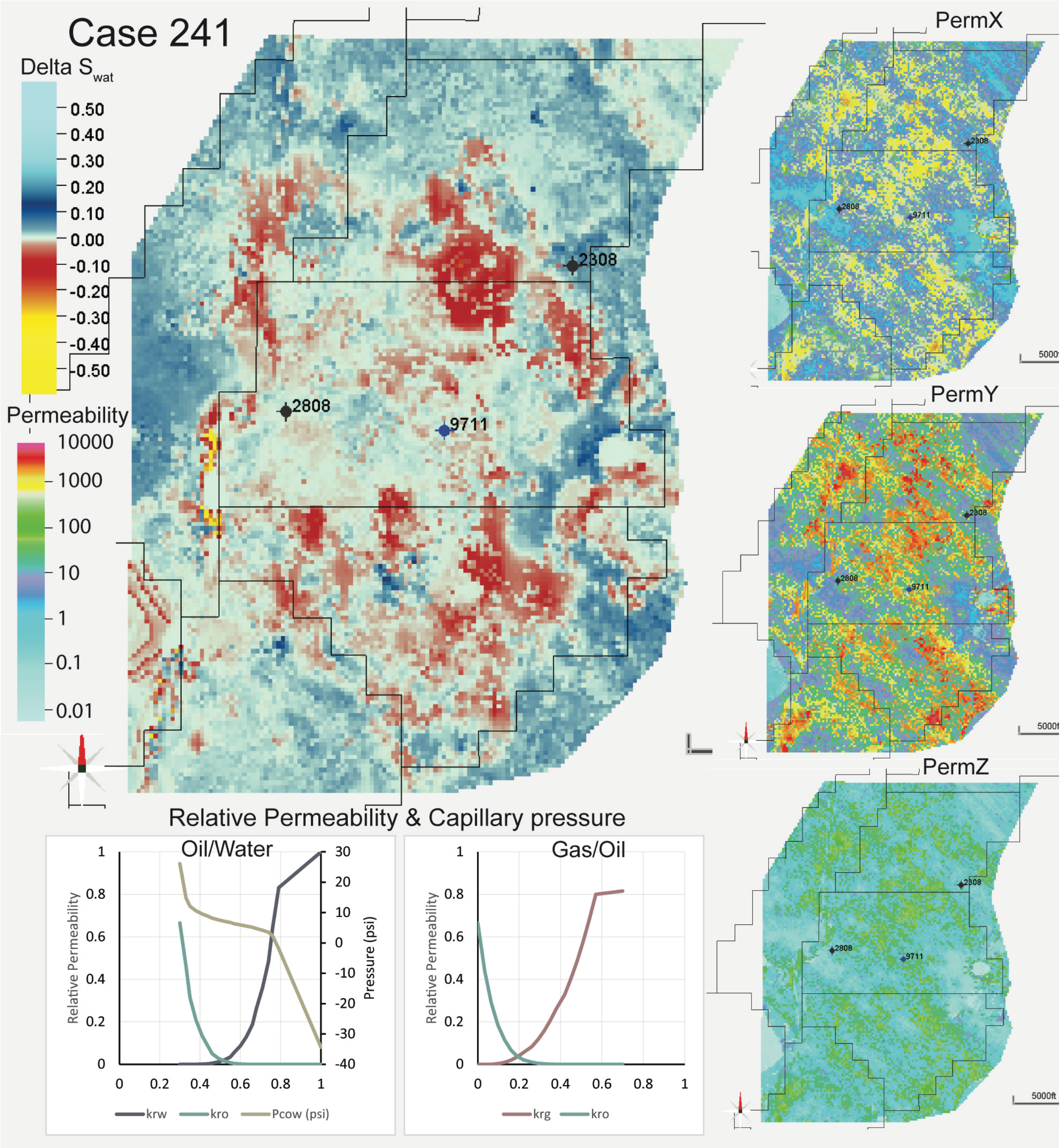

Figure A3.6.4 This figure shows the difference in water saturation between September 30, 2017, and July 31, 2019 for Case 241 in the large central plot. The permeability assigned to the X, Y, and Z is shown on the right and the oil/water and gas/oil relative permeability, with oil/water capillary pressure.

Cluster 2

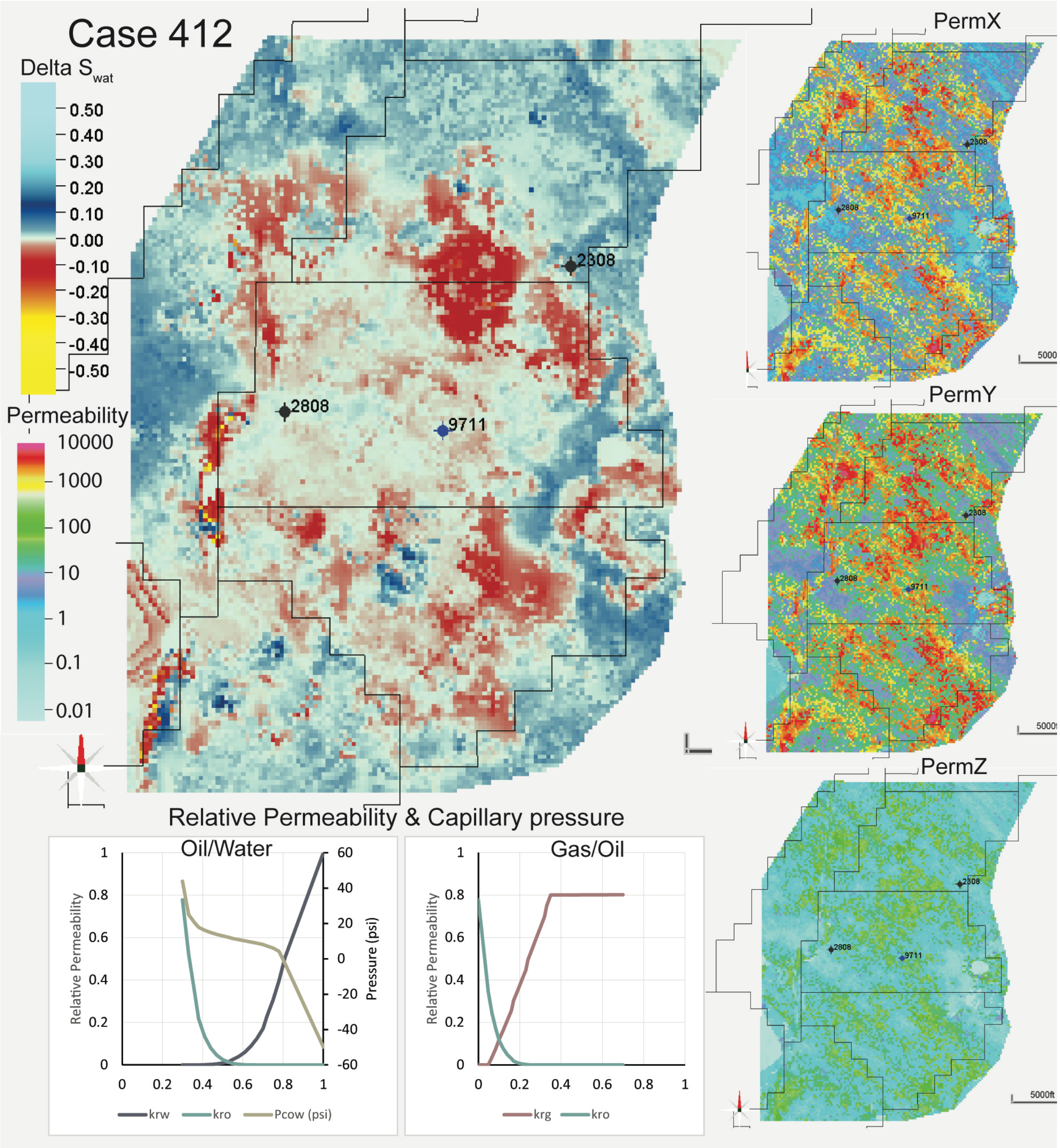

Figure A3.6.5 This figure shows the difference in water saturation between September 30, 2017, and July 31, 2019 for Case 412 in the large central plot. The permeability assigned to the X, Y, and Z is shown on the right and the oil/water and gas/oil relative permeability, with oil/water capillary pressure.

Cluster 3

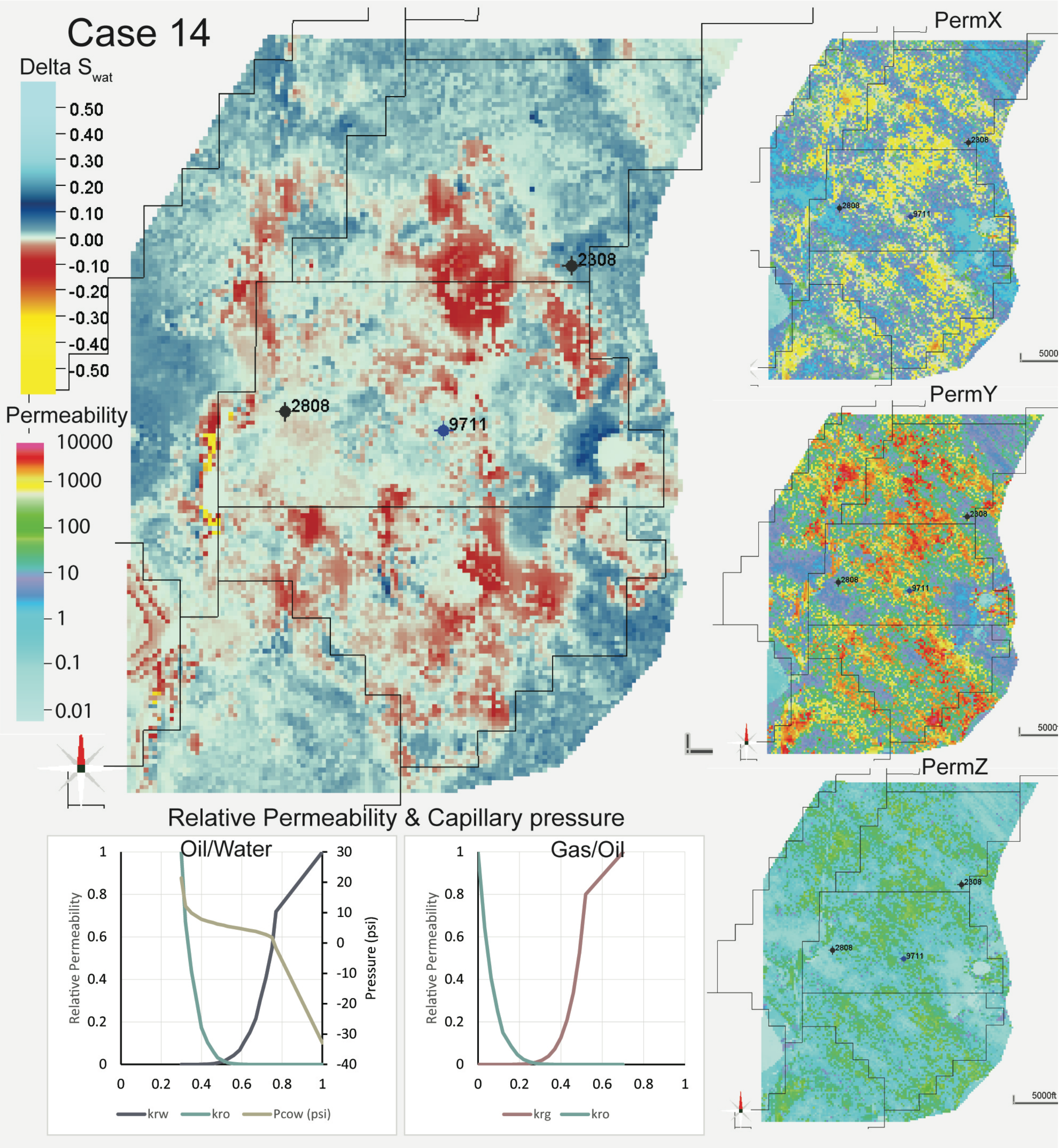

Figure A3.6.6 This figure shows the difference in water saturation between September 30, 2017, and July 31, 2019 for Case 14 in the large central plot. The permeability assigned to the X, Y, and Z is shown on the right and the oil/water and gas/oil relative permeability, with oil/water capillary pressure.

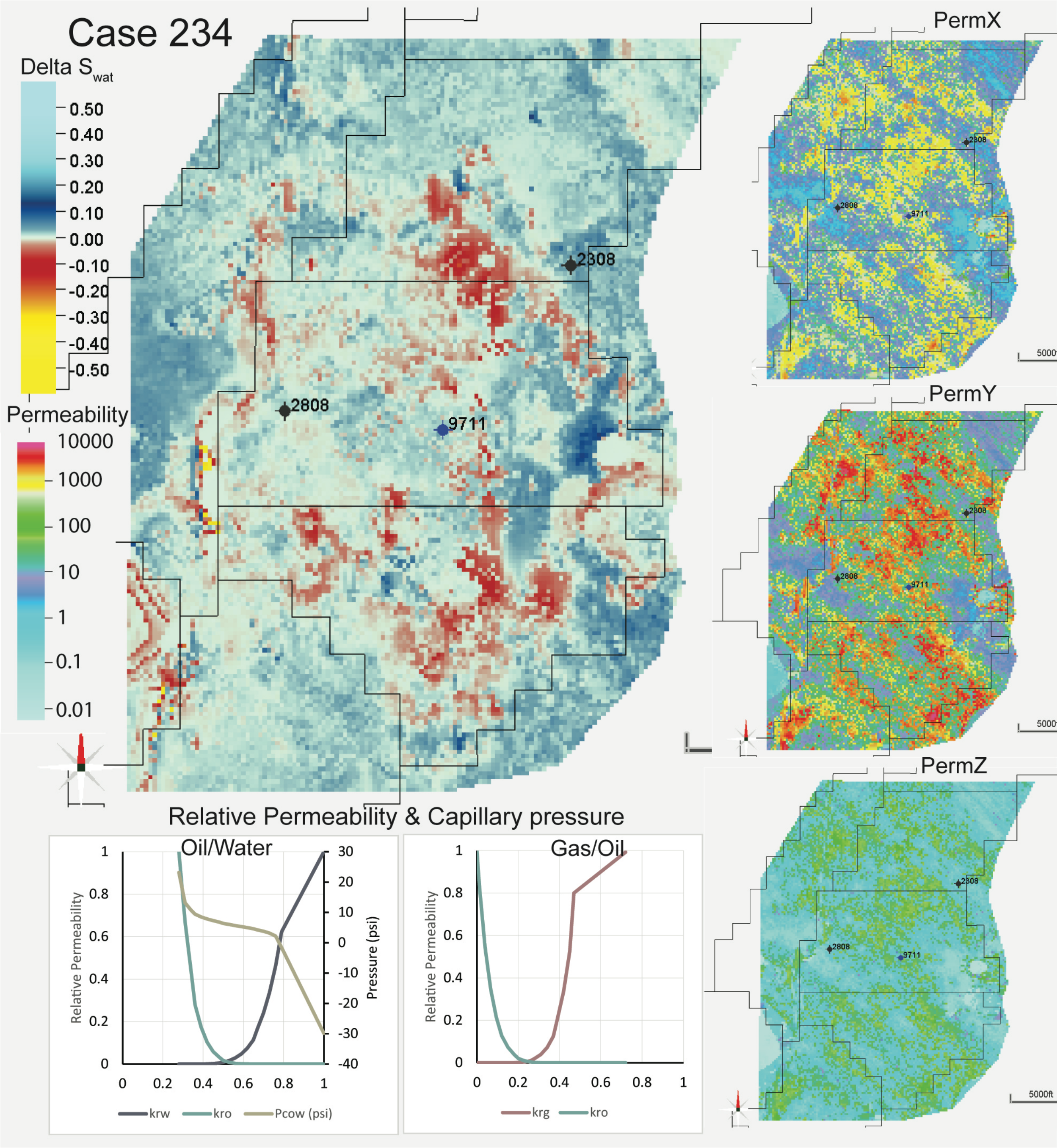

Figure A3.6.7 This figure shows the difference in water saturation between September 30, 2017, and July 31, 2019 for Case 14 in the large central plot. The permeability assigned to the X, Y, and Z is shown on the right and the oil/water and gas/oil relative permeability, with oil/water capillary pressure.

Cluster 4

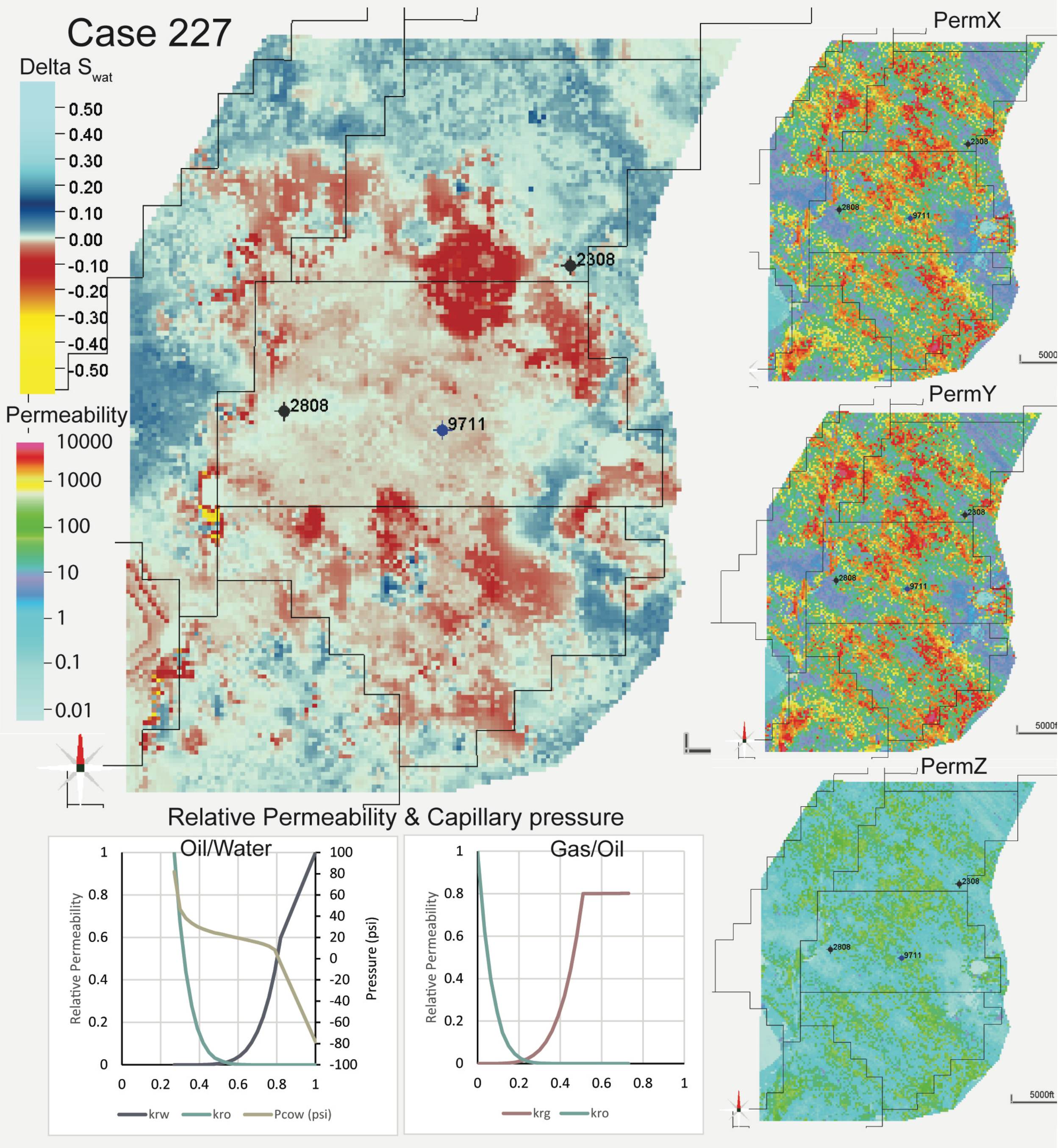

Figure A3.6.8 This figure shows the difference in water saturation between September 30, 2017, and July 31, 2019 for Case 227 in the large central plot. The permeability assigned to the X, Y, and Z is shown on the right and the oil/water and gas/oil relative permeability, with oil/water capillary pressure.

A3.7: Model Resolution Information

Table A3.7.1 ANOVA results for the coarse resolution model data

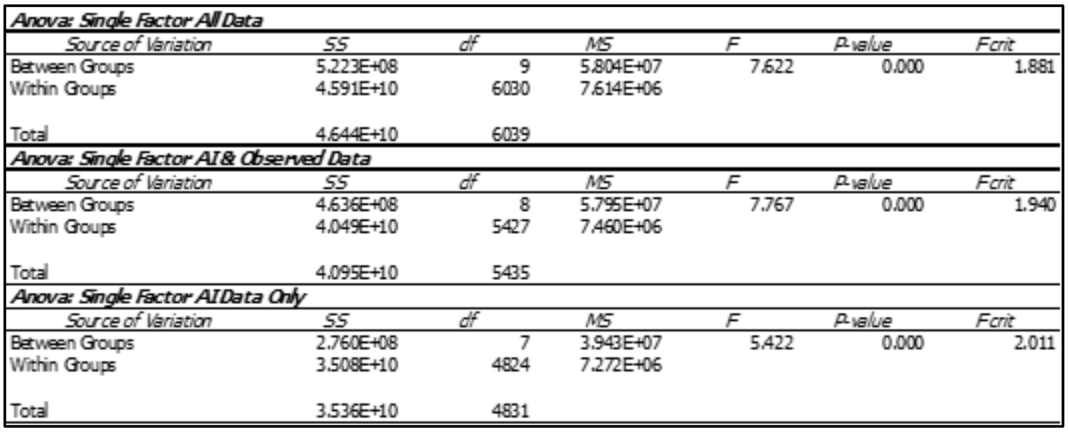

Anova: Single Factor All Data						
Source of Variation	*SS*	*df*	*MS*	*F*	*P-value*	*F crit*
Between Groups	5.223E+08	9	5.804E+07	7.622	0.000	1.881
Within Groups	4.591E+10	6030	7.614E+06			
Total	4.644E+10	6039				
Anova: Single Factor AI & Observed Data						
Source of Variation	*SS*	*df*	*MS*	*F*	*P-value*	*F crit*
Between Groups	4.636E+08	8	5.795E+07	7.767	0.000	1.940
Within Groups	4.049E+10	5427	7.460E+06			
Total	4.095E+10	5435				
Anova: Single Factor AI Data Only						
Source of Variation	*SS*	*df*	*MS*	*F*	*P-value*	*F crit*
Between Groups	2.760E+08	7	3.943E+07	5.422	0.000	2.011
Within Groups	3.508E+10	4824	7.272E+06			
Total	3.536E+10	4831				

Table A3.7.2 T-test results for the coarse-resolution model cases

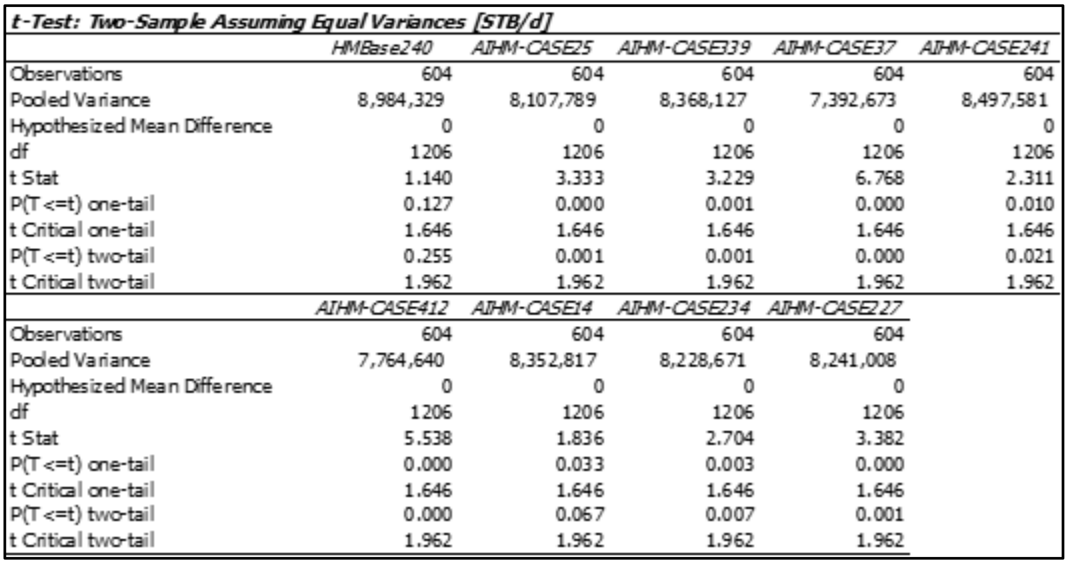

t-Test: Two-Sample Assuming Equal Variances [STB/d]					
	HMBase240	*AIHM-CASE25*	*AIHM-CASE339*	*AIHM-CASE37*	*AIHM-CASE241*
Observations	604	604	604	604	604
Pooled Variance	8,984,329	8,107,789	8,368,127	7,392,673	8,497,581
Hypothesized Mean Difference	0	0	0	0	0
df	1206	1206	1206	1206	1206
t Stat	1.140	3.333	3.229	6.768	2.311
P(T<=t) one-tail	0.127	0.000	0.001	0.000	0.010
t Critical one-tail	1.646	1.646	1.646	1.646	1.646
P(T<=t) two-tail	0.255	0.001	0.001	0.000	0.021
t Critical two-tail	1.962	1.962	1.962	1.962	1.962
	AIHM-CASE412	*AIHM-CASE14*	*AIHM-CASE234*	*AIHM-CASE227*	
Observations	604	604	604	604	
Pooled Variance	7,764,640	8,352,817	8,228,671	8,241,008	
Hypothesized Mean Difference	0	0	0	0	
df	1206	1206	1206	1206	
t Stat	5.538	1.836	2.704	3.382	
P(T<=t) one-tail	0.000	0.033	0.003	0.000	
t Critical one-tail	1.646	1.646	1.646	1.646	
P(T<=t) two-tail	0.000	0.067	0.007	0.001	
t Critical two-tail	1.962	1.962	1.962	1.962	

Table A3.7.3 Regression analysis results for the coarse resolution simulations.

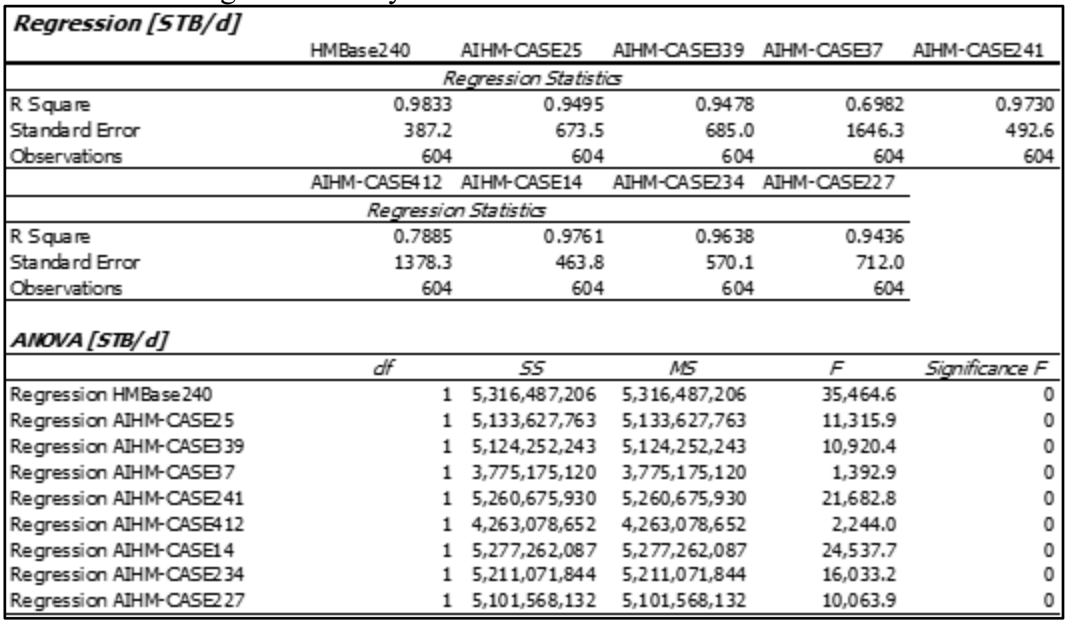

Regression [STB/d]

	HMBase240	AIHM-CASE25	AIHM-CASE339	AIHM-CASE37	AIHM-CASE241
	Regression Statistics				
R Square	0.9833	0.9495	0.9478	0.6982	0.9730
Standard Error	387.2	673.5	685.0	1646.3	492.6
Observations	604	604	604	604	604

	AIHM-CASE412	AIHM-CASE14	AIHM-CASE234	AIHM-CASE227
	Regression Statistics			
R Square	0.7885	0.9761	0.9638	0.9436
Standard Error	1378.3	463.8	570.1	712.0
Observations	604	604	604	604

ANOVA [STB/d]

	df	*SS*	*MS*	*F*	*Significance F*
Regression HMBase240	1	5,316,487,206	5,316,487,206	35,464.6	0
Regression AIHM-CASE25	1	5,133,627,763	5,133,627,763	11,315.9	0
Regression AIHM-CASE339	1	5,124,252,243	5,124,252,243	10,920.4	0
Regression AIHM-CASE37	1	3,775,175,120	3,775,175,120	1,392.9	0
Regression AIHM-CASE241	1	5,260,675,930	5,260,675,930	21,682.8	0
Regression AIHM-CASE412	1	4,263,078,652	4,263,078,652	2,244.0	0
Regression AIHM-CASE14	1	5,277,262,087	5,277,262,087	24,537.7	0
Regression AIHM-CASE234	1	5,211,071,844	5,211,071,844	16,033.2	0
Regression AIHM-CASE227	1	5,101,568,132	5,101,568,132	10,063.9	0

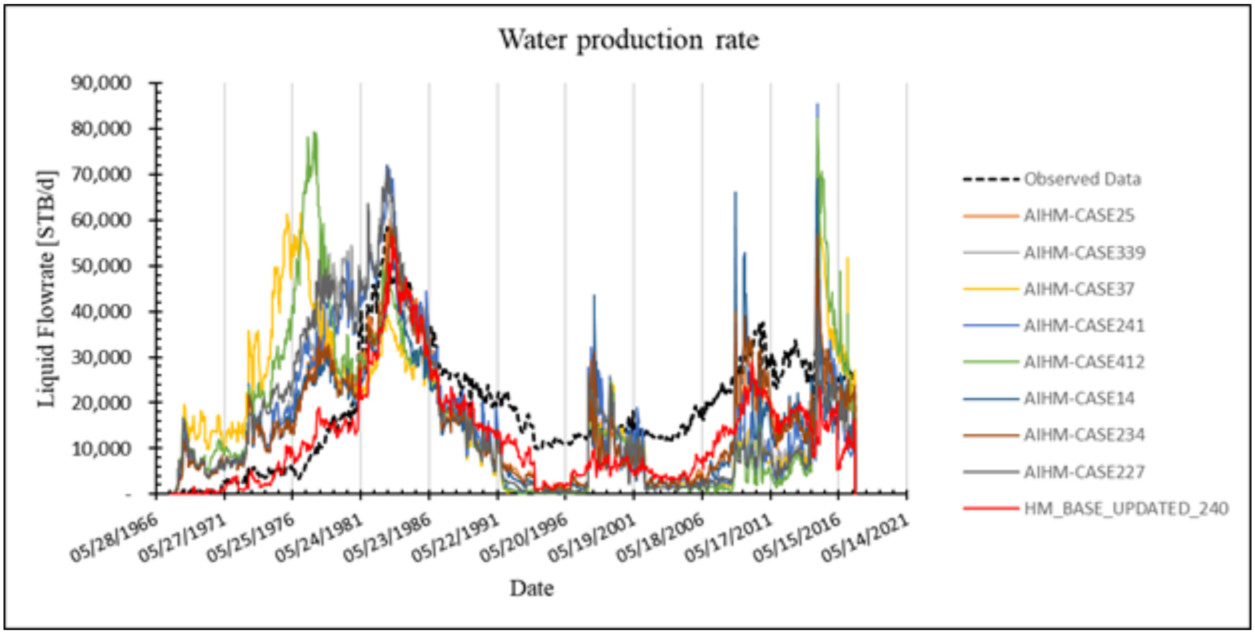

Figure A3.7.1 Water production for the coarse-resolution model cases.

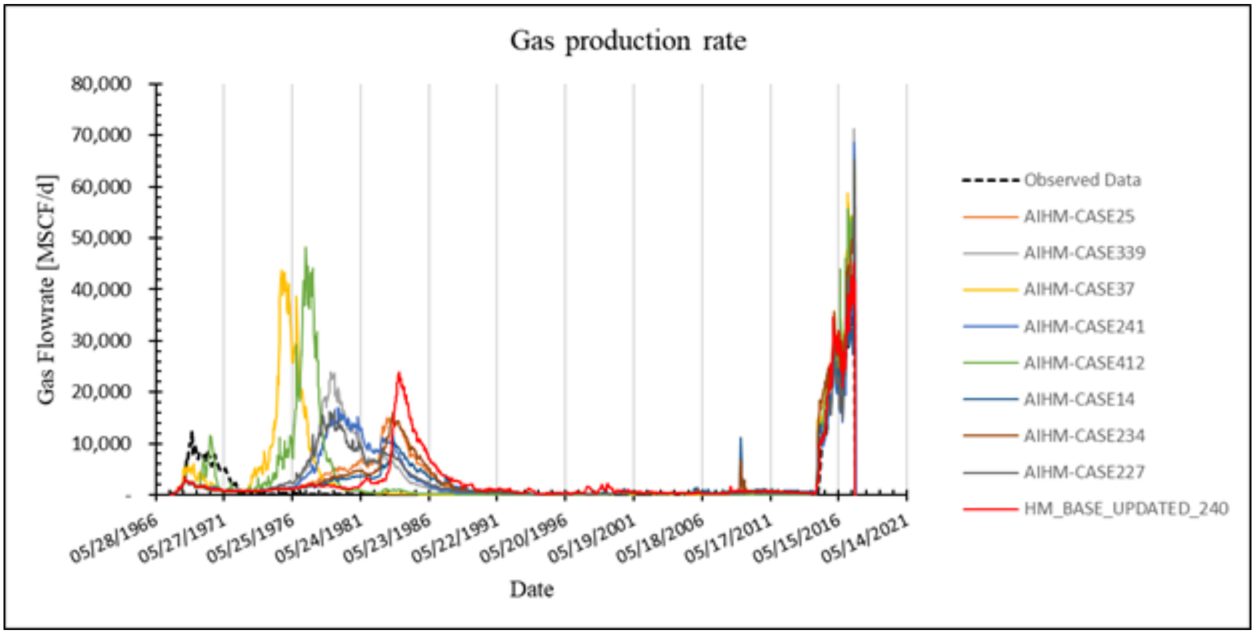

Figure A3.7.2 Gas production for the coarse-resolution model cases.

Table A3.7.4 ANOVA results for the fine-grid model cases.

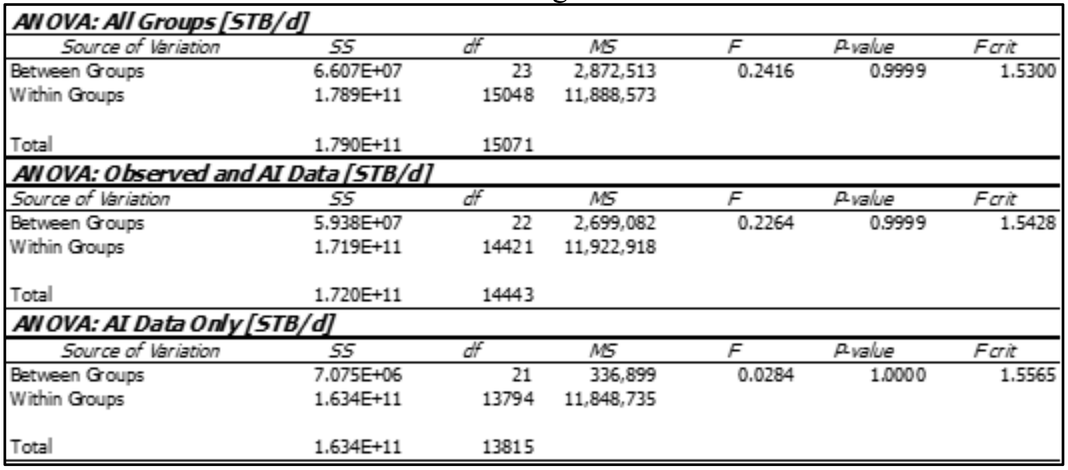

ANOVA: All Groups [STB/d]						
Source of Variation	SS	df	MS	F	P-value	F crit
Between Groups	6.607E+07	23	2,872,513	0.2416	0.9999	1.5300
Within Groups	1.789E+11	15048	11,888,573			
Total	1.790E+11	15071				
ANOVA: Observed and AI Data [STB/d]						
Source of Variation	SS	df	MS	F	P-value	F crit
Between Groups	5.938E+07	22	2,699,082	0.2264	0.9999	1.5428
Within Groups	1.719E+11	14421	11,922,918			
Total	1.720E+11	14443				
ANOVA: AI Data Only [STB/d]						
Source of Variation	SS	df	MS	F	P-value	F crit
Between Groups	7.075E+06	21	336,899	0.0284	1.0000	1.5565
Within Groups	1.634E+11	13794	11,848,735			
Total	1.634E+11	13815				

Table A3.7.5 T-test analysis results for the fine-resolution model.

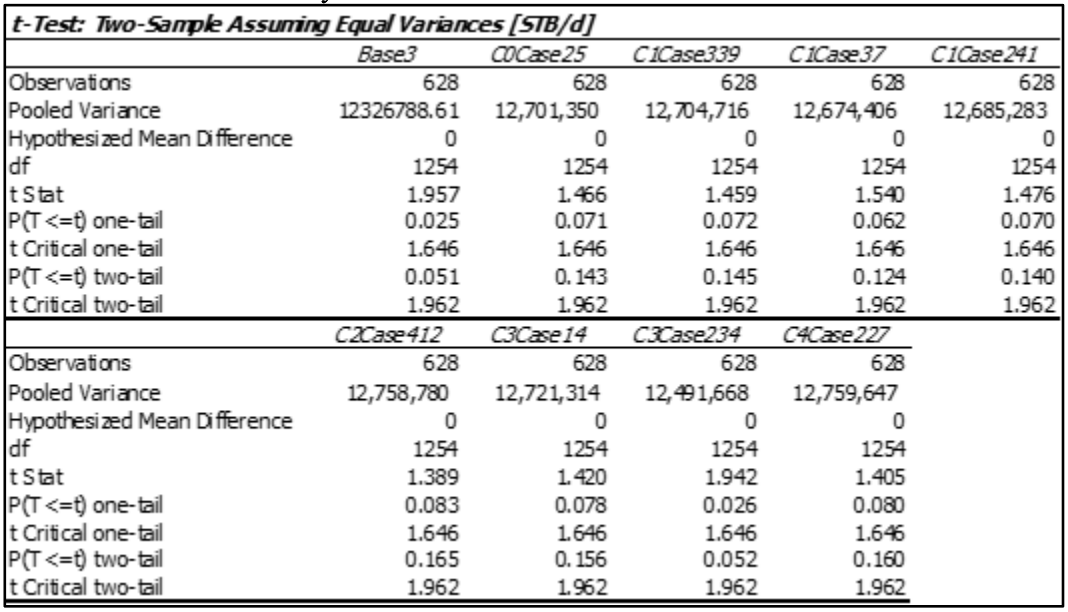

t-Test: Two-Sample Assuming Equal Variances [STB/d]	*Base3*	*C0Case25*	*C1Case339*	*C1Case37*	*C1Case241*
Observations	628	628	628	628	628
Pooled Variance	12326788.61	12,701,350	12,704,716	12,674,406	12,685,283
Hypothesized Mean Difference	0	0	0	0	0
df	1254	1254	1254	1254	1254
t Stat	1.957	1.466	1.459	1.540	1.476
P(T <=t) one-tail	0.025	0.071	0.072	0.062	0.070
t Critical one-tail	1.646	1.646	1.646	1.646	1.646
P(T <=t) two-tail	0.051	0.143	0.145	0.124	0.140
t Critical two-tail	1.962	1.962	1.962	1.962	1.962

	C2Case412	*C3Case14*	*C3Case234*	*C4Case227*
Observations	628	628	628	628
Pooled Variance	12,758,780	12,721,314	12,491,668	12,759,647
Hypothesized Mean Difference	0	0	0	0
df	1254	1254	1254	1254
t Stat	1.389	1.420	1.942	1.405
P(T <=t) one-tail	0.083	0.078	0.026	0.080
t Critical one-tail	1.646	1.646	1.646	1.646
P(T <=t) two-tail	0.165	0.156	0.052	0.160
t Critical two-tail	1.962	1.962	1.962	1.962

Table A3.7.6 Regression analysis results for the fine-resolution model cases.

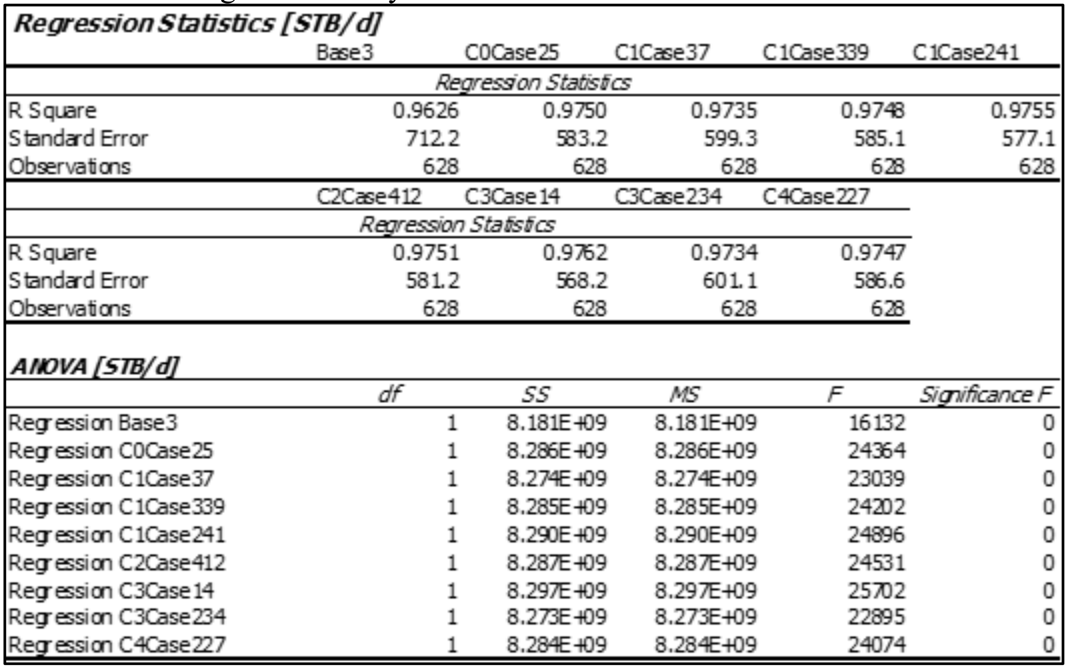

Regression Statistics [STB/d]	Base3	C0Case25	C1Case37	C1Case339	C1Case241
	Regression Statistics				
R Square	0.9626	0.9750	0.9735	0.9748	0.9755
Standard Error	712.2	583.2	599.3	585.1	577.1
Observations	628	628	628	628	628

	C2Case412	C3Case14	C3Case234	C4Case227
	Regression Statistics			
R Square	0.9751	0.9762	0.9734	0.9747
Standard Error	581.2	568.2	601.1	586.6
Observations	628	628	628	628

ANOVA [STB/d]	*df*	*SS*	*MS*	*F*	*Significance F*
Regression Base3	1	8.181E+09	8.181E+09	16132	0
Regression C0Case25	1	8.286E+09	8.286E+09	24364	0
Regression C1Case37	1	8.274E+09	8.274E+09	23039	0
Regression C1Case339	1	8.285E+09	8.285E+09	24202	0
Regression C1Case241	1	8.290E+09	8.290E+09	24896	0
Regression C2Case412	1	8.287E+09	8.287E+09	24531	0
Regression C3Case14	1	8.297E+09	8.297E+09	25702	0
Regression C3Case234	1	8.273E+09	8.273E+09	22895	0
Regression C4Case227	1	8.284E+09	8.284E+09	24074	0

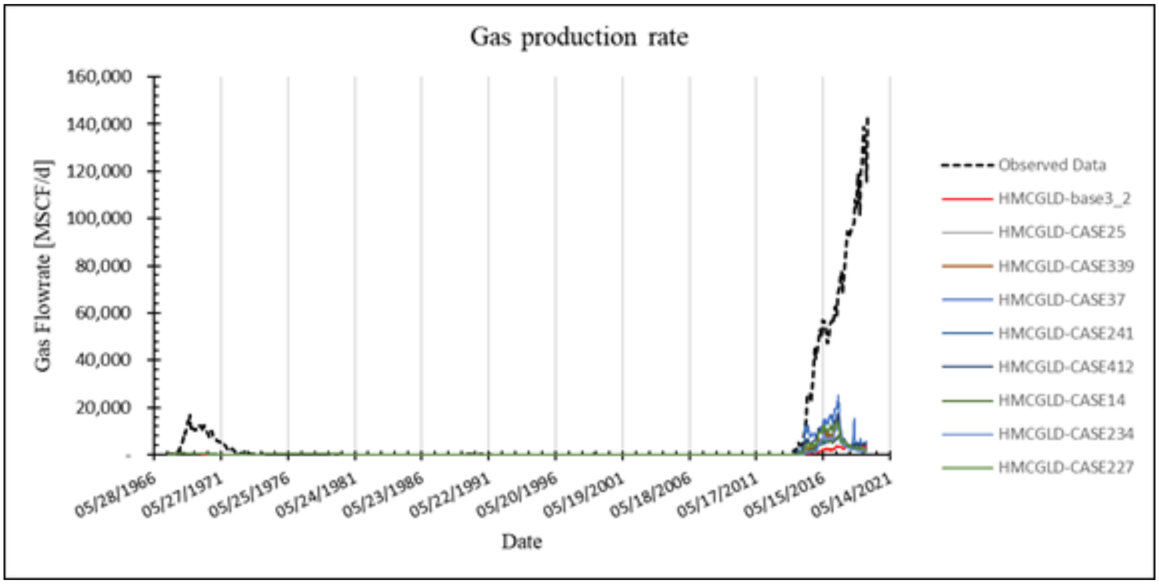

Figure A3.7.3 Gas production from the fine resolution model.

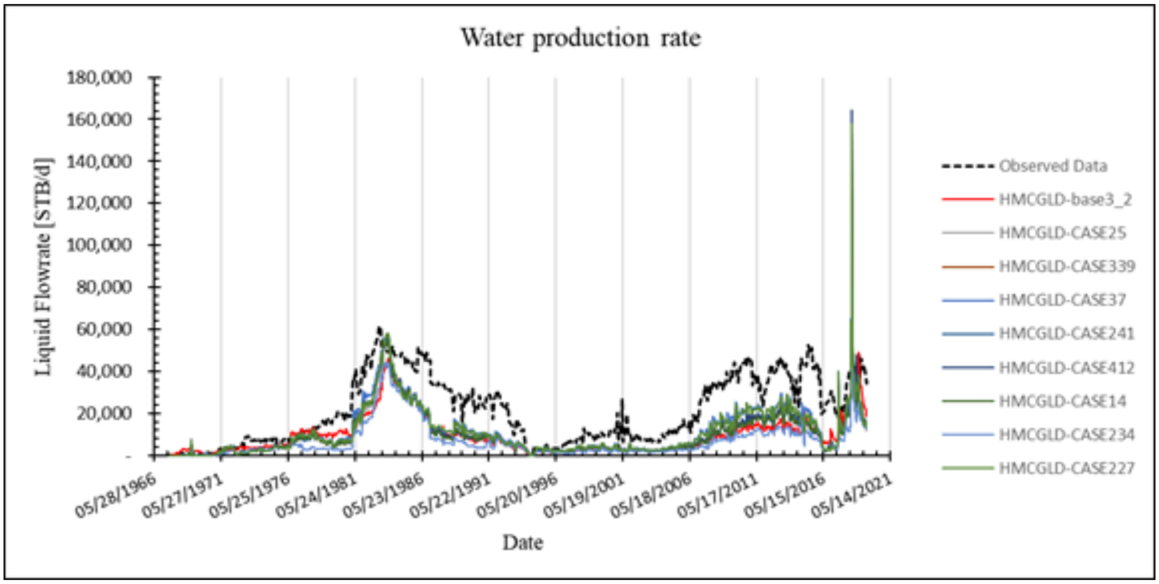

Figure A3.7.4 Water production for the fine resolution model.

A4. DOZEN: CSEM DATA PROCESSING LIBRARY

DoZen's major advantages lie in three areas: automation, data quality control, and variance analysis. Advantages in these three areas all reinforce one another. Automation allows us to quickly and iteratively evaluate and improve our workflow. Improved data quality control tools aid the evaluation of the workflow by identifying data outliers and exposing trends in the data. The full time-lapse dataset consists of over 50,000 separate time series, so a streamlined process for identifying and minimizing the effects of noisy data is critical for ensuring the highest data quality. Variance analysis can be used for identifying such noisy data. Identifying and removing parts of the time series that are corrupted by cultural noise reduces the variance. Accurate estimation of the variance and reduction of data variance both improve our capability to image subsurface CO2 movement, since the appropriate level of CSEM data misfit can be identified using the data variance.

Having written custom processing code, we are able to automate our processing workflow via scripts. This automation allows different processing parameters to be tested to efficiently determine the optimal processing workflow. It also facilitates error handling, since reprocessing the data after error identification is much quicker.

DoZen allows efficient plotting and quality control checks. Zonge receiver data files (.z3d format) for a full campaign can be read all at once, and a timeline showing which receivers were active during which times is shown (**Figure A4.1**). Clicking within this plot opens waveform plots for the corresponding transmitter/receiver pair. This allows data anomalies to be visualized and understood much more rapidly. Times when receivers collected usable magnetotelluric data overnight are also easily identifiable from the timeline.

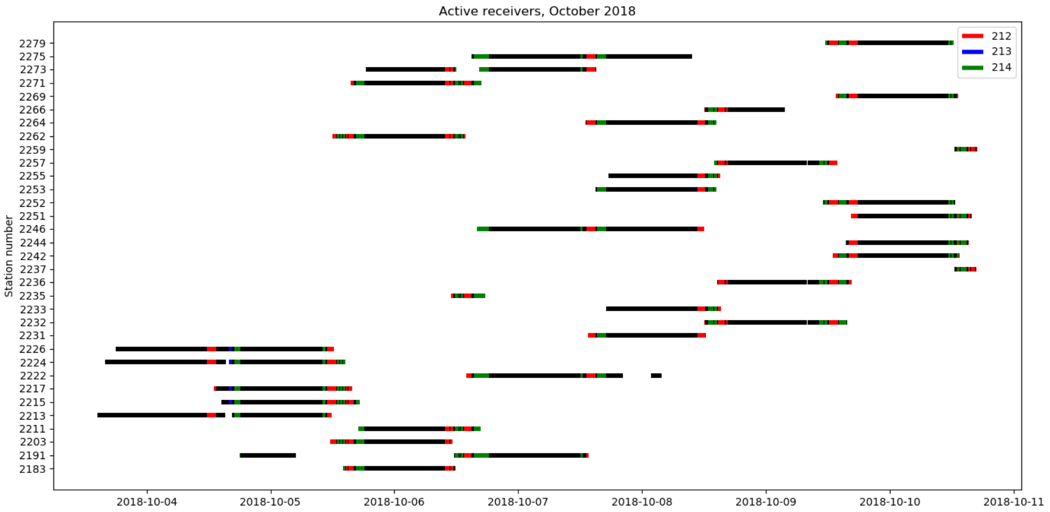

Figure A4.1: Screen shot from DoZen, showing which receiver stations were active during which times over the course of the October 2018 CSEM campaign. Red lines denote times when wells 97-11 and 23-08 were used as source electrodes. Blue lines show when wells 97-11 and 97-14 were used, and green lines show when wells 97-14 and 23-08 were used. Black lines indicate times when the transmitter was inactive. Long black lines correspond to overnight receiver deployments.

In DoZen, this plot is interactive. Clicking a colored line opens a plot of the transmitter and receiver waveforms corresponding to that time and receiver station.

DoZen provides several other tools for data processing and quality control. One tool facilitates numbering and locating stations, given GPS measurements stored in CSEM data files (**Figure A4.2**). It both allows easy correction of misnumbered receiver stations, and allows the user to dictate which measurements should be averaged together, which is useful when a station has been occupied multiple times during the same campaign.

Another useful tool displays a timeline of when receivers were in the ground, and which transmissions occurred during that time (**Figure A4.3**). The user can select any receiver station and component, and view time series data as well.

These tools are run in a browser with a Python backend, allowing platform-agnostic deployment of these tools. Some tools, like the timeline shown in **Figure A4.3**, can be saved as html files which can then be opened in any web browser, requiring no installation.

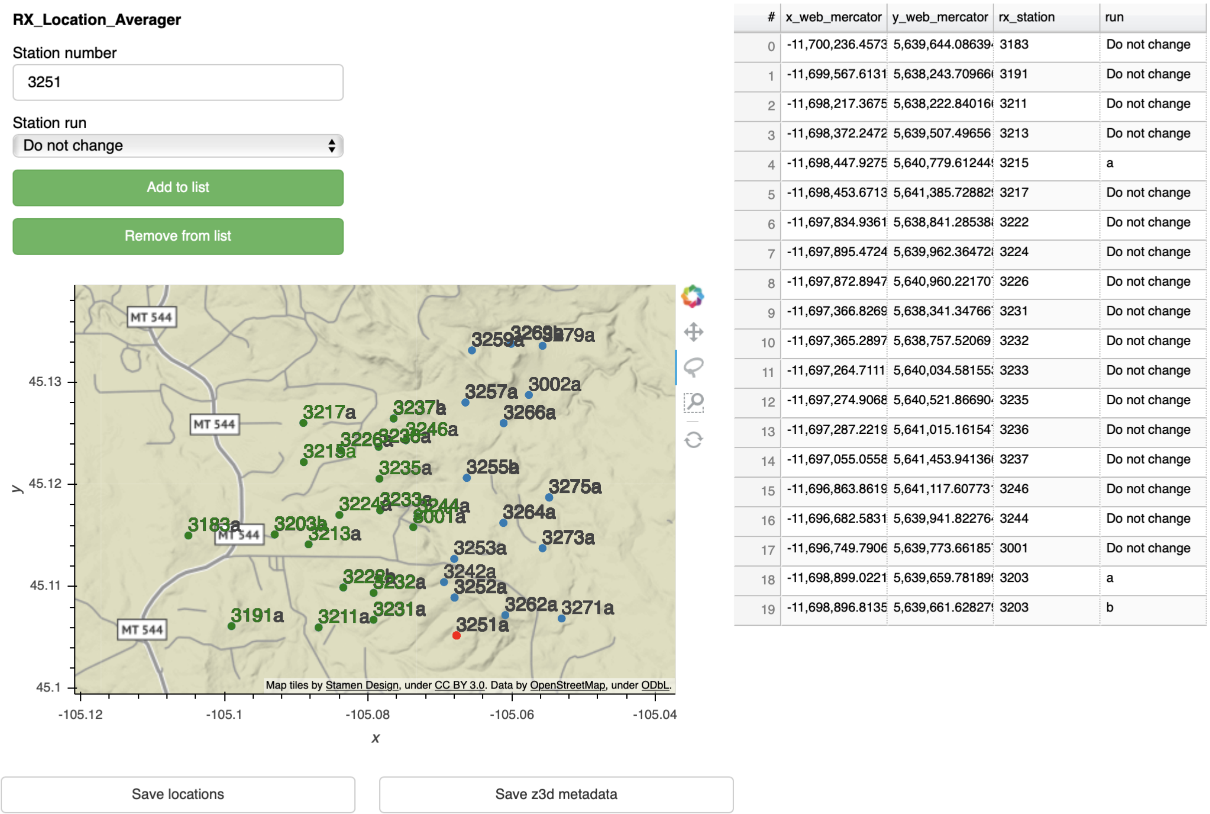

RX_Location_Averager

Station number: 3251

Station run: Do not change

#	x_web_mercator	y_web_mercator	rx_station	run
0	-11,700,236.4573	5,639,644.08639	3183	Do not change
1	-11,699,567.6131	5,638,243.70966	3191	Do not change
2	-11,698,217.3675	5,638,222.84016	3211	Do not change
3	-11,698,372.2472	5,639,507.49656	3213	Do not change
4	-11,698,447.9275	5,640,779.61244	3215	a
5	-11,698,453.6713	5,641,385.72882	3217	Do not change
6	-11,697,834.9361	5,638,841.28538	3222	Do not change
7	-11,697,895.4724	5,639,962.36472	3224	Do not change
8	-11,697,872.8947	5,640,960.22170	3226	Do not change
9	-11,697,366.8269	5,638,341.34766	3231	Do not change
10	-11,697,365.2897	5,638,757.52069	3232	Do not change
11	-11,697,264.7111	5,640,034.58155	3233	Do not change
12	-11,697,274.9068	5,640,521.86690	3235	Do not change
13	-11,697,287.2219	5,641,015.16154	3236	Do not change
14	-11,697,055.0558	5,641,453.94136	3237	Do not change
15	-11,696,863.8619	5,641,117.60773	3246	Do not change
16	-11,696,682.5831	5,639,941.82276	3244	Do not change
17	-11,696,749.7906	5,639,773.66185	3001	Do not change
18	-11,698,899.0221	5,639,659.78189	3203	a
19	-11,698,896.8135	5,639,661.62827	3203	b

Figure A4.2: A screenshot of a browser-based tool for determining station locations interactively. The CSEM data loggers record GPS positions multiple times during an occupation. If a receiver station was moved or occupied twice, the two locations should not be averaged together. The tool allows a user to both select the GPS locations that should be averaged together and to specify station ID to assign to the averaged location. Here, locations shown in green on the map have been added to a station location database. Those stations are also detailed in the table on the right.

Locations in blue are raw GPS locations from the data logger, yet to be averaged and added to the database. The red dot shows a group of GPS locations that has been selected by the user.

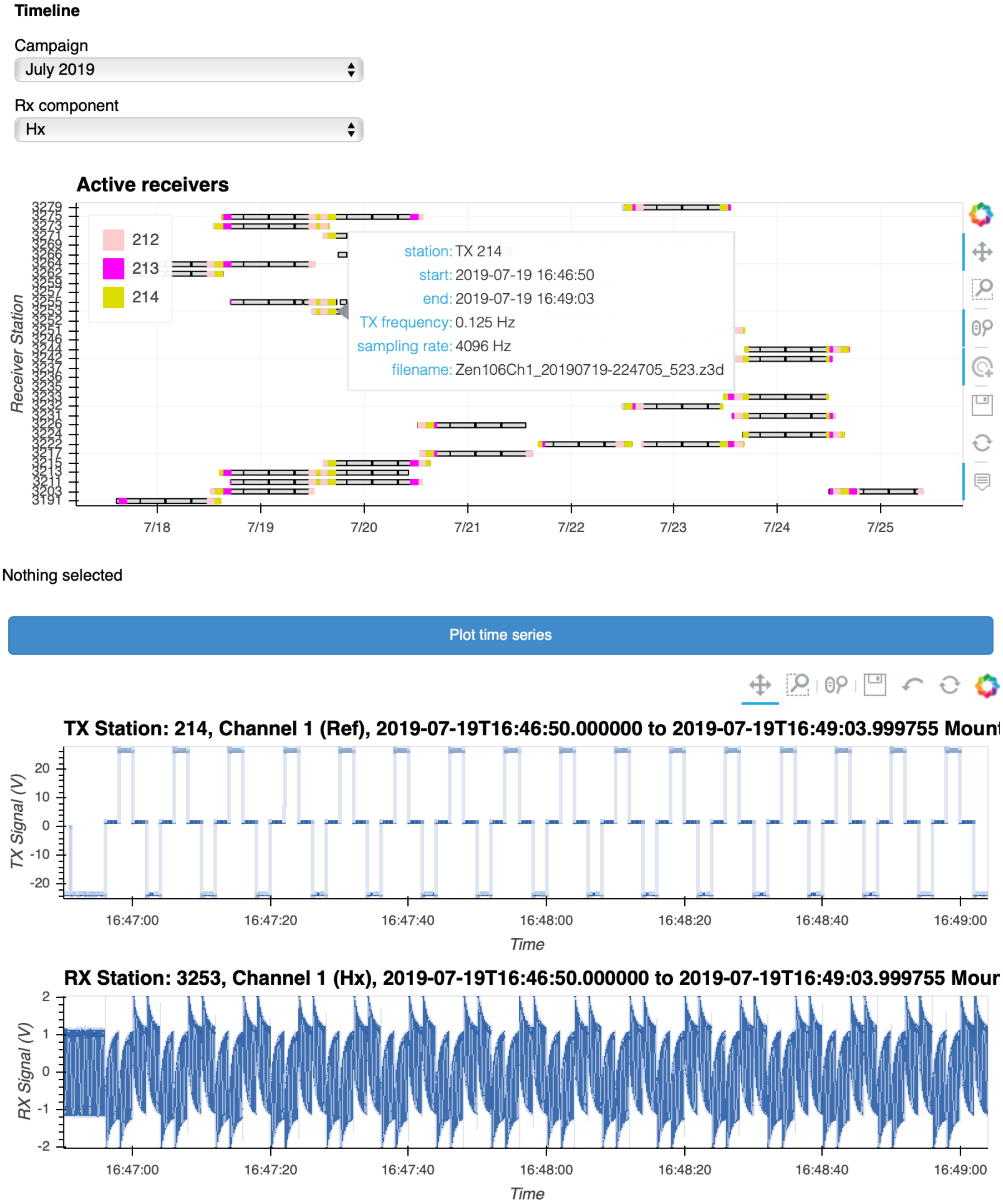

Timeline

Campaign: July 2019

Rx component: Hx

Active receivers

station: TX 214
start: 2019-07-19 16:46:50
end: 2019-07-19 16:49:03
TX frequency: 0.125 Hz
sampling rate: 4096 Hz
filename: Zen106Ch1_20190719-224705_523.z3d

Nothing selected

TX Station: 214, Channel 1 (Ref), 2019-07-19T16:46:50.000000 to 2019-07-19T16:49:03.999755 Moun

RX Station: 3253, Channel 1 (Hx), 2019-07-19T16:46:50.000000 to 2019-07-19T16:49:03.999755 Mour

Figure A4.3: A screenshot of a browser-based tool for easily viewing time series data. Any transmitter-receiver time series pair can be quickly selected and plotted, and metadata can be displayed.

Two further tools were developed. The first allows any pair of transmitter/receiver time series to be viewed, either as a pure time series (**Figure A4.4a**) or as the response at a chosen harmonic of the transmission frequency evaluated at successive time windows (**Figure A4.4b**).

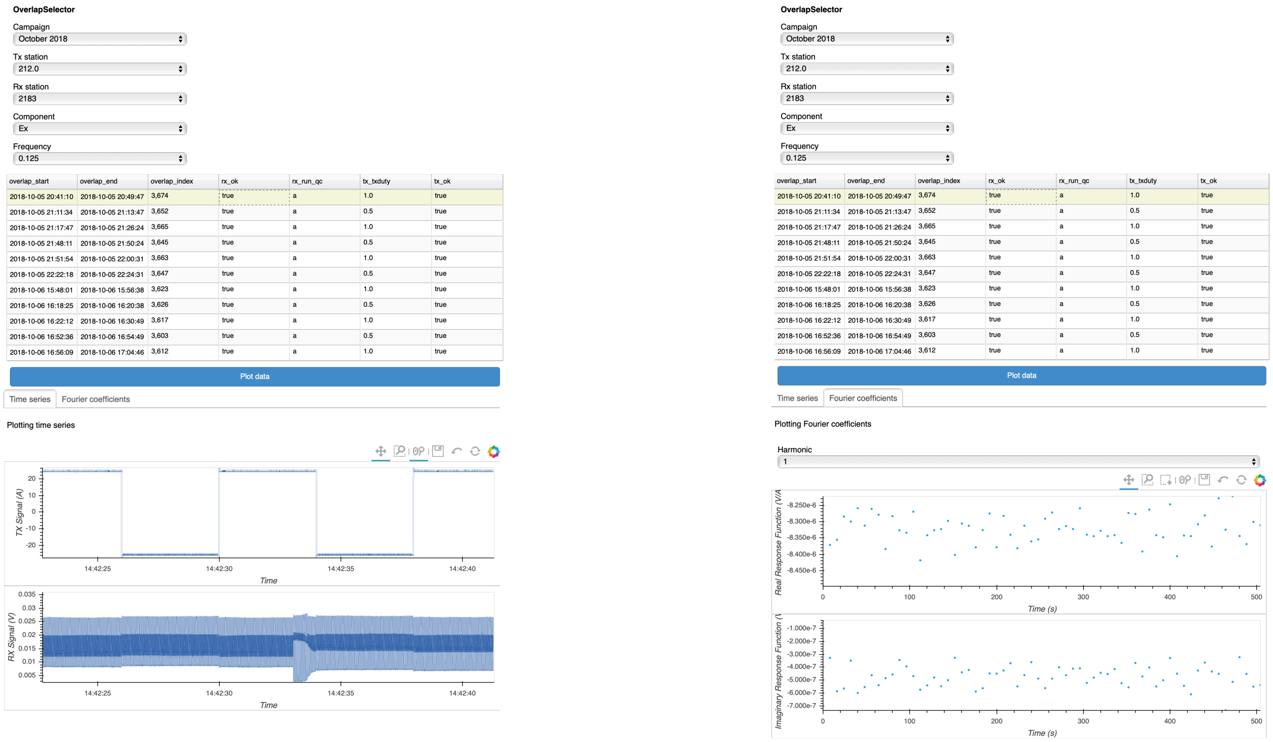

OverlapSelector

Campaign: October 2018
Tx station: 212.0
Rx station: 2183
Component: Ex
Frequency: 0.125

overlap_start	overlap_end	overlap_index	rx_ok	rx_run_qc	tx_txduty	tx_ok
2018-10-05 20:41:10	2018-10-05 20:49:47	3,674	true	a	1.0	true
2018-10-05 21:11:34	2018-10-05 21:13:47	3,652	true	a	0.5	true
2018-10-05 21:17:47	2018-10-05 21:26:24	3,665	true	a	1.0	true
2018-10-05 21:48:11	2018-10-05 21:50:24	3,645	true	a	0.5	true
2018-10-05 21:51:54	2018-10-05 22:00:31	3,663	true	a	1.0	true
2018-10-05 22:22:18	2018-10-05 22:24:31	3,647	true	a	0.5	true
2018-10-06 15:48:01	2018-10-06 15:56:38	3,623	true	a	1.0	true
2018-10-06 16:18:25	2018-10-06 16:20:38	3,626	true	a	0.5	true
2018-10-06 16:22:12	2018-10-06 16:30:49	3,617	true	a	1.0	true
2018-10-06 16:52:36	2018-10-06 16:54:49	3,603	true	a	0.5	true
2018-10-06 16:56:09	2018-10-06 17:04:46	3,612	true	a	1.0	true

Plotting time series

(a) Data viewer showing time series.

OverlapSelector

Campaign: October 2018
Tx station: 212.0
Rx station: 2183
Component: Ex
Frequency: 0.125

overlap_start	overlap_end	overlap_index	rx_ok	rx_run_qc	tx_txduty	tx_ok
2018-10-05 20:41:10	2018-10-05 20:49:47	3,674	true	a	1.0	true
2018-10-05 21:11:34	2018-10-05 21:13:47	3,652	true	a	0.5	true
2018-10-05 21:17:47	2018-10-05 21:26:24	3,665	true	a	1.0	true
2018-10-05 21:48:11	2018-10-05 21:50:24	3,645	true	a	0.5	true
2018-10-05 21:51:54	2018-10-05 22:00:31	3,663	true	a	1.0	true
2018-10-05 22:22:18	2018-10-05 22:24:31	3,647	true	a	0.5	true
2018-10-06 15:48:01	2018-10-06 15:56:38	3,623	true	a	1.0	true
2018-10-06 16:18:25	2018-10-06 16:20:38	3,626	true	a	0.5	true
2018-10-06 16:22:12	2018-10-06 16:30:49	3,617	true	a	1.0	true
2018-10-06 16:52:36	2018-10-06 16:54:49	3,603	true	a	0.5	true
2018-10-06 16:56:09	2018-10-06 17:04:46	3,612	true	a	1.0	true

Plotting Fourier coefficients

Harmonic: 1

(b) Viewer showing Fourier coefficients for the first harmonic of the transmission frequency

Figure A4.4: Browser-based data viewer tool

The second tool allows any response function to be viewed and analyzed in terms of its variance at every frequency. (**Figure A4.5**). Electromagnetic noise due to man-made sources can vary over the course of the day, affecting separate transmissions differently. This quality control tool can be used to identify unusually noisy transmissions and exclude them from the processed data. This improves the signal-to-noise ratio in the data and increases the power of the CSEM data to resolve spatial variations in CO_2 saturation.

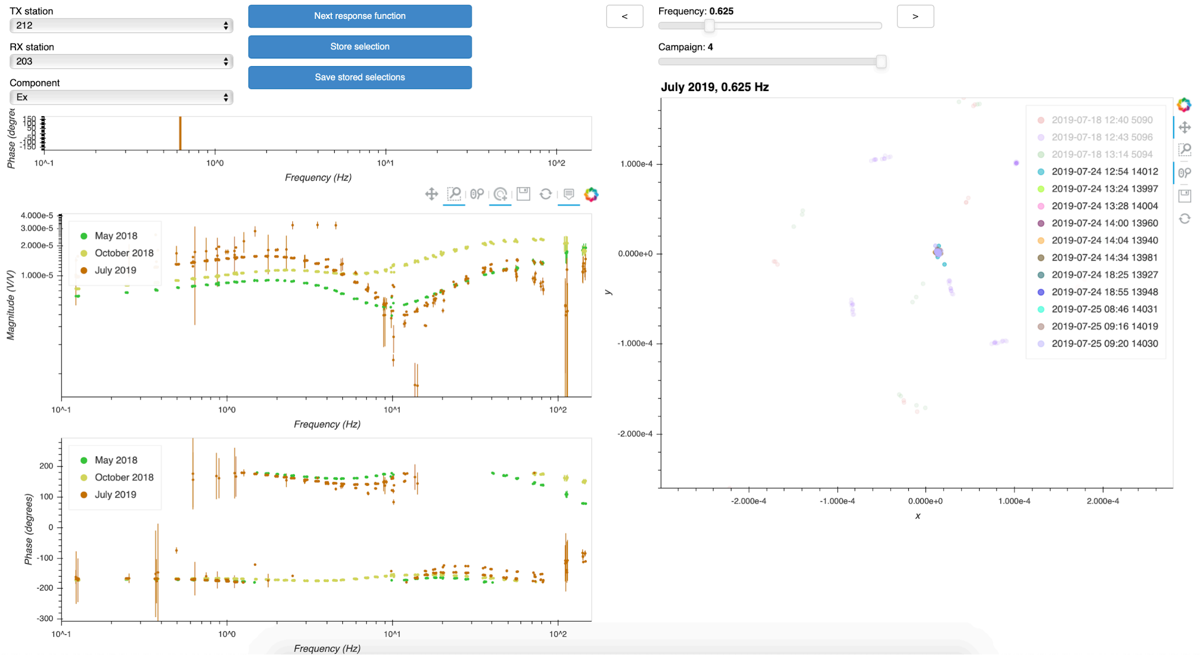

TX station: 212
RX station: 203
Component: Ex
Frequency: 0.625
Campaign: 4

Figure A4.5: Screenshot of post-processing quality control tool. At the top left, dropdown menus allow response functions to be selected for any transmitter configuration, receiver location, and EM field component. On the left, the response function for all field campaigns are plotting with error bars. On the right, the Fourier coefficients for one campaign and one frequency are plotted in the complex plane. In this example, the first three transmissions in the legend are far noisier than the rest (the rest all fall within the small cluster in the middle of the plot on the right). These have been muted due to their high noise levels.

These tools work well when used in tandem. Response functions, which combine all the transmissions for a given receiver station into one plot, can be viewed first as an overview. If any transmission looks suspiciously noisy, that transmission can be isolated and viewed in detail in the time series viewer. This provides a way to quickly identify overly noisy data within the large dataset, understand the nature of the noise, and mute noisy data as needed via an interactive graphical interface. The tools are run in a browser with a Python backend, allowing platform-agnostic deployment of the tools.

A5. TIME-DOMAIN ELECTROMAGNETIC RESULTSS

SBC_TEM_171013_BC_01a

Data_Residiual: 0.75
Total_Residiual: 0.56

Latitude, Longitude, Elev_m
45.12184002, -105.09061500, 1102.0

UTMzone, Easting_UTM_WGS84, Northing_UTM_WGS84, Elev_m
13, 492873.0, 4996489.0, 1102.0

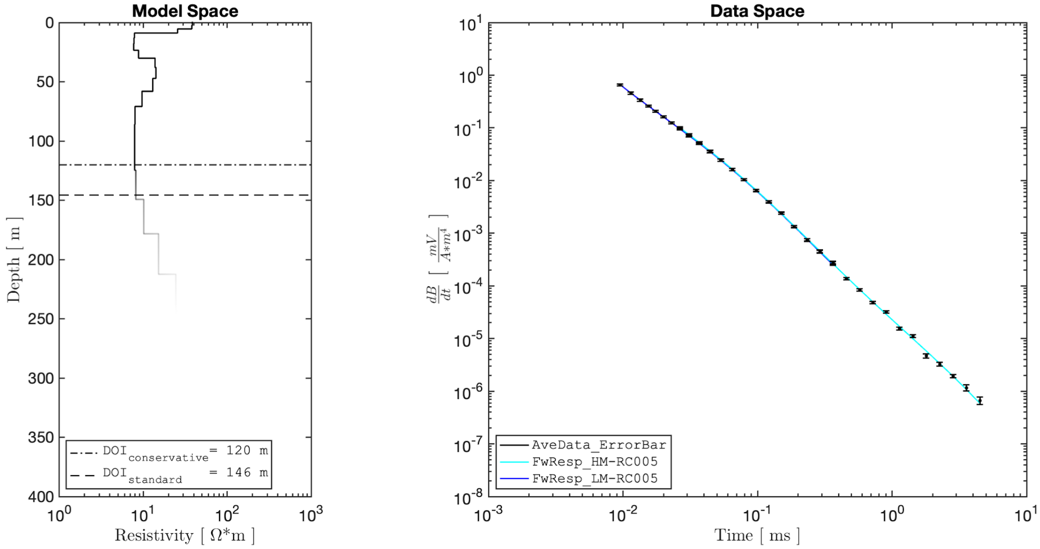

SBC_TEM_171013_BC_02a

Data_Residiual: 0.58
Total_Residiual: 0.46

Latitude, Longitude, Elev_m
45.12427102, -105.10045400, 1090.5

UTMzone, Easting_UTM_WGS84, Northing_UTM_WGS84, Elev_m
13, 492099.0, 4996760.0, 1090.5

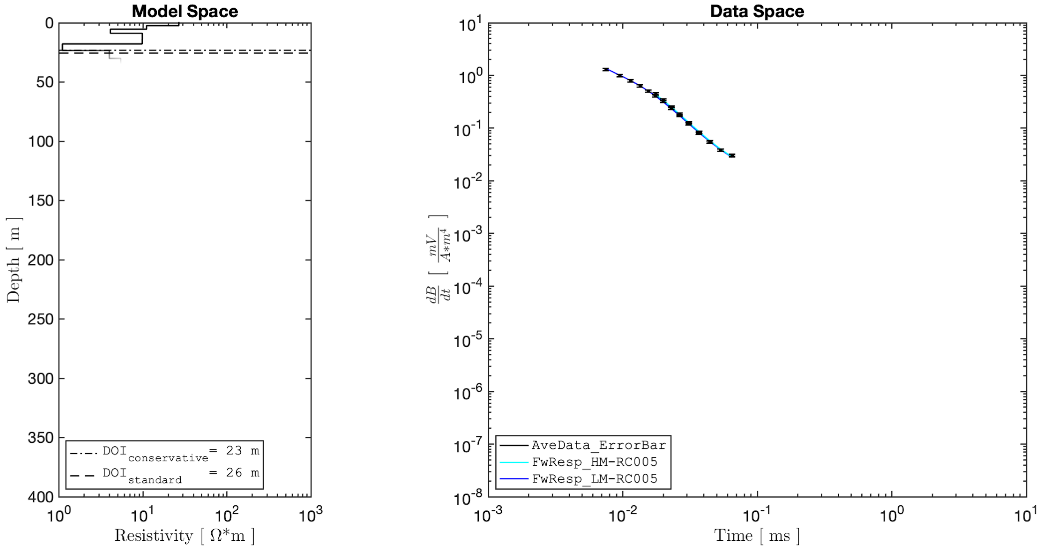

SBC_TEM_180526_R2_01a

```
 Data_Residiual: 1.55
Total_Residiual: 1.35
```

```
                         Latitude,     Longitude, Elev_m
                      45.11601651, -105.05562190, 1188.5

UTMzone, Easting_UTM_WGS84, Northing_UTM_WGS84, Elev_m
     13,          495625.0,          4995840.0, 1188.5
```

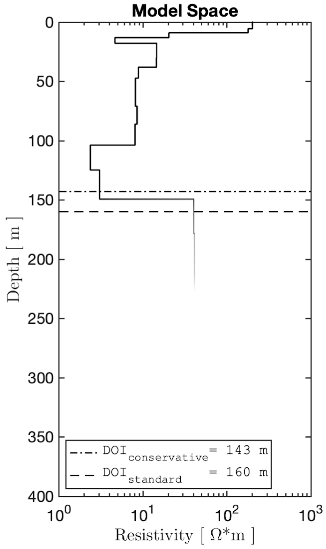

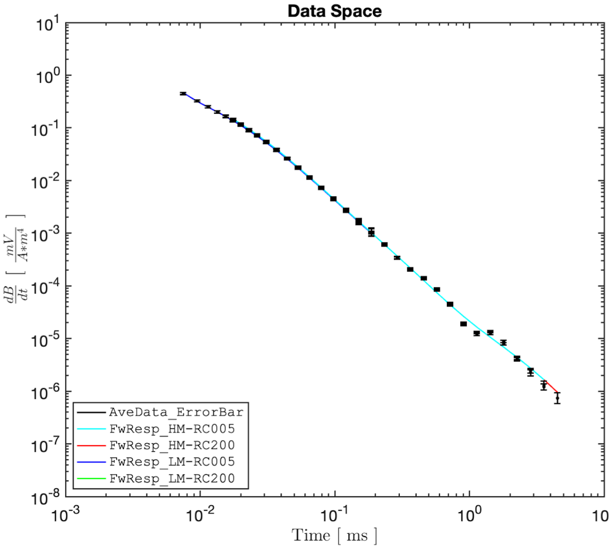

SBC_TEM_180526_R2_02a

```
 Data_Residiual: 0.62
Total_Residiual: 0.59
```

```
                         Latitude,     Longitude, Elev_m
                      45.11601505, -105.05853330, 1189.9

UTMzone, Easting_UTM_WGS84, Northing_UTM_WGS84, Elev_m
     13,          495396.0,          4995840.0, 1189.9
```

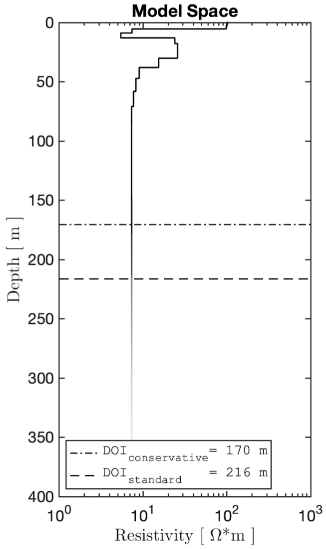

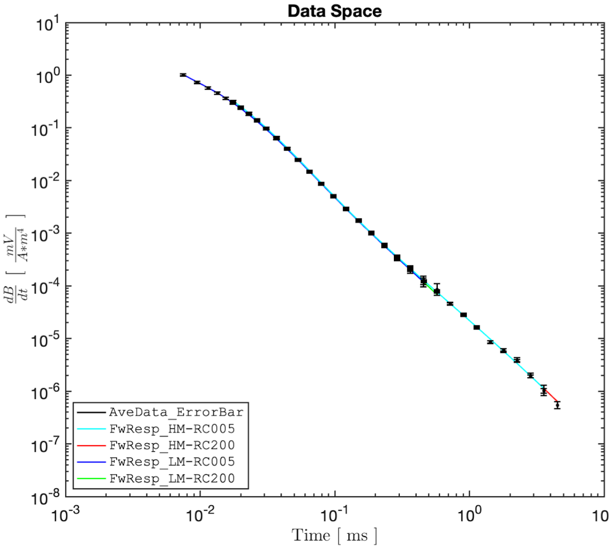

SBC_TEM_180526_R2_03a

Data_Residiual: 0.44
Total_Residiual: 0.46

Latitude	Longitude	Elev_m
45.12297222	-105.06079100	1175.6

UTMzone	Easting_UTM_WGS84	Northing_UTM_WGS84	Elev_m
13	495219.0	4996613.0	1175.6

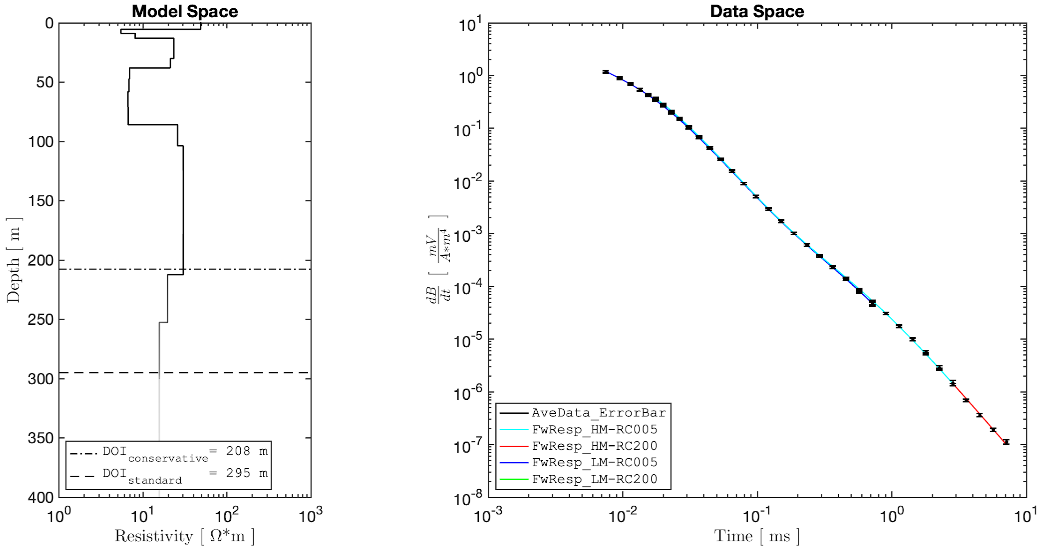

SBC_TEM_180526_R2_04a

Data_Residiual: 0.84
Total_Residiual: 0.72

Latitude	Longitude	Elev_m
45.12011542	-105.06661120	1182.5

UTMzone	Easting_UTM_WGS84	Northing_UTM_WGS84	Elev_m
13	494761.0	4996296.0	1182.5

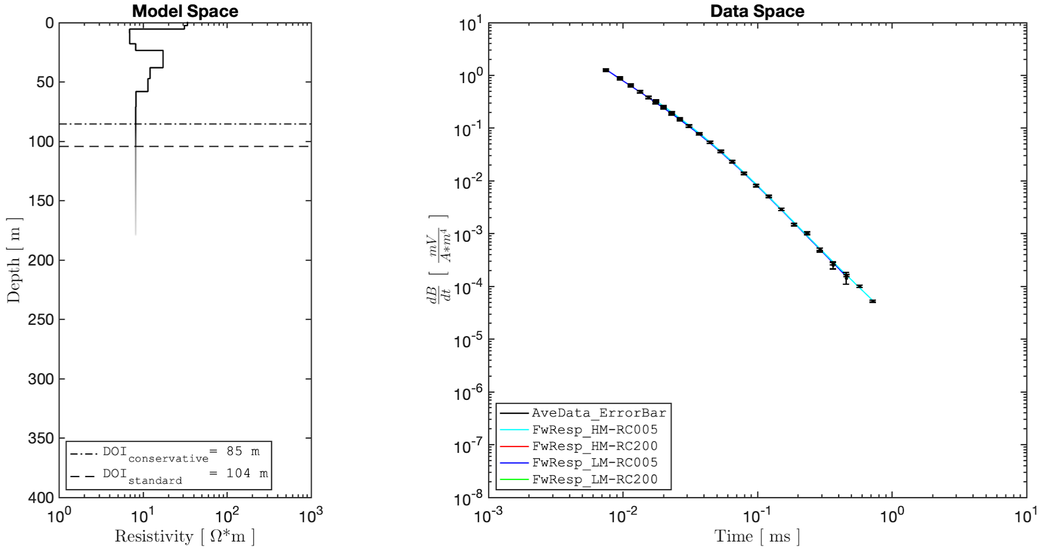

SBC_TEM_180526_R2_05a

```
                        Latitude,     Longitude, Elev_m
                     45.12669981, -105.07451550, 1165.9
```

```
 Data_Residiual: 0.49
Total_Residiual: 0.47
```

```
UTMzone, Easting_UTM_WGS84, Northing_UTM_WGS84, Elev_m
     13,          494140.0,          4997028.0, 1165.9
```

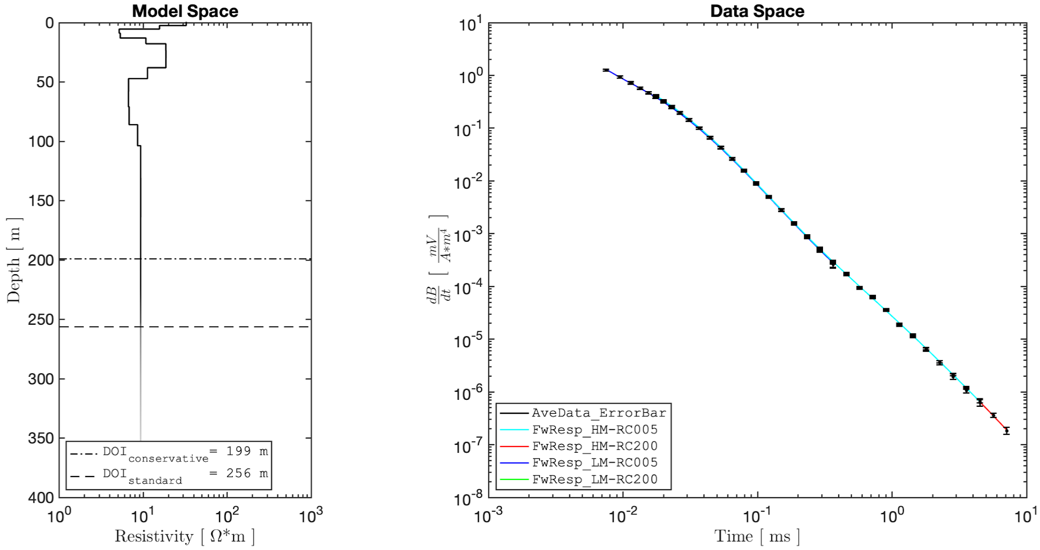

SBC_TEM_180526_R2_06a

```
                        Latitude,     Longitude, Elev_m
                     45.13294338, -105.06576130, 1214.0
```

```
 Data_Residiual: 0.68
Total_Residiual: 0.54
```

```
UTMzone, Easting_UTM_WGS84, Northing_UTM_WGS84, Elev_m
     13,          494829.0,          4997721.0, 1214.0
```

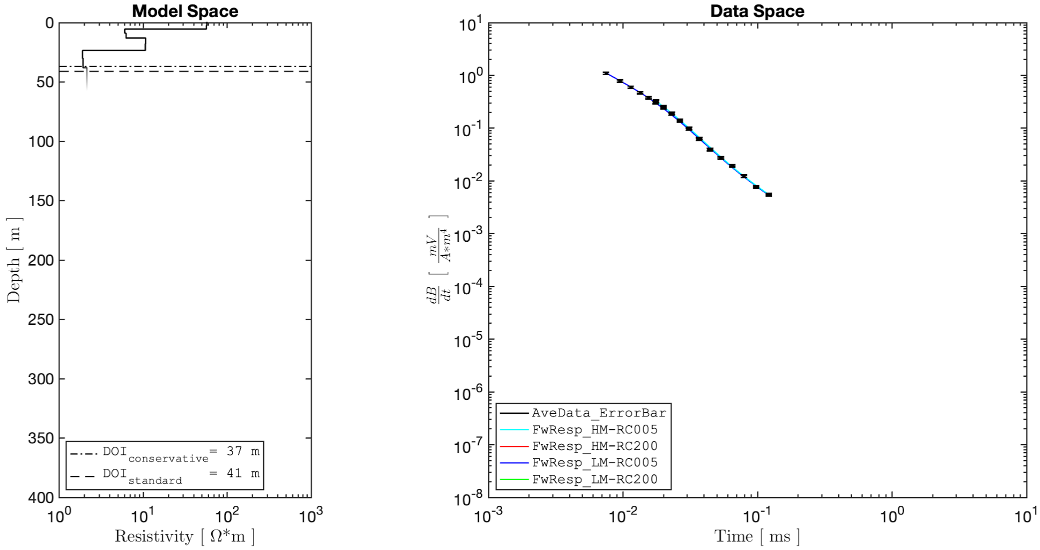

SBC_TEM_180526_R2_07a

```
Data_Residiual: 0.49
Total_Residiual: 0.46
```

```
                    Latitude,     Longitude, Elev_m
                 45.13363189, -105.05764840, 1188.9

UTMzone, Easting_UTM_WGS84, Northing_UTM_WGS84, Elev_m
     13,          495467.0,          4997797.0, 1188.9
```

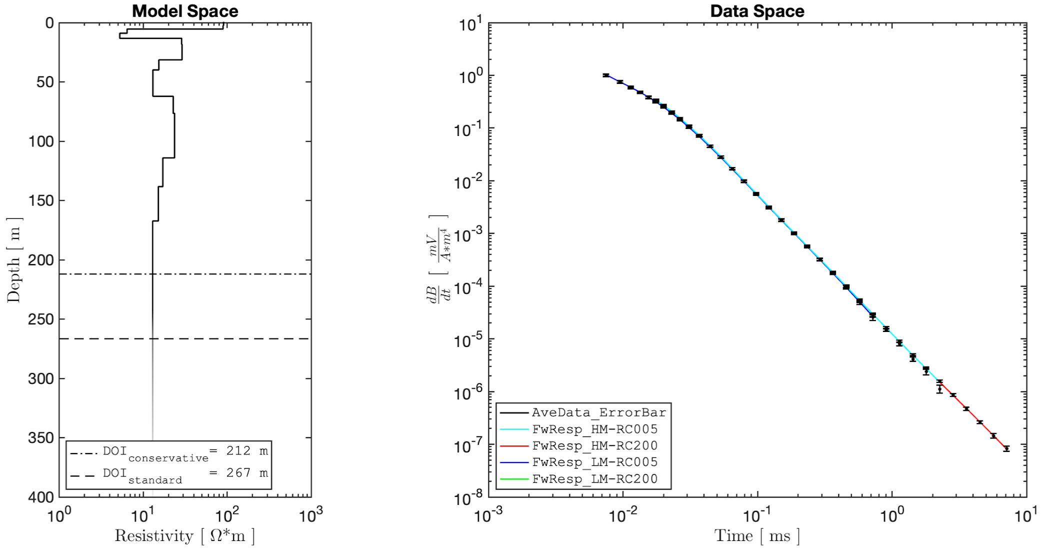

SBC_TEM_180526_R2_08a

```
Data_Residiual: 0.58
Total_Residiual: 0.52
```

```
                    Latitude,     Longitude, Elev_m
                 45.12043530, -105.07343930, 1153.6

UTMzone, Easting_UTM_WGS84, Northing_UTM_WGS84, Elev_m
     13,          494224.0,          4996332.0, 1153.6
```

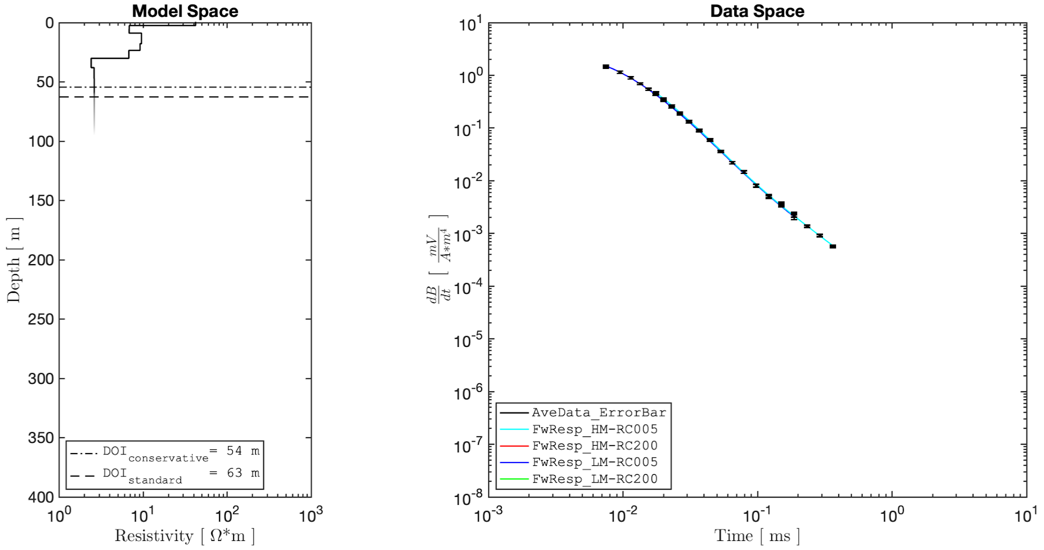

SBC_TEM_181001_R3_10a

Data_Residiual: 1.3
Total_Residiual: 1.15

Latitude,	Longitude,	Elev_m
45.10588456,	-105.07665950,	1131.2

UTMzone,	Easting_UTM_WGS84,	Northing_UTM_WGS84,	Elev_m
13,	493969.2,	4994715.8,	1131.2

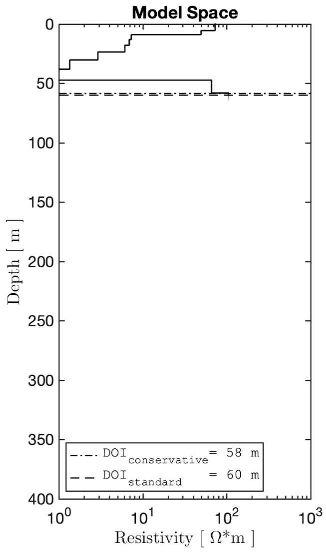

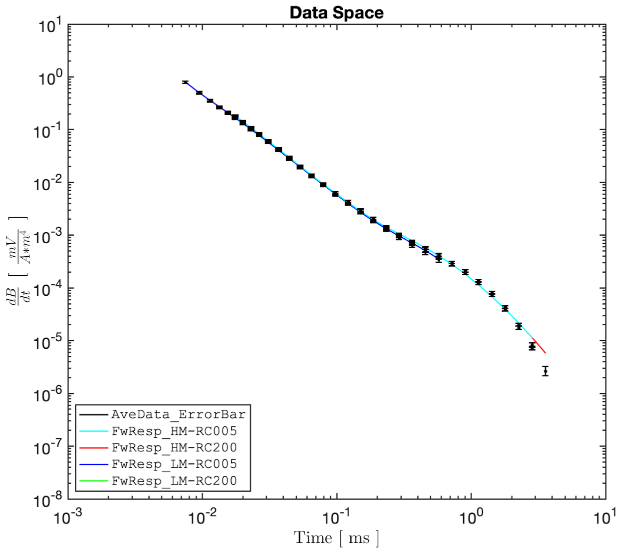

SBC_TEM_181001_R3_11a

Data_Residiual: 0.36
Total_Residiual: 0.39

Latitude,	Longitude,	Elev_m
45.10636240,	-105.08573610,	1113.3

UTMzone,	Easting_UTM_WGS84,	Northing_UTM_WGS84,	Elev_m
13,	493255.2,	4994769.6,	1113.3

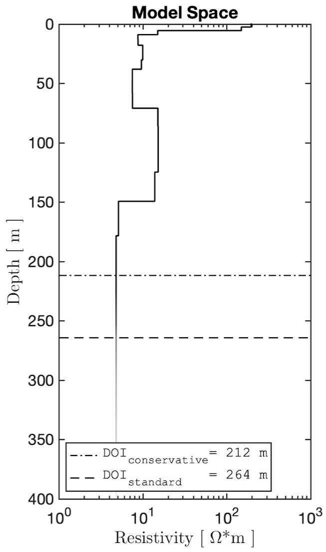

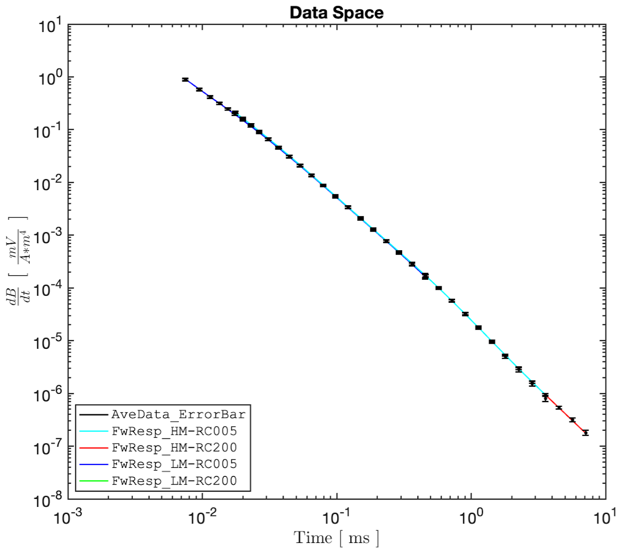

SBC_TEM_181001_R3_12a

Data_Residiual: 0.36
Total_Residiual: 0.36

Latitude,	Longitude,	Elev_m
45.11010116,	-105.08159370,	1117.9

UTMzone,	Easting_UTM_WGS84,	Northing_UTM_WGS84,	Elev_m
13,	493581.5,	4995184.6,	1117.9

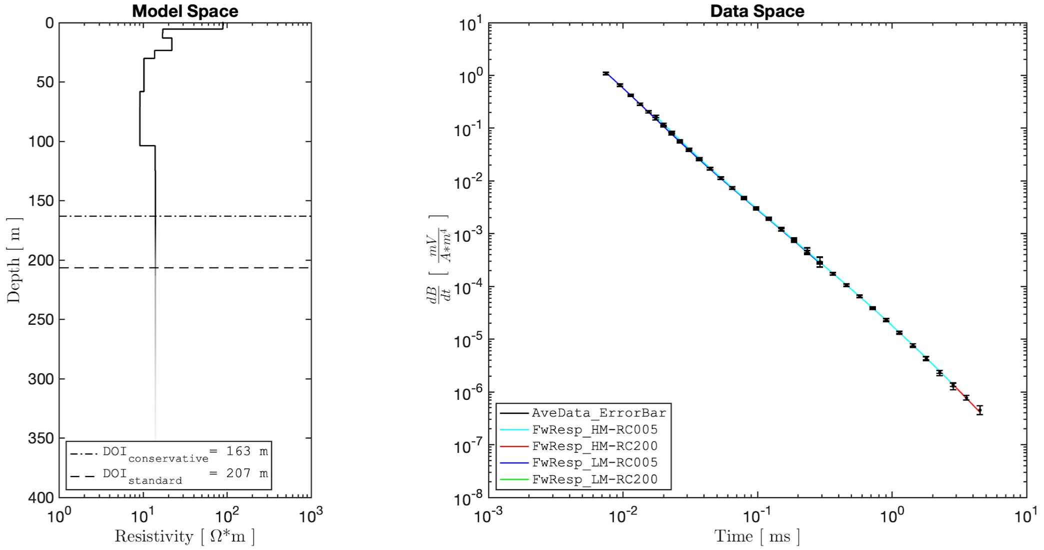

SBC_TEM_181001_R3_13a

Data_Residiual: 0.62
Total_Residiual: 0.57

Latitude,	Longitude,	Elev_m
45.11408839,	-105.08721220,	1119.6

UTMzone,	Easting_UTM_WGS84,	Northing_UTM_WGS84,	Elev_m
13,	493140.0,	4995628.0,	1119.6

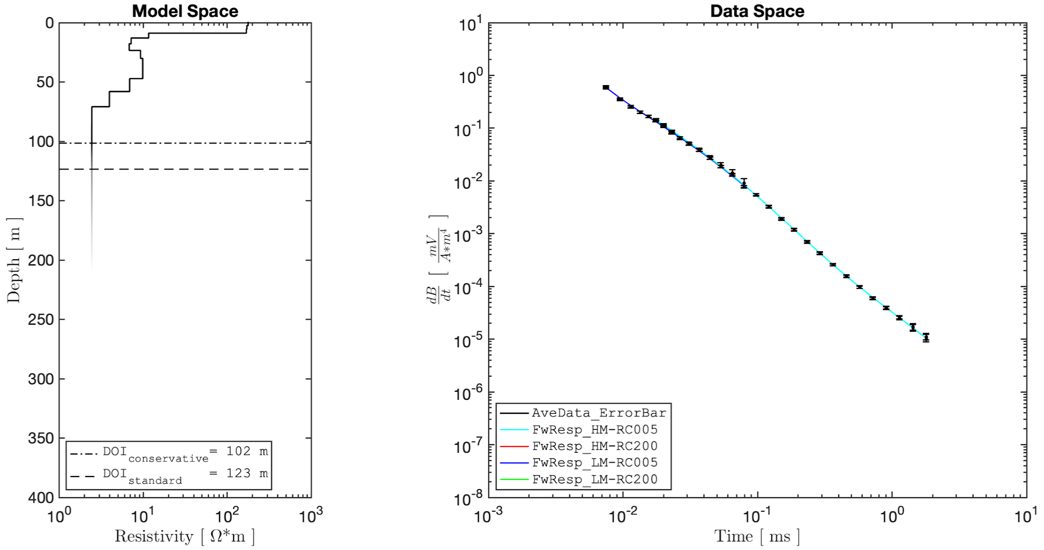

SBC_TEM_181001_R3_14a

Data_Residiual: 0.71
Total_Residiual: 0.63

Latitude,	Longitude,	Elev_m
45.12245175,	-105.08740680,	1108.3

UTMzone,	Easting_UTM_WGS84,	Northing_UTM_WGS84,	Elev_m
13,	493125.7,	4996557.1,	1108.3

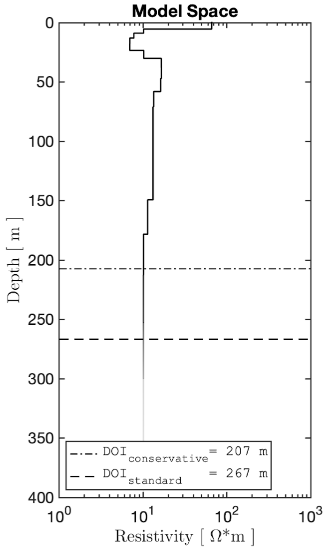

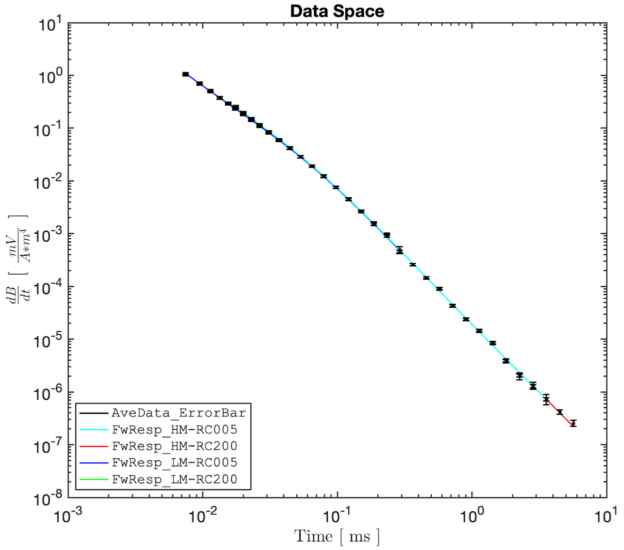

SBC_TEM_181001_R3_15a

Data_Residiual: 0.36
Total_Residiual: 0.37

Latitude,	Longitude,	Elev_m
45.12643885,	-105.08828010,	1115.6

UTMzone,	Easting_UTM_WGS84,	Northing_UTM_WGS84,	Elev_m
13,	493057.5,	4997000.1,	1115.6

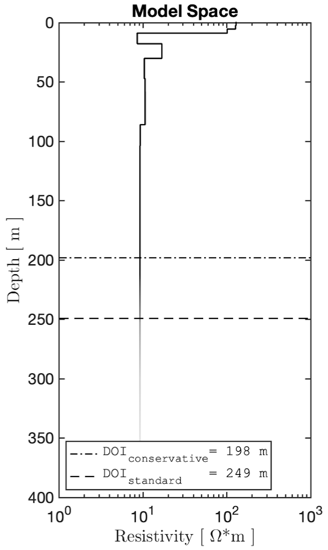

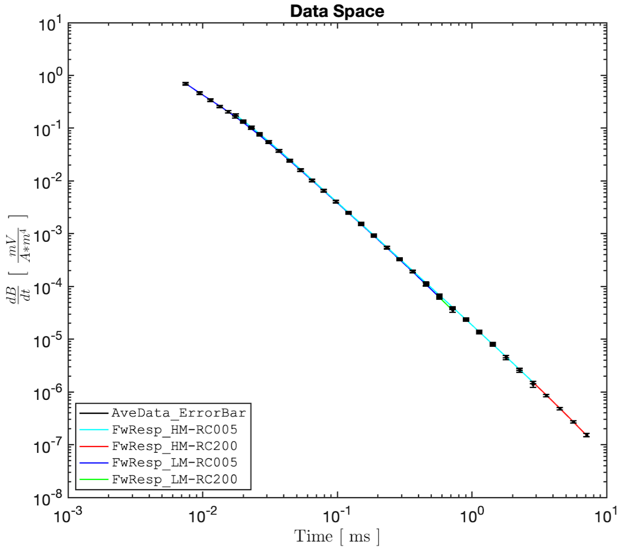

SBC_TEM_181001_R3_16a

Data_Residiual: 0.67
Total_Residiual: 0.58

Latitude, Longitude, Elev_m
45.12161726, -105.08261710, 1122.1

UTMzone, Easting_UTM_WGS84, Northing_UTM_WGS84, Elev_m
13, 493502.3, 4996464.0, 1122.1

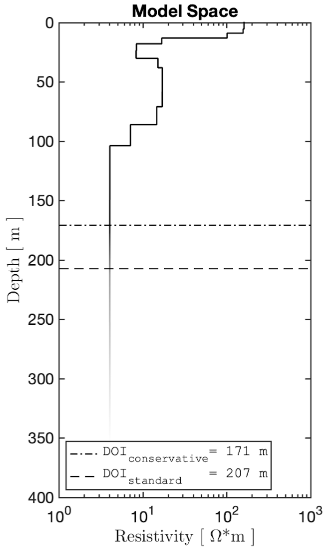

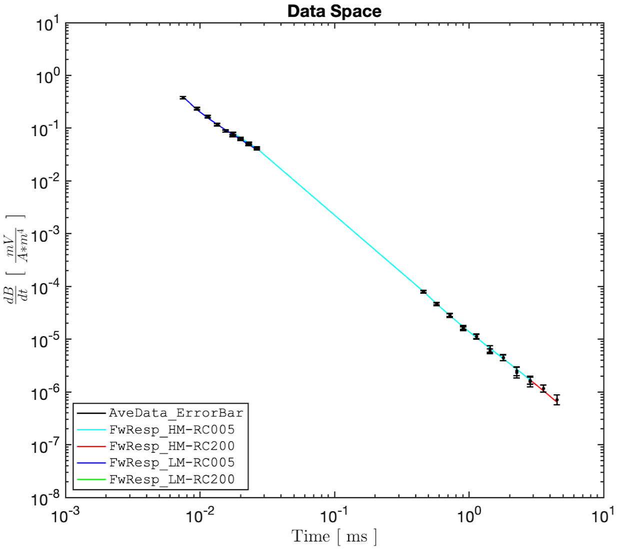

SBC_TEM_181002_R3_17a

Data_Residiual: 0.57
Total_Residiual: 0.54

Latitude, Longitude, Elev_m
45.10649793, -105.09745120, 1147.7

UTMzone, Easting_UTM_WGS84, Northing_UTM_WGS84, Elev_m
13, 492333.6, 4994785.7, 1147.7

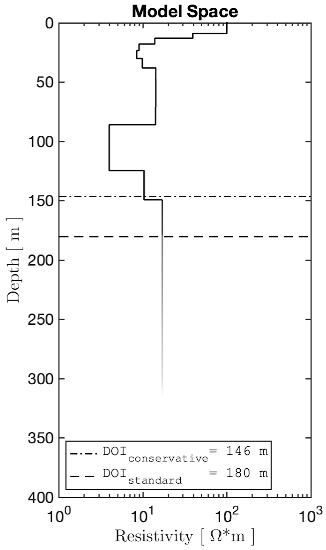

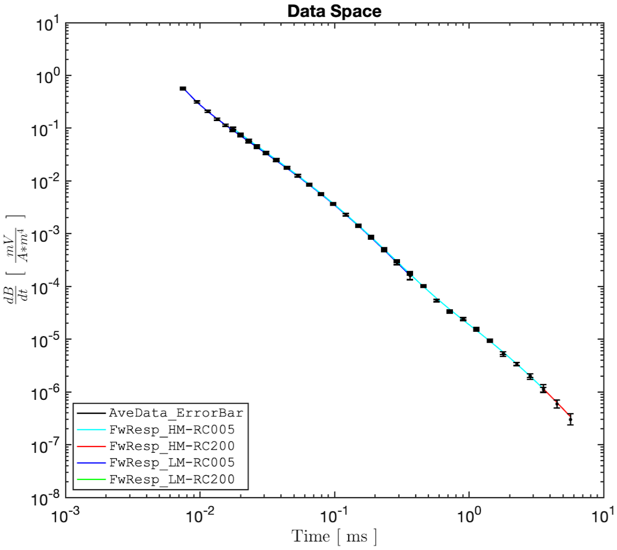

SBC_TEM_181002_R3_18a

Data_Residiual: 0.37
Total_Residiual: 0.35

Latitude,	Longitude,	Elev_m
45.11538834,	-105.10327510,	1110.4

UTMzone,	Easting_UTM_WGS84,	Northing_UTM_WGS84,	Elev_m
13,	491876.7,	4995773.9,	1110.4

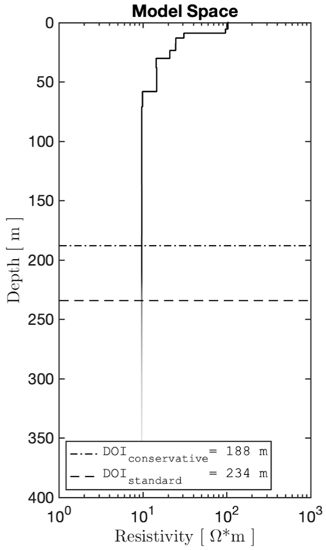

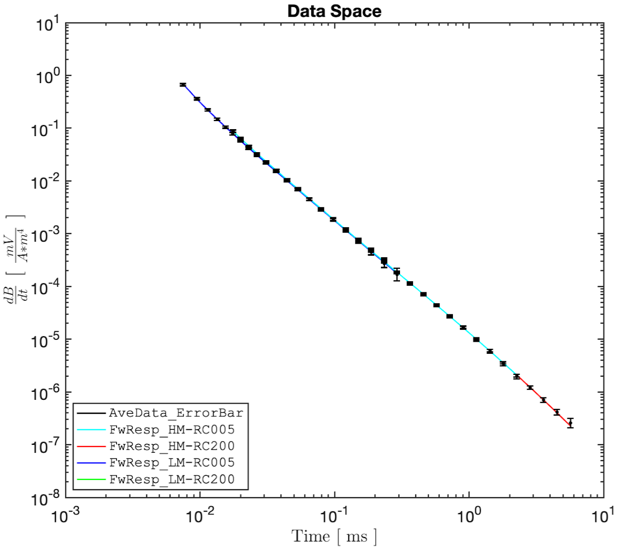

SBC_TEM_181002_R3_19a

Data_Residiual: 0.42
Total_Residiual: 0.42

Latitude,	Longitude,	Elev_m
45.10744327,	-105.06086350,	1233.9

UTMzone,	Easting_UTM_WGS84,	Northing_UTM_WGS84,	Elev_m
13,	495212.0,	4994887.9,	1233.9